

**ÉCOLE DOCTORALE DES SCIENCES CHIMIQUES**  
**Laboratoire de Biophotonique et Pharmacologie – UMR 7213**

**THÈSE** présentée par:

**Bohdan Andreiuk**

soutenue le : **29 août 2017**

pour obtenir le grade de : **Docteur de l'université de Strasbourg**

Discipline/ Spécialité : chimie/nanochimie

**Self-assembly of ionic fluorescent dyes  
inside polymer nanoparticles:  
engineering bright fluorescence and  
switching**

**THÈSE dirigée par :**

**M. KLYMCHENKO Andrey**  
**M. PIVOVARENKO Vasyl**

Directeur de recherche CNRS, Université de Strasbourg  
Professeur, Université nationale Taras Chevtchenko de Kiev

**RAPPORTEURS :**

**Mme. ANDRAUD Chantal**  
**Mme. MEALLET-RENAULT Rachel**

Directeur de recherche CNRS, ENS de Lyon  
Professeur, Université Paris-Sud

---

**AUTRES MEMBRES DU JURY :**

**M. GIUSEPPONE Nicolas**

Professeur, Université de Strasbourg, ICS



## Acknowledgements

My strongest gratitude goes to my supervisors – Dr. Andrey Klymchenko and Prof. Vasyl Pivovarenko, without whom I definitely wouldn't have become who I am, and I consider meeting them in my life being a huge luck. Prof. Pivovarenko has been my supervisor for more than 6 years, and has always been a deep source of knowledge, inspiration and support for me – Thank You. Under the supervision of Dr. Klymchenko in just three years I have learnt about science and research more than I could ever imagine, and during our every discussion I feel how much more I can learn - Thank You.

I thank committee members for accepting the invitation to examine my work: Dr. Chantal Andraud from ENS de Lyon, Prof. Rachel Meallet-Renault from Université Paris-Sud and Prof. Nicolas Giuseppone from Strasbourg University. Hope you will find my results interesting.

I thank Dr. Andreas Reisch for all our fruitful collaboration and discussions, Dr. Mayeul Collot for his advices and all the fun we had in the chemlab, Dr. Frédéric Przybilla, Dr. Pascal Didier, Dr. Nicolas Humbert, and Dr. Ludovic Richert for their guidance and help with all the instrumental issues. I am thankful to PACSI team for all the analysis they made, often really urgent and tricky. I thank Dr. Guy Duportail, Marlyse Wernert and Ingrid Barthel for their help in various situations.

Many thanks, of course, goes to my family for their constant support and belief in me.

My labmates and colleagues, fellow PhD and master students – we had so much fun together, learnt from each other and I thank you all for that.

LabEx Chimie des Systèmes Complexes and ERC Consolidator grant BrightSens 648528 are acknowledged for providing financial support for this work.

# Contents

Acknowledgements .....	3
Contents.....	4
List of used Abbreviations .....	6
1. Bibliographical overview.....	7
1.1. Basics of fluorescence.....	8
1.1.1. Photophysics of aggregated dyes .....	10
1.1.2. Fluorescence anisotropy .....	15
1.2. Main types of luminescent nanoparticles.....	17
1.2.1. Inorganics-based nanoparticles .....	17
1.2.2. Fluorescent organic nanoparticles .....	21
1.3. Encapsulation of dyes inside nanoparticles .....	28
1.4. Preventing dye self-quenching.....	40
1.4.1. NPs with covalent fixation of dyes inside polymer matrix .....	40
1.4.2. NPs encapsulated with bulky dyes .....	44
1.4.3. Aggregation-induced emission NPs .....	48
1.5. Weakly coordinating anions in fluorescent nanomaterials .....	51
Aim of my PhD project.....	61
2. Results and discussions.....	62
2.1. Enhancing emission of cyanine dyes.....	63
2.1.1. Article 1: “Fluorescent Polymer Nanoparticles for Cell Barcoding In Vitro and In Vivo” .....	63
2.2. Investigating the effect of a counterion structure on fluorescent NPs properties.....	119

2.2.1. Counterion-enhanced encapsulation and emission of cationic dyes in polymeric nanoparticles: the role of counterion nature.....	119
2.2.2. Article 2: Aluminium-based fluorinated counterion for enhanced encapsulation and emission of dyes in biodegradable polymer nanoparticles	137
2.2.3. Bulky hydrophobic barbiturates for enhanced encapsulation and emission of cationic dyes inside polymer nanoparticles .....	159
Conclusions and perspectives.....	167
3. Materials and Methods .....	169
3.1. Chemical synthesis.....	170
3.1.1. Fluorescent Polymer Nanoparticles for Cell Barcoding In Vitro and In Vivo .....	170
3.1.2. Counterion-enhanced encapsulation and emission of cationic dyes in polymeric nanoparticles: the role of counterion nature.....	176
3.1.3. Aluminium-based fluorinated counterion for enhanced encapsulation and emission of dyes in biodegradable polymer nanoparticles .....	182
3.1.4. Bulky hydrophobic barbiturates for enhanced encapsulation and emission of cationic dyes inside polymer nanoparticles .....	184
3.2. Preparation of nanoparticles .....	191
3.3. Characterisation of nanoparticles .....	191
3.4. Wide-field microscopy.....	192
3.5. Cellular studies .....	193
References.....	197
4. Resume of thesis in English .....	206
5. Résumé de these en Français .....	216
List of publications.....	227
List of presentations .....	229

## List of used Abbreviations

ACQ	Aggregation-caused quenching
AIE	Aggregation-induced emission
EET	Excitation energy transfer
FNPs	Fluorescent nanoparticles
FRET	Forster resonance energy transfer
HOMO	Higher occupied molecular orbital
IPS	Ideal polymethine state
LC	Lipophilic compartment
LNC	Lipid nanocapsules
LR	Lumogen Red
LUMO	Lower unoccupied molecular orbital
MWCO	Molecular weight cut-off
NE	Nanoemulsion
NIR	Near-Infrared
NPs	Nanoparticles
PBCA	Poly(butylcyanoacrylate)
PDI	Perylenediimide
PDLLA	Poly(D,L-lactic acid)
PFC	Perfluorocarbon
PIC	Pseudoisocyanine
PLGA	Poly(lactic-co-glycolic acid)
PM	Polymeric micelle
QY	Quantum yield
TICT	Twisted intramolecular charge transfer
WCA	Weakly coordinating anion

# 1. Bibliographical overview

## 1.1. Basics of fluorescence

Despite there are several definitions of what is *fluorescence*, the most common way to define it would be “emission of light from excited singlet state of a molecule after light absorption”. Fluorescent molecules are called *fluorophores*. After a fluorophore receives a portion of energy in form of, for example, electromagnetic irradiation (light), it transitions to excited state with higher energy. There are different ways for a molecule to relax to its ground state, and several of them are depicted at this simplified version of Jablonski diagram (Figure 1.1.1).

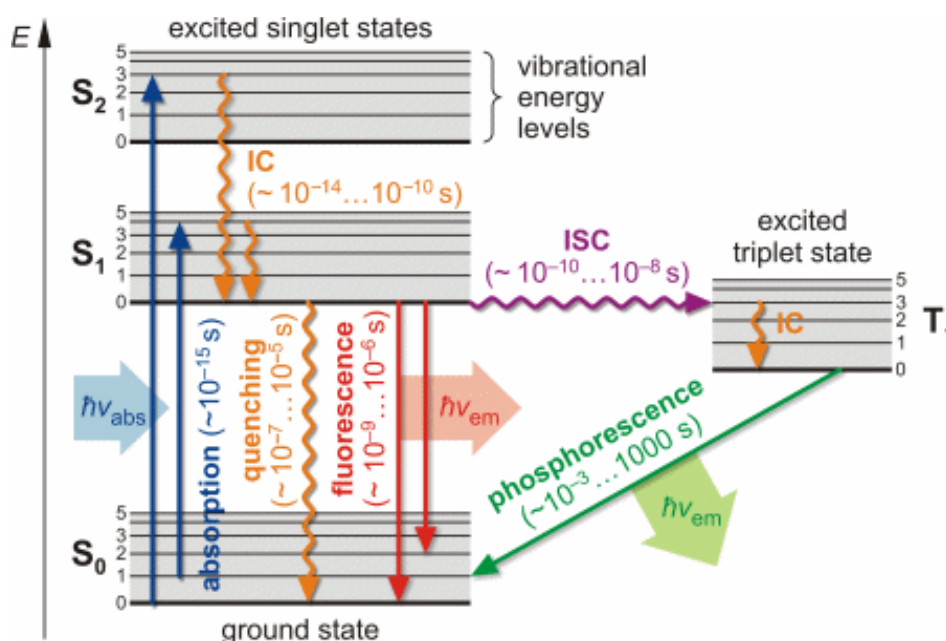


**Figure 1.1.1.** Jablonski diagram illustrates the transitions between different electronic states of a molecule for fluorescence and phosphorescence phenomena.  
Adapted from <http://home.uni-leipzig.de>.

Whenever a molecule in the ground state (S<sub>0</sub>) gets excited (straight blue line) to higher energy states (S<sub>1</sub>, S<sub>2</sub>, etc.), it can get rid of the excessive energy by radiative (straight lines) or nonradiative (wavy lines) pathways<sup>1</sup>. Fluorescence (red straight line) occurs from S<sub>1</sub> state (Kasha’s rule), as a molecule, excited to higher levels would rapidly relax to S<sub>1</sub> state through nonradiative processes generally called *internal conversion* (IC, orange wavy lines). Except fluorescence, other paths for energy migration from S<sub>1</sub> level are nonradiative transitions to S<sub>0</sub> (quenching, internal motions etc.) or intersystem crossing (ISC, purple wavy line) to T<sub>1</sub>, excited triplet state. As the transition from T<sub>1</sub> to S<sub>0</sub> is one of the forbidden ones, its probability is very low, therefore

fluorophore can remain in  $T_1$  state for up to  $10^{12}$  longer than its usual lifetime in  $S_1$  state. Radiative transition from  $T_1$  to  $S_1$  is called *phosphorescence* (green straight line).

Despite the time that fluorophore would spend in excited state cannot be precisely predicted due to quantum world limitations, the average value for a population can be determined. The average time, spent in singlet excited state, is called *fluorescence lifetime*<sup>2</sup>. It depends on radiative (fluorescence) and non-radiative decay rates of the selected molecule in excited state. Changes in fluorescence lifetimes can occur depending on the fluorophore surroundings, for example, trapping a dye in a rigid matrix, like polymer, can increase lifetime, comparing to the dye in solution, while adding a quencher, energy acceptor, to the system, can decrease it. Generally, decreasing the non-radiative decay rate increases fluorescence lifetimes, which leads to more efficient dye fluorescence.

*Quantum yield* (QY) of the system is the ratio of the number of emitted photons to the number of absorbed photons. It is one of the key characteristics of system brightness and decreases with increasing number of non-radiative decay rate. It is in the range of  $0 < QY < 1$ . *Stokes shift* is a phenomenon of emitted photons having lower energy than absorbed ones. It occurs because of ultrafast relaxation to the lowest vibrational level of  $S_1$ , while radiative transition can take place to higher vibrational levels of  $S_0$ , resulting in an additional loss of energy. Fluorophores can display larger Stokes shifts due to solvent effects, complex formation, excited state reactions, and/or transfer of energy.

Characteristic, responsible for light absorption efficiency of a molecule, is called *molar extinction coefficient* and is measured in  $M^{-1}cm^{-1}$ . It depends on excitation wavelength and is governed by fluorophore structure. Finally, *brightness* is defined as a product of quantum yield and molar extinction coefficient.

### 1.1.1. Photophysics of aggregated dyes

Upon dyes aggregation due to, for example, low solubility, they can form supramolecular structures, like dimers or more complicated assemblies, in general called aggregates. This aggregation process can change optical properties of the system, depending on the nature of the formed aggregates (Figure 1.1.2).

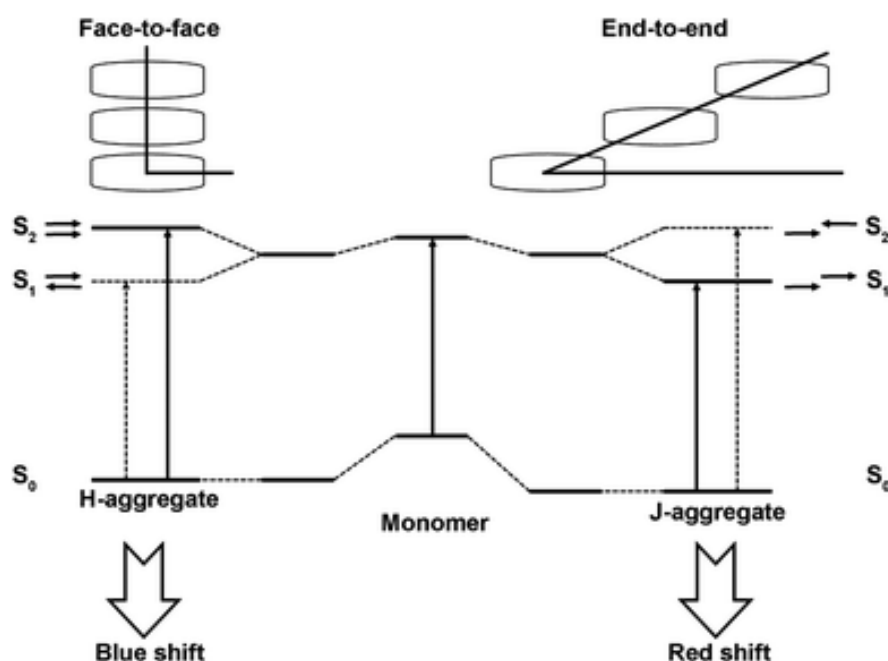


**Figure 1.1.2.** Schematic presentation of the relationship between dye molecule arrangement and spectral shift of H-aggregate and J-aggregate based on the molecular exciton theory. Adapted from ref.<sup>3</sup>

Aggregates of dyes, which are arranged in a face-to-face manner (parallel, plane-to-plane, sandwiched etc.), demonstrating blue shift in absorption (comparing to monomer) and no fluorescence, are called *H-aggregates*<sup>4, 5</sup>. Typical change in absorption spectra due to H-aggregate formation is depicted in Figure 1.1.3 – the short-wavelength shoulder of the spectrum increases with increasing concentration of aggregates. Their formation is one of the main reasons of aggregation-caused quenching (ACQ).

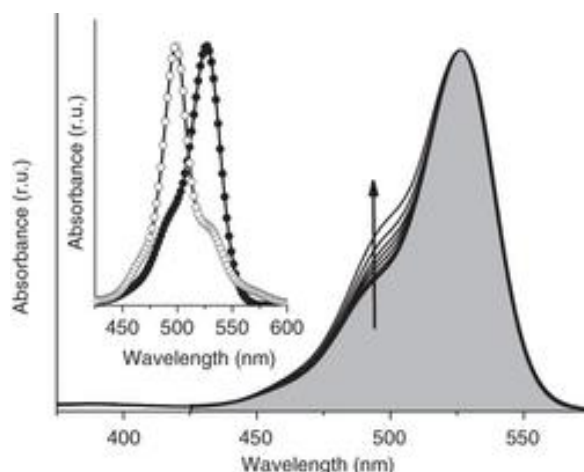


**Figure 1.1.3.** Typical changes in the absorption spectrum caused by dye aggregation (H-type aggregates). The inset shows the pure spectra of the monomer (filled circles) and the aggregate (open circles). Adapted from ref.<sup>6</sup>

When the dyes are organised in an end-to-end manner (head-to-tail, ladder etc.), absorption and emission of such system are shifted to the red and become narrower, while the Stokes shift gets very small. Such system is called *J-aggregate*<sup>5, 7</sup>. In Figure 1.1.4 the sharp peak about 605 nm is a typical example of a J-aggregate absorption.

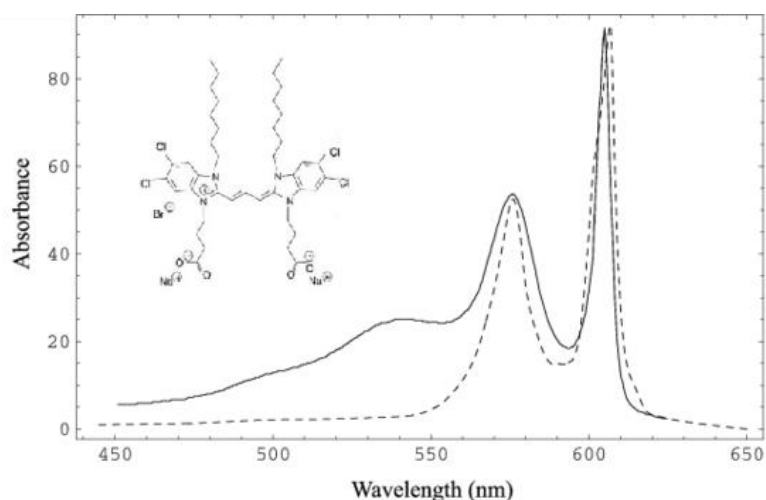


**Figure 1.1.4.** The J-aggregate absorption spectrum of the depicted molecule. Continuous line - the measured spectrum. Dashed line - the theoretical spectrum. Adapted from ref.<sup>8</sup>

As a molecule in the excited state becomes more reactive, it obtains the ability to form complexes (e.g. intermolecular charge-transfer complexes) with other molecules, which leads to changes in spectral behaviour. Such excited-state complexes are called *exciplexes*. Classical example – exciplex of anthracene with diethylaniline. Formation of this exciplex can be detected in fluorescence spectra as the appearance of new broad red-shifted band (Figure 1.1.5).

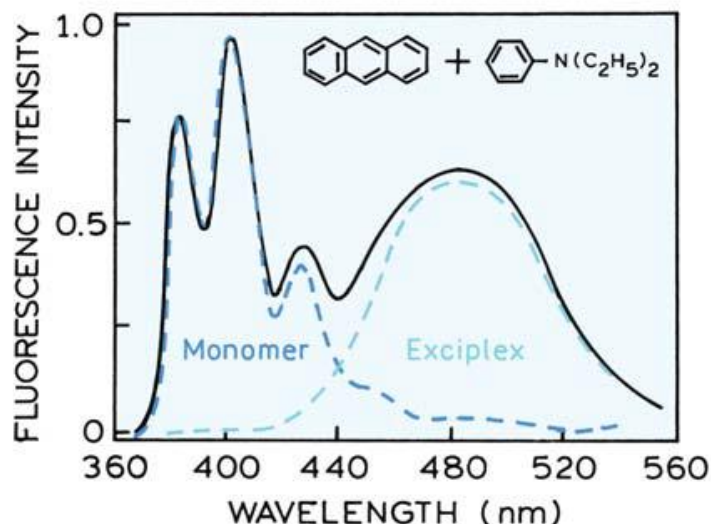


**Figure 1.1.5.** Emission spectrum of anthracene in toluene containing 0.2 M diethylaniline. The dashed lines show the emission spectra of anthracene or its exciplex with diethylaniline. Adapted from ref.<sup>9</sup>

When the dye in excited state forms a complex with itself, such complex is called *excimer* (abbreviated from excited-state dimer). One of the most famous excimers are formed by pyrene dye and are detected in fluorescence spectra as new red-shifted band without fine structure of pyrene monomer emission (Figure 1.1.6).

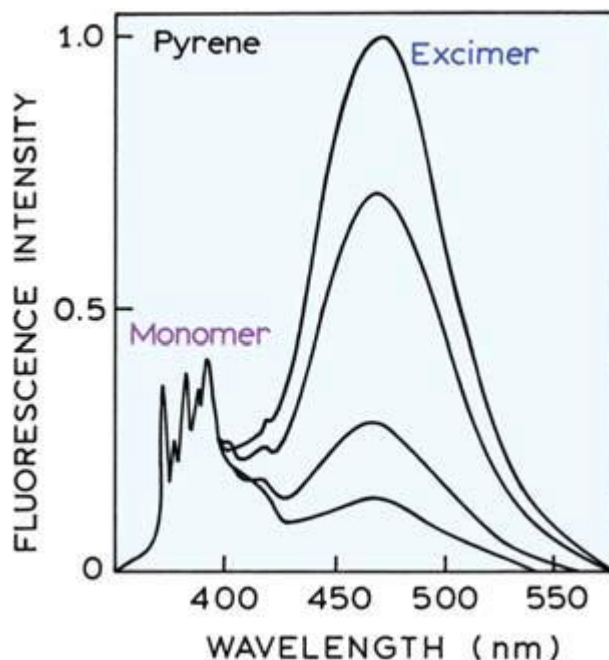


**Figure 1.1.6.** Emission spectra of pyrene and its excimer. The relative intensity of the excimer peak (470 nm) decreases as the total concentration of pyrene is decreased from  $6 \times 10^{-3}$  M (top) to  $0.9 \times 10^{-4}$  (bottom). Adapted from ref.<sup>10</sup>

Another type of interaction in excited state is *Dexter interaction*, also called *electron exchange*. It occurs between an electron donor and electron acceptor molecules. Excited donor molecule transfers an electron from its lower unoccupied

molecular orbital (LUMO) to acceptor's LUMO, while acceptor transfers an electron from its higher occupied molecular orbital (HOMO) to donor's HOMO (Figure 1.1.7). This process results in energy transfer from donor to acceptor, therefore quenching the donor's fluorescence. It should be noted, that it requires distances between dyes below 1 nm and therefore it is a quite rare phenomenon.

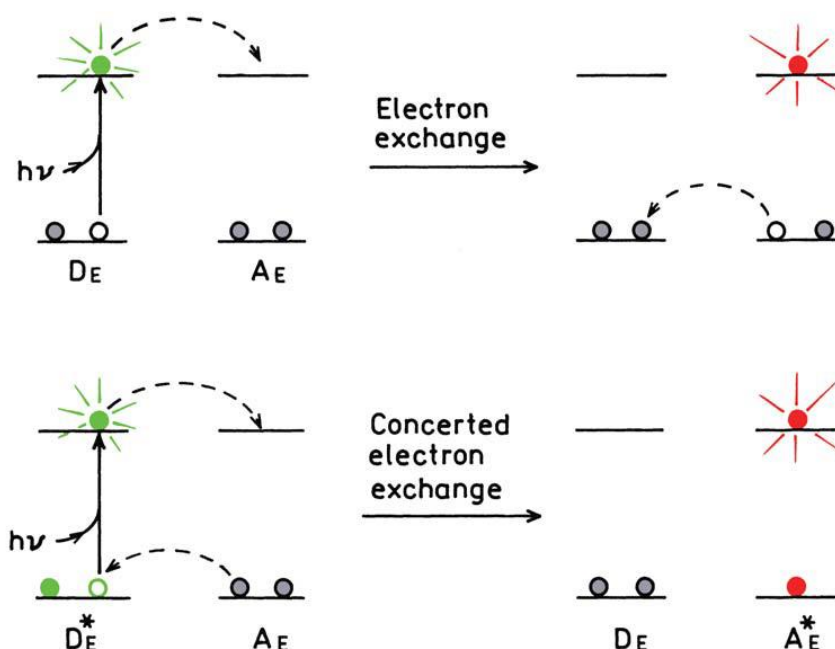


**Figure 1.1.7.** Schematic for stepwise (top) or concerted (bottom) electron exchange. Adapted from ref.<sup>1</sup>

An interaction between electron donor and an electron acceptor in the excited state can also lead to a complex formation of a  $D^+A^-$  form, where an electron is transferred from electron-donor to electron-acceptor (Figure 1.1.8). This transfer is called *photoinduced electron transfer* (PET), and is well-known as a fluorescence quenching mechanism. The obtained charge-transfer complex is able to return to the ground state with (rare) or without (more often) emission of a photon.

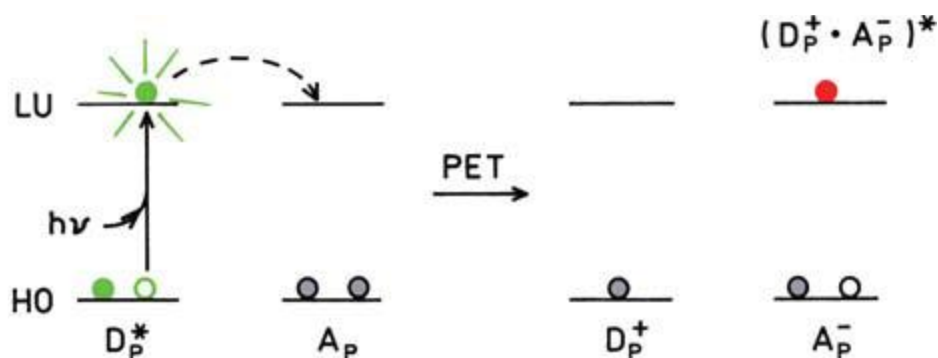


**Figure 1.1.8.** Molecular orbital schematic for photoinduced electron transfer. Adapted from ref.<sup>1</sup>

One of the most well-known and widely used<sup>11-14</sup> types of excitation energy transfer is *Förster resonance energy transfer* (FRET) – a nonradiative process of energy transfer from an excited donor to a proximal ground state acceptor through long-distance dipole–dipole interactions. This process requires spectral overlap between donor emission and acceptor absorption (Figure 1.1.9) and is effective at distances up to 10 nm. FRET efficiency depends on spectral overlap and intermolecular distance, as well as on relative orientation of the transition dipoles.

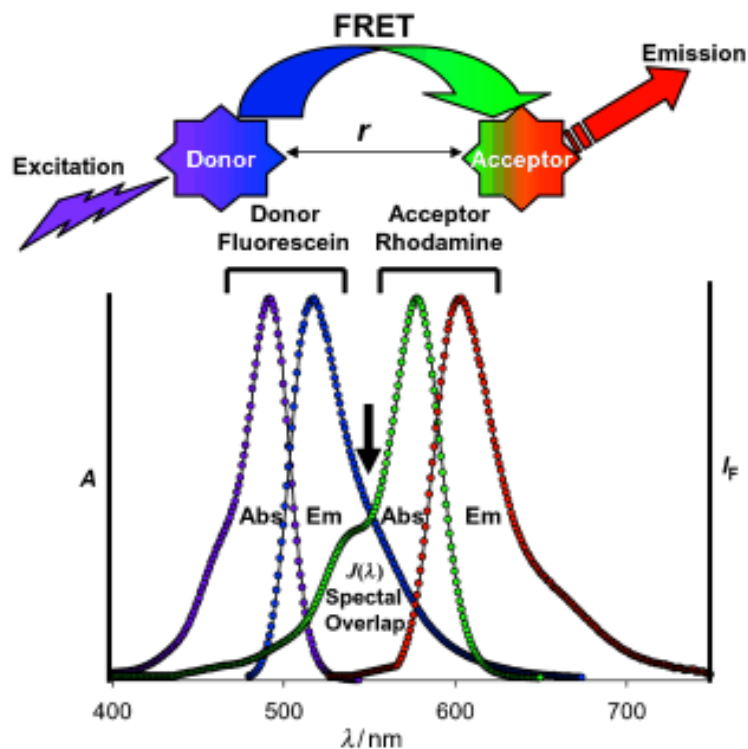


**Figure 1.1.9.** Schematic representation of the FRET process: the donor molecule in excited-state nonradiatively transfers energy to a proximal acceptor molecule which is at distance  $r$  from the donor. Adapted from ref.<sup>15</sup>

When donor and acceptor are different dyes, the energy transfer is called *heteroFRET*, which is the most classic situation. However, in some cases FRET can be observed between the same dyes, when donor and acceptor are structurally identical. This case is called *homoFRET* and mostly occurs in situations when the dyes are highly concentrated in a small volume and have small Stokes shift. If an energy acceptor molecule serves as a donor for another acceptor molecule and this process repeats as a chain between multiple molecules, such process is called *energy migration*.

### 1.1.2. Fluorescence anisotropy

The last important characteristic of fluorescence that should be mentioned in this chapter is *fluorescence anisotropy* – ratio of polarized component of emitted light to total its amount. When a sample is irradiated by polarized light, it is preferentially absorbed by those fluorophores, whose transition moments are aligned parallel to electric vectors of exciting photons. When fluorophores are oriented randomly in a solution, it is called *isotropic* solution. In this case only a fraction of fluorophores will be excited. If a fluorophore doesn't change its orientation during excited state lifetime, the emitted light is anisotropic, characterised by so-called fundamental anisotropy. If the fluorophore orientation changes, this leads to change in its emission polarisation, decreasing fluorescence anisotropy value (Figure 1.1.10).

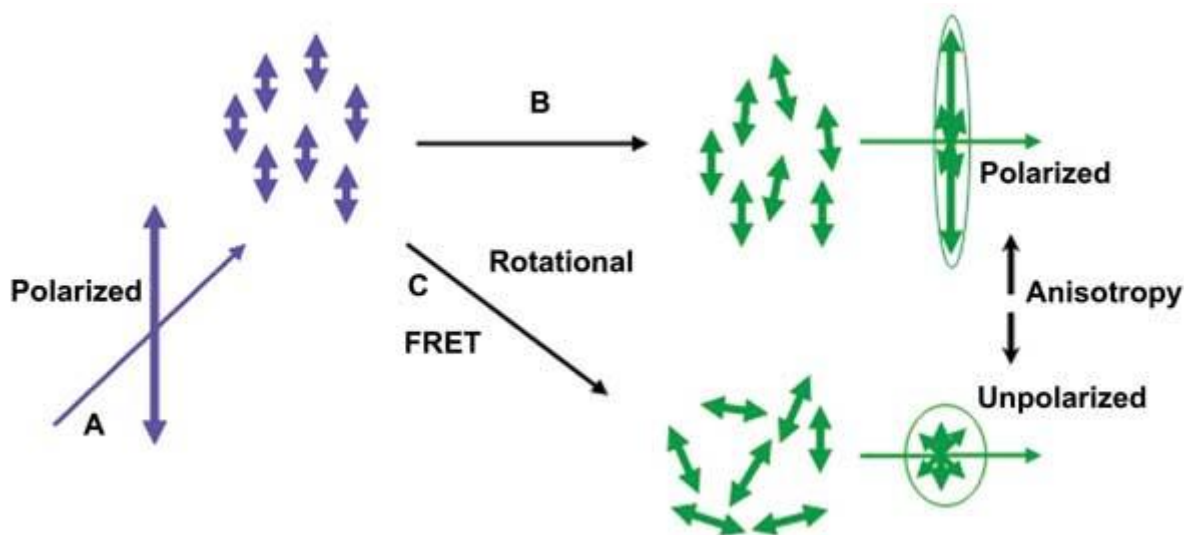


**Figure 1.1.10.** Fluorescence polarization and anisotropy: (a) Polarized excitation is used to selectively excite dipole-aligned fluorophores. (b) Fluorophores bound or in high-viscosity media diffuse or rotate more slowly – higher anisotropy. (c) Rotational diffusion or resonance energy transfer reduces polarization – lower anisotropy. Adapted from <https://www.photonics.com>

Another reason of losing fluorescence anisotropy is excitation energy transfer, most commonly homoFRET. Fluorophore, excited by polarized light may transfer the energy to another fluorophore with different orientation and that second fluorophore will emit differently polarized light. Fluorescence anisotropy measurements are widely used in biophysical<sup>16, 17</sup> and photophysical<sup>18, 19</sup> researches. Typical values of fluorescence anisotropy<sup>20</sup> for a freely rotating fluorophore (in a non-viscous solvent) have the order of magnitude about  $10^{-2}$ . In polymer matrices or viscous solvents it

increases to  $10^{-1}$ , but for systems with efficient energy migration between fluorophores it can fall even to  $10^{-3}$ .

## 1.2. Main types of luminescent nanoparticles

### 1.2.1. Inorganics-based nanoparticles

Nanoparticles, based on inorganic luminescent materials, have several common features worth noting – they are generally not biodegradable (despite they can be made biocompatible), brighter and more photostable than single organic fluorophores, and their optical properties (except dye-loaded ones) are different from those of organic dyes and are often controlled by size and morphology, allowing them to occupy their own niche in the world of imaging. Several popular classes of these luminescent nanoparticles will be briefly described in this chapter.

#### 1.2.1.1 Quantum dots

Quantum dots (QDs) are semiconductor nanocrystals of 2-10 nm size<sup>21</sup> (up to 30 nm with biocompatible shell) typically made of elements of groups II-VI (CdSe, CdS, CdTe etc.) or III-V (InP). They possess intermediate electronic properties between those of molecules and bulk semiconductors. Since the size of QDs is smaller than distance between an electron, transferred to conduction band, and a hole in the valence band it leaves behind, discrete energy levels appear, just like in atoms. Increase in size of QDs leads to decrease in the energy difference between valence band and conduction band, therefore less energy gets released after returning to ground state<sup>22</sup> (Figure 1.2.1). This results in tunability of emission spectrum (emission wavelength) by size<sup>23</sup> and composition of quantum dots, allowing to obtain any emission colour from UV to NIR<sup>24</sup>. Their emission is usually quite narrow and symmetric, though absorption is broad, therefore they can be excited at different wavelengths.

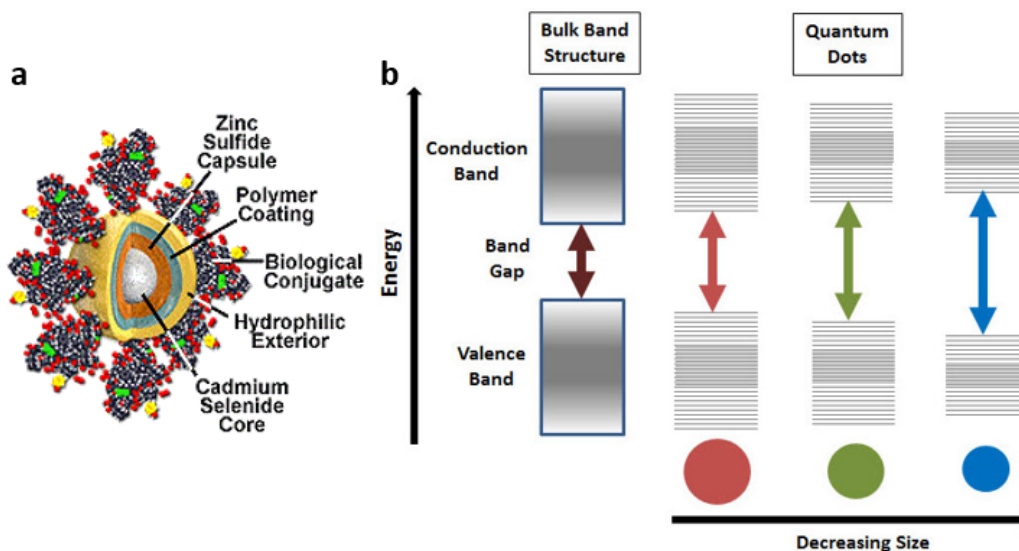


**Figure 1.2.1.** Schematic representation of a QD and its energy levels. a) Schematic structure of QDs. Adapted from [www.olympusmicro.com](http://www.olympusmicro.com). b) Splitting of energy levels in QDs due to the quantum confinement effect: semiconductor band gap increases with decrease in size of the nanocrystal. Adapted from [www.sigmaaldrich.com](http://www.sigmaaldrich.com).

Quantum dots are known for their high brightness (extinction coefficients up to  $10^7$  and QY from 0.3 to 1), narrow blinking emission<sup>25</sup> and high photostability, which provided them with multiple applications<sup>26</sup>. However, being made of toxic elements, QDs are arising toxicity questions<sup>27</sup>.

### 1.2.1.2 Carbon dots

Carbon dots, or C-dots, are nanoclusters of carbon of less than 10 nm size with small amounts of Oxygen and Nitrogen. Their preparation is quite simple - burning<sup>28</sup> or heating by microwaves<sup>29</sup> of organic material (Figure 1.2.2). One step synthetic procedure allows placing amino groups on the NPs surface for further functionalization<sup>30</sup>. The colour of their emission can be tuned by variations in synthetic procedure, but both absorption and emission bands are wide, therefore making impossible multiplex imaging<sup>31</sup>. Among attractive features are their biocompatibility, nanosecond order lifetime, good photostability and high two-photon absorption. Despite having moderate quantum yields of 5-30%, they found numerous applications in imaging<sup>32</sup>.



ETU – energy transfer upconversion – excited-state Ion 1 transfers energy to the excited (E1) state and ground (G) state of Ion 2.

CSU – cooperative sensitization upconversion – Ion 1 and Ion 3 in excited state simultaneously transfer energy to Ion 2, exciting it to E1 state.

CR – cross relaxation – partial energy transfer process, where Ion 1 transfers some of its energy to Ion 2, still staying in excited state.

PA – photon avalanche – phenomenon of producing upconversion at high laser powers thanks to ESA and CR processes.

Such peculiar spectral behaviour produces background-free imaging, and the possibility of NIR excitation makes this type of NPs perspective for in vivo applications.

#### **1.2.1.4 Dye-doped silica nanoparticles**

Silica nanoparticles (SiNPs) can serve as a matrix for encapsulation of organic/inorganic emissive species<sup>35</sup>, as it protects them from environment and keeps them in a confined space. Spectral properties of such NPs would depend on type and quantity of encapsulated material and can be finely tuned.

SiNPs can be prepared by several methods described in Figure 1.2.4 - in *Stöber method* tetraethyl orthosilicate (TEOS) is hydrolysed in a mixture of ethanol and aqueous ammonium hydroxide, forming silicic acid. When its concentration exceeds its solubility in ethanol, it nucleates and forms silica nanoparticles. The drawback of this method is comparatively large size distribution of the formed NPs. *Reversed microemulsion method* is based on water-in-oil system formation, where water nanodroplets act as small microreactors, where silane hydrolysis and NPs growth takes place<sup>36</sup>. Formed NPs have narrow size distribution and their size can be tuned by altering proportions and types of solvents and surfactants. In *direct micelle assisted method* a surfactant or their mixture is aggregated to form micelles, which are used as templates for SiNPs formation. In this case, hydrophobic TEOS together with hydrophobic doping dyes gets encapsulated inside the micelles, and after TEOS hydrolysis homogeneous particles of 10-90 nm are obtained<sup>37</sup>.

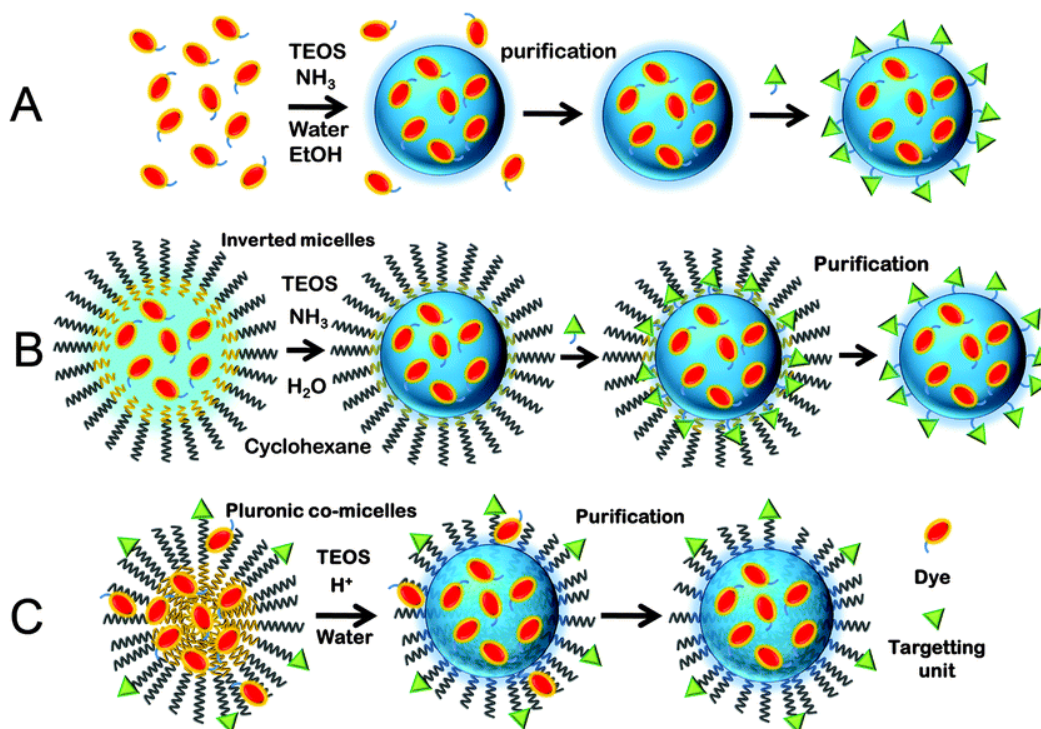


**Figure 1.2.4.** Schematic representation of different synthetic strategies to obtain dye-doped silica nanoparticles: Stöber method (A), reverse microemulsion method (B) and direct micelle assisted method (C). Adapted from ref.<sup>38</sup>

Due to biocompatibility and high tunability, these NPs have found numerous applications<sup>39, 40</sup>.

## 1.2.2. Fluorescent organic nanoparticles

Unlike inorganic-based nanoparticles, optical properties of organic NPs generally do not depend on their size or morphology, but rather on the encapsulated fluorescent dye. Encapsulating matrix (lipid, polymer, etc.) can gather lots of fluorophores into a single ultrabright object, protecting them from environment and even improving fluorescence properties. Moreover, by using biodegradable matrix it is possible to develop biodegradable fluorescent nanoparticles, which makes this type of NPs especially interesting for in vivo applications. Several key types of such systems will be briefly introduced in this chapter.

### 1.2.2.1 Dye-doped lipid droplets

*Nanoemulsion* is a dispersion of two immiscible liquids<sup>41</sup> (oil-in-water in our case) that consists of *lipid droplets* of submicron size (usually 100-400 nm) stabilised by

surfactants. They are generally prepared<sup>42</sup> by ultrasonication, microfluidization, spontaneous emulsification or phase inversion method.

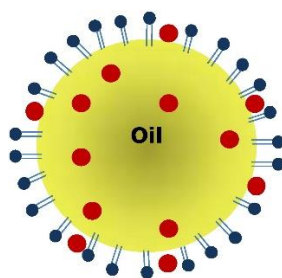


**Figure 1.2.5.** Oil in water emulsion lipid droplet, stabilized with surfactants (blue) with dissolved drug/dye molecules (red dots). Adapted from ref.<sup>43</sup>

Special type of lipid droplets with diameter of 30-120 nm, which have prolonged colloidal stability were designed by the group of Texier<sup>44</sup>. They were loaded with lipophilic cyanine dyes at <0.3% w/w loading, where no quenching occurs, and have shown to be comparable with QDs in terms of brightness<sup>45</sup>. These fluorescent lipid nanocarriers were referred as *Lipidots* (Figure 1.2.6)

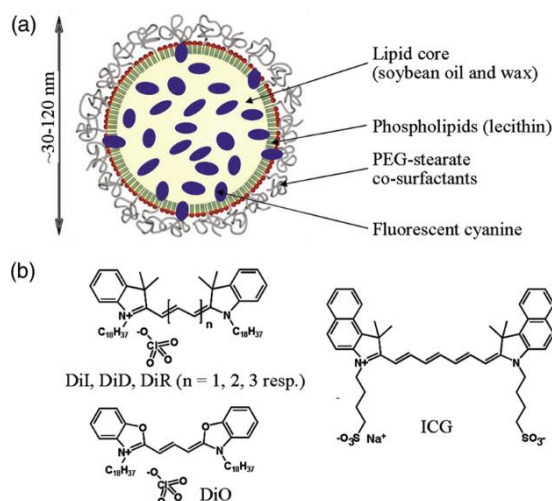


**Figure 1.2.6.** Lipidot structure. (a) Lipidots are dye-loaded oily droplets dispersed in aqueous buffer, whose diameter can be adjusted between 30 and 120 nm. Their fluorescent properties are conferred by lipophilic or amphiphilic cyanine dyes (b), encapsulated in the lipid core and/or the surfactant layer. Adapted from ref.<sup>45</sup>

Works of our group on non-leaking ultrabright fluorescent nanodroplets will be discussed in Chapter 1.3.

### 1.2.2.2 Dye-doped lipoproteins

*Lipoproteins* are natural biochemical nanoassemblies, which transport fatty compounds in the bloodstream. They consist of a lipid core (cholesterol, triglycerides) and a phospholipid membrane with special apolipoproteins for stabilisation and

biorecognition. As they are natural components of blood, they have become attractive nanocarriers for theranostics<sup>46</sup> and contrast agents for medical imaging<sup>47</sup>.

By modifying surface of lipoproteins they can be targeted towards specific receptors, like folate receptors, overexpressed in cancer cells. Such modified lipoproteins were called *lipoprotein-based nanoplatfoms* (LBNP)<sup>48</sup> (Figure 1.2.7). They were loaded with fluorescent dyes and have shown to be selectively uptaken by KB cells with overexpressed folate receptors<sup>48</sup>.

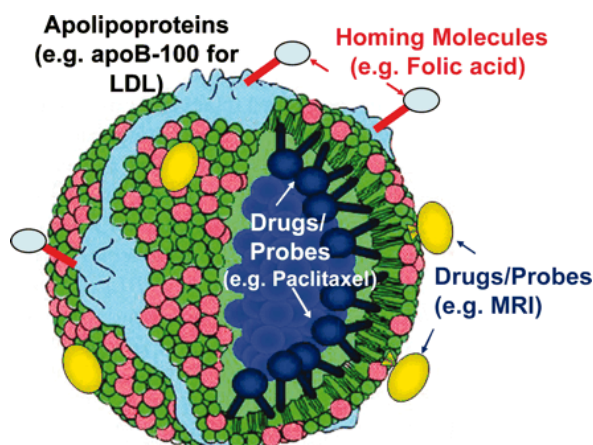
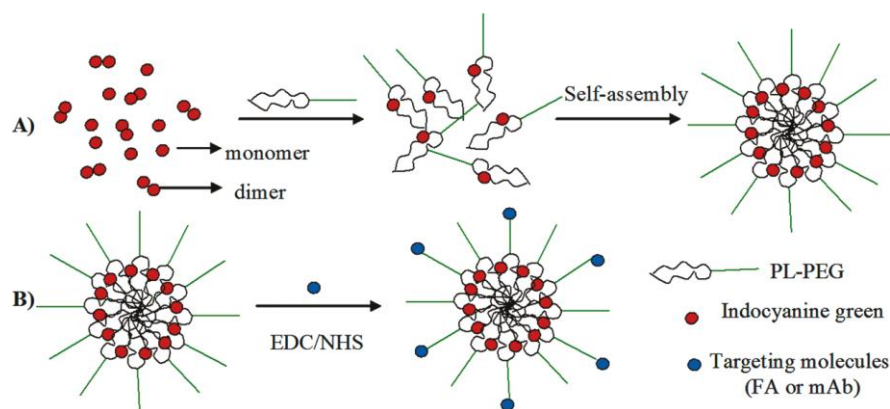


Figure 1.2.7. The LBNP concept. Adapted from ref.<sup>48</sup>

### 1.2.2.3 Dye-doped lipid micelles

*Micelles* are self-organised supramolecular assemblies of amphiphilic molecules that are in thermodynamic equilibrium with dissolved amphiphiles. They are generally spherical structures, formed by an amphiphiles monolayer, where hydrophobic part is inside the micelle, and hydrophilic is outside. Fluorescent micelles can be formed from both amphiphilic dyes<sup>49, 50</sup> or lipids, loaded with fluorescent agents<sup>51-53</sup> (Figure 1.2.8). In the latter case, stability and optical properties of the loaded cargo can be significantly improved. Moreover, surface modification can target these nanocarriers towards cancer cells<sup>51</sup>.



**Figure 1.2.8.** (A) Self-assembly process of ICG-PL-PEG probe. (B) Targeted modification of ICG-PL-PEG probe. Adapted from ref.<sup>51</sup>

### 1.2.2.4 Dye-doped liposomes

*Liposomes* are self-assembled lipid-based structures of generally spherical shape, which consist of a membrane bilayer, separating inner aqueous environment from outer environment. As they have both aqueous core and hydrophobic membrane, they can be loaded by both hydrophilic<sup>54, 55</sup> and hydrophobic<sup>53, 56</sup> fluorescent dyes, located in the core and membrane, respectively (Figure 1.2.9). Such loaded fluorescent liposomes are widely used in fluorescence imaging<sup>57, 58</sup> and theranostics<sup>59</sup>.

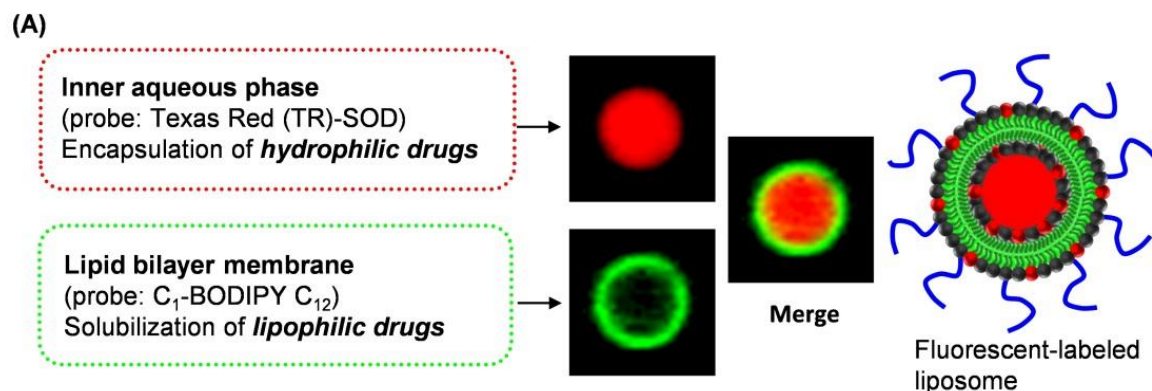


**Figure 1.2.9.** Fluorescence localization in double fluorescence-labeled large multilamellar bone marrow-targeted liposomes. Adapted from ref.<sup>58</sup>

### 1.2.2.5 Conjugated polymer nanoparticles

*Conjugated polymers* are defined as polymeric macromolecules with alternating single and double bonds in the backbone, which results in system with delocalised  $\pi$ -electrons, possessing interesting optical and electronic properties. Most of conjugated polymers are polyaromatic systems, often based on fluorene or thiophene scaffolds (Figure 1.2.10).

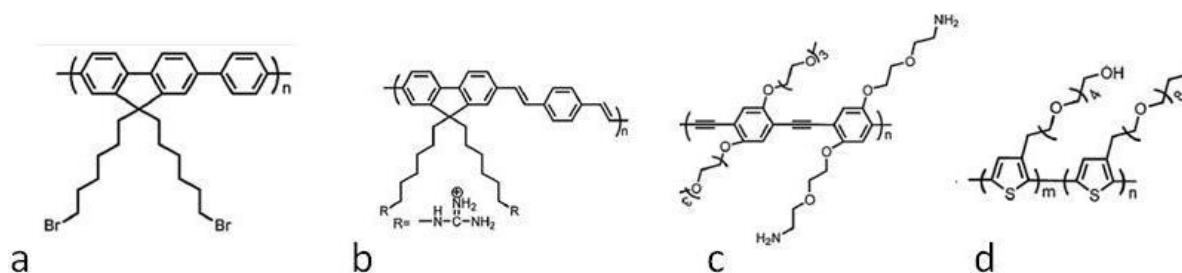


**Figure 1.2.10.** Examples of conjugated polymers: poly(fluorene) and its derivatives, (a), poly(p-phenylenevinylene) and its derivatives (b) poly(p-phenyleneethynylene) and its derivatives (c), and poly(thiophene) (d). Adapted from ref.<sup>60</sup>

Preparing nanoparticles from such polymers results in highly fluorescent systems with tuneable properties<sup>60, 61</sup>. Among common synthetic procedures for NPs preparation are nanoprecipitation, mini-emulsion and self-assembly methods (Figure 1.2.11). By varying concentration<sup>62</sup> and amphiphilic additives<sup>63</sup> it is possible to obtain ultrasmall NPs down to 15 nm size.

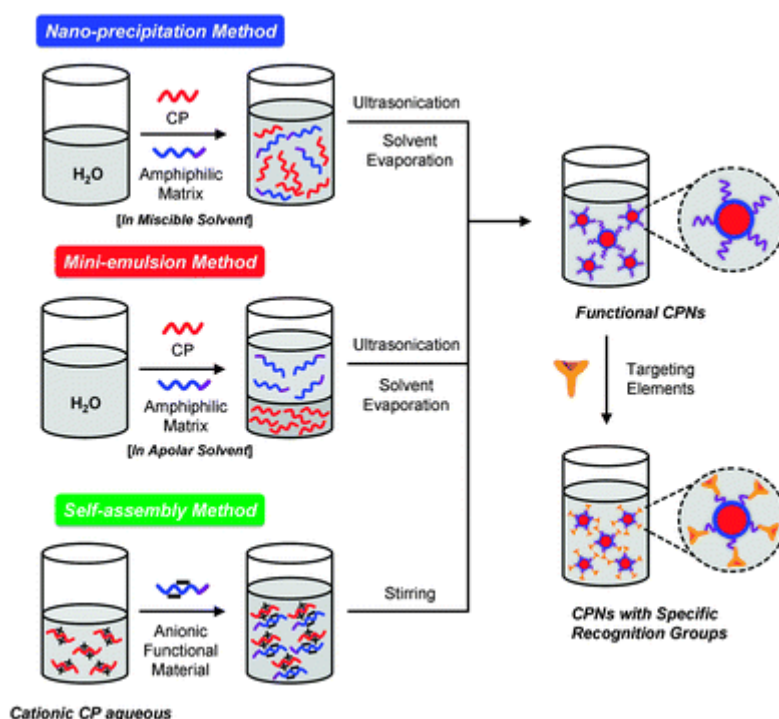


**Figure 1.2.11.** Common methods to prepare conjugated polymer NPs. Adapted from ref.<sup>60</sup>

### 1.2.2.6 Dye-doped polymer nanoparticles

Unlike conjugated polymers, that have intrinsic fluorescence, *dye-doped polymer nanoparticles* are composed of a non-fluorescent polymer matrix and a fluorescent dye to create highly fluorescent nanoobjects with tuneable properties.

There is a wide variety of methods to prepare polymer nanoparticles<sup>64</sup>. First group of methods - polymerisation of monomers in a confined space, like in case of emulsion system (Figure 1.2.12). Depending on the reaction conditions and surfactant nature and quantity, such emulsion polymerisations are divided into conventional<sup>65</sup>, mini-emulsion<sup>66</sup> and micro-emulsion<sup>67</sup> polymerisations, the latter allowing to create the smallest NPs of even less than 10 nm.

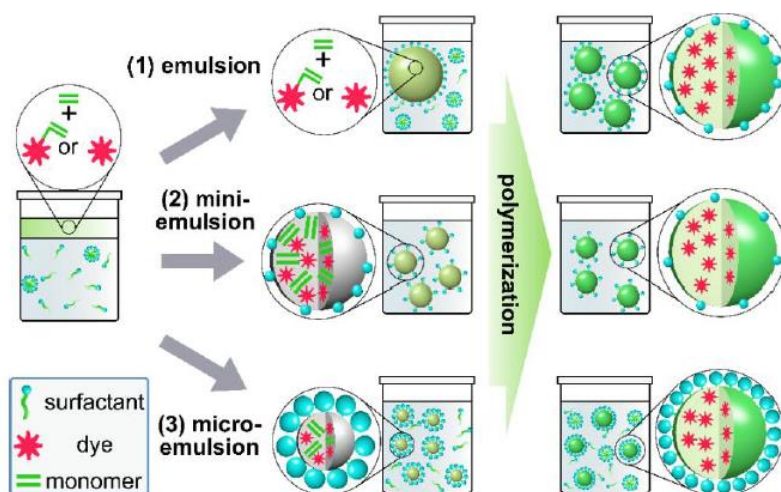


**Figure 1.2.12.** Synthesis of dye-loaded polymer NPs by polymerization of monomers. Adapted from ref.<sup>68</sup>

Second group of methods is based on making nanoparticles from already preformed polymers (Figure 1.2.13). In *nanoprecipitation method*<sup>69</sup> the dye and polymer are dissolved in a solvent, miscible with water, and this solution is added to water forcing the polymer to precipitate as nanoparticles. As it is a kinetically controlled process, NPs of different sizes (10 - 1000nm), depending on polymer and solvent type and concentration, formulation conditions etc. During *emulsification-solvent evaporation* a dissolved in a water-immiscible solvent polymer is dispersed in water with surfactant under sonication or high-speed homogenization. This gives an emulsion of droplets of non-miscible solvent with dissolved polymer as a result. Evaporation of organic solvents results in NPs of several hundred nanometres<sup>70</sup>. *Self-assembly method*<sup>71</sup> is only viable for amphiphilic polymers, which can spontaneously form thermodynamically stable structures, like micelles. Such micelles are called *polymeric micelles* and usually have critical micelle concentrations several orders of magnitude lower than their lipidic relatives.

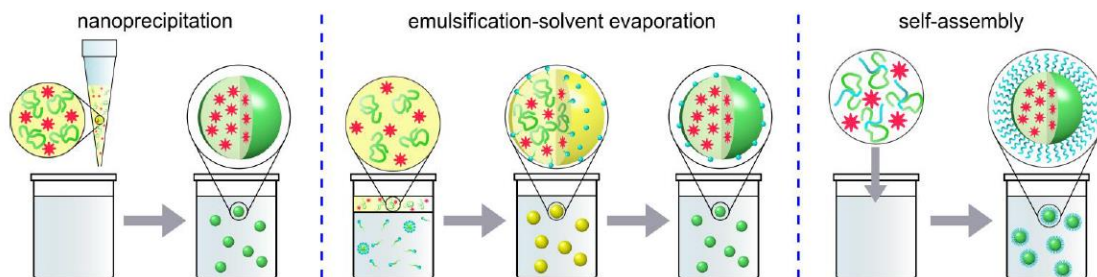


**Figure 1.2.13.** Methods of preparation of dye-loaded NPs from preformed polymers.  
Adapted from ref.<sup>68</sup>

Despite the approach of encapsulating dyes into polymer matrices is becoming more and more popular, there are several key challenges in the field – obtaining high encapsulation efficiency and preventing dye self-quenching. They become more and more important with increasing dye loading and will be discussed in the next chapters.

### 1.3. Encapsulation of dyes inside nanoparticles

As described in the previous chapter, imaging agents of nanoscale size are widely used for different applications, however their formulation has its challenges. Loading of a dye inside a particle matrix is much simpler than its covalent conjugation to NPs, and usually it does not affect matrix properties or NPs behaviour *in vivo*. However, when the dye loading is incomplete, additional purification steps are required, which can be time-consuming and often quite tricky. Moreover, often the cargo is not properly encapsulated, when, for instance it is just adsorbed to the surface. Then, any contact with a lipophilic environment would cause leakage of the dye. In this chapter overview will be made on how different factors affect dye encapsulation and leakage from several popular nanocarrier types, and how dye leakage is investigated and prevented.

A study on encapsulation of photodynamic therapy agents (Figure 1.3.1) inside poly(D,L-lactic acid) nanoparticles has revealed a huge impact of the dyes hydrophobicity not only on encapsulation, but also on release kinetics.<sup>72</sup>

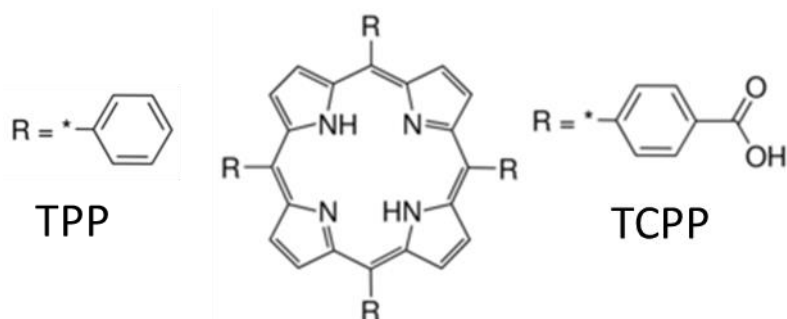


**Figure 1.3.1.** Chemical structures of TPP and TCPP molecules. Adapted from [www.sigmaaldrich.com](http://www.sigmaaldrich.com)

It was measured, that for TCPP-loaded nanoparticles encapsulation efficiency was only 21%, versus 87% for TPP-loaded NPs. Authors hypothesize that decreased encapsulation of dye is due to its release during purification, however it could also be incomplete dye entrapment during nanoparticle fabrication process. As for bloodstream release, it was found that even purified TCPP-loaded NPs demonstrate a two-fold decrease in fluorescence contrast over about half an hour, indicating dye leakage, while almost no change in fluorescence of TPP-loaded NPs was observed.

A release of dyes from polymeric micelles, as a model for drug release, was investigated by *Chen et al.*<sup>73</sup>. They used FRET-based approach to monitor cargo release from monomethoxypoly(ethyleneglycol)-block-poly(D,L-lactic acid) (PEG-PDLLA) polymeric micelles, loaded with hydrophobic dyes DiO (energy donor) and DiI (energy acceptor) (Figure 1.3.2).

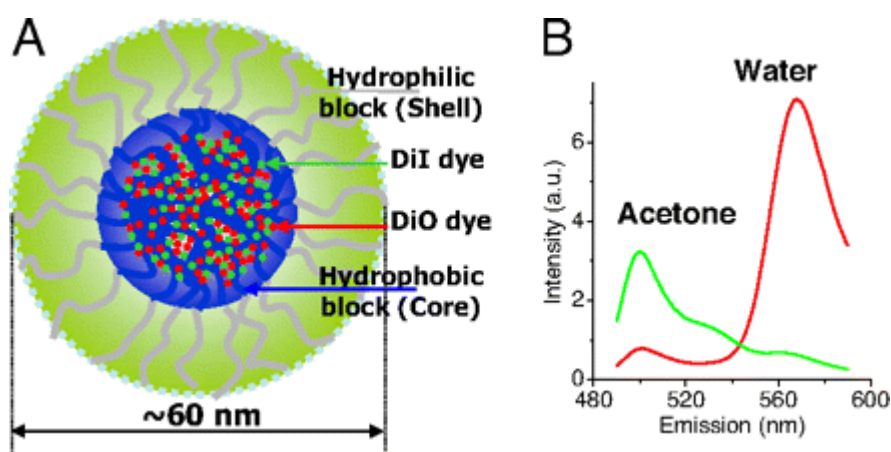


**Figure 1.3.2.** PEG-PDLLA FRET micelles. (A) Diagram of a FRET micelle prepared with 0.75% DiO and 0.75% DiI at 2 mg/ml polymer concentration. (B) Spectra of micelles diluted by 10× water (red curve) and 10× acetone (green curve), respectively. Adapted from ref.<sup>73</sup>

Their results showed absence of signal from FRET channel inside cells, while having strong signal from donor dye, indicating that designed polymeric micelles release loaded hydrophobic dyes into plasma membrane upon contact with the cell much faster than internalisation of polymeric micelles occurs. Interestingly, upon incubation at 4°C, no dye leakage from micelles to membrane was observed, probably due to the fact that PDLLA polymer is in glass state at this temperature. So, using polymers with high glass transition temperature might be one of the ways to prevent dye leakage from PMs.

The group of Law published a study<sup>74</sup> on NIR fluorescent polymer NPs for *in vivo* imaging, where they encapsulated DiD and DiR dyes into NPs made of PLGA-PEG-Maleimide to create single-dye NPs and FRET NPs (Figure 1.3.3).

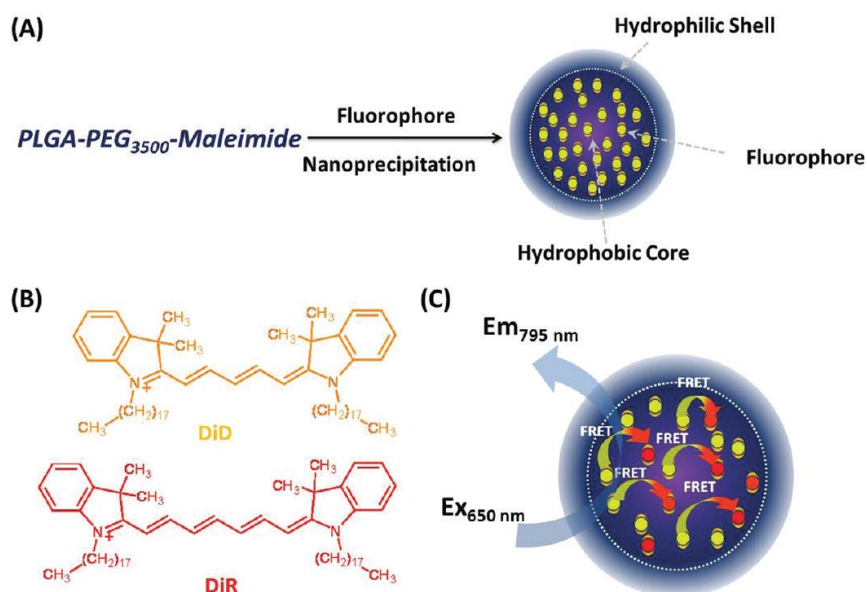


**Figure 1.3.3.** Design of FRET-NPs. (A) Nanoparticles were synthesized by the nanoprecipitation method. (B) Chemical structures of DiD and DiR fluorophores. (C) The close proximity between the entrapped DiD and DiR fluorophores favored the fluorescence resonance energy transfer (FRET). Adapted from ref.<sup>74</sup>

The NPs were obtained by nanoprecipitation and were further purified using centrifuge concentrator with molecular weight cut off (MWCO) of 10000. Encapsulation efficiency was tested by freeze-drying NPs solutions, dissolving it in DMSO and measuring dye concentration of the solution. It was found that for both dyes encapsulation efficiency was about 70% for NPs loaded with 3%(w/w) expected dye loading. Although the used purification method does not use any agents to desorb hydrophobic dyes from NPs surface, the encapsulation efficiency sounds reasonable.

Salvati *et al.*<sup>75</sup> performed an interesting research on dye leakage from commercially available polystyrene beads. They compared beads from *Polysciences* (P<sub>1</sub>) and *Invitrogen* (I<sub>1</sub>), both made by swelling of polystyrene with dye solution, but having different dyes encapsulated and, most likely, different production procedures.

It was found that despite similarity of the beads, P<sub>1</sub> burst-released encapsulated dye in biological media, while I<sub>1</sub> did not. Moreover, cellular experiments on particle uptake in the presence of sodium azide (to deplete cellular energy and stop NPs endocytosis) have shown dramatic difference between the samples – labile dye-rich P<sub>1</sub> NPs still stained the cells, just like free dye, while labile dye-poor I<sub>1</sub> NPs did not provide any cellular fluorescence (Figure 1.3.4). This signifies that even some of polystyrene dye-swollen polymer NPs can be effective leakage-free nanocarriers.

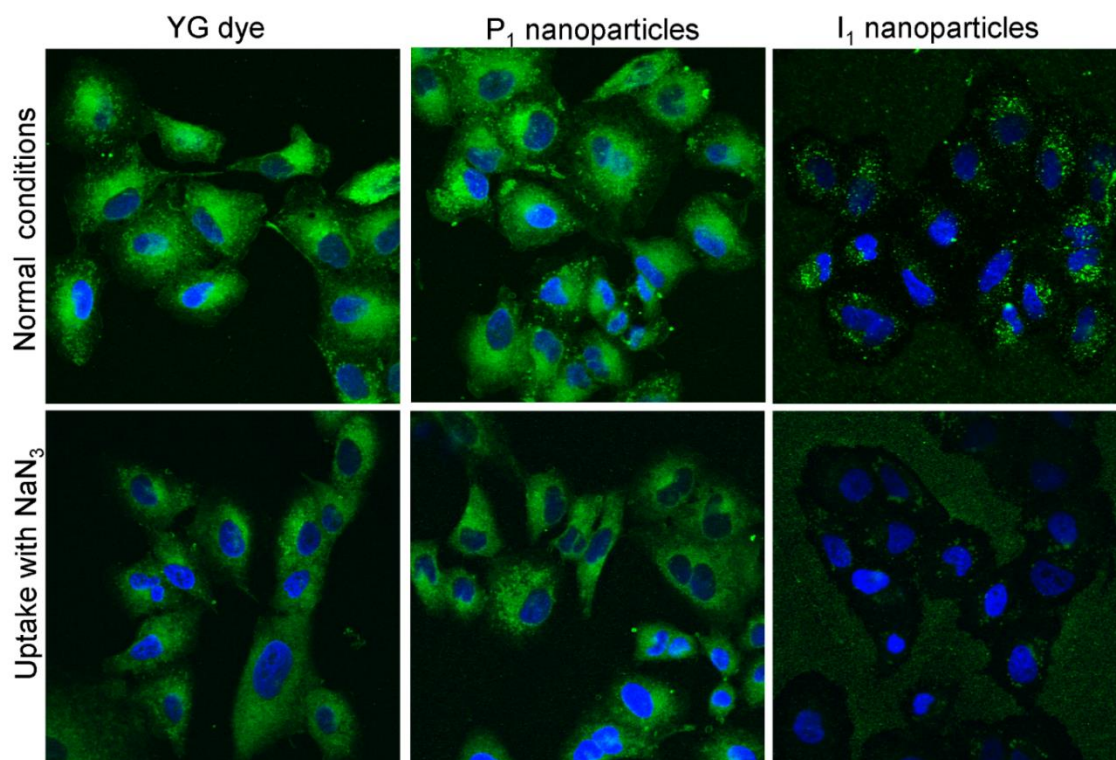


**Figure 1.3.4.** Confocal images of cells treated with YG dye, or with either sample P<sub>1</sub> (YG-loaded NPs) or I<sub>1</sub> under normal cell culture conditions (37 °C, cMEM) and in medium containing 5mg/ml NaN<sub>3</sub> to deplete cellular energy. Adapted from ref.<sup>75</sup>

Later the same group<sup>76</sup> performed another research on dye leakage, this time co-polymerizing functionalized for polymerisation rhodamine B with N-isopropylacrylamide in an emulsion polymerisation procedure, obtaining polymer nanoparticles as a result. These nanoparticles were subjected to 20 days of dialysis against water (20 water changes) to remove free dye and surfactants. Nevertheless, incubation of these NPs with cells showed strong dye leakage. Therefore, particles were further dialyzed for 23 days with ethanol, removing all unbound dye and further proving this removal by gel electrophoresis of the particles. Unfortunately, the removal of all unbound dye led to nearly complete loss of NPs fluorescence, effectively resulting in NPs becoming useless for imaging (Figure 1.3.5c) and indicating, that dye was not copolymerised, but just entrapped inside polymer. However, particles dialysed for 7 days appeared to provide no dye leakage and be still quite bright due to high amount of free dye entrapped inside the particles (Figure 1.3.5b).

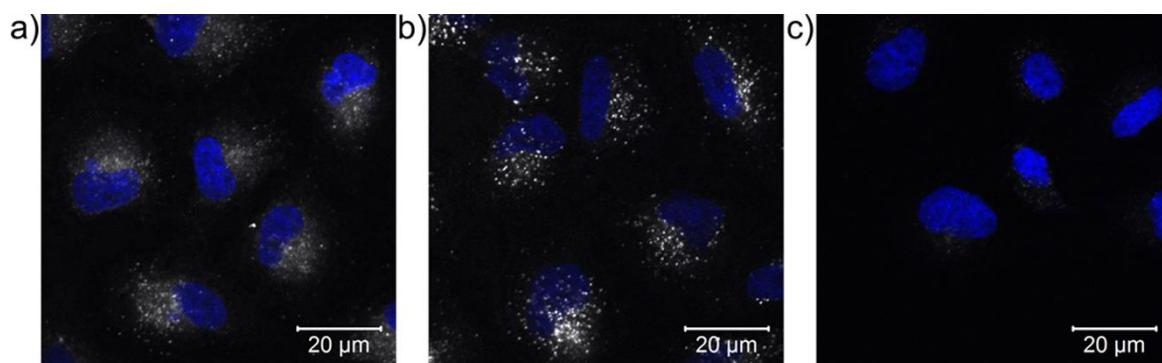


**Figure 1.3.5.** Comparison of the distribution of fluorescence in A549 cells following 24 hours of exposure to rhodamine-labelled nanoparticles cleaned by dialysis against ethanol for (a) 1 day; (b) 7 days; and (c) 23 days. Blue: DAPI stained nuclei; White: fluorescence intensity (free dye and/or nanoparticles; greyscale). Adapted from ref.<sup>76</sup>

Despite the authors failed to properly covalently insert the dye into polymer backbone, it is still interesting that high amount of physically entrapped dye, which can be washed out by ethanol, doesn't leak into biological media.

A good example of how high hydrophobicity of dye prevents it from leakage is the work of *Klymchenko et al.*<sup>77</sup>, where the authors compare stability of dye-loaded lipid droplets against dye leakage into different media for two dyes of different hydrophobicity – conventional Nile Red and a more hydrophobic Nile Red derivative, NR668 (Figure 1.3.6).

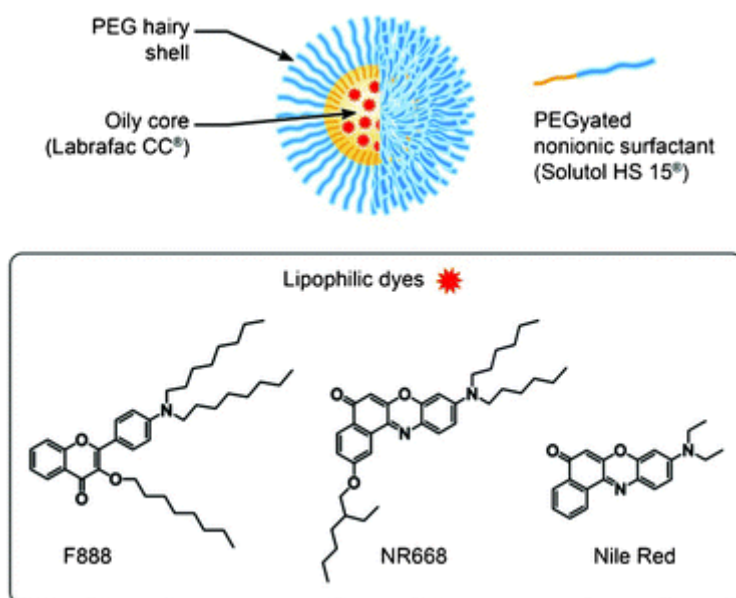


**Figure 1.3.6.** Schematic presentation of a nanodroplet and chemical structures of encapsulated dyes. Adapted from ref.<sup>77</sup>

Using FRET between lipophilic dye F888 and, in one case, Nile Red, in the other – NR668 inside lipid droplets, they have observed rapid (3 min) release of Nile Red

from droplets into Opti-MEM, and it was even higher in case of Opti-MEM containing 10wt.% of serum. As for FRET lipid droplets loaded with F888-NR668 pair, no increase in donor/acceptor ratio (leakage indicator) was observed in Opti-MEM with 10% of serum even after 6 hrs, indicating absence of dye leakage from lipid droplets. These results on dye leakage were also confirmed by fluorescence correlation spectroscopy (FCS) measurements of Nile Red-loaded and NR668-loaded lipid droplets in Opti-MEM. Nile Red lipid droplets have shown continuous drop of fluorescence brightness and increase in number of emissive species, which indicated leakage of the dye from droplets and its binding to components of the medium. Again, no leakage was observed for NR668 even after 6 hours, proving that increasing hydrophobicity is a good way to prevent nanocarriers from dyes leakage.

Stability of lipid nanocapsules (LNCs) against leakage of encapsulated dyes was studied by *Bastiat et al.*<sup>78</sup> They encapsulated separately five dyes: Nile Red, Coumarin-6, DiO, Dil, DiD into LNCs with Labrafac as oil phase, stabilized by lipid-based and PEGylated surfactants. The obtained LNCs were purified by dialysis vs water with membrane MWCO of 15000.

To study dye leakage from LNCs, the suspension was mixed with lipophilic compartment (LC, Labrafac oil in this study) and the distribution of dye between LNCs in aqueous phase and LC phase (Figure 1.3.7) was measured.

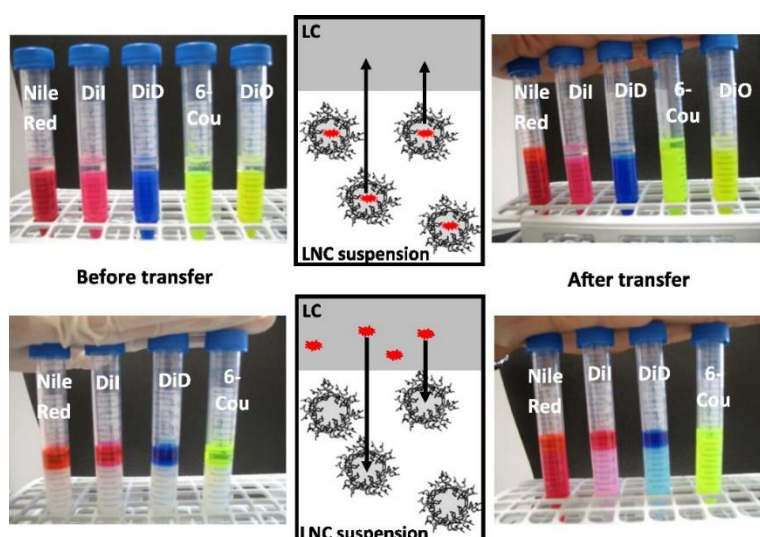


**Figure 1.3.7.** Dye transfer from lipid nanocapsule suspension to lipophilic compartment (direct way, upper panel) and from lipophilic compartment to lipid nanocapsule suspension (reversed way, lower panel). Adapted from ref.<sup>78</sup>

It was found that Nile Red and Coumarin-6 dyes, the least hydrophobic of the tested dyes, get distributed between LNC phase and LC phase upon mixing. The partition ratio depends on the phase volume ratio, being governed by principles of thermodynamic equilibrium. For DiO, Dil and DiD, which are much more hydrophobic, almost no partition was observed, signifying that those dyes are well-trapped inside LNCs and cannot be extracted by hydrophobic medium of Labrafac phase.

For further evaluation, a reversed experiment was conducted – the dyes were dissolved in Labrafac and mixed with dispersions of blank LNCs. Again, Nile Red and Coumarin-6 have shown thermodynamically-driven equilibrium distribution between phases, while DiO, Dil and DiD were almost not transferred to LNC-containing aqueous phase.

The authors attribute such behaviour of dyes not to hydrophobicity, but assume their different localisation in LNCs – Nile Red and Coumarin-6 are supposedly in the core and are transferred by direct contact of oil phases, while cyanine dyes are trapped in the surfactant shell. Despite this explanation is not convincing, the data on dependence of LNC stability against leakage on dye structure is still worth noting.

In a very recent paper<sup>79</sup> the same group performs another research on dye leakage, this time getting even closer to *in vivo* conditions (Figure 1.3.8). They chose Nile Red and DiO as model dyes and performed several types of experiments: 1) Transfer from dye-loaded LNCs to blank LNCs: Nile Red gets instantly transferred, demonstrating equilibrium-based partitioning, while DiO does not. 2) Transfer from labelled LNCs or cells to non-labelled cells and from labelled cells to blank LNCs – again same picture of rapid transfer of Nile Red and absence of transfer for DiO during experiment time (30 s).

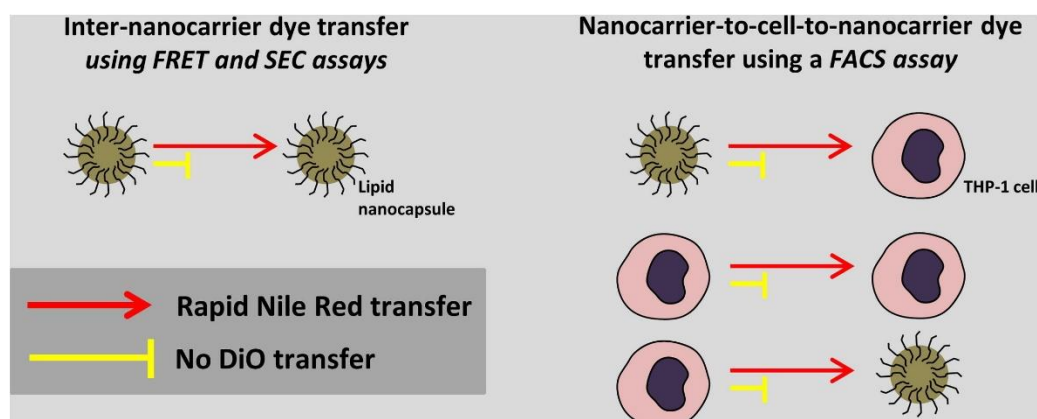


**Figure 1.3.8.** Schematic presentation of study and results described in ref.<sup>79</sup> Adapted from ref.<sup>79</sup>

These results confirm earlier studies of the group and prove that their simple method of oil extraction for monitoring dye leakage from LNCs is effective for predicting dye leakage *in vivo*.

A similar research on hydrophobic dyes transfer between lipid phases was performed by *Petersen et al.*<sup>80</sup> They tried to mimic the transfer of drugs from lipid NPs to lipid-containing environment of blood, so they formulated ~100 nm liposomes, loaded with three different dyes of different hydrophobicity – Nile Red (LogP ~3.6), temoporfin (LogP ~9.2) and Dil (LogP ~20.0). These liposomes were exposed to excess amounts of lipid droplets of large size (~10 µm) and the amount of transferred dye and speed of transfer were analysed by flow cytometry using specific calibration curves.

The results appear to be in line with expectations – least lipophilic Nile Red is transferred rapidly and reaches the equilibrium of concentration in droplets and liposomes, while most lipophilic Dil showed almost no transfer. Intermediate in lipophilicity temoporfin has shown intermediate values of dye transfer amount, but transfer speed close to that of Nile Red, probably indicating inhomogeneous distribution inside liposomes. Authors conclude that lipophilicity of the dye is the key factor of dye leakage from liposomes to lipid droplets and it is hard to disagree.

*Snipstad et al.* recently published a multidimensional research<sup>81</sup> on dye leakage from various NPs into cells, where they varied 6 dyes (Figure 1.3.9), encapsulating them inside 3 types of nanocarriers and incubating with two types of cells at two different temperatures.

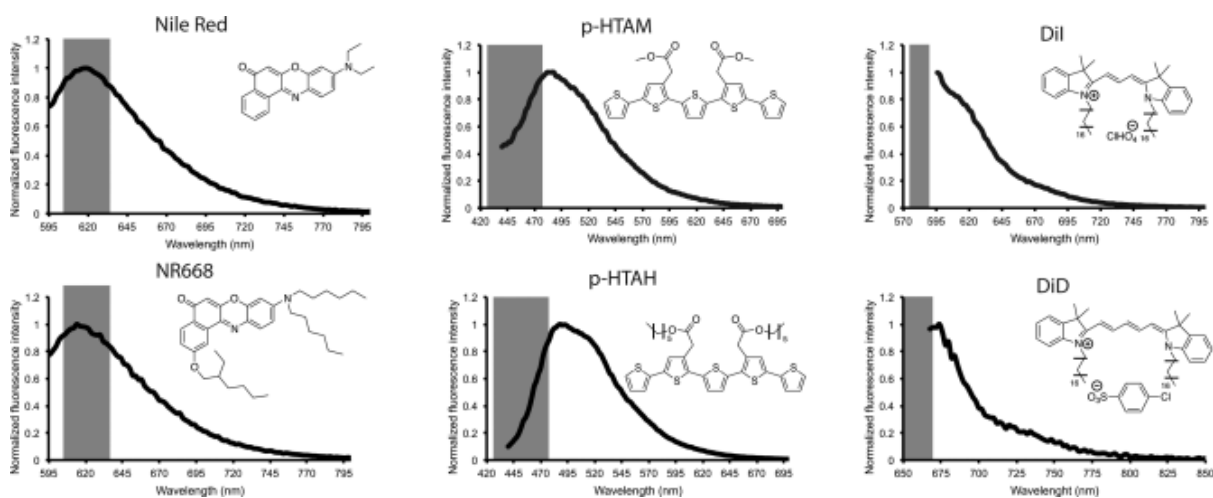


**Figure 1.3.9.** Chemical structures and emission spectra of the six dyes encapsulated in NPs at the excitation wavelengths used for FCM: 561 nm for NR and NR668; 405 nm for p-HTAM and p-HTAH; 561 nm for Dil and 633 nm for DiD. The detection bandpass filter used in FCM is shown in gray. Adapted from ref.<sup>81</sup>

The cells were incubated with dye-loaded poly(butylcyanoacrylate) (PBCA) nanoparticles, nanoemulsions (NE) or liposomes for 3 hours at 37 °C and at 4 °C. Incubation at the lower temperature does not allow energy-dependent internalisation of nanoparticles (endocytosis), therefore any dye found in the cell after incubation at this temperature is a proof of dye leakage from nanocarrier. After such incubation fluorescence of cells was analysed by flow cytometry and the judgements on dye leakage were made according to presence/absence of cell fluorescence at 4 °C and the ratio of cell fluorescence at these temperatures.

It was found that Nile Red leaks out of all tested nanocarriers, while its more hydrophobic version NR668 is retained in PBCA NPs, but leaks out of liposomes and nanoemulsions. The dye p-HTAM only leaked from liposomes, and cyanines Dil and DiD did not leak out of any nanocarrier. These results once again demonstrate how important is dye hydrophobicity for efficient encapsulation and prevention of leakage from nanocarriers, but also points out on differences in retention of the same dye in different nanocarriers.

In a work by *Sletten et al.*<sup>82</sup> it was shown, how adding fluorinated ponytails to fluorophores can dramatically increase the stability of perfluorocarbon (PFC) nanoemulsions against dye leakage (Figure 1.3.10).

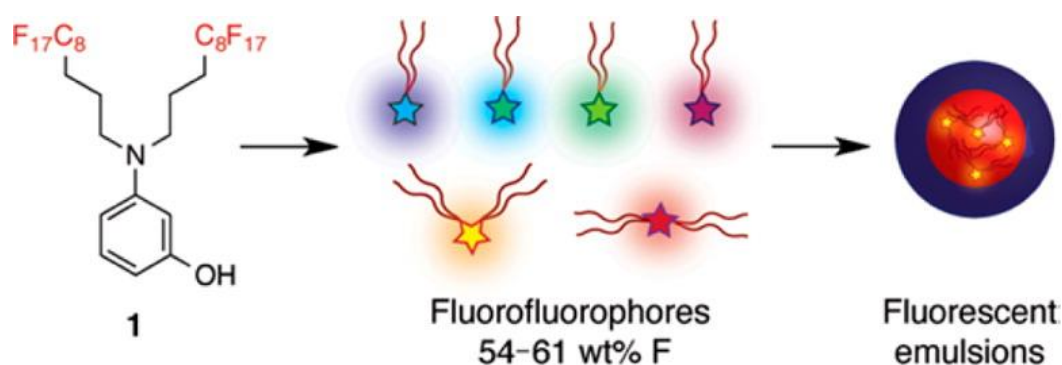


**Figure 1.3.10.** Aminophenol **1** as a building block for fluorinated fluorophores and preparation of fluorescent perfluorocarbon emulsions. Adapted from ref.<sup>82</sup>

By preparing separately perfluorocarbon nanoemulsions, containing fluorinated coumarin and fluorinated rhodamine and mixing them afterwards, they observed no FRET between the dyes even after multiple days and even in the presence of serum. However, after sonication of this mixture, the same FRET signal was observed as in the case of co-encapsulation of both dyes into one emulsion.

To clearly demonstrate the effect of amount of fluorines in the molecule on encapsulation efficiency, they synthesized coumarins with different length of fluorinated ponytails and encapsulated them into perfluorocarbon nanoemulsions. These emulsions were stirred with octanol for 2 weeks and the concentration of dyes in octanol phase was periodically measured, revealing that release times increase strongly with increase in fluorine content (>60 times difference in release amount between the most and least fluorinated dye after two days).

A quite unconventional example of increasing dye hydrophobicity was presented in our group<sup>83</sup> – Dil, a cationic dye with long hydrocarbon chains, was encapsulated into lipid nanodroplets at high loading with the help of bulky and hydrophobic tetraphenylborate as an anionic partner (Figure 1.3.11).

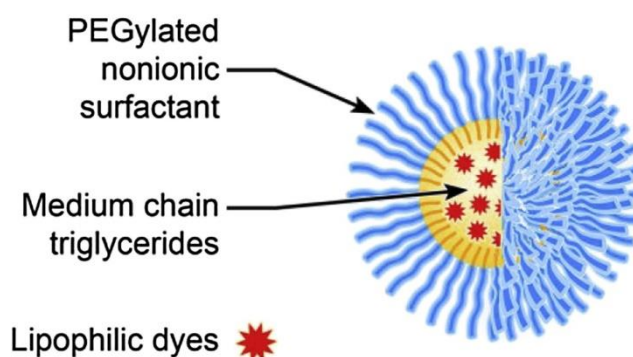
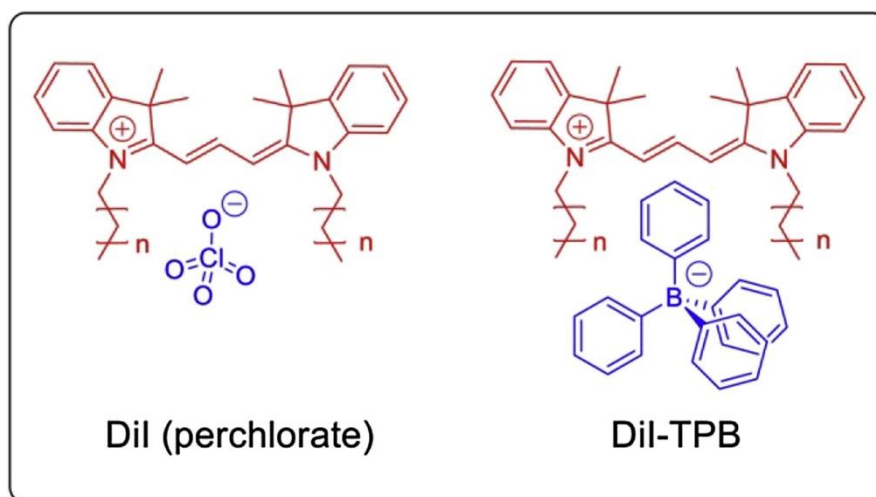


**Figure 1.3.11.** Chemical structures of Dil perchlorate and Dil-TPB and schematic presentation of nanodroplet encapsulating them. Adapted from ref.<sup>83</sup>

To encapsulate a dye inside a lipid nanodroplet, it is first dissolved in the corresponding oil, Labrafac in this case. And already at this step Dil-TPB has shown major improvement comparing to commercial Dil perchlorate – it could be dissolved at more than 8% w/w, while the latter topped at 0.2% w/w. Such huge dye concentration in the oil allowed preparing ~90-nm nanodroplets with ~12000 dyes per particle that were ~5 times brighter than commercial FluoSpheres of 45 nm size. Moreover, when these droplets were used for blood flow imaging in living zebrafish embryo, they have shown no sign of dye leakage *in vivo*. This indicates that adding a hydrophobic counterion to an ionic dye is an effective way to increase the dye hydrophobicity and prevent it from leakage from nanocarriers.

Summing up the overviewed examples in this chapter, we can clearly state that both matrix, dye and their combination strongly affect dye encapsulation and leakage. The high affinity between the dye and the matrix obviously plays the key role in stability of PFC nanoemulsions loaded with fluorinated dyes, while the affinity of a hydrophobic dye to lipid matrix or polymer NPs is not always enough to prevent it from leaking to

another hydrophobic environment upon contact. However, the probability of such transfer strongly decreases with increasing lipophilicity of the loaded dye.

## 1.4. Preventing dye self-quenching

Most of the examples of dye-loaded fluorescent polymer NPs, found in literature, show that quantum yield of the NPs drops dramatically on increase in dye loading higher than ~0.5% w/w, would it be copolymerised dye<sup>84</sup>, covalently attached to a polymer backbone<sup>85</sup>, swollen into a polymer<sup>86-89</sup> or loaded during nanoparticle preparation<sup>74, 90-92</sup>. The main reason of this loss of fluorescence is attributed to aggregation-caused quenching (ACQ) – formation of non-fluorescent dye aggregates of otherwise emissive fluorophores. It is especially pronounced for flat dyes with extended  $\pi$ -conjugation chains that favour  $\pi$ - $\pi$  stacking<sup>68</sup>. As most of conventional dyes belong to that group, it limits their use for creation of ultra-bright highly-loaded fluorescent nanoparticles.

This chapter will be dedicated to different examples of dyes aggregation-caused quenching inside nanoparticles and ways to decrease it, like covalent fixation of dye within polymer matrix or introducing bulky side groups to fluorophores. Also, a brief introduction to the concept of aggregation-induced emission (AIE) inside polymer NPs will be presented. Finally, the recently developed method of combining bulky counterions with ionic dyes for ACQ prevention will be discussed in a separate chapter.

### 1.4.1. NPs with covalent fixation of dyes inside polymer matrix

The dye self-quenching in polymer nanoparticles was investigated in depth by the group of Méallet-Renault.<sup>93</sup> They synthesized polymer nanoparticles composed of triblock copolymer with hydrophilic and hydrophobic chain fragments, copolymerizing a functionalised BODIPY fluorophore (1 to 10% w/w) in the hydrophobic part of the polymer chain (Figure 1.4.1).

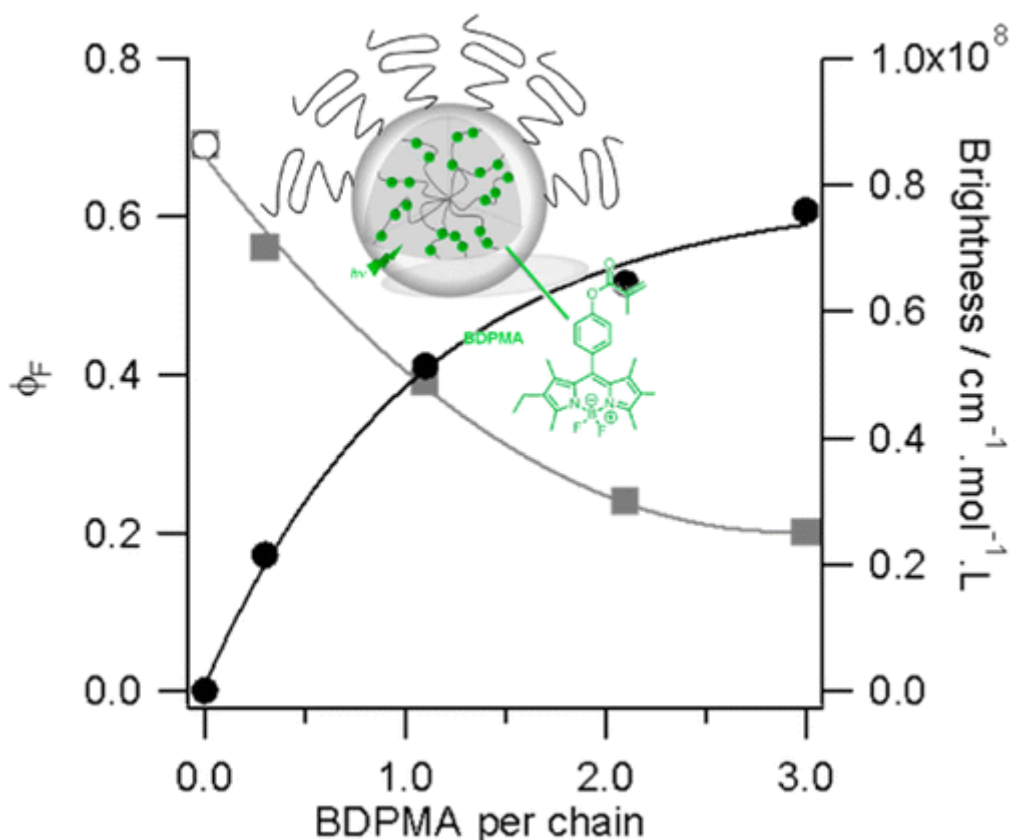


**Figure 1.4.1.** Graphical abstract of the ref.<sup>93</sup>: Schematic representation of the fluorescent core-shell nanoparticles and evolution of the brightness (circles) and of the fluorescence quantum yield  $\phi_F$  (squares) of the different FNP in water as a function of the average BDPMA per polymer chain. The open circle (○) corresponds to the fluorescence quantum yield of the monomer BDPMA in toluene. Adapted from ref.<sup>93</sup>

It is shown, that with increasing the concentration of dye component in the polymer chain, quantum yield of the NPs decreases, however overall brightness still increases. Fluorescence lifetime measurements of NPs solutions suggested that loss of fluorescence is caused by increased concentration of dyes – for the particles with the lowest concentration of BODIPY fluorescence decay is purely monoexponential, signifying isolated state of fluorophores. However, for higher loadings additionally to isolated fluorophores there is an increasing fraction of fluorophores with various decreased lifetimes.

To further investigate this quenching phenomenon, nanoparticles were extracted with toluene from acidified water, and quantum yields and fluorescence lifetimes of those dissolved polymer chains were measured. For all but the most BODIPY-rich polymer chains quantum yields and lifetimes were equal to that of pure dye in toluene, while for the most dye-loaded polymer quantum yield was lower and lifetime was slightly shorter. The latter case clearly showed that there is a fraction of intrachain ACQ, most likely due to inhomogeneous distribution of BODIPY in the chain during

polymerisation<sup>94</sup>, however the fraction of interchain ACQ is still much more significant. These results clearly show the importance of controlling fluorophore's spatial distribution inside FNPs to ensure highest possible brightness.

In a study on PDI aggregation by Wurthner group<sup>95</sup> self-assembling PDI molecules were synthesized. Due to structure asymmetry (Figure 1.4.2) they formed micelles or, upon mixing them with small amounts of symmetrical PDIs, vesicles. Further polymerisation of vesicles locked their structure to prevent it from disassembly.

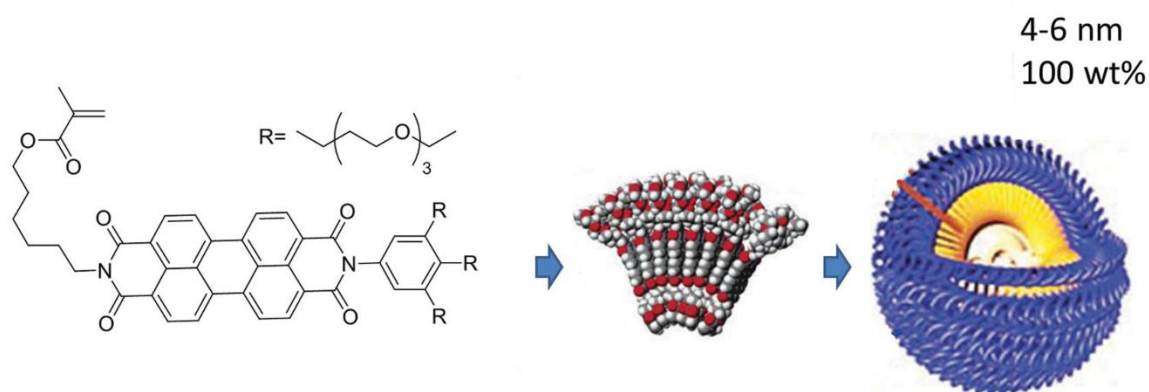


**Figure 1.4.2.** Structure and schematic self-assembly of polymerisable PDIs. Adapted from ref.<sup>68</sup>

Importantly, fluorescence of these nanoassembled structures shifted from strong, narrow and green (monomer emission) to rather weak, broad and red, this being an evidence of fluorescent aggregates formation (excimers according to the authors).

This feature of PDIs shifting their emission to the red was exploited by *Yang et al*<sup>96</sup> to create NIR-emitting nanoparticles. The designed perylenediimide acrylate (PDA) was copolymerised with (poly(ethyleneglycol)methacrylate (PEGMA) into diblock copolymer poly(perylenediimide acrylate)-*block*-poly-(poly(ethyleneglycol)methacrylate), or shortly PPDA-b-P(PEGMA) (Figure 1.4.3).

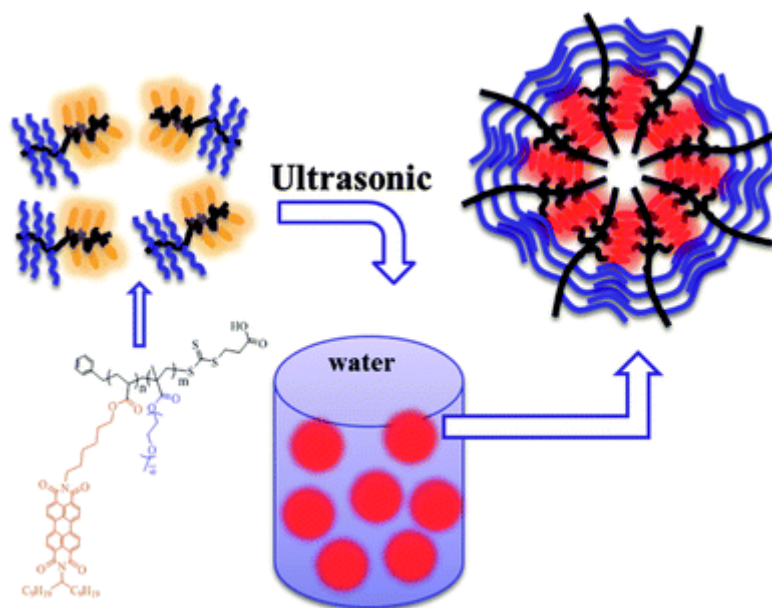


**Figure 1.4.3.** Scheme of the preparation of PPDA-b-P(PEGMA) PNPs. Adapted from ref.<sup>96</sup>

Being of amphiphilic nature, this polymer forms ~60 nm core-shell nanoparticles in water, the dye being located in hydrophobic core, tightly packed. This packing results in PDI aggregation and shifting of the emission maximum to 660 nm. Depending on the polymer concentration in water, the ratio of fluorescence of monomeric and aggregated form of PDI changes, the fluorescence shifting to the red upon increasing concentration. At already 0.3 mg/ml polymer concentration in water only NIR emission is observed.

In a work by *Tian et al.*<sup>65</sup>, the approaches of covalent fixation of dye and its structural modification towards decreased quenching are combined. The group prepared polymeric nanoparticles of about 40 nm size using emulsion polymerisation with bay-substituted polymerisable perylenediimide (PDI) as one of the monomers, varying its amount from 0.3 to 2.4 wt% (Figure 1.4.4).

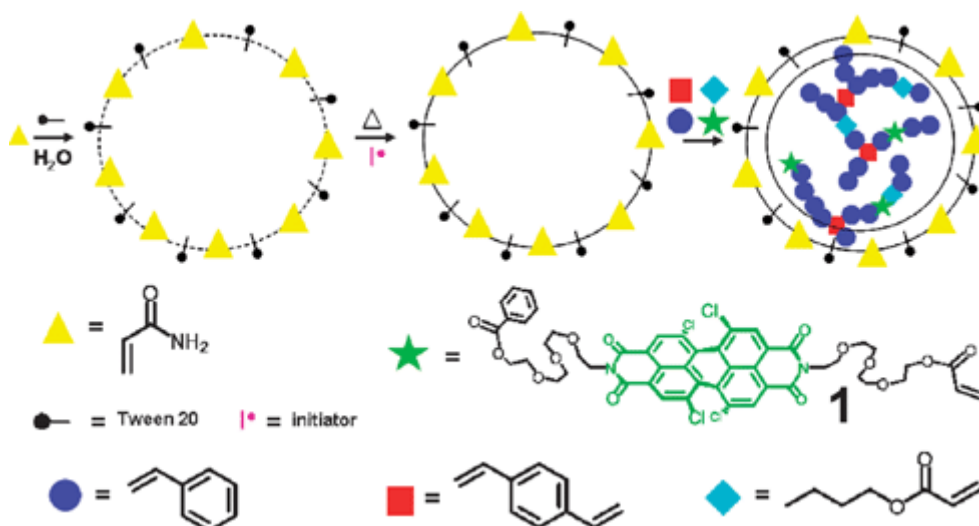
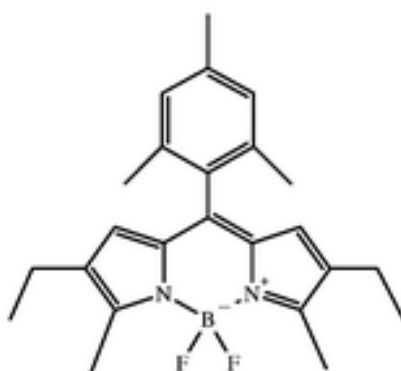


**Figure 1.4.4.** Polymeric nanoparticle synthesis with twisted PDI monomer. Adapted from ref.<sup>65</sup>

The obtained FNPs demonstrate a drop of quantum yield upon increasing the loading (from 0.5 for 0.3 wt% to 0.2 for 2.4 wt% versus 0.9 for monomer), however overall brightness of the nanoparticles still increases. Such drop of quantum yield with concentration is not accompanied by strong changes in absorption or fluorescence spectra, unlike the situation with PDI molecules without substituents in bay positions (strong shift to the red in emission spectra, dramatic change in the shape of absorption spectra). Another interesting thing they noticed is the differences in fluorescence traces of nanoparticles depending on PDI amount. All tested nanoparticles demonstrated 3-4 times drop in fluorescence upon illumination, however after this drop fluorescence remains stable, and the rapidity of the drop increases with increase in the fluorophore loading. Authors attribute this peculiar behaviour to a fraction of “non-photostable” fluorophores, although one could assume that this non-photostable fraction is just dye aggregates. In this case, after photobleaching of these aggregates, only the fluorescence of isolated well-dispersed fluorophores remains.

### **1.4.2. NPs encapsulated with bulky dyes**

In another paper of *Méallet-Renault et al*<sup>97</sup>, also with BODIPY-loaded polymer NPs, the structure of BODIPY itself was modified (Figure 1.4.5) to prevent it from self-quenching. The *ortho*-methyls of phenyl ring of BODIPY ensure the restriction of phenyl ring rotation and, being orthogonal to fluorophoric part of the molecule, should prevent them from stacking.



**1**

**Figure 1.4.5.** Structure of Mes-BODIPY 1. Adapted from ref.<sup>93</sup>

Cross-linked polystyrene NPs of 16 nm in size were swollen with DCM solutions of different concentrations of their bulky BODIPY dye, Mes-BODIPY, and after DCM evaporation the dye remained in the NPs, homogeneously distributed inside the NPs matrices. This procedure allowed obtaining fluorescent NPs with about 3% w/w dye loading and quantum yield as high as 77%. This high value is obtained even despite dyes proximity, which is close enough to demonstrate excitation energy transfer, as shown by fluorescence anisotropy studies.

Another bright and photostable dye, that needed structure modifications to prevent it from ACQ, was PDI. It was previously shown, that adding bulky substituents to bay positions<sup>98</sup> of PDI can prevent  $\pi$ - $\pi$  stacking of the dyes and significantly decrease self-quenching. One of the most successful examples of such bay substitution, Lumogen Red (LR) (Figure 1.4.6), started to be used in high loadings in, for example, PMMA polymer films<sup>99</sup>, where it demonstrated minimal self-quenching.

A work on comparing properties of NPs, encapsulating differently substituted PDI dyes was done in our group<sup>100</sup>. 40-nm PLGA NPs were loaded with PDI-1 and LR dyes (Figure 1.4.6) at different loadings (from 0.02% to 5% w/w) and their properties were investigated.

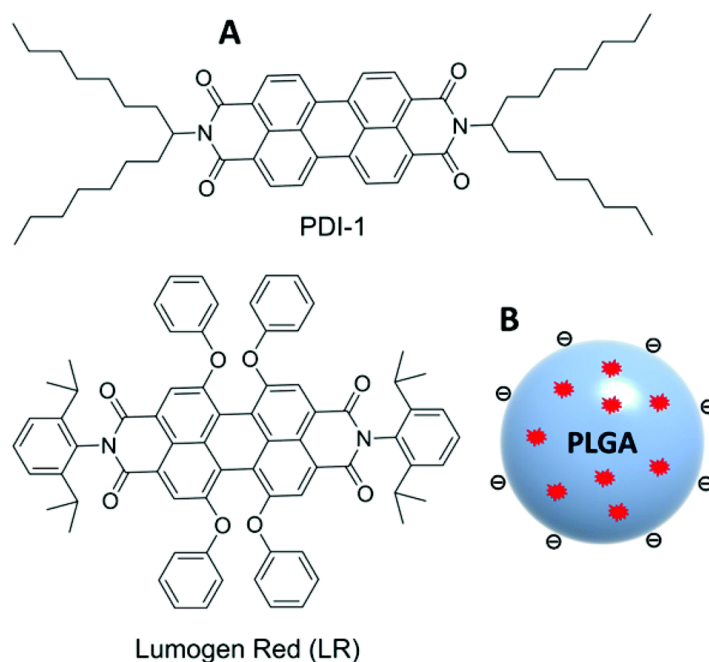


**Figure 1.4.6.** Chemical structure of PDI-1 and LR dyes (A) and schematic presentation of dye-doped PLGA nanoparticles (B). Adapted from ref.<sup>100</sup>

Spectral changes upon increasing loading were dramatically different for the two dyes. For PDI-1, in line with previously described<sup>95, 101, 102</sup> behaviour during aggregation, absorption maximum shifted from usual 530 nm to a more short-wavelength peak at 490 nm, and this was also accompanied by spectral broadening. In fluorescence spectra the increase in loading lead to appearance of a broad fluorescent peak with maximum about 660 nm, which becomes the major peak at 5% loading (w/w). None of this was observed for LR-loaded dyes – only minimal increase in short-wavelength peak was observed in absorption spectra, accompanied by slight shift of fluorescence spectra to the red, without significant shape changes.

Quantum yields of both dyes dropped with loading - to 31% for PDI-1 and to 47% for LR at the same (5%) dye loading, however this drop is astonishingly low considering the high loading. Another difference in NPs behaviour was revealed during single-molecule microscopy. 5%-loaded LR particles demonstrated excellent brightness (14-fold higher than QDs) and photostability (more stable than commercial FluoSpheres®), while PDI-1 loaded particles already at 1% loading have shown dramatic drop of fluorescence intensity in the first seconds of acquisition. This absence of photostability of PDI-1 is attributed to aggregates formation, which is avoided in case of bulky bay-substituted LR, once again proving the importance of bulky groups for prevention of dyes aggregation inside nanoparticles.

Despite substitution of perylenes in bay positions has become a conventional way to prevent their aggregation, this modification shifts absorption of the molecule to the red. To avoid altering the optical properties of conventional PDI, Banal et al<sup>103</sup> designed a new PDI, substituted in the imide region with bulky groups (Figure 1.4.7a). They encapsulated it into PMMA film and found that it has very promising optical properties.

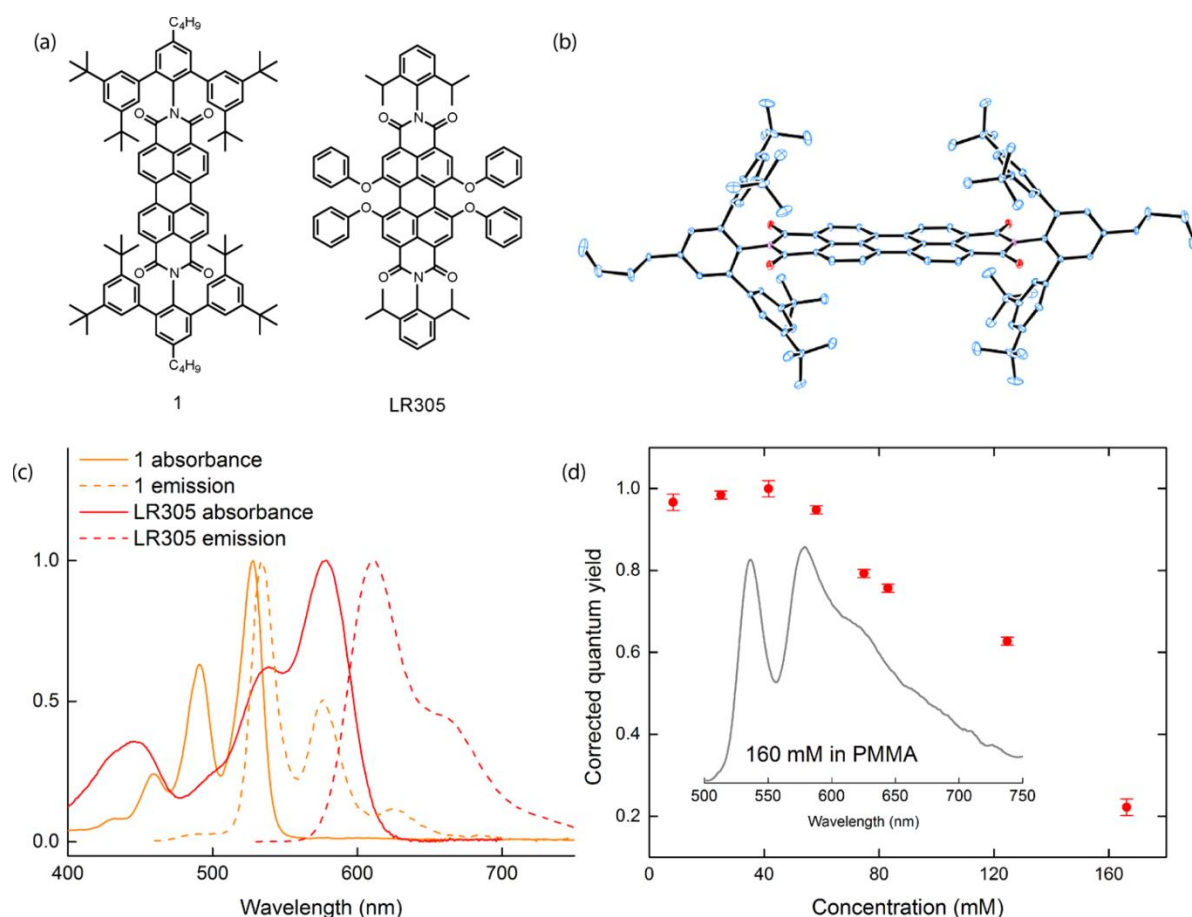


**Figure 1.4.7.** Molecularly insulated perylenediimide. (a) Chemical structures for 1 and LR305. (b) Crystal structure of 1. (c) Comparison of the normalized absorption and emission spectra of 1 and LR305 in chloroform. (d) Fluorescence quantum yield concentration dependence for 1 in PMMA as host. Inset shows the loss of vibronic structure in the emission due to the possible formation of excited complexes at the highest concentration studied. Adapted from ref.<sup>103</sup>

As intended, absorption and emission maxima of the new molecule **1** did not shift to the red (Figure 1.4.7c), and quantum yield studies have shown that up to 60 mM loading (~8.4 % w/w) the new dye **1** retains incredible quantum yield close to unity (Figure 1.4.7d). However, after 60 mM loading the quantum yield gradually drops. Authors attribute that to reabsorption and excited complexes formation that serve as energy traps. They calculated that already at 60 mM the molecules are located so close, that energy migration through homoFRET is close to unity, therefore even the

slightest concentrations of energy traps could quench the whole particle. At the highest studied concentration, 170 mM (~23.8% w/w), quantum yield dropped to about 20%, and the fluorescence spectrum lost its fine vibronic structure. This indicates that the number of “imperfections” – irregular aggregates/excimer complexes increased sufficiently to quench most of dyes in the polymer matrix due to superefficient homoFRET at such concentrations.

### 1.4.3. Aggregation-induced emission NPs

While ACQ is a great problem for most of fluorophores localized at high concentrations in a nanoscale object, it is absolutely not the case for the new, but rapidly expanding field of aggregation-induced emission (AIE)<sup>104</sup> fluorophores.

AIE approach exploits special fluorophores, which are not fluorescent in solutions, but are highly emissive in the aggregated state<sup>105</sup>. Unlike conventional fluorophores, which are usually flat aromatic systems with  $\pi$ -conjugation of different length, AIE fluorophores usually have propeller-like structures (Figure 1.4.8), which make impossible their  $\pi$ - $\pi$  stacking in aggregated state. However, this propeller-like structure strongly enhances the nonradiative decay channel produced by internal rotation<sup>105</sup> or sends the molecule to non-fluorescent twisted intramolecular charge transfer (TICT)<sup>106</sup> state, unless the intramolecular rotation is restricted by, for instance, dye aggregation.

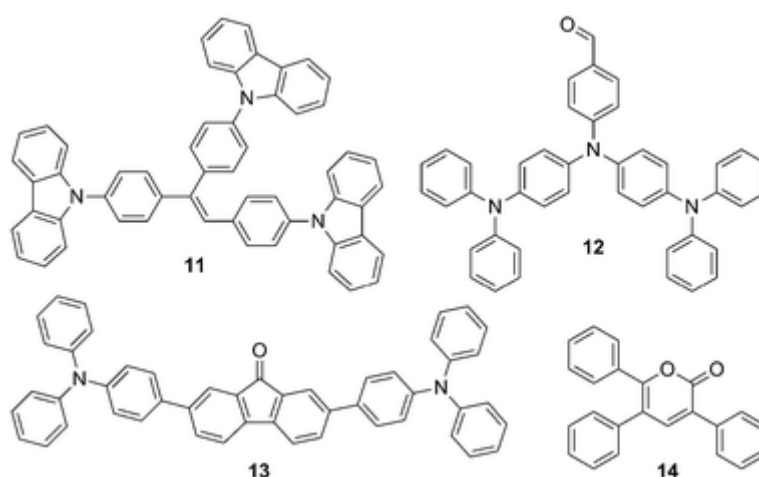


**Figure 1.4.8.** Examples of AIE luminogens. Adapted from ref.<sup>105</sup>

As for AIE dyes aggregation is an advantage, they are very promising candidates for encapsulation into nanoparticles, especially at high dye loading. Indeed, a recent

review by Li and Liu<sup>107</sup> shows numerous examples of different AIE dyes, encapsulated into polymer particles. These AIE-based NPs were used for in vitro and in vivo bioimaging studies.

One of the bright examples of AIE-based fluorescent NPs was the work<sup>108</sup> of Tang group, where a selected AIE dye was incorporated into ~30 nm nanoparticles made of lipid-PEG conjugate (Figure 1.4.9).

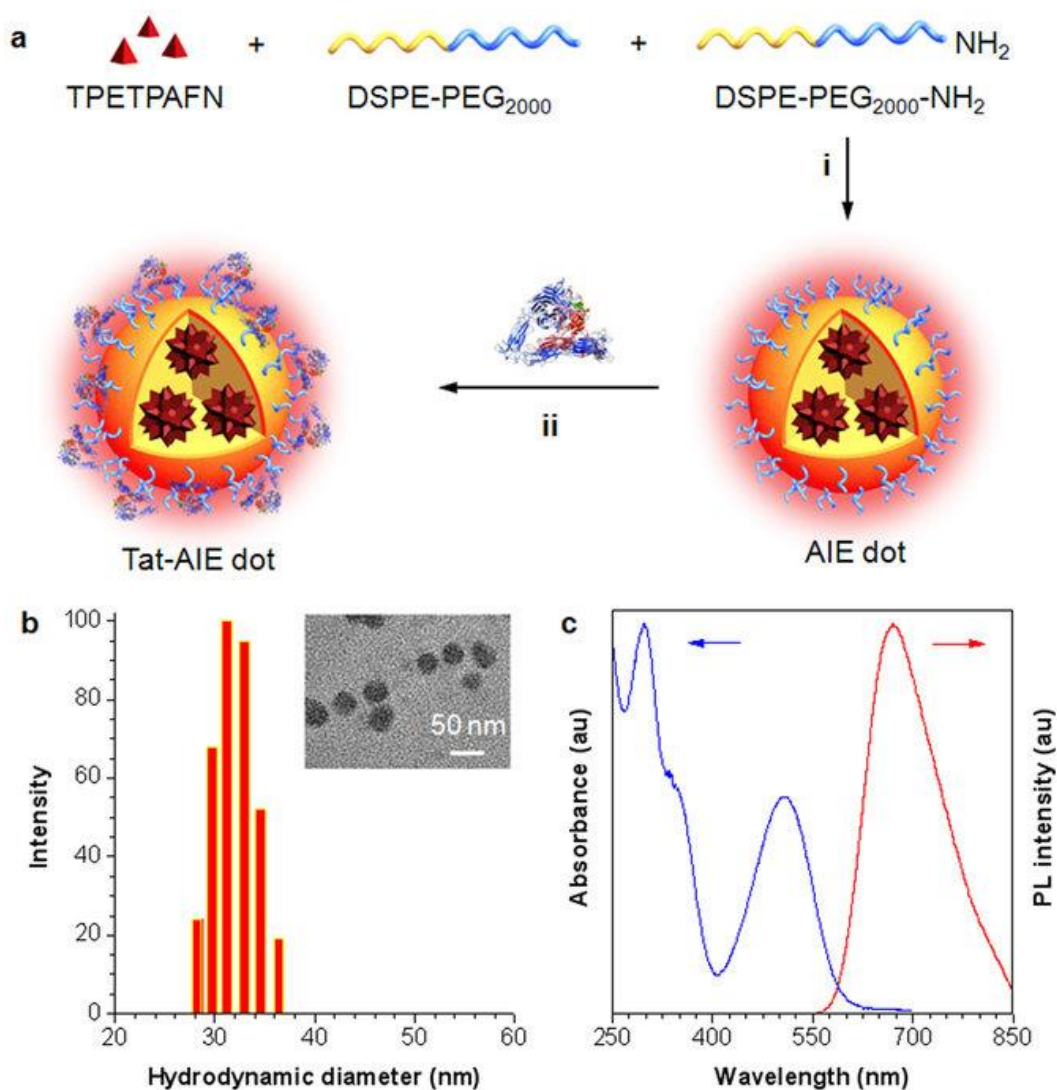


**Figure 1.4.9.** (a) Fabrication of Tat-AIE dots (b) Particle size distribution and morphological structure of Tat-AIE dots studied by laser light scattering (LLS) and (inset) high-resolution transmission electron microscopy (HR-TEM). (c) Absorption and emission spectra of Tat-AIE dots suspended in water. Adapted from ref.<sup>108</sup>

The NPs demonstrated unconventional for AIE dyes far red to NIR emission and reasonable quantum yield of 24% at a super high loading of ~40% w/w (which is typical for AIE systems). These NPs were also 10 times brighter than QDs 655, colloiddally

stable for weeks and were modified with cell-penetrating peptides to be used for cell labelling.

Another research worth noting in the context of my PhD work is dedicated to encapsulating AIE dyes into PLGA matrix.<sup>70</sup> The NPs were prepared using an oil-in-water single emulsion and solvent evaporation method (Figure 1.4.10).

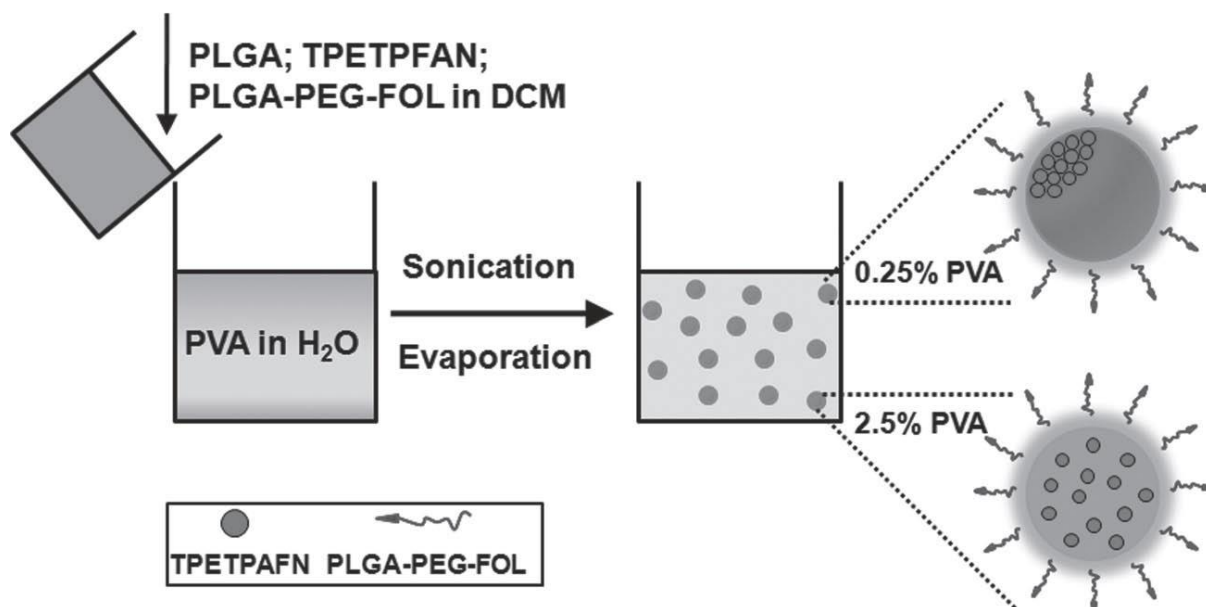


**Figure 1.4.10.** Schematic illustration of the fabrication of folate functionalized PLGA NPs eccentrically or homogeneously loaded with TPETPAFN. Adapted from ref.<sup>70</sup>

One of the interesting findings of this work was that location of the AIE dye inside nanoparticle strongly depends on emulsifier quantity (polyvinyl alcohol, PVA, in this case). At lower quantities of PVA dye is segregated inside nanoparticle, while at higher quantities it is more homogeneously dispersed (Figure 1.4.10). Homogeneous dispersion leads to weaker aggregation and, therefore, weaker emission of AIE-based dyes, which is confirmed by the results – for “segregated” batch of NPs the quantum yield is 65% higher.

Despite particularly interesting points that AIE approach proposes to the field of fluorescent nanoparticles, it has some drawbacks – AIE fluorophores have about 10 times lower extinction coefficients, examples of NIR-emitting dyes are rare, and currently no examples of NIR-absorbing dyes are reported to the best of our knowledge.

## 1.5. Weakly coordinating anions in fluorescent nanomaterials

As it is stated from the name, weakly coordinating anions (WCA) should coordinate weakly their cationic partners<sup>109</sup>. This is usually achieved by having the negative charge to be delocalized over a large area of non-nucleophilic, chemically robust moieties (Figure 1.5.1). However, it is important to remember that coordinating ability of an anion is limited by the most basic and/or most nucleophilic site.

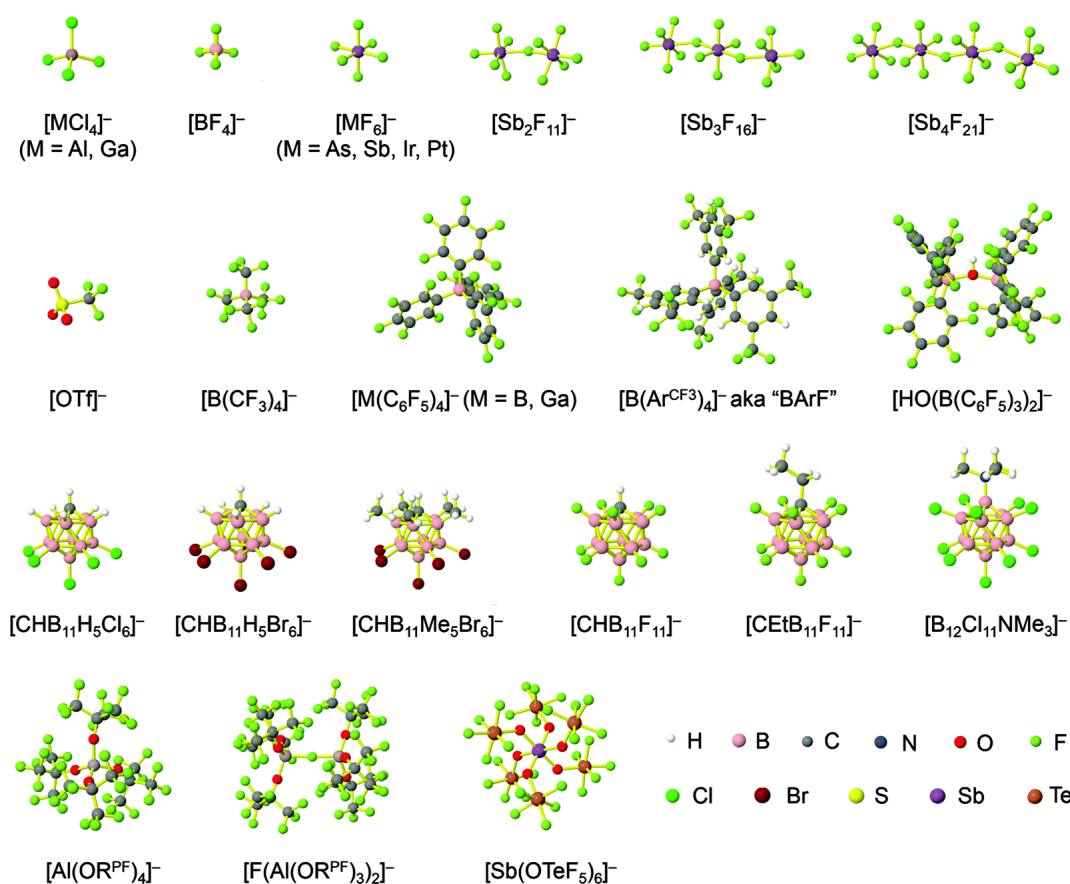


**Figure 1.5.1.** Typical structures of weakly coordinating anions. Adapted from ref.<sup>110</sup>

As "weakly coordinating" is a relative term, primarily it was applied to anions like perchlorate or tetrafluoroborate, which are now known to bind to strong electrophilic centres<sup>111</sup>. Development of new, more and more weakly coordinating anions is a hot topic in materials science and especially inorganic chemistry communities. Being primarily developed to stabilize reactive and unstable cations<sup>110</sup>, they found numerous applications in catalysis<sup>112</sup>, electrochemistry<sup>113</sup>, became components of lithium

batteries<sup>114</sup>, ionic liquids<sup>115</sup>, microporous materials<sup>116</sup>, ion-selective electrodes<sup>117</sup>, ion sensors<sup>118</sup>, solar cells<sup>119</sup> and organic light-emitting diodes<sup>120</sup>.

As modern WCA are generally bulky (to hinder reactive centre and/or achieve charge delocalisation) and hydrophobic (result of absence of basic/nucleophilic sites), they become interesting candidates to use in fluorescent materials – their bulk nature might prevent ACQ of cationic dyes, while hydrophobicity can increase encapsulation of dye-WCA ion pairs into hydrophobic matrices. And indeed, in the last decade there is a rising interest in using WCAs to develop fluorescent materials and improve their optical properties.

The studies of interactions of charged dyes with WCAs in solutions can be traced back to the beginning of 90s. It was shown, for example, that upon formation of ion pairs by cationic cyanines and their anionic partners in nonpolar solvents, the symmetry of cationic cyanine gets distorted<sup>121, 122</sup>: alteration of single and double bonds in polymethine chain of a symmetrical cyanine replaces the usual bond order of 1.5 (also called *ideal polymethine state*, IPS). However, the counterions used back then were perchlorate and tetrafluoroborate, which do not have clear WCA characteristics from the modern point of view. The association of ionic cyanines with hydrophobic counterions (including oppositely-charged dyes) in water was also studied in the 90s<sup>123</sup> – it was found that anionic cyanines disrupt symmetry of cationic cyanines even more than tetraphenylborate anion. Moreover, association constants show that both hydrophobic forces and Coulomb interactions play important role in hydrophobic ions association in water.

In a much more recent work by *Bouit et al.*<sup>124</sup> a comparison of properties of the same heptamethine cyanine with a series different counterions was made – from the smallest and hardest bromide to larger and softer organic anions. It was shown, that modern WCAs,  $B(C_6F_5)_4^-$  or TRISPHAT (Structure in Figure 1.5.2) do not disrupt the symmetric structure of cyanine polymethine chain, probably due to anion charge delocalisation and therefore low polarising ability. As a result, even in a nonpolar solvent, toluene, where dye-counterion ion pairs exist in contact (associated, intimate) form, the ideal polymethine state of cyanine is not disrupted. In the same conditions but with bromide as a counterion, the ideal polymethine state was lost, leading to broadening of the absorption spectrum and decrease in molar extinction coefficient. Similar effects were later observed in another research<sup>125</sup> on counterion effect for NIR

dyes, but this time it was done for photovoltaics application, using a different cyanine dye and only two counterions (Figure 1.5.2).

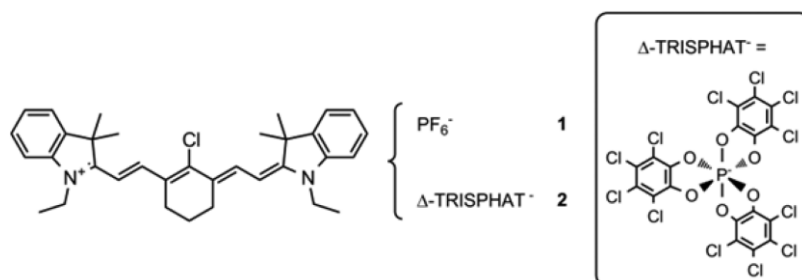


**Figure 1.5.2.** Structure of the heptamethine cation with the counterions hexafluorophosphate and TRISPHAT. Adapted from ref.<sup>125</sup>

In a brief communication<sup>126</sup> it was reported, that  $B(C_6F_5)_4^-$  anion strongly increases photo- and thermostability of the studied NIR cyanine dyes (Figure 1.5.3) comparing to the parent counterion, iodide. Interestingly, non-fluorinated tetraphenylborate does not increase thermal stability and even decreases photostability of the tested dyes comparing to iodide. Such difference in tetraphenylborates behaviour is attributed to effect of fluorination on the HOMO level of the anion – it was calculated to be lower in  $B(C_6F_5)_4^-$ , which decreases the probability of photoinduced electron transfer as a mechanism of dye photodegradation.

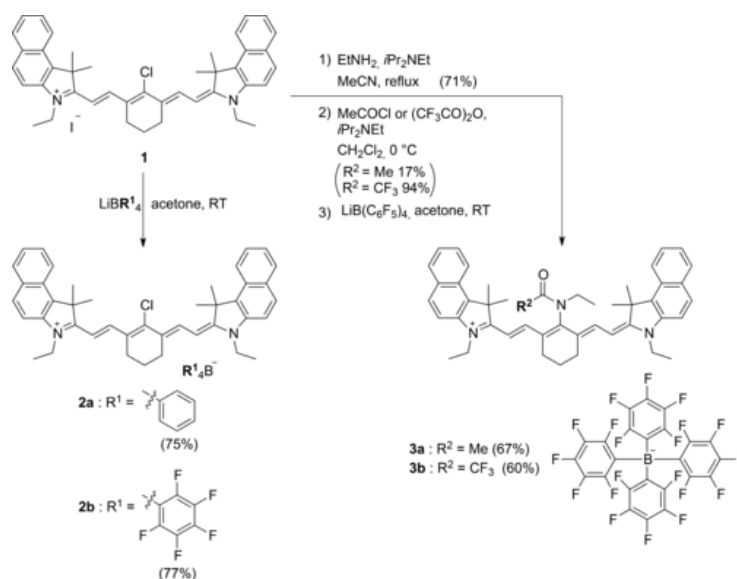


**Figure 1.5.3.** Preparation of heptamethine cyanine dyes, described in the work. Adapted from ref.<sup>126</sup>

One of the pioneers in the field of using counterions for fabrication of fluorescent nanoparticles and tuning their emission properties was Hiroshi Yao<sup>127</sup>. He started with describing formation of nanoparticles from pseudoisocyanine (PIC) dye and tetraphenylborate-based anions, showing the influence of components ratio on size (52-120 nm) and optical properties (maxima shifts and intensity) of the formed ion-associated nanoparticles. Later on, his group reported<sup>128</sup> preparation of malachite green (MG)-based fluorescent nanoparticles, formed by ion association of tetrakis(4-fluorophenyl)borate (TFPB) anion and MG in water (Figure 1.5.2).

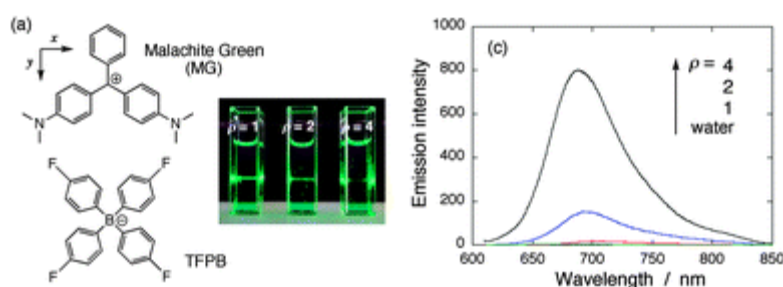


**Figure 1.5.4.** (a) Chemical structures of the malachite green (MG) cation and the tetrakis(4-fluorophenyl)borate (TFPB) anion. A photo of Tyndall scattering taken under green laser irradiation is also shown (c) Fluorescence spectra of MG nanoparticle samples prepared at  $\rho = 1, 2,$  and  $4,$  along with that of the liberated MG dye in aqueous solution ( $\lambda_{\text{ex}} = 600 \text{ nm}$ ) The molar ratio  $\rho$  is defined as  $[\text{TFPB}]/[\text{MG}]$ . Adapted from ref.<sup>128</sup>

Those fluorescent nanoparticles possessed about 200-fold enhancement of fluorescence quantum yield comparing to free MG dye in water, probably due to restriction of rotational and vibrational deexcitation. However, a significant ACQ effect was observed for these NPs due to H-aggregates formation. By preparing NPs with addition of tetraphenylphosphonium (TPP) to MG dye as a co-cation at the ratio of TPP/MG 5/1 it was possible to further increase quantum yield of the NPs twice. Nevertheless, this increased quantum yield was only about 3% in absolute value, which is still not very high. Worth noting, that in previous work<sup>129</sup> Yao group could obtain NPs with quantum yield close to 0.9 using the same approach, but different fluorophore – blue-emitting thiocyanine (3,3'-diethylthiocyanine). The dye has quantum yield of less than 1% in solution due to intramolecular rotation, however it increases about 200-fold upon formation of rigid nanoparticles. Another interesting point is simultaneous increase of short wavelength shoulder in absorption spectra (usually attributed to non-fluorescent H-aggregates) and fluorescence intensity in different NP formulations. This was explained by formation of inclined H-aggregates with non-forbidden fluorescence.

The group of Warner is another pioneer in counterion-assembled fluorescent nanoparticles. They call their materials as GUMBOS (Group of Uniform Materials Based on Organic Salts), with properties similar to frozen ionic liquids, and nanoparticles made of those salts are, respectively, nanoGUMBOS. One of the first works<sup>130</sup> was dedicated to preparation of NIR cyanine 7-based fluorescent nanoparticles. The ethanolic solution of the dye and one of the counterions (lipid-like bis(2-ethylhexyl) sulfosuccinate (AOT), triflate-imide NTf<sub>2</sub><sup>-</sup>, BF<sub>4</sub><sup>-</sup> and its monoaromatic-substituted derivative) was precipitated into excess of water under sonication, forming nanoparticles. Properties of NPs, such as size and absorption/fluorescence spectra appeared to be counterion-dependent. Unfortunately, no quantitative data on brightness or quantum yield of the formed NPs was provided, but presence of large amount of H-aggregates was evident from the spectral data.

Later on, they published a paper<sup>131</sup> on controlling aggregation in PIC-based nanoGUMBOS by counterion variation (Figure 1.5.5). It was found that NTf<sub>2</sub><sup>-</sup> counterion assembles PIC into diamond-like particles with a large fraction of J-aggregates and quantum yield of 1%. Quite similar counterion, BETI, induces rod-like assemblies with dominating H-aggregation and quantum yield of 0.2%. Therefore, even the slight change in counterion structure was able to induce dramatic changes in nanomaterials properties.

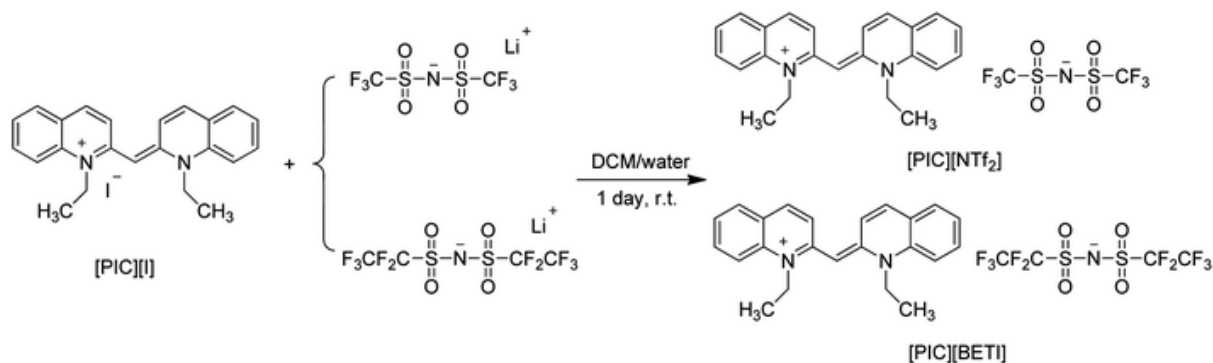


**Figure 1.5.5.** Synthesis of [PIC][NTf<sub>2</sub>] and [PIC][BETI] using an anion exchange reaction. Adapted from ref.<sup>131</sup>

In the further development of nanoGUMBOS, Warner group chose Rhodamine 6G as fluorophore and several new counterions to test (Figure 1.5.6). They found that among the tested series only TPB and BETI counterions induce NPs formation, with size about 100 nm. Those NPs with negative and pH-dependent zeta potential appeared to be selectively uptaken by cancer cells, where they acted as anticancer agents, presumably by inhibiting mitochondria functioning. Unfortunately, no data on

brightness of the obtained NPs could be found in the article, as the quantum yield measurements were performed at the concentrations below the critical association constant. This explains why neither quantum yield nor fluorescence lifetime of the tested systems depended on the counterion – the dyes were measured in the molecular form.

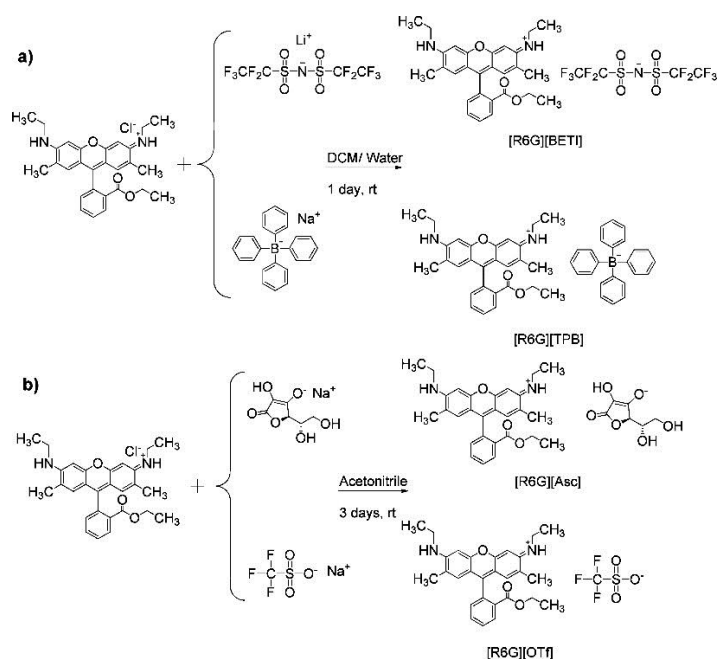


**Figure 1.5.6.** Synthesis of (a) Hydrophobic and (b) Hydrophilic R6G-Based GUMBOS. Adapted from ref.<sup>132</sup>

The group of Fery-Forgues also investigated the influence of counterions on properties of fluorescent materials. In a very recent paper<sup>133</sup> they shed light on their previous studies<sup>134</sup> on the counterion effect in fluorescent nanomaterials. Ion pairs of berberine (weakly fluorescent natural alkaloid) with different anions (Figure 1.5.7) were prepared and their properties were studied.

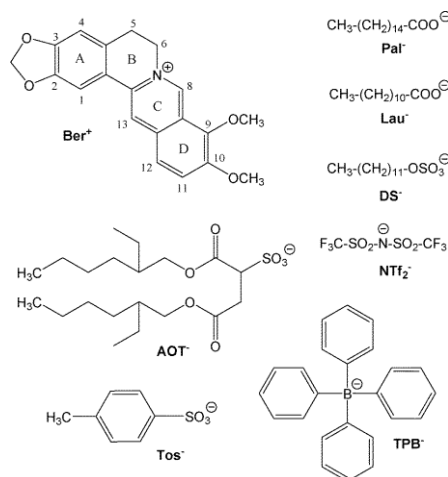


**Figure 1.5.7.** Chemical structures of the berberine cation (Ber<sup>+</sup>) and some associated anions: palmitate (Pal<sup>-</sup>), laurate (Lau<sup>-</sup>), dodecylsulfate (DS<sup>-</sup>), dioctylsulfosuccinate (AOT<sup>-</sup>), bis(trifluoromethane)sulfonimide (NTf<sub>2</sub><sup>-</sup>), *p*-tosylate (Tos<sup>-</sup>) and tetraphenylborate (TPB<sup>-</sup>).

They found that berberine forms fluorescent nanoaggregates in water with tested counterions, shape and size of those nanoassemblies being dependent on the counterion. Moreover, quantum yields of bulk solid salts were studied using integration sphere, showing tetraphenylborate salt being the least fluorescent with about 1% QY, while dodecylsulfate topping at about 7%. Strong influence of counterion structure on fluorescence spectra was also observed, showing emission maxima 512 and 552 nm for tosylate and tetraphenylborate counterions, respectively.

In our group the concept of *counterion-enhanced encapsulation and emission* has been proposed for several different types of fluorescent nanoparticles. The initial research<sup>135</sup> was dedicated to preventing ACQ in octadecylrhodamine B (R18)-loaded PLGA nanoparticles using different counterions (Figure 1.5.8).

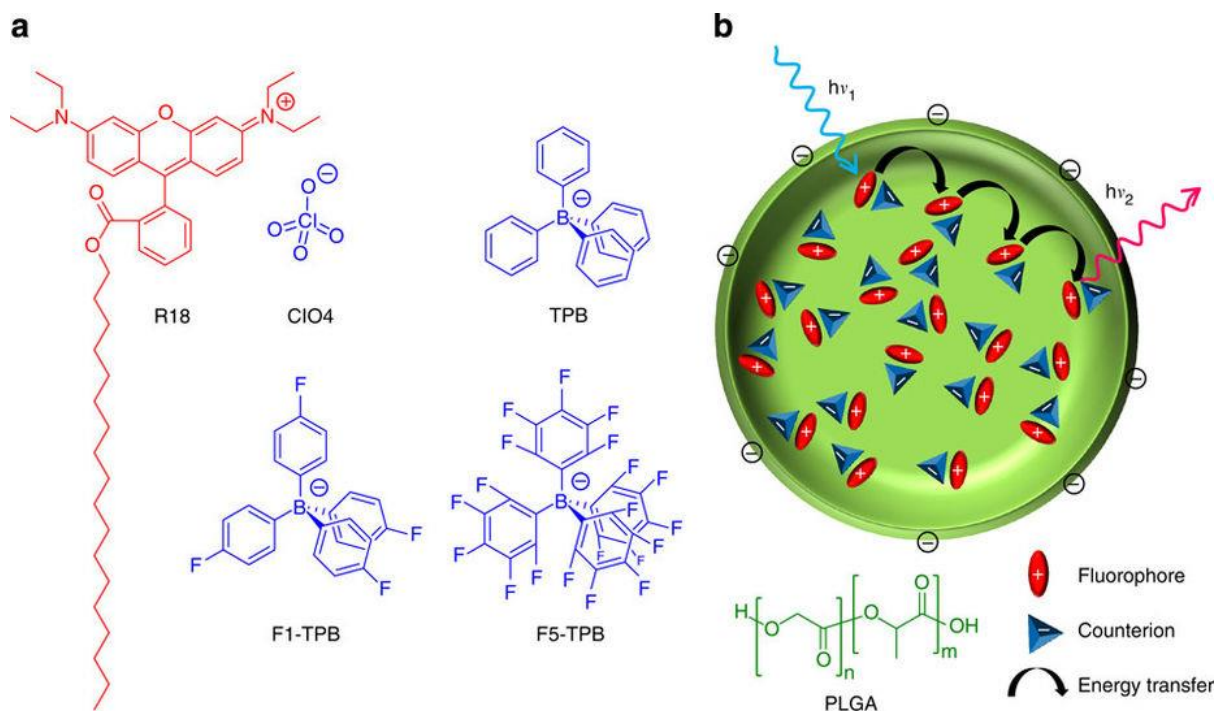


**Figure 1.5.8.** (a) Chemical structures of rhodamine B octadecyl ester (R18) and its different counterions: perchlorate (ClO<sub>4</sub>), tetraphenylborate (TPB), tetrakis(4-fluorophenyl)borate (F1-TPB) and tetrakis(pentafluorophenyl)borate (F5-TPB). (b) Schematic representation of PLGA NPs loaded with these dye salts. Adapted from ref.<sup>135</sup>

It was found that replacing perchlorate with tetraphenylborates as counterions for R18 dye significantly decreases polymer NPs size (from hundreds to ~40 nm) and increases their colloidal stability. However, only the most fluorinated tetraphenylborate, F5-TPB, could efficiently prevent ACQ in formed NPs, providing quantum yield as high as 23% at 5% dye loading (w/w). Such high brightness even exceeded that of quantum dots – the obtained NPs appeared to be 6 times brighter than QD-605. Moreover, upon illumination particles demonstrated reversible ON/OFF switching – hundreds of fluorophores behaved collectively due to counterion-driven assembly inside NPs, being able to be quenched by single acceptor or a dark species. The obtained nanoparticles at 1% loading (w/w) could enter cells by endocytosis and were used for cell labelling without signs of dye leakage.

The approach was further validated<sup>136</sup> for 20 nm PMMA-based polymer NPs, loaded with the same R18 dye with F5-TPB counterion. At 5% dye loading (w/w) the NPs have shown quantum yield of 60%, being 10 times brighter than QD-585.

It was also shown by *Shulov et al.*<sup>137</sup>, that tetraphenylborates can assemble rhodamine B-based dyes into polymer-free ~ 20 nm nanoparticles by simple excessive addition of counterion to the aqueous solution of the dye (Figure 1.5.9).

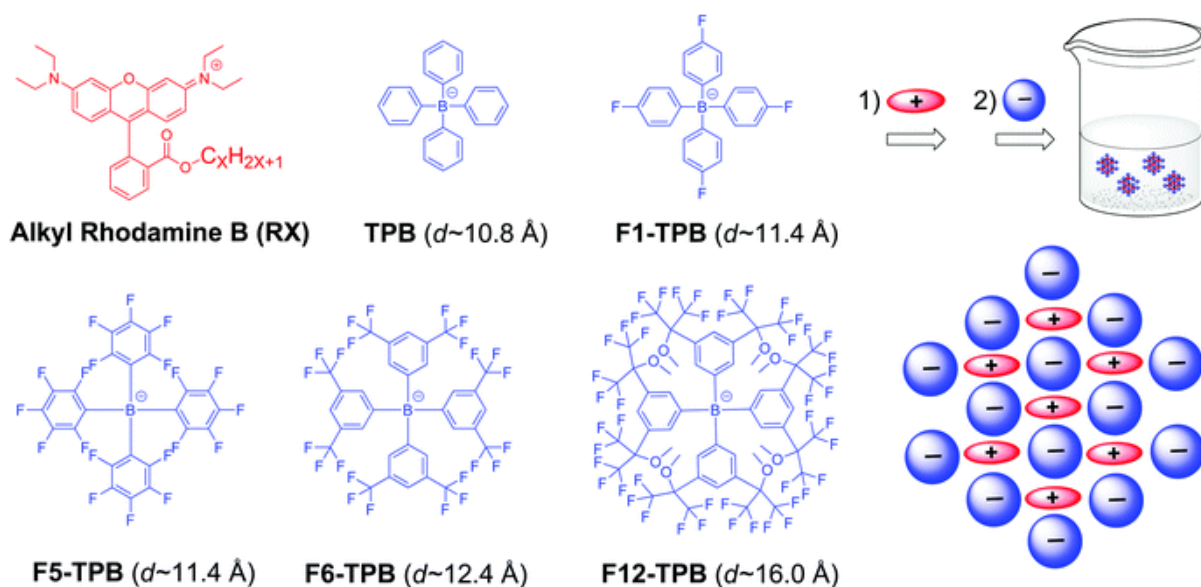


**Figure 1.5.9.** Chemical structures of the rhodamine B derivatives (RX, X varies from 2 to 18) and the different tetraphenylborate counterions used in the cited work. Adapted from ref.<sup>137</sup>

The obtained results clearly demonstrated correlation between fluorination level of tetraphenylborate counterion and photophysical properties of the obtained NPs: the most fluorinated F12-TPB being the brightest (QY  $\sim 60\%$ ), followed by F6-TPB and F5-TPB (QY  $\sim 50\%$ ). TPB did not show any ACQ-preventing effect, and F1-TPB has shown only minor one. F5-TPB and F12-TPB-based NPs appeared to have exceptional light-harvesting properties, single acceptor being able to harvest energy from hundreds of rhodamine donors. Interestingly, particles based on F5-TPB showed the same blinking behaviour as in the case of PLGA NPs, described earlier<sup>135</sup>, but in case of F12-TPB as a counterion no blinking was observed.

In another work by *Shulov et al.*<sup>50</sup> it is shown how cyanine-based amphiphilic molecules are assembled in to fluorescent nanoparticles without strong self-quenching (Figure 1.5.10).

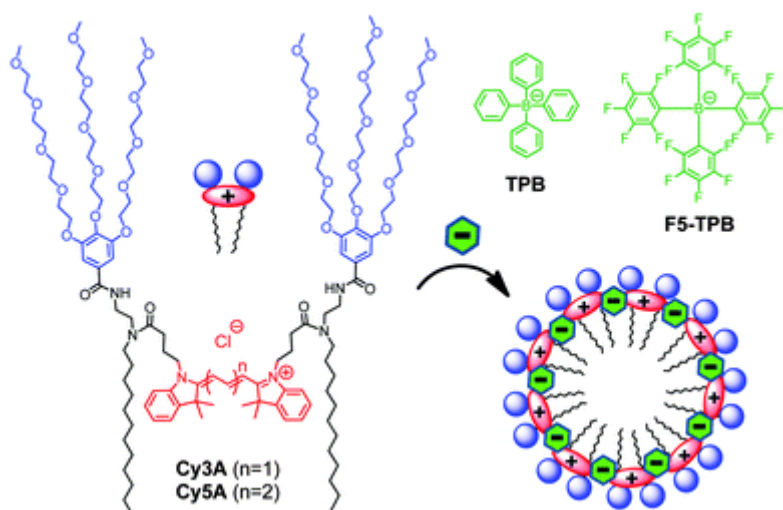


**Figure 1.5.10.** Cyanine amphiphiles and their expected assembly into micelles in the presence of non-coordinating anions. Adapted from ref.<sup>50</sup>

The obtained ~7 nm NPs of Cy3A and Cy5A amphiphiles with F5-TPB counterion have quantum yields of 25% and 8%, respectively. High cooperativity of dyes in this NPs was proven by anisotropy measurements and FRET experiments, showing efficient energy transfer from multiple donor dyes to a single acceptor.

Overall, WCA emerged recently as a promising tool for preparation of highly emissive nanomaterials. However, their role in the encapsulation of dyes inside polymer NPs as well as the structure-property relationships has not been studied well do date. Moreover, examples of WCA for preparation of fluorescent nanomaterials are still limited.

## Aim of my PhD project

Fluorescent organic nanoparticles are potentially the most bright and versatile imaging agents. However, as it was shown in the bibliographical overview above, there are several key challenges that arise on the way to these brightest nanoprobes – aggregation-caused quenching and inefficient encapsulation of the fluorescent dyes. Each of these problems has been studied, and several strategies to overcome those challenges have been proposed. However, the approach we recently suggested, namely *counterion-enhanced encapsulation and emission*, could solve both of them at the same time.

My PhD project focuses on development of this counterion-based approach, as the primary successful results were validated for only one dye-counterion pair: rhodamine B octadecyl ester with tetrakis(pentafluorophenyl)borate. Therefore, several questions should be addressed:

- Is the approach universal, e.g. is it compatible with other cationic dyes?
- How does the counterion structure affect NPs properties?
- What are the requirements for an effective counterion?
- Is it possible to find any other scaffolds that could substitute tetraphenylborates in the approach?

Answering those questions would allow developing ultra-bright non-leaking nanoparticles with customisable properties that would impact both fields of bioimaging and fluorescent organic materials.

## **2. Results and discussions**

## 2.1. Enhancing emission of cyanine dyes

### 2.1.1. Article 1: “Fluorescent Polymer Nanoparticles for Cell Barcoding In Vitro and In Vivo”

Development of ultra-bright bright fluorescent polymer nanoparticles has made a step forward after introduction of *counterion-enhanced emission* approach to fight aggregation-caused quenching<sup>135</sup>. However, as this approach was validated only for rhodamine B octadecyl ester (R18), it was important to show that this system is compatible with different cationic dyes. We chose five cyanine dyes, emitting from green to near-infrared, and tested their ion pairs with four different counterions (Fig. 1A) in PLGA (poly(lactide-co-glycolide)) nanoparticles at different dye loadings (5, 20 and 50 mM).

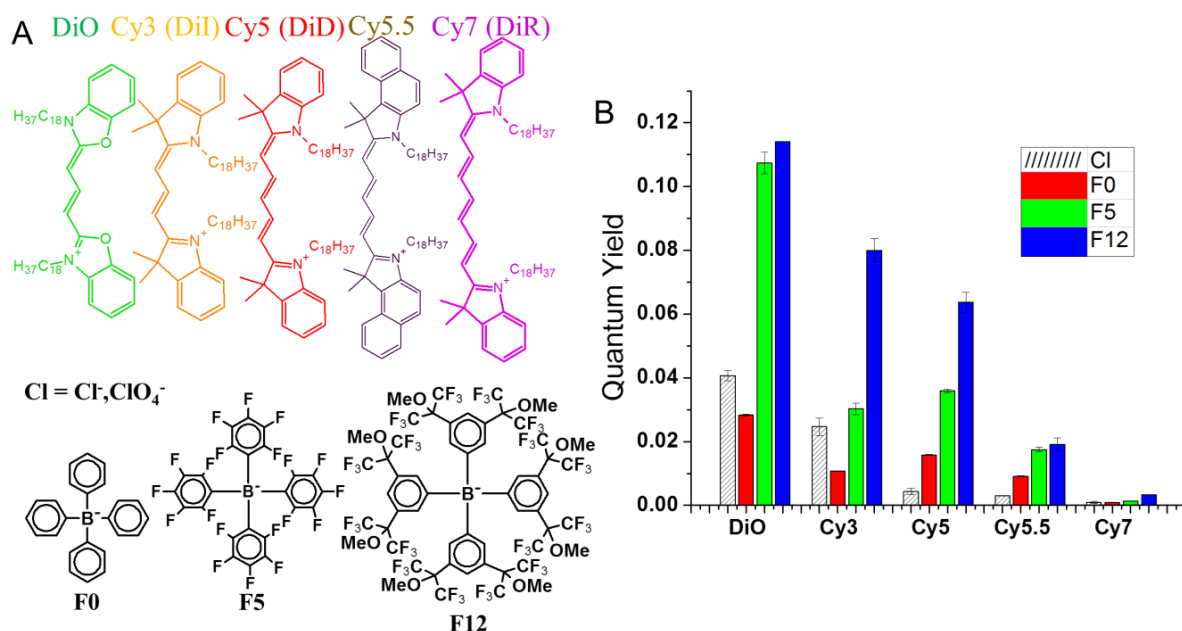


**Figure 1.** (A) Chemical structures of dyes and counterions used in this study. (B) Quantum yields of 50 mM-loaded nanoparticles of different dyes with different counterions.

It was found that with increasing size and hydrophobicity of the counterion, quantum yields of fluorescent nanoparticles increase independently on the cyanine dye, and the most performant counterion is **F12** (Fig. 1B). Size of the nanoparticles is

also affected by counterion nature: unlike derivatives of tetraphenylborate, allowing preparation of small nanoparticles around 40-50 nm, nanoparticles, encapsulating dyes with chloride/perchlorate counterion, are several hundred nanometres in diameter and are not colloiddally stable. Generally, quantum yield drops upon increasing dye loading, however in case of **F5** and **F12** counterions this drop is much less pronounced than in case of **Cl**. This decrease in quantum yield is also observed upon increasing the conjugation chain of encapsulated cyanines and moving from green to NIR part of the spectrum (Fig. 1B) independently on the counterion. Thus, it is clear that bulky counterions F5 and F12 minimize self-quenching, however they become less effective in case of near-infrared dyes.

Based on the obtained data, we chose **DiO**, **DiI** and **DiD** dyes with **F12** counterion at 20 mM loading to develop a colour coding system for long-term tracking of living cells. Importantly, surface properties of the three types of NPs (size, zeta potential etc.) were identical. Therefore, during cell labelling through endocytosis equal uptake of NPs was achieved. By mixing these 3 types of particles in different proportions, it was possible to create 13 colour codes (seven are presented in Fig. 2A) for cell labelling. The technique was validated on 6 cell lines (Fig. 2B), that could be distinguished by colour code even after 24 hrs of co-incubation.

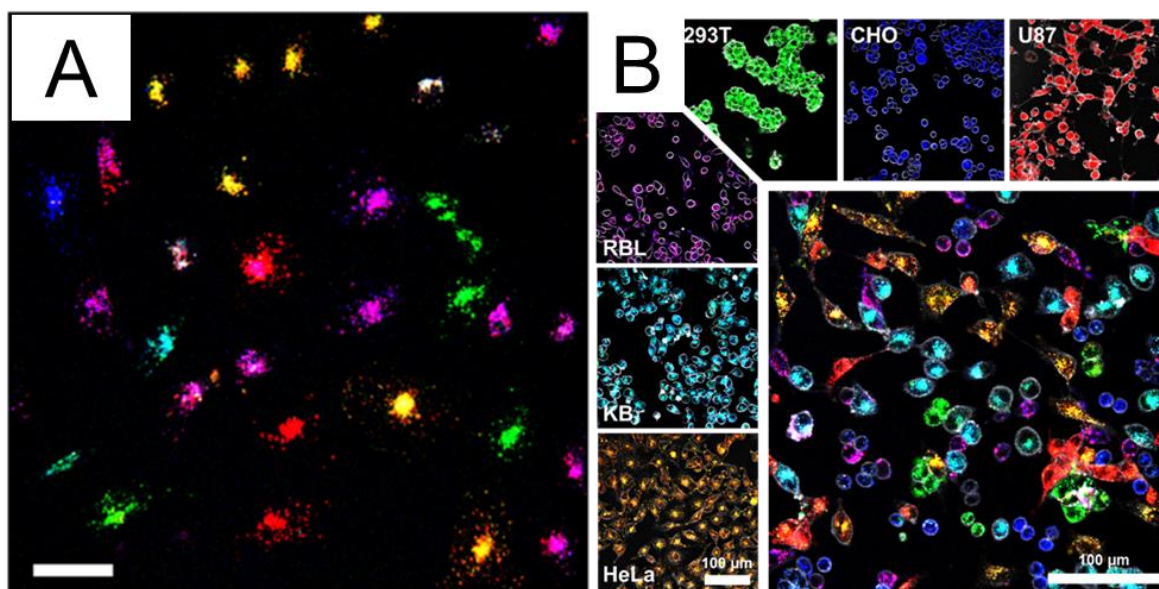


**Figure 2.** (A) Confocal image of a mixture of seven cell populations of different colors four days after labelling. (B) Confocal image of six cell types (HeLa, KB, 293T, U87, RBL, and CHO) mixed and co-cultured for 24 h. Each cell type was labelled with an RGB colour code (orange, cyan, green, red, magenta, and blue, respectively), also shown separately in the smaller images.

Developed method was further applied for 6-color tracking of tumour cells in a living zebrafish embryo (in collaboration with Jacky GOETZ) and cell tracking in the developing zebrafish embryo (4 or 8-cell stage, in collaboration with Nadine PEYRIÉRAS).

Results of the project were accepted to *Small* journal, the manuscript is enclosed below.

**Article type: Full paper**

## **Fluorescent Polymer Nanoparticles for Cell Barcoding in Vitro and in Vivo**

*Bohdan Andreiuk, Andreas Reisch\*, Marion Lindecker, Gautier Follain, Nadine Peyri ras, Jacky G. Goetz, Andrey S. Klymchenko\**

B. Andreiuk, Dr. A. Reisch, M. Lindecker, Dr. A. S. Klymchenko  
Laboratoire de Biophotonique et Pharmacologie,  
UMR 7213 CNRS, Facult  de Pharmacie, Universit  de Strasbourg,  
74, Route du Rhin, BP 60024, 67401 Illkirch, France.  
E-mail: andrey.klymchenko@unistra.fr ; reisch@unistra.fr.

G. Follain, Dr. J. G. Goetz  
MN3T, Inserm U1109, LabEx Medalis, F d ration de M decine Translationnelle de Strasbourg  
(FMTS), Universit  de Strasbourg, Strasbourg, 67000, France

Dr. N. Peyri ras  
CNRS USR3695 BioEmergences, Avenue de la Terrasse, 91190 Gif-sur-Yvette, France

**Keywords:** dye-loaded polymer nanoparticles, optical coding, long-term cell tracking, fluorescence microscopy, zebrafish

## **Abstract**

Fluorescent polymer nanoparticles for long-term labeling and tracking of living cells with any desired color code are developed. They are built from biodegradable PLGA polymer loaded with cyanine dyes (DiO, DiI and DiD) with the help of bulky fluorinated counterions, which minimize aggregation-caused quenching. At the single particle level these particles are *ca* 20-fold brighter than quantum dots of similar color. Due to their identical 40-nm size and surface properties, these nanoparticles are endocytosed equally well by living cells. Mixing nanoparticles of three colors in different proportions generates a homogeneous RGB barcode in cells, which is transmitted through many cell generations. Cell barcoding is validated on seven cell lines (HeLa, KB, 293T, CHO, RBL, U97 and D2A1), 13 color codes, and it enables simultaneous tracking of co-cultured barcoded cell populations for >2 weeks. It is also applied to studying competition among drug-treated cell populations. This technology enabled six-color imaging *in vivo* for (1) tracking xenografted cancer cells and (2) monitoring morphogenesis after microinjection in zebrafish embryos. In addition to a robust method of multi-color cell labeling and tracking, our work suggests that multiple functions can be co-localized inside cells by combining structurally close nanoparticles carrying different functions.

## 1. Introduction

The current trend in nanotechnology for biological applications is implementation of multiple functions within the same nanoparticle (NP). One should mention multimodal NP probes that enable simultaneous use of several imaging modalities, such as magnetic, X-ray and/or fluorescence.<sup>[1]</sup> Another example is co-encapsulation of a drug with an imaging agent, which enables developing highly promising tools for theranostics.<sup>[1b, 2]</sup> Finally, in optical imaging, which is currently undergoing remarkable growth, multiple colors are included within the same particles, thus providing them with unique color fingerprints (barcodes) for multiplex detection.<sup>[3]</sup> However, implementation of multiple functions within the same NP requires complicated synthetic protocols, which have to be revalidated for the whole system once a single function is changed, added, or removed. Moreover, these protocols do not always allow achieving high reproducibility of nanoparticle properties, so that the important challenges related to cost, effectiveness and toxicity of these NPs in the biomedical context are still to be addressed.<sup>[4]</sup> A totally different approach is to implement multiple functions separately into different NPs of practically identical characteristics, and then to combine them together to achieve a desired multifunctional effect in biological samples. In this case, the similar size and surface properties of the NPs ensure their identical delivery in biological samples so that multiple functions of these NPs are co-localized. This approach could be realized within optical modality, where structurally close NPs of different colors, undergoing identical delivery into live cells, could generate any desired barcode for long-term cell tracking *in vitro* and *in vivo*, something that has not been realized to date.

Long-term fluorescence staining of living cells in multiple colors is of high importance for tracking different cell populations *in vitro* and *in vivo*, and in this way helps to address key questions in cancer research, cell differentiation, cell therapy, regenerative medicine, embryogenesis.<sup>[5]</sup> However, due to the relatively broad absorption and emission bands of organic dyes, fluorescent nanoparticles and fluorescent proteins standard fluorescent microscopy can distinguish only 4-5 individual colors. A recently proposed concept, named “Brainbow”,<sup>[6]</sup> overcomes this problem by using RGB optical (color) coding, where a practically unlimited number of barcodes can be generated by co-expressing blue, green and red fluorescent proteins in a stochastic and thus unique combination. This method has been successfully used for visualizing neuronal networks *in vitro* and *in vivo*<sup>[7]</sup> and cellular organization and development in small animals,<sup>[8]</sup> and was recently proposed for stem cells<sup>[9]</sup> and cancer research.<sup>[10]</sup> However, color coding of living cells without their genetic modification is underexplored. To develop such a method, several fundamental problems have to be addressed: (i) long-term cell staining should be achieved; (ii) this implies that staining should be sufficiently bright despite multiple cellular divisions; (iii) the individual colors should be stable and

well resolved, so that each color code and thus each cell population could be recognized even after several weeks; (iv) the staining should not produce toxic effects, especially in the view of long-term studies. Organic dyes, such as hydrophobic cyanine dyes (DiO, DiI, DiR and PKH family) and the specially designed CellTracker™ and CellTrace™ families (CFSE, CM-DiI, CMTMR, etc) can be used for long-term cell staining.<sup>[11]</sup> However, the staining generally remains for only about 3 days.<sup>[12]</sup> Moreover, no reports showed that these dyes could be used in combination to generate multiple colors, as it is done by Brainbow using fluorescent proteins. New possibilities emerge with fluorescent nanoparticles.<sup>[4b, 13]</sup> Recent reports described long-term staining using NPs based on aggregation induced emission of dyes,<sup>[14]</sup> although their application for RGB color coding has not been shown. Studies of color coding using nanoparticles were mainly focused on multiplex detection of biomolecules in solution.<sup>[15]</sup> The only attempts to barcode living cells using NPs were performed with quantum dots (QDs).<sup>[16]</sup> However, due to the stochastic nature of their internalization,<sup>[17]</sup> cell labeling by QDs of three different colors generated randomly distributed color codes within the same population of cells.<sup>[16b]</sup> At the moment, there is no method for exogenous cell labeling that can generate in a whole cell population a defined RGB barcode readable directly by fluorescence microscopy. One solution is to use fluorescent dye-loaded polymer nanoparticles (NPs), which attracted attention due to their extreme brightness (>10 brighter than QDs), color variability, biodegradability and low toxicity.<sup>[18]</sup> Significant efforts have been done to design multi-color dye-loaded polymer nanoparticles through encapsulation of multiple dyes within the same NPs, which ensures cascade FRET and multiband emission.<sup>[3a, 19]</sup> One of these systems was applied for RGB color coding, where two cell populations were distinguished without long-term measurements.<sup>[3a]</sup> Recently, we developed 40-nm polymer NPs based on the biodegradable polymer poly(lactic-co-glycolic acid) (PLGA).<sup>[20]</sup> To achieve high dye loading with excellent brightness, we combined a hydrophobic cationic dye, octadecyl-rhodamine, with bulky fluorinated counterions. These NPs showed very fast internalization into cells by endocytosis, thus providing efficient cellular labeling.<sup>[20]</sup> We hypothesized that the counterion approach could be expanded to other cationic dyes, such as cyanines, so that we could generate NPs bearing three well-separated absorption/emission bands. Then, if these NPs are of similar size and surface properties, they may present identical internalization inside cells, so that their co-incubation with cells in different proportions could generate labeled cells of any desired color far beyond the commonly used three colors. Presently, we successfully realized this hypothesis, where the obtained ultrabright NPs of three different colors could label living cells with at least 13 different RGB barcodes. These color codes are transmitted through many cell generations, so that the cells could be tracked in culture for >2 weeks. In addition, we showed that such barcoded cells can be easily tracked in living animals such as zebrafish embryos.

## 2. Results

### 2.1. Preparation and characterization of nanoparticles.

To obtain fluorescent polymer NPs of small size, we used our recently developed protocol of charge-controlled nanoprecipitation,<sup>[20-21]</sup> where a diluted solution of a polymer bearing one charged group per chain and a dye in an organic solvent is rapidly added into aqueous media. In case of PLGA, bearing one negatively charged carboxylate at the polymer terminus, NPs of 35-40 nm diameter can be obtained. To generate NPs of three distinct colors we selected cyanine dyes, which are known to exhibit sharp absorption and emission bands. For successful encapsulation inside polymer NPs, the dyes should be hydrophobic, so that they will co-precipitate together with the polymer. Hence, we selected cyanine derivatives bearing two octadecyl chains: DiO, DiI and DiD (Figure 1A). The choice of the counterion was of high importance for obtaining small NPs. While the use of small inorganic counterion (e.g. chloride or perchlorate) led to a strong increase in NP size, using bulky hydrophobic tetraphenylborate counterions (F0, F5 and F12, Figure 1A) led to a minimal dependence of the size of NPs on the dye loading (Figure 1C, Supplementary Tables 1 and 2). The best results were obtained with the fluorinated counterions F5 and F12, showing that the super-hydrophobicity of fluorinated compounds<sup>[22]</sup> plays a key role in efficient encapsulation of cationic dyes into polymer NPs. Increase in the dye loading produced a systematic decrease in the fluorescence quantum yield (QY) of NPs (Figure 1D) and broadening of absorption bands (Figure S1-3), which are clearly related to aggregation caused quenching (ACQ)<sup>[23]</sup>. However, these unwanted effects were minimized by using the fluorinated counterions F5 and F12 (Figure 1D, Figure S1-3). The most efficient in this respect was the largest counterion F12, as the QY values were the highest for most of the formulations, notably in the case of Cy5, where F12 allowed obtaining QYs of 14 % even at 20 mM loading.

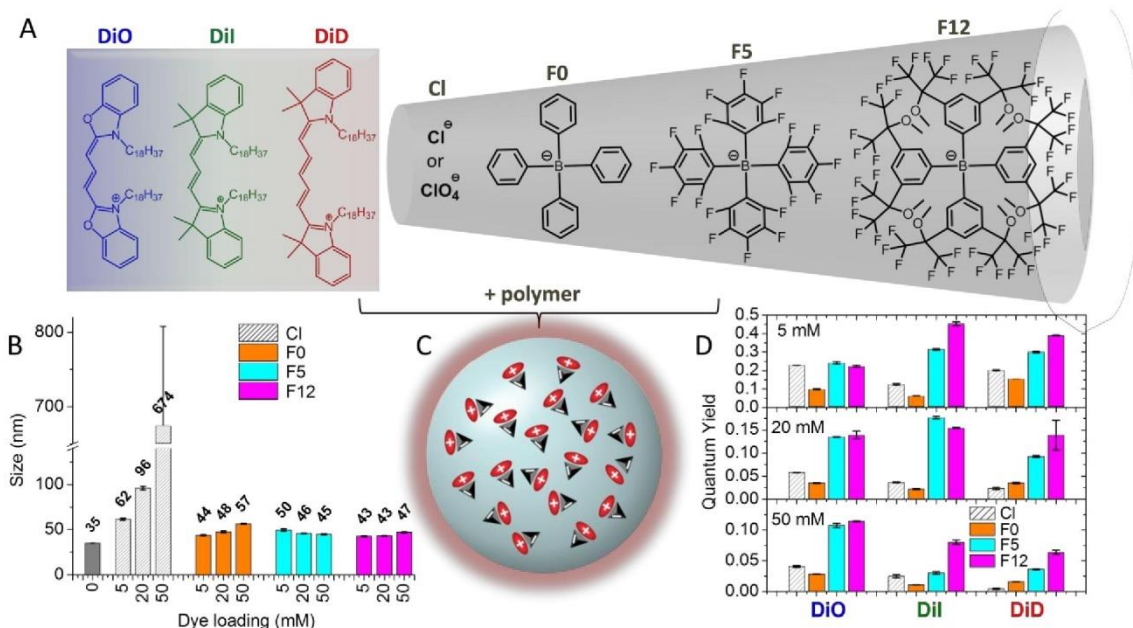


**Figure 1.** Polymer NPs loaded with cyanine dyes using different counterions. (A) Chemical structures of cationic cyanine dyes (blue, green and red) and their counterions (in black). (B) Effect of dye loading on the hydrodynamic diameter of NPs doped with DiO bearing inorganic (perchlorate) or different bulky organic counterions (F0, F5 and F12). (C) Schematic presentation of dye-loaded polymer nanoparticles. (D) Fluorescent quantum yields of NPs loaded at different concentration with three cyanine dyes: role of counterions for preventing self-quenching. The error bars are standard error of the mean ( $n = 3$ ).

Based on the obtained results we selected 20 mM loading of cyanine dyes with the F12 counterion and further characterized the obtained NPs in detail. Absorption spectra of these NPs presented maxima at 488, 553 and 651 nm (Figure 2A), which corresponded well to those of DiO, DiI and DiD dyes in methanol (Figure S1-3) and matched the most common laser lines at 488, 561 and 640 nm. The emission bands were rather sharp for DiI-F12 and DiD-F12 dye loaded NPs (Figure 2A), similar to those in methanol (Figure S1-3), which confirmed minimal aggregation of dyes at this high loading. Despite a broader emission spectrum of DiO-F12 NPs, it is clear that, using appropriate excitation wavelengths and emission filters, it would be possible to detect each of these three types of NPs, without cross-talk in the detection (Figure 2A). Electron microscopy revealed that, independently of the loaded dye, NPs displayed the same size and spherical structure (Figure 2B,C). Moreover, the dye-loaded NPs showed practically the same zeta-potential of around -40 mV as the corresponding blank NPs (Figure 2B). Therefore, we can conclude that encapsulation of dyes

did not alter the surface properties of the NPs. Thus, we obtained fluorescent NPs of three different colors presenting the same size and surface properties. In wide-field fluorescence microscopy all three types of NPs appeared as bright fluorescent dots (Figure 2D). Remarkably, the brightness of DiI-F12 NPs was 22-fold larger than that of QDs of similar color (QD585, Figure 2E).

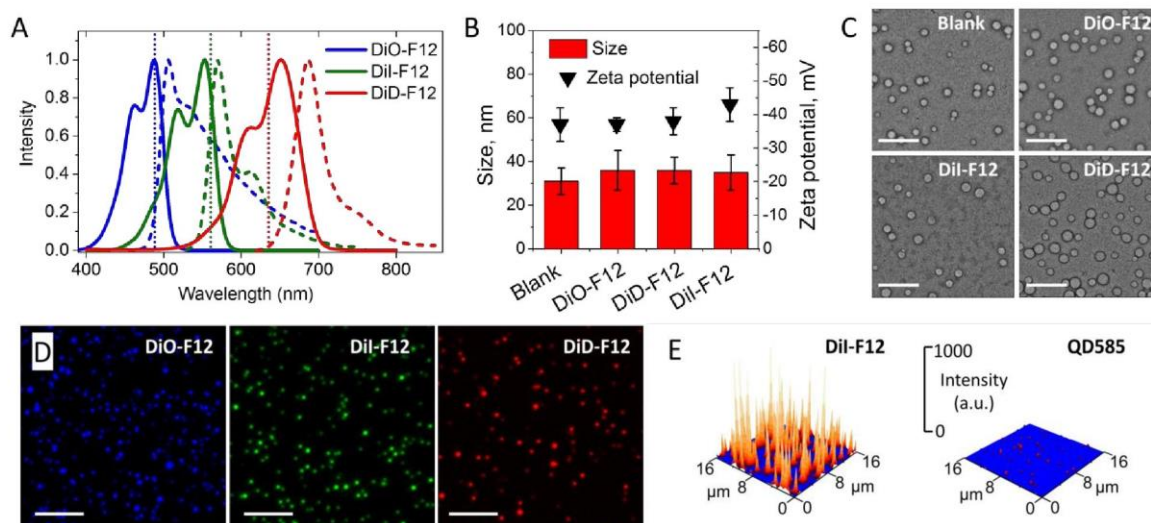


**Figure 2.** Properties of the three types of NPs loaded with the three cyanine dyes DiO, DiI and DiD and the F12 counterion at 20 mM. (A) Normalized absorption and fluorescence spectra of cyanine-loaded polymer NPs. (B) Diameter based on TEM images and zeta potential of these NPs. The error bars are standard error of the mean ( $n = 3$ ). (C) Electron microscopy of blank and dye-loaded NPs. Scale bar is 200 nm. (D) Wide-field fluorescence microscopy images of dye-loaded NPs. Scale bar is 5  $\mu\text{m}$ . Illumination power was 1  $\text{W cm}^{-2}$  at 488 nm (DiO-F12), 532 nm (DiI-F12) and 645 nm (DiD-F12). (E) 3D representation of fluorescence image of DiI-F12 NPs in comparison to quantum dots QD585. Excitation wavelength was 532 nm.

## 2.2. Cell labeling by NPs.

For labeling, the cells were incubated with NPs for 3 h at 37°C, followed by rinsing and transfer to chambered microscope slides. Then, the cells were imaged using three excitation/detection channels (displayed in blue, green, and red) corresponding to the DiO-F12, DiI-F12, and DiI-F12 NPs, using similar laser powers and detection sensitivities. In order to delimit the cells, they were additionally stained with the violet membrane probe F2N12SM<sup>[24]</sup> (displayed in grey). In total, we tested our NPs on six cell lines: HeLa (studied the most extensively), KB, 293T, U87, RBL and CHO. Fluorescence microscopy revealed homogeneous staining of virtually all imaged cells (Figure 3A), and this phenomenon was observed for the three types of NPs in all six cell lines (Figure S4 and 5).

Moreover, the signal from the labeled cells was observed only in the corresponding blue, green or red channel (Figure 3A), indicating minimal cross-talk of the channels. Finally, analysis of fluorescence images revealed similar intensities of the cells labeled with all three types of NPs (Figure S6). Flow cytometry analysis confirmed the observed similar staining of cells by NPs of different colors and showed that practically all cells were labeled (Figure S7). These results suggest that internalization of NPs is independent of the encapsulated dyes, in agreement with invariant sizes and surface properties of these NPs.

A closer look in the case of KB and HeLa cells (Figure 3B,C), revealed that after 24 h the NPs were mainly located in the perinuclear regions in form of bright spots. This is in agreement with an endosomal entry of these NPs, as we have shown earlier for the same type of PLGA NPs loaded with a rhodamine dye.<sup>[20]</sup> The observed high contrast between the perinuclear regions and the rest of the cells suggested minimal dye leaching from NPs even after 24h of incubation. By contrast, when NPs were loaded with DiO perchlorate (i.e. without hydrophobic counterion), the images showed a diffuse fluorescence throughout the cell, probably due to leaching of the poorly encapsulated dye from the NPs (Figure S8).

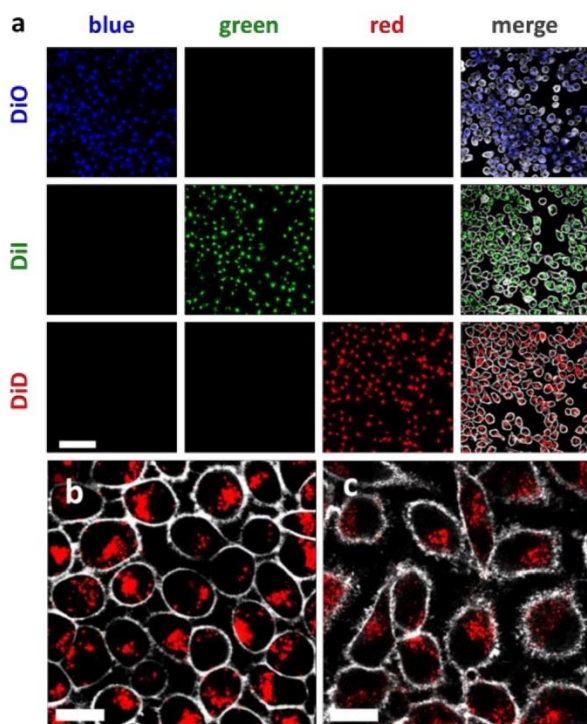


**Figure 3:** Fluorescence micrographs of cells incubated for 3 h with nanoparticles. (a) KB cells labeled with DiO-F12 (top row), DiI-F12 (middle row), and DiD-F12 (bottom row) NPs. The images obtained in the different channels are shown (blue, green and red). Merged images from all

three channels are shown on the right; membrane staining is shown in grey. A 20x objective was used; scale bar is 100  $\mu\text{m}$ . (b,c) Localization of DiD-F12 NPs in KB (b) and HeLa (c) cells. The membrane was labeled with F2N12SM. Before imaging, the cells were incubated with NPs for 3h, rinsed, transferred into microscopy chambers and then incubated for 24h. A 63x objective was used; scale bar is 20  $\mu\text{m}$ .

We then estimated the number of NPs per cell using two methods: (i) The fluorescence emission of labeled cells was measured in suspension using a fluorometer and compared to the emission of solutions of the corresponding NPs of known concentrations (Figure S9). (ii) The intensities of total fluorescence emission per cell were determined from confocal microscopy images at low magnification (20x objective) and compared to that of standard 200 nm beads (Figure S10). The two methods gave remarkably close results, respectively, 9400 and 10500 NPs per HeLa cell 24 h after labeling with 0.15 nM of DiI-F12 NPs (0.002 g/L of polymer). The analyzed per cell fluorescence revealed a relatively narrow distribution of the number of NPs per cell (Figure S10). Increasing the particle concentration to 0.45 and 1.5 nM (corresponding to 0.006 and 0.02 g/L of polymer), led to an increase in the labeling intensity (Figure S11A), corresponding to 23000 and 45000 NPs per cell.

Finally, according to MTT assays, the NPs did not show significant cytotoxicity after 72h of incubation with HeLa cells at concentrations more than 10 times those used for labeling (Figure S12). Thus, our NPs can internalize equally well into all cells, independently of the encapsulated dye and display minimal crosstalk between the RGB channels, high stability and low toxicity over extended periods of culture.

### **2.3. RGB barcoding of living cells.**

The described unique properties of our NPs gave the possibility to label cells by a variety of color codes simply by incubating the cells with different mixtures of these NPs (Figure 4). For example, to achieve an orange labeling, we mixed DiI-F12 NPs and DiD-F12 NPs in a 0.25 to 0.75 ratio in Opti-MEM, followed by incubation for 3h. After 24 h of culture the labeled cells showed an intensity of the DiD channel about three times that of the DiI channel, and negligible signal in the DiO channel (Figure 4B), so that the merged images yielded an orange color for all the imaged cells. Applying this procedure to different mixtures of NPs resulted in cell populations labeled homogeneously with 13 clearly distinguished colors (Figure 4C), while keeping all the instrumental

and analysis setting identical. The colors of the individual cells were then analyzed quantitatively. Owing to the perinuclear localization of the NPs, each labeled cell appeared as a separate region of high density of dots, which facilitated greatly an automated image analysis using an ImageJ macro (Supplementary file 1). The measured relative intensities of the three channels provided RGB barcodes for each cell, which were then represented in a ternary diagram of an RGB color triangle (Figure 4D). Analysis of over 2000 cells, showed 13 well-separated populations, which implies robust color coding of live cells by at least 13 different barcodes. It should be noted that incubation of cells with a simple mixture of dyes (DiI and DiD) without nanoparticles resulted rather heterogeneous color code (Figure S13). The latter could be explained by very poor solubility of these dyes in water, so that the aggregates of these dyes in water do not provide as homogeneous cell staining as PLGA NPs loaded with these dyes.

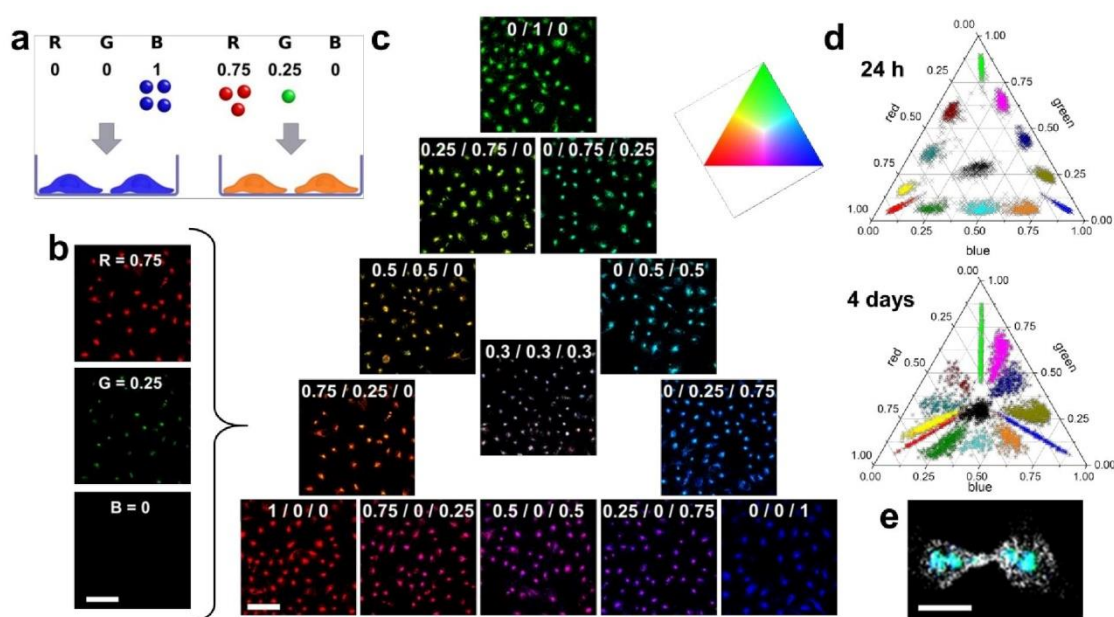


**Figure 4.** Multi-color labeling of HeLa cells. (a) Principle of cell color coding by NPs. (b) Example of cells labeled with orange: the images on the left show the three channels, the single image in the color triangle corresponds to the superposition of the three. (c) Images of cells after labeling with the different NP mixtures (13 colors). Scale bar is 100  $\mu\text{m}$ . (d) Representation of the relative intensities of DiO (blue), DiI (green) and DiD (red) channels of individual cells in a ternary diagram at 1 and 4 days after labeling with 13 colors. The relative intensities were determined for about 200 cells per condition. Only the basic colors red, green, and blue are represented in these colors, all other colors are false colors in order to facilitate the distinction of adjacent colors. (e) Confocal image of selected dividing cell.

#### **2.4. Transmission of RGB barcode to daughter cells.**

When HeLa cells labeled with different colors were cultured separately for longer periods, the color of each cell population was preserved, so that 13 colors remained easily distinguishable at 4 days (lower part of Figure 4D) and even at 8 days (Figure S14) after labeling. However, the decrease in the intensity of the signal produced some displacement of the color codes towards the center of the color triangle (Figure 4D). The preservation of the colors of cell populations after such long periods requires the NPs of different colors to be transmitted to the daughter cells in equal proportions. Indeed, in the observed cases of dividing cells (Figure 4E and Figure S15), both daughter cells displayed very similar fluorescence intensities and identical RGB barcodes. On the other hand, this implies that the mean fluorescence intensity of individual cells should decrease 2-fold after each division, which ultimately limits the overall time over which RGB barcodes were detectable. Consistently, the mean number of NPs per cell, as determined from microscopy, was 10500 after one day, 3300 after three days and 600 after seven days. Taking day one as the first cell generation, we could estimate that on day three and seven, we observed 2.7th and 5th generation of HeLa cells, which is a reasonable division rate (about 0.8 times per 24h).

#### **2.5. Distinguishing mixed populations of cells by color.**

When three cell populations labeled with NPs of different colors were mixed together, they could be easily distinguished after 1 day and even after 14 days of co-culture (Figure 5A,B). This result implied the cells did not exchange their internalized NPs and thus did not mix the colors. The color mixing was also not observed for higher NP concentration (0.45 nM), which enabled observation of distinct cell populations even after 19 days (Figure S16). However, at the highest used concentration (1.5 nM) the color mixing was detectable already after 24h (Figure S11B), which shows the upper concentration limit of this method. Then, we mixed seven populations of barcoded cells and after 4 days all of them were easily distinguishable both visually (Figure 5C) and as distinct regions in the color triangle (Figure S17), which should enable their automatized identification. Strikingly, our method also worked to distinguish 13 barcoded cell populations co-cultured at least for 24h (Figure S18).

We then applied our labeling method to barcode 6 different cell lines: HeLa, KB, embryonic kidney (293T), astrocytoma (U87), rat basophilic leukemia (RBL) and Chinese hamster ovary (CHO) cells. These cell lines were labeled with 6 different RGB barcodes and then either incubated separately or together by mixing in equal numbers for 24 h before imaging. Within the individual cell lines the applied barcode was identical in all imaged cells. In the mixture of cell lines, each cell type could be easily recognized by its color code as well as by its expected morphology (Figure 5D, Figure S19).

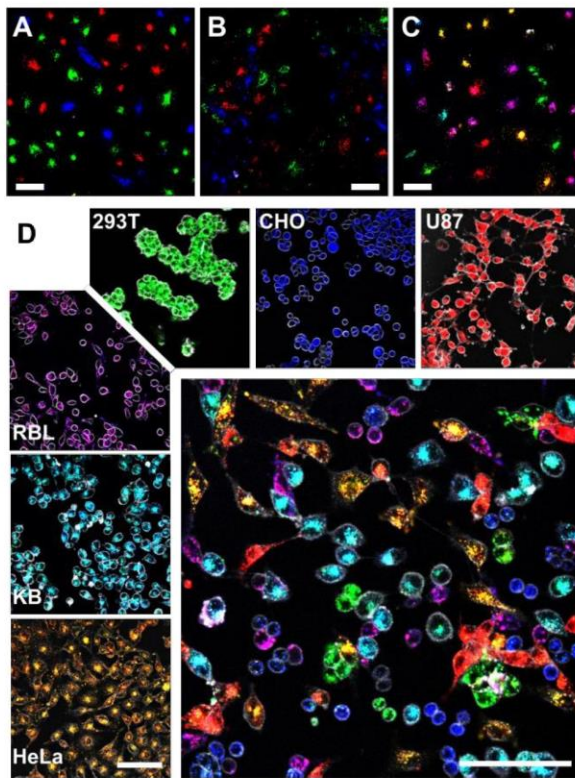


**Figure 5.** Co-culture of mixed RGB barcoded cell populations. (A,B) Confocal image of a mixture of three cell populations labeled with the three different NPs, respectively, 1 day (A) and 14 days (B) after labeling. Scale bar is 60  $\mu\text{m}$ . (C) Confocal image of a mixture of seven cell populations of different colors four days after labeling. (D) The large micrograph shows a confocal image six cell types (HeLa, KB, 293T, U87, RBL, and CHO) mixed and co-cultured for 24 h. Each cell type was labeled with an RGB barcode (orange, cyan, green, red, magenta and blue, respectively), also shown separately in the smaller images. Images are superpositions of the three NP channels with identical settings and of the membrane channel in gray. Scale bar is 100  $\mu\text{m}$ .

## 2.6. Competition among mixed cell populations after drug treatment.

Finally, we used this method to distinguish the behavior of HeLa cells that underwent different doxorubicin treatments in direct competition for adhesion to the surface. Six populations of HeLa cells, where individual color corresponded to the level of doxorubicin treatment, were seeded in chambered microscope slides for 4 h and then imaged at different heights from the surface. (Figure S20). We found that non-treated cells in green had an approximately equal relative distribution throughout the three imaged z-planes. However, HeLa cells that had undergone a doxorubicin treatment at low concentration (magenta) were significantly more present close to the surface and

showed a more surface-spread morphology. By contrast, those treated with intermediate concentrations (blue) were relatively more abundant further away from the surface and showed rather rounded shapes at the surface. Higher doxorubicin concentrations decreased significantly the cell fraction at all studied distances from the surface, probably because of fast cell death and aggregation (Figure S21).

### **2.7. Multi-color tumor cell tracking in living animals.**

We then applied our color-coding approach to the tracking of tumor cells (D2A1, murine mammary carcinoma cells) directly in a living animal. To this end, six cell populations of tumor cells were labeled by distinct RGB barcodes of our NPs (Figure 6A) and then injected in the duct of Cuvier of zebrafish embryos (2 days post-fertilization, 2 dpf) and imaged 3 hours post-injection (3 hpi). Single cells and clusters of injected tumor cells can be found in the caudal plexus regions of the zebrafish embryo and are easily distinguishable based on their color (Figure 6B-D). Importantly, according to the images in 3 channels (Figure 6D) and the merged image (Figure 6B) all six colors are clearly defined without appearance of other colors (except cases of cell overlap). This means that the RGB barcode is well preserved inside the cells without leakage *in vivo*.

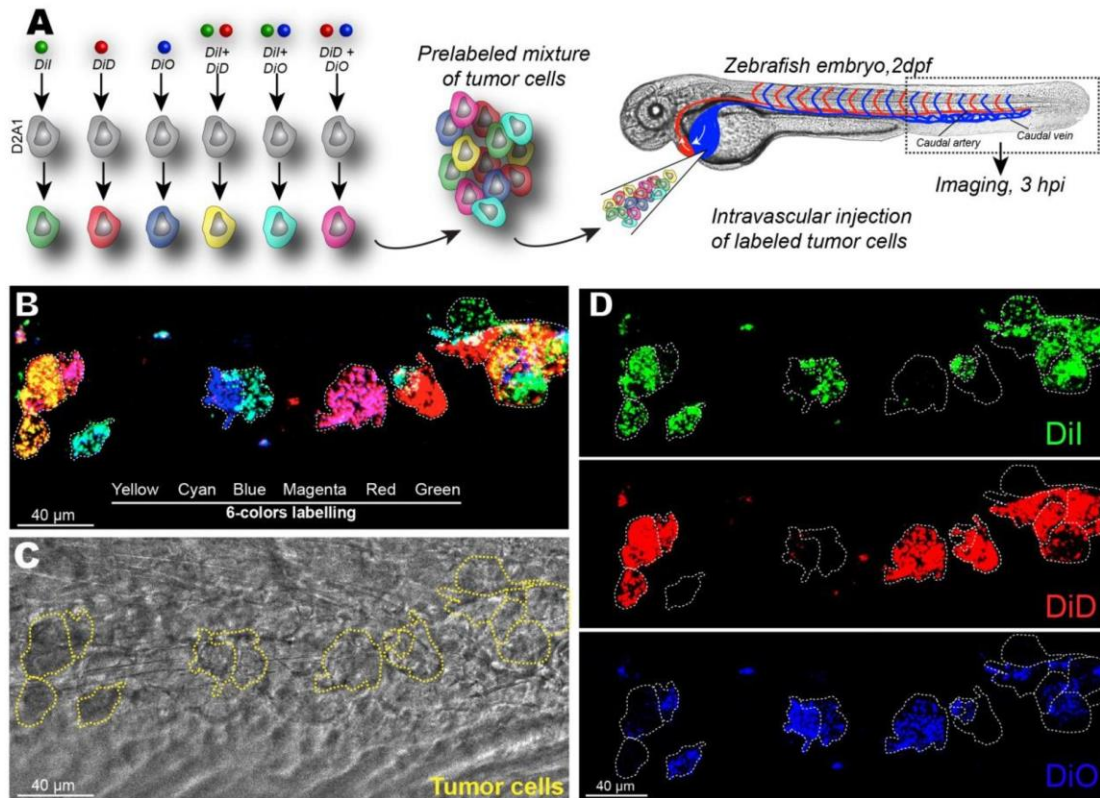


**Figure 6.** Tracking RGB barcoded cancer cells in zebrafish embryo. (A) Experimental design: Six batches of D2A1 cells were labeled with fluorescent NPs generating RGB barcodes (green, red, blue, yellow, magenta and cyan). Labeled cells were then mixed and injected intravascularly in 2 dpf zebrafish embryos. (B-D) Tumor cells that arrested in the vasculature are imaged at 3 hpi, in the caudal plexus region of the zebrafish embryo. Clusters and individuals cells can be found and distinguished based on their color.

## 2.8. Cell tracking in the developing embryo.

We further investigated the usefulness of our cell-labeling technology for developmental studies using zebrafish embryos. To do so, solutions of our NPs and NP mixtures were injected directly into the cytoplasm of distinct cells at the four- or eight-cell stage (Figure 7). Using this procedure the NPs distributed homogeneously throughout the cytoplasm of the injected cells (Figure 7A,C), which was clearly different from cell staining through endocytosis (Figure 3B,C). After embryo

development, populations of daughter cells of the same color code were observed for both 3 and 6 color staining protocols (Figure 6B,D). Again, even for the 6 color protocol, all colors could be readily identified, indicating minimal exchange of the NPs among the cells. These results showed that upon cell division the NPs were equally shared by the daughter cells, leading to a homogeneous, bright staining of all cells derived from a given cell during embryonic morphogenesis. Labelling with our NPs thus provides an easy way of tracing the distribution of cells throughout the whole embryo for several hours and this can be done for at least six cell populations simultaneously.

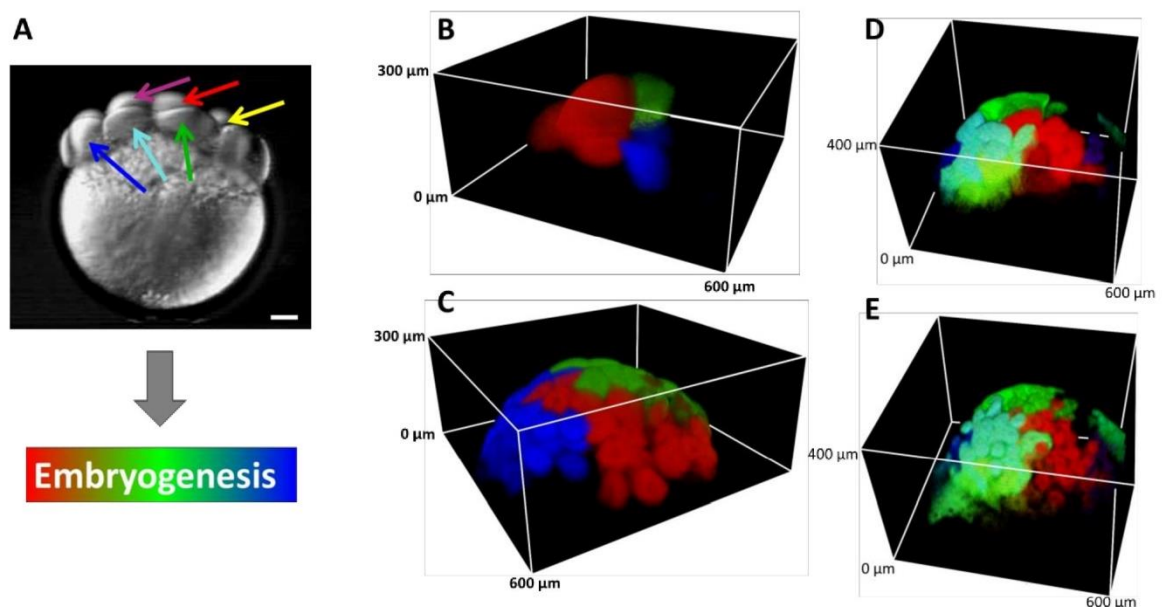


**Figure 7.** Imaging of the development of zebrafish embryos labeled by intracellular injection of fluorescent NPs. (A) Scheme of experiment: Multiple intracellular injections of NPs into 8 cell stage zebrafish embryos. Transmission image is shown, scale bar 100  $\mu\text{m}$ . (B) and (C): 3D reconstruction of embryos labeled with, respectively DiO, DiI, and DiD NPs through microinjection inside the cytoplasm of three distinct cells at the 4 cell stage imaged 30 min after injection (B), and 80 min after injection (C). (D) and (E): 3D reconstruction of embryos labeled with 6 NP mixtures (red: DiD NPs, green: DiI NPs, blue: DiO NPs, cyan: DiO NPs and DiI NPs, magenta: DiD NPs and DiO NPs, yellow: DiD NPs and DiI NPs) through microinjection inside the cytoplasm of six distinct cells at the 8 cell stage imaged 75 min after injection (D), and 135 min after injection (E).

### 3. Discussion and conclusions

For successful multi-color labeling of cells, we needed fluorescent NPs having three distinct absorption and emission colors, identical sizes and surface properties. To achieve this, we designed polymer NPs loaded with hydrophobic cyanine dyes, DiO, DiI and DiD, corresponding to the most frequently used laser lines. However, encapsulation of these cationic dyes with inorganic counterions (chloride or perchlorate) increased the size of the NPs, probably due to dye adsorption at the particle surface leading to neutralization of the particle negative charge, as we observed earlier with rhodamine derivatives.<sup>[20]</sup> Remarkably, when these counterions were replaced by bulky hydrophobic counterions, no influence of the dye loading on the size of the NPs was observed. In this case, more hydrophobic dye salts are expected to form, which are better integrated into NPs. The identical size for different colors is a key advantage of our NPs compared to QDs, where color is directly linked to the size of the NPs.<sup>[25]</sup> Moreover, bulky counterions significantly decreased ACQ of cyanines. F12 performed particularly well, especially for the longest dye DiD, probably because it isolates better the dyes from direct  $\pi$ -stacking.<sup>[26]</sup> The F12 counterion thus allowed obtaining QYs of 14 % for DiD at 20 mM loading, in contrast to only 2 % for DiD 4-chlorobenzenesulfonate<sup>[27]</sup> and for DiD chloride at the same loading. The use of bulky counterions is probably a generic approach to better encapsulate and prevent ACQ of cationic dyes in polymer NPs, as the concept works for both cyanines and octadecyl rhodamine B <sup>[20]</sup>. Importantly, single particle measurements suggest that obtained DiI-F12 NPs are ~20-fold brighter than QDs. Taking into account the expected number of DiI-F12 dyes per NP (~300), their extinction coefficient of  $94000 \text{ M}^{-1}\text{cm}^{-1}$  at 532 nm excitation and a fluorescence quantum yield of 0.15, the expected brightness is  $300 \times 94000 \times 0.15 = 4.2 \times 10^6 \text{ M}^{-1} \text{ cm}^{-1}$ . For QDs585, the brightness at 532 nm excitation is  $2.1 \times 10^5 \text{ M}^{-1} \text{ cm}^{-1}$ , which is 20-fold lower than that of our DiI-F12 NPs. The other two types of NPs should present similar brightness, because of close values of their size, QY and the extinction coefficients of the loaded dyes.

The optimized NPs showed efficient internalization into the cells within 3 h of incubation. The observed perinuclear localization of NPs in form of dots especially in HeLa and KB cells, together with previous results on rhodamine-loaded PLGA NPs showing their lysosomal localization,<sup>[20]</sup> suggest an endocytic pathway. As PLGA NPs biodegrade on the time scale of several months,<sup>[28]</sup> they remain entrapped inside lysosomes similarly to other NPs,<sup>[29]</sup> which enables their long-term imaging. Moreover, the perinuclear localization of the NPs facilitated greatly the automatic recognition of cells and the analysis of their color codes.

The simple incubation of cells with our NPs thus led to a bright, homogeneous and long-term labeling of virtually all cells of a given population, and this for all the six different cell types tested. Owing to the same size and surface properties, NPs of three distinct colors exhibit similar internalization, so their mixing in different combinations enabled RGB coding of cells with at least 13 colors. Remarkably, each cell of the population received the same combination of RGB NPs and, therefore, the identical barcode. The behavior of our NPs is different from that reported for QDs, where stochastic combination of color codes was observed for cells within the same population.<sup>[16b]</sup> Importantly, the color code generated by our NPs can be transmitted through many generations of daughter cells. As every division decreases twice the number of NPs, the method can be used to track cell division, as it is done by the fluorescein-based probe CFSE,<sup>[30]</sup> but in our case multiple color codes can be used. Finally, multiple populations of cells bearing different RGB barcodes can be co-incubated together for weeks without signs of color mixing. Remarkably, the method works well even for a mixture of 13 barcoded cell populations, showing that it can be readily used to study complex multicellular systems. Although we did not test more than 13 barcodes, it is clear that the method could be further extended to a larger number of color codes.

The long-term color coding by NPs is suitable to study the organization and interactions of different cell types in complex co-cultures as was demonstrated on two examples. First, we showed that up to 6 different cell lines labeled with different colors could be readily distinguished in co-cultures. Second, it enabled monitoring competition within six cell populations differently treated by doxorubicin. Our observations suggest that at very small doxorubicin concentrations, the capacity of the cells to adhere could be similar or even higher than that of non-treated cells, while higher concentrations of the drug inhibit cell adherence. This experiment not only shows the effect of drug on the cell behavior, but it may also reveal the heterogeneous nature of the cells in culture.<sup>[31]</sup> Indeed, whereas some fraction of the cells was killed by low concentrations (0.2  $\mu\text{M}$ ) of doxorubicin (Figure S20), the surviving fraction showed excellent adhesion properties. Understanding the reasons for this heterogeneity and distinct adhesion behaviors of the drug-treated cells is outside the scope of this work. However, we showed that it is a powerful method to study multiple cell populations in direct contact and competition and it enables new ways to test drugs, such as high-content screening.<sup>[32]</sup>

The experiments performed in the zebrafish embryo showed that the new methodology of cell labeling allows also multiple applications *in vivo*. The first one relies on the fast and efficient fluorescent labeling of cells prior to transplantation *in vivo* to map up to 6 different cell populations and potentially track individual cells. Multi-color labeling of distinct populations of tumor cells should allow fine tracking of single population's behavior, where one could tune gene expression or

metastatic abilities for example. Such a protocol should be of choice to study invasion and metastasis of pre-labeled tumor cells, and further assess drug resistance using intravital imaging.<sup>[33]</sup> Second, we showed that NPs can be used to directly label cells *in vivo* with at least 6 different colors to follow individual cells and cell populations during embryonic development. Intracellular injection of NPs at the early developmental stage proved to be suitable to explore cell behavior in morphogenetic processes in zebrafish embryos and should be useful in other species as well, especially those not amenable to genetic engineering. The high brightness of our NPs and their homogenous distribution in the cytosol after intracellular microinjection ensures high performance in terms of signal to noise ratio and spatial and temporal resolution in large 3D field of views.

Compared to RGB coding of cells by fluorescent proteins, as for instance realized by Brainbow<sup>[6]</sup>, our method, based on fluorescent NPs, presents several important features: i) It does not require genetic modification, ii) it is extremely easy, fast and can in principle operate in any cell type and the brightness of labeling can be tuned much easier compared to fluorescent proteins in rainbow-type animals. The fast labeling without genetic modification is particularly promising to study primary cell cultures. It is also important in early embryogenesis studies, where multiple division cycles take places within hours.<sup>[34]</sup> In our method, a given cell population bears an identical RGB barcode, whereas Brainbow labeling generates a variety of color codes within the same population. Thus, these two methods are complementary. In the method presented here, cell division leads to a reduction of the number of NPs per cell, which ultimately limits the observation time in rapidly dividing cells (like HeLa). Nevertheless, by optimizing the NPs concentration we could detect labeled HeLa cells for at least 19 days. This is significantly longer than the one week labeling reported earlier for QDs,<sup>[5b]</sup> probably because our NPs are much brighter. Moreover, in contrast to the stochastic distribution of colors within the same labeled population using QDs,<sup>[16b]</sup> our approach generates a uniform color code within the same population stable throughout multiple generations. Finally, our NP-based method is advantageous over direct cell labeling by dyes (1). Cell trackers work efficiently only for a few days.<sup>[12]</sup> Encapsulation of dyes inside NPs, on the other hand, prevents dye leakage from cells and prolongs staining for weeks. This feature minimizes the loss of staining and enables co-culture of multiple cell populations with different barcodes with minimized exchange of colors (2). It features homogeneous cell staining, while classical dyes, like DiD or CellVue® Claret (PKH type), provide rather heterogeneous cell staining because of their poor water solubility.<sup>[35]</sup> Therefore, as we observed in this work, simple mixing of two different dyes (DiI and DiD) does not generate a homogeneous color code within the same cell population. All these points probably explain why organic dyes have never been used to date to generate multiple color codes transmittable to daughter cells. The only examples are limited to color coding of fixed cells.<sup>[36]</sup>

Thus, the proposed method of multi-color coding, being complementary to Brainbow, does not have analogues in literature and opens the way to a variety of applications related to long-term cell tracking *in vitro* and *in vivo*.

Finally, this work provides new insights for interfacing nanotechnology and biology. Rather than creating complex multimodal nanoparticles bearing simultaneously multiple functions, we propose to implement different functions/modalities (colors in our case) separately into “homologous” nanoparticles of identical size and surface properties. The latter ensure their identical delivery into live cells, where these NPs can then combine forces to perform sophisticated tasks.

#### 4. Experimental section

*Synthesis of dye salt:* **DiI-Cl** and **DiD-Cl** were synthesized according to a previously described procedure<sup>[37]</sup>. Synthesis of all ion pairs of cyanine dyes with tetraphenyl borate counterions was done by ion exchange of corresponding dye chloride with a borate salt in dichloromethane followed by purification by column chromatography. The details are described in Supporting Information.

*Preparation of fluorescent NPs:* PLGA (lactide:glycolide, 1:1, mole:mole, Mn 24000) was dissolved at 2 mg ml<sup>-1</sup> in acetonitrile containing different amounts of dye. These solutions were added quickly and under stirring (shaking) using a micropipette to a tenfold volume excess of 20 mM phosphate buffer at pH 7.4. The particle solution was then quickly diluted fivefold with the same buffer.

*Characterization of NPs:* DLS measurements were performed on a Zetasizer Nano series DTS 1060 (Malvern Instruments S.A.). Electron microscopy was performed on Philips CM120 transmission electron microscope. Absorption and emission spectra were recorded on a Cary 400 Scan ultraviolet–visible spectrophotometer (Varian) and FluoroMax-4 spectrofluorometer (Horiba Jobin Yvon) equipped with a thermostated cell compartment, respectively. QYs were calculated using rhodamine B in methanol (QY = 0.7) for DiI series, fluorescein in 0.1M NaOH (QY = 0.92) for DiO series and DiD in MeOH (QY = 0.33) for DiD series.

*Cell labeling:* For labeling, cells were seeded in 6 well plates at 200 000 cells/well (21 000 cells / cm<sup>2</sup>) or at 500 000 cells/well in 25 cm<sup>2</sup> cell culture flasks (20 000 cells / cm<sup>2</sup>). After letting the cells adhere for 18 h, the cell culture medium was removed and the cells were rinsed twice with optiMEM, followed by incubation with a freshly prepared solution of the NPs (0.15 nM in particles, 2.5 mL for 6 well plates, 10 mL for 25 cm<sup>2</sup> cell culture flasks). NP suspensions for cell labeling were prepared starting from stock solutions in 20 mM phosphate buffer at a pH of 7.4 with a

particle concentration of 3 nM (0.04 g/L of polymer). Depending on the desired color the stock solutions were mixed in the needed proportions (e.g. DiO:DiI:DiD 1:0:0 for “blue”, or 0.5:0.5:0 for “cyan”) and diluted in optiMEM to a concentration of 0.15 nM (0.002 g/L of polymer). After 3 h of incubation the NP suspension was removed, the cells were rinsed first with optiMEM, then with PBS, and finally with the corresponding cell culture medium.

The resulting cells were then either cultured for longer periods, mixed, or transferred for imaging. For transfer or mixing the wells were rinsed twice with PBS followed by incubation for 2 to 5 min with 0.4 mL of trypsin at 37°C, and collection of the detached cells in 3 mL of the corresponding medium. After centrifugation and redispersion in 1 to 5 mL of medium (depending on the obtained number of cells), the cells were counted. For mixing of different cell populations, equal numbers of cells were combined in a centrifugation tube and thoroughly mixed before further use (for example “blue”, “green”, and “red” cells or HeLa, KB, and CHO cells). For imaging, the cells, after the desired labeling, mixing, and time of culture, were seeded in LabTek 8 well plates at 60 000 cells/well and left to adhere for at least 18 h.

*Confocal microscopy:* Fluorescence imaging of the cells in chambered microscope slides (LabTek or Ibidi 8 well plates) was performed on a Leica TSC SPE confocal microscope using either a 20x air objective or a 63x oil immersion objective. The different channels were recorded as follows: excitation 405 nm, emission recorded from 430 nm to 480 nm; excitation 488 nm, emission recorded from 495 nm to 560 nm; excitation 561 nm, emission recorded from 570 nm to 610 nm; excitation 635 nm, emission recorded from 650 nm to 750 nm. The power of the 405 nm laser was adjusted as needed. The power of the 488, 561, and 635 nm lasers was set either to 10 or to 20 % of the nominal power (same for all three) and the gain and offset were set to the same value for all three. Three successive sequences were recorded for each image.

*Image analysis:* Image analysis was performed using the Fiji software and, for data analysis, the R software. The three consecutive images were averaged for each channel. The intensity levels were set to the same levels for the three NP channels for all images presented here. An ImageJ macro was programmed to determine automatically the colors of the individual cells (macro code can be found in the Supporting information). Briefly, the macro combines the intensities from the three NP channels in a single gray scale image. This image is then used to detect the locations of the individual cells and so to create a mask, which allows measuring the intensities of the three channels for each individual cell. The intensities are then normalized to 1 in order to obtain the RGB barcode of each cell.

*Tracking cancer cells in zebrafish embryos:* Wild-type *Golden* zebrafish embryos (48 hours post-fertilization (hpf)) were anesthetized in Danieau containing 650  $\mu\text{M}$  tricain and mounted in 0.8% low melting point (LMP) agarose. Meanwhile, unlabeled D2A1 cells (murine mammary carcinoma cells) were cultured in 6-well plates and incubated for 3h at 37°/5% CO<sub>2</sub> with NPs (2 mg L<sup>-1</sup>) of different color and their one-to-one mixtures (red: DiD NPs, green: DiI NPs, blue: DiO NPs, cyan: DiO NPs and DiI NPs, magenta: DiD NPs and DiO NPs, yellow: DiD NPs and DiI NPs) before being trypsinized. A mixture of RGB barcoded cells at equal quantities was prepared at a concentration of 100x10<sup>6</sup> per ml. Embryos were injected under a stereomicroscope (LEICA M205 FA) equipped with fluorescence module. The mixture of barcoded cells was loaded in a microforged glass capillary and 18 nL of the mixture was injected in the duct of Cuvier of the embryos using a microinjector (Nanoject, Drummond). Injected embryos were then imaged at 3 h post-injection using a confocal microscope (Leica TCS SP5, 25X/ON 0.95 N.A. water immersion objective).

*Labeling and imaging early zebrafish embryos:* Wild-type *Danio rerio* (zebrafish) embryos were reared and staged as described elsewhere.<sup>[34b]</sup> Embryos were collected at the one-cell-stage and kept in embryo medium (EM) at 28.5°C until the desired stage.<sup>[34a]</sup> Intracellular injection at the 4-cell or 8-cell stage were performed into chorionated embryos with solutions of DiO, DiI, and DiD NPs or one-to-one mixtures to generate three or six RGB barcodes (red: DiD NPs, green: DiI NPs, blue: DiO NPs, cyan: DiO NPs and DiI NPs, magenta: DiD NPs and DiO NPs, yellow: DiD NPs and DiI NPs), all at global NP concentrations of 0.2 g L<sup>-1</sup>. The injected volume was about 1nl per cell. Injected embryos were immediately mounted in a 3-cm Petri dish with a glass coverslip bottom, sealing a hole of 0.5 mm at the dish centre, where a Teflon tore (ALPHAnov) with a hole of 780  $\mu\text{m}$  received the dechorionated embryo. The embryo was maintained and properly oriented (animal pole up) by infiltrating around it 0.5% low-melting-point agarose (Sigma) in embryo medium as described elsewhere.<sup>[34b]</sup> 3D+time imaging was performed with a Zeiss LSM780 confocal upright microscope with a high NA, water dipping lens objective (either 20x or 25x) for up to 12 hours. Temperature control was achieved with and Okolab chamber (26°C in the Petri dish). All the investigations using the zebrafish model were carried out in compliance with the European and international guidelines on animal welfare (Directive 2010/63/EU).

### **Supporting Information**

Supporting Information is available from the Wiley Online Library or from the author.

**Acknowledgements.** This work was supported by the European Research Council ERC Consolidator grant BrightSens 648528. BA was supported by LabEx Chimie des Systèmes Complexes. We thank Y. Mely and P. Didier for providing access to wide-field fluorescence microscopy and C. Ruhlmann for help with electron microscopy. We thank Romain Vauchelles for help with image analysis using the ImageJ software and Claudine Ebel for help with flow cytometry. We are very much grateful to Francesca PERI (EMBL) and Kerstin RICHTER (EMBL) for providing zebrafish embryos. We thank the BioEmergences platform and FBI ANR-10-INBS-04 for injections and 3D+time imaging.

Received: ((will be filled in by the editorial staff))

Revised: ((will be filled in by the editorial staff))

Published online: ((will be filled in by the editorial staff))

- [1] a) J. H. Gao, H. W. Gu, B. Xu, *Accounts Chem. Res.* **2009**, *42*, 1097; b) D. E. Lee, H. Koo, I. C. Sun, J. H. Ryu, K. Kim, I. C. Kwon, *Chem. Soc. Rev.* **2012**, *41*, 2656; c) N. Lee, D. Yoo, D. Ling, M. H. Cho, T. Hyeon, J. Cheon, *Chem. Rev.* **2015**, *115*, 10637; d) S. K. Yen, D. Janczewski, J. L. Lakshmi, S. Bin Dolmanan, S. Tripathy, V. H. B. Ho, V. Vijayaragavan, A. Hariharan, P. Padmanabhan, K. K. Bhakoo, T. Sudhaharan, S. Ahmed, Y. Zhang, S. T. Selvan, *ACS Nano* **2013**, *7*, 6796; e) H. M. Kim, H. Lee, K. S. Hong, M. Y. Cho, M. H. Sung, H. Poo, Y. T. Lim, *ACS Nano* **2011**, *5*, 8230.
- [2] a) E. K. Lim, T. Kim, S. Paik, S. Haam, Y. M. Huh, K. Lee, *Chem. Rev.* **2015**, *115*, 327; b) C. M. Spillmann, J. Naciri, W. R. Algar, I. L. Medintz, J. B. Delehanty, *ACS Nano* **2014**, *8*, 6986.
- [3] a) A. Wagh, F. Jyoti, S. Mallik, S. Qian, E. Leclerc, B. Law, *Small* **2013**, *9*, 2129; b) Y. W. C. Cao, R. C. Jin, C. A. Mirkin, *Science* **2002**, *297*, 1536; c) G. Wang, Y. K. Leng, H. J. Dou, L. Wang, W. W. Li, X. B. Wang, K. Sun, L. S. Shen, X. L. Yuan, J. Y. Li, J. S. Han, H. S. Xiao, Y. Li, *ACS Nano* **2013**, *7*, 471; d) S. Giri, E. A. Sykes, T. L. Jennings, W. C. W. Chan, *ACS Nano* **2011**, *5*, 1580.
- [4] a) Z. Cheng, A. Al Zaki, J. Z. Hui, V. R. Muzykantov, A. Tsourkas, *Science* **2012**, *338*, 903; b) P. D. Howes, R. Chandrawati, M. M. Stevens, *Science* **2014**, *346*, 1247390.
- [5] a) A. Taylor, K. M. Wilson, P. Murray, D. G. Fernig, R. Levy, *Chem. Soc. Rev.* **2012**, *41*, 2707; b) J. K. Jaiswal, H. Mattoussi, J. M. Mauro, S. M. Simon, *Nat. Biotechnol.* **2003**, *21*, 47; c) T. J. Wu, Y. K. Tzeng, W. W. Chang, C. A. Cheng, Y. Kuo, C. H. Chien, H. C. Chang, J. Yu, *Nat. Nanotechnol.* **2013**, *8*, 682; d) K. M. Dupont, K. Sharma, H. Y. Stevens, J. D. Boerckel, A. J. Garcia, R. E. Guldberg, *Proc. Natl. Acad. Sci. U.S.A.* **2010**, *107*, 3305.
- [6] a) J. Livet, T. A. Weissman, H. N. Kang, R. W. Draft, J. Lu, R. A. Bennis, J. R. Sanes, J. W. Lichtman, *Nature* **2007**, *450*, 56; b) D. Cai, K. B. Cohen, T. Luo, J. W. Lichtman, J. R. Sanes, *Nat. Methods* **2013**, *10*, 540.
- [7] a) J. P. Card, O. Kobiler, J. McCambridge, S. Ebdlahad, Z. Y. Shan, M. K. Raizada, A. F. Sved, L. W. Enquist, *Proc. Natl. Acad. Sci. U.S.A.* **2011**, *108*, 3377; b) D. Hadjieconomou, S. Rotkopf, C. Alexandre, D. M. Bell, B. J. Dickson, I. Salecker, *Nat. Methods* **2011**, *8*, 260; c) S. Hampel, P. Chung, C. E. McKellar, D. Hall, L. L. Looger, J. H. Simpson, *Nat. Methods* **2011**, *8*, 253.
- [8] Y. A. Pan, T. Freundlich, T. A. Weissman, D. Schoppik, X. C. Wang, S. Zimmerman, B. Ciruna, J. R. Sanes, J. W. Lichtman, A. F. Schier, *Development* **2013**, *140*, 2835.
- [9] N. Di Girolamo, S. Bobba, V. Raviraj, N. C. Delic, I. Slapetova, P. R. Nicovich, G. M. Halliday, D. Wakefield, R. Whan, J. G. Lyons, *Stem Cells* **2015**, *33*, 157.
- [10] J. W. Wu, R. Turcotte, C. Alt, J. M. Runnels, H. Tsao, C. P. Lin, *Sci. Rep.* **2016**, *6*.
- [11] C. R. Parish, *Immunol. Cell Biol.* **1999**, *77*, 499.
- [12] S. K. Lee, M. S. Han, C. H. Tung, *Small* **2012**, *8*, 3315.
- [13] a) O. S. Wolfbeis, *Chem. Soc. Rev.* **2015**, *44*, 4743; b) S. Liu, L. M. Tay, R. Anggara, Y. J. Chuah, Y. Kang, *ACS Applied Materials & Interfaces* **2016**, *8*, 11925.

- [14] a) Y. Yu, C. Feng, Y. Hong, J. Liu, S. Chen, K. M. Ng, K. Q. Luo, B. Z. Tang, *Adv. Mater.* **2011**, *23*, 3298; b) D. Ding, D. Mao, K. Li, X. M. Wang, W. Qin, R. R. Liu, D. S. Chiam, N. Tomczak, Z. M. Yang, B. Z. Tang, D. L. Kong, B. Liu, *ACS Nano* **2014**, *8*, 12620.
- [15] a) S. Rana, N. D. B. Le, R. Mout, K. Saha, G. Y. Tonga, R. E. S. Bain, O. R. Miranda, C. M. Rotello, V. M. Rotello, *Nat. Nanotechnol.* **2015**, *10*, 65; b) M. Y. Han, X. H. Gao, J. Z. Su, S. Nie, *Nat. Biotechnol.* **2001**, *19*, 631; c) K. Ming, J. Kim, M. J. Biondi, A. Syed, K. Chen, A. Lam, M. Ostrowski, A. Rebbapragada, J. J. Feld, W. C. W. Chan, *ACS Nano* **2015**, *9*, 3060.
- [16] a) L. C. Mattheakis, J. M. Dias, Y. J. Choi, J. Gong, M. P. Bruchez, J. Q. Liu, E. Wang, *Anal. Biochem.* **2004**, *327*, 200; b) P. Rees, J. W. Wills, M. R. Brown, J. Tonkin, M. D. Holton, N. Hondow, A. P. Brown, R. Brydson, V. Millar, A. E. Carpenter, H. D. Summers, *Nat. Methods* **2014**, *11*, 1177.
- [17] H. D. Summers, P. Rees, M. D. Holton, M. R. Brown, S. C. Chappell, P. J. Smith, R. J. Errington, *Nat. Nanotechnol.* **2011**, *6*, 170.
- [18] a) K. Li, B. Liu, *Chem. Soc. Rev.* **2014**, *43*, 6570; b) A. Reisch, A. S. Klymchenko, *Small* **2016**, *12*, 1968.
- [19] a) J. Chen, P. Zhang, G. Fang, P. Yi, F. Zeng, S. Wu, *The Journal of Physical Chemistry B* **2012**, *116*, 4354; b) J. Chen, F. Huang, H. Wang, Y. Li, S. Liu, P. Yi, *Journal of Applied Polymer Science* **2015**, *132*, 41492.
- [20] A. Reisch, P. Didier, L. Richert, S. Oncul, Y. Arntz, Y. Mely, A. S. Klymchenko, *Nat. Commun.* **2014**, *5*, 4089.
- [21] A. Reisch, A. Runser, Y. Arntz, Y. Mély, A. S. Klymchenko, *ACS Nano* **2015**, *9*, 5104.
- [22] a) M. Cametti, B. Crousse, P. Mentrangolo, R. Milani, G. Resnati, *Chem. Soc. Rev.* **2012**, *41*, 31; b) I. T. Horváth, *Acc. Chem. Res.* **1998**, *31*, 641.
- [23] Y. N. Hong, J. W. Y. Lam, B. Z. Tang, *Chem. Soc. Rev.* **2011**, *40*, 5361.
- [24] R. Kreder, S. Oncul, O. A. Kucherak, K. A. Pyrshev, E. Real, Y. Mely, A. S. Klymchenko, *RSC Adv.* **2015**, *5*, 22899.
- [25] a) A. P. Alivisatos, *Science* **1996**, *271*, 933; b) I. L. Medintz, H. T. Uyeda, E. R. Goldman, H. Mattoussi, *Nat. Mater.* **2005**, *4*, 435.
- [26] I. Shulov, S. Oncul, A. Reisch, Y. Arntz, M. Collot, Y. Mely, A. S. Klymchenko, *Nanoscale* **2015**, *7*, 18198.
- [27] A. Wagh, S. Y. Qian, B. Law, *Bioconjugate Chem.* **2012**, *23*, 981.
- [28] N. Samadi, A. Abbadessa, A. Di Stefano, C. F. van Nostrum, T. Vermonden, S. Rahimian, E. A. Teunissen, M. J. van Steenberghe, M. Amidi, W. E. Hennink, *J Control Release* **2013**, *172*, 436.
- [29] G. Sahay, D. Y. Alakhova, A. V. Kabanov, *J. Control. Release* **2010**, *145*, 182.
- [30] A. B. Lyons, C. R. Parish, *J. Immunol. Meth.* **1994**, *171*, 131.
- [31] a) B. Snijder, R. Sacher, P. Ramo, E. M. Damm, P. Liberali, L. Pelkmans, *Nature* **2009**, *461*, 520; b) B. Snijder, L. Pelkmans, *Nat. Rev. Mol. Cell Biol.* **2011**, *12*, 119.
- [32] F. Zanella, J. B. Lorens, W. Link, *Trends Biotechnol.* **2010**, *28*, 237.
- [33] R. White, K. Rose, L. Zon, *Nat. Rev. Cancer* **2013**, *13*, 624.
- [34] a) C. B. Kimmel, W. W. Ballard, S. R. Kimmel, B. Ullmann, T. F. Schilling, *Dev. Dyn.* **1995**, *203*, 253; b) E. Faure, T. Savy, B. Rizzi, C. Melani, O. Stasova, D. Fabreges, R. Spir, M. Hammons, R. Cunderlik, G. Recher, B. Lombardot, L. Duloquin, I. Colin, J. Kollar, S. Desnoulez, P. Affaticati, B. Maury, A. Boyreau, J. Y. Nief, P. Calvat, P. Vernier, M. Frain, G. Lutfalla, Y. Kergosien, P. Suret, M. Remesikova, R. Doursat, A. Sarti, K. Mikula, N. Peyrieras, P. Bourguine, *Nat. Commun.* **2016**, *7*, 8674.
- [35] M. Collot, R. Kreder, A. L. Tatarets, L. D. Patsenker, Y. Mely, A. S. Klymchenko, *Chem. Commun.* **2015**, *51*, 17136.
- [36] P. O. Krutzik, G. P. Nolan, *Nat. Methods* **2006**, *3*, 361.
- [37] X. J. Peng, Z. G. Yang, J. Y. Wang, J. L. Fan, Y. X. He, F. L. Song, B. S. Wang, S. G. Sun, J. L. Qu, J. Qi, M. Yang, *J. Am. Chem. Soc.* **2011**, *133*, 6626.

## Supporting Information

### **Fluorescent Polymer Nanoparticles for Cell Barcoding in vitro and in vivo**

*Bohdan Andreiuk, Andreas Reisch\*, Marion Lindecker, Gautier Follain, Nadine Peyri ras, Jacky G. Goetz, Andrey S. Klymchenko\**

#### **Content**

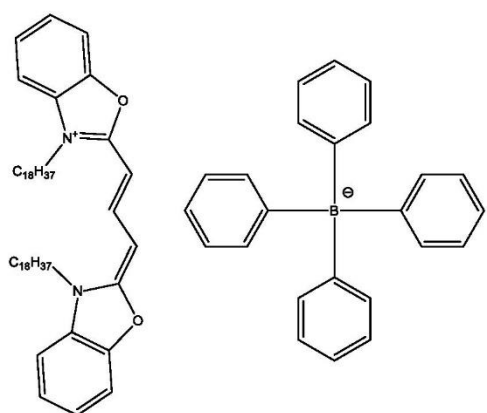
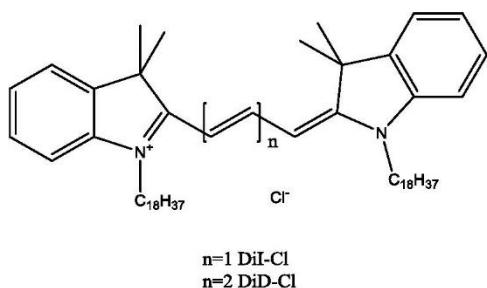
- 1. Materials**
- 2. Synthesis of dye salts**
- 3. Some cellular methods**
- 4. Tables S1-S2**
- 5. Figures S1-S18**
- 6. References**

## 1. Materials

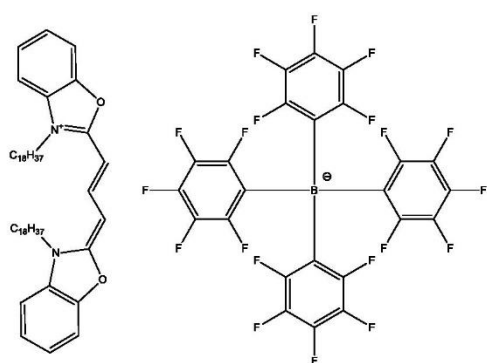
PLGA (poly(lactide-co-glycolic acid), lactide 50 mole%, glycolide 50 mole%, Mn 24,000; PDI 1.7), sodium tetraphenylborate (F0), sodium tetrakis[3,5-bis(1,1,1,3,3,3-hexafluoro-2-methoxy-2-propyl)phenyl]borate trihydrate (F12), 3,3'-Dioctadecyloxacarbocyanine perchlorate (DiO-Cl), acetonitrile ( $\geq 99.5\%$ ) were purchased from Sigma-Aldrich and used as received. DiI-Cl and DiD-Cl were synthesized according to a previously described procedure.<sup>41</sup> Lithium tetrakis(pentafluorophenyl)borate - ethyl ether complex (F5) was purchased from TCI and used as received. Sodium phosphate monobasic (99.0%, Sigma-Aldrich) and sodium phosphate dibasic dihydrate (99.0%, Sigma-Aldrich) were used to prepare 20 mM phosphate buffer solutions at pH 7.4. MilliQ-water (Millipore) was used in all experiments. Modified Eagle's Medium (MEM), Dulbecco's Modified Eagle's Medium (DMEM), reduced serum medium (optiMEM), fetal bovine serum (FBS), phosphate buffered saline (PBS), non-essential amino acids (100x), MEM vitamins (100x), L-Glutamine (100x), HBSS, and Penicillin and Streptomycin (10000 U/mL were purchased from FisherScientific), Sodium bicarbonate solution (3.5 g/L) and Gentamicin (50 mg/mL) were purchased from Sigma Aldrich. Synthesis of dye salts with bulky hydrophobic counterions is described in supplementary information. NMR spectra of new compounds were recorded at 20 °C on Bruker Avance III 500 MHz spectrometer. Mass spectra were obtained using an Agilent Q-TOF 6520 mass spectrometer. Flow cytometry measurements were performed on a Beckton-Dickenson Fortessa X50 flow cytometer.

## 2. Synthesis of dye salts

**DiI-Cl** and **DiD-Cl** were synthesized according to a previously described procedure.<sup>[1]</sup>

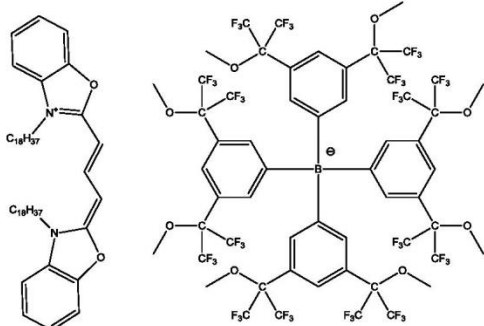


**DiO-F0.** DiO-Cl (1 eq., 8 mg, 0.00907 mmol) and sodium tetraphenylborate (F0) (3 eq., 9.32 mg, 0.0272 mmol) were mixed in 0.5 ml of dichloromethane, TLC has shown instant conversion. Product was purified by TLC using dichloromethane/methanol 95/5 as eluent. After evaporation of solvents 8 mg of DiO-F0 was obtained (80% yield).



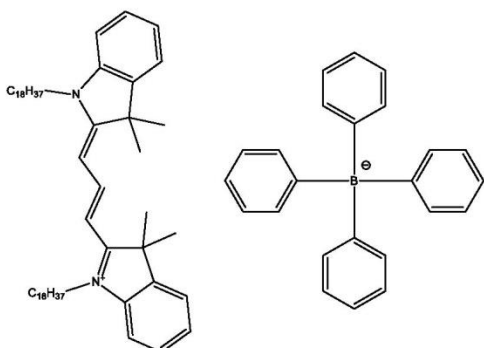
**DiO-F5.** DiO-Cl (1 eq., 8 mg, 0.00907 mmol) and lithium tetrakis(pentafluorophenyl)borate (F5) (3 eq., 26.7 mg, 0.0272 mmol) were mixed in 0.5 ml of dichloromethane, TLC has shown instant conversion. Product was purified by TLC using dichloromethane/methanol 95/5 as eluent. After evaporation of solvents 11 mg of DiO-F5 was obtained (83% yield). <sup>1</sup>H NMR (500 MHz, acetone-d<sub>6</sub>) δ ppm 0.85 - 0.90 (6 H, m) 1.25 - 1.30 (52 H, m) 1.36 - 1.43 (4 H, m) 1.47 - 1.54 (4 H, m) 1.93 - 2.00 (4 H, m) 4.34 (4 H, t, *J*=7.48 Hz) 6.13 (2 H, d) 7.45 - 7.53 (4 H, m) 7.70

(2 H, br d, *J*=7.94 Hz) 7.73 (2 H, br d, *J*=7.94 Hz) 8.56 (1 H, t, *J*=13.25 Hz). <sup>19</sup>F NMR (376 MHz, acetone-d<sub>6</sub>) δ ppm -168.36 (8 F, br t, *J*=17.16 Hz) -164.42 (4 F, br t, *J*=19.45 Hz) -133.03 (8 F, s). <sup>11</sup>B NMR (128 MHz, acetone-d<sub>6</sub>) δ ppm -11.39 (1 B, s). <sup>13</sup>C NMR (126 MHz, acetone-d<sub>6</sub>) δ ppm 13.46 (s), 22.44 (s), 26.46 (s), 27.77 (s), 28.89 (s), 28.95 (s), 29.04 (s), 29.07 (s), 29.19 (s), 29.30 (s), 29.35 (s), 29.45 (s), 29.48 (s), 29.50 (s), 29.51 (s), 29.52 (s), 31.76 (s), 44.29 (s), 85.06 (s), 110.83 (s), 111.19 (s), 125.31 (s), 126.10 (s), 131.63 (s), 147.02 (s), 147.26 (s), 162.46 (s). HRMS (m/z): [M]<sup>+</sup> calcd. for C<sub>53</sub>H<sub>85</sub>N<sub>2</sub>O<sub>2</sub> 781.6606; found 781.6605; [M]<sup>-</sup> calcd. For C<sub>24</sub>BF<sub>20</sub> 678.9779; found 678.9768.

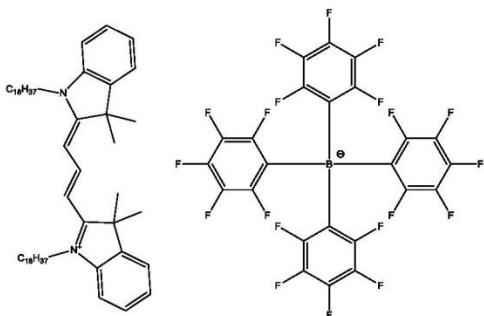


**DiO-F12.** DiO-Cl (1 eq., 8 mg, 0.00907 mmol) and sodium tetrakis[3,5-bis(1,1,1,3,3,3-hexafluoro-2-methoxy-2-propyl)phenyl]borate trihydrate (F12) (2 eq., 33.3 mg, 0.0181 mmol) were mixed in 0.5 ml of dichloromethane, TLC has shown instant conversion. Product was purified by TLC using dichloromethane/methanol 95/5 as eluent. After evaporation of solvents 17 mg of DiO-F12 was obtained (74 % yield).  $^1\text{H}$  NMR (500 MHz, acetone- $d_6$ )  $\delta$  ppm 0.86 - 0.89 (6 H, m) 1.28 (52 H, s) 1.37 - 1.42 (4 H, m)

1.48 - 1.53 (4 H, m) 1.94 - 2.00 (4 H, m) 3.30 (24 H, s) 4.34 (4 H, t,  $J=7.48$  Hz) 6.14 (2 H, d) 7.43 (4 H, s) 7.46 - 7.49 (2 H, m) 7.51 (2 H, dd,  $J=7.78, 1.07$  Hz) 7.59 (8 H, br s) 7.70 (2 H, d,  $J=7.63$  Hz) 7.74 (2 H, d,  $J=7.94$  Hz) 8.56 (1 H, m).  $^{19}\text{F}$  NMR (376 MHz, acetone- $d_6$ )  $\delta$  ppm -71.69 (48 F, s).  $^{11}\text{B}$  NMR (128 MHz, acetone- $d_6$ )  $\delta$  ppm -0.65 (1 B, s).  $^{13}\text{C}$  NMR (126 MHz, acetone- $d_6$ )  $\delta$  ppm 13.46 (s), 22.44 (s), 26.46 (s), 27.77 (s), 29.04 (s), 29.07 (s), 29.19 (s), 29.30 (s), 29.35 (s), 29.45 (s), 29.48 (s), 29.49 (s), 29.50 (s), 29.52 (s), 31.75 (s), 44.29 (s), 53.24 (s), 83.33 (sept,  $J=28$  Hz), 110.84 (s), 111.19 (s), 121.50 (s), 122.83 (s), 123.81 (s), 125.29 (dd), 125.31 (s), 126.10 (s), 131.63 (s), 136.98 (s), 147.03 (s), 147.10 (s), 162.13 (dd), 162.44 (s), 162.46 (s). HRMS ( $m/z$ ):  $[\text{M}]^+$  calcd. for  $\text{C}_{53}\text{H}_{85}\text{N}_2\text{O}_2$  781.6606; found 781.6614;  $[\text{M}]^-$  calcd. for  $\text{C}_{56}\text{H}_{36}\text{BF}_4\text{O}_8$  1759.1742; found 1759.1720.



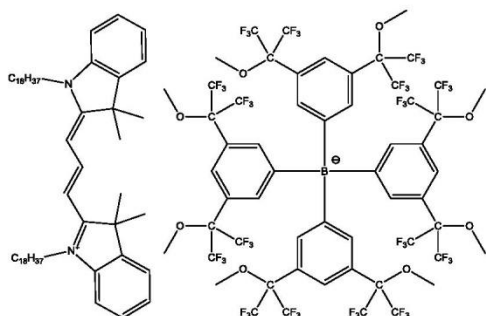
**DiI-F0.** DiI-Cl (1 eq., 15 mg, 0.0156 mmol) and sodium tetraphenylborate (F0) (3 eq., 16 mg, 0.0468 mmol) were mixed in 0.5 ml of dichloromethane, TLC has shown instant conversion. Product was purified by TLC using dichloromethane/methanol 95/5 as eluent. After evaporation of solvents 14 mg of DiI-F0 was obtained (78% yield).



**DiI-F5.** DiI-Cl (1 eq., 10 mg, 0.0104 mmol) and lithium tetrakis(pentafluorophenyl)borate (F5) (3 eq., 30.6 mg, 0.0312 mmol) were mixed in 0.5 ml of dichloromethane, TLC has shown instant conversion. Product was purified by TLC using dichloromethane/methanol 95/5 as eluent. After evaporation of solvents 13 mg of DiI-F5 was obtained (83% yield).  $^1\text{H}$  NMR (500 MHz, acetone- $d_6$ )  $\delta$  ppm 0.84 - 0.89 (6 H, m) 1.25 - 1.33 (52 H, m) 1.36 - 1.43 (4 H, m) 1.46 - 1.52 (4 H, m) 1.83 (12 H, s) 1.86 -

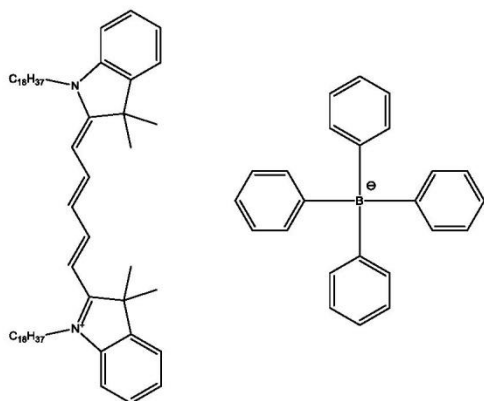
1.92 (4 H, m) 4.23 (4 H, t,  $J=7.63$  Hz) 6.58 (2 H, d,  $J=13.43$  Hz) 7.33 (2 H, t,  $J=6.53$  Hz) 7.45 - 7.49 (4 H, m) 7.63 (2 H, d,  $J=7.63$  Hz) 8.62 (1 H, t,  $J=13.58$  Hz).  $^{19}\text{F}$  NMR (376 MHz, acetone- $d_6$ )  $\delta$  ppm -168.33 (8 F, br t,  $J=18.31$  Hz) -164.40 (4 F, br t,  $J=20.03$  Hz) -133.01 (8 F, s).  $^{11}\text{B}$  NMR

(128 MHz, acetone-d<sub>6</sub>)  $\delta$  ppm -16.60 (1 B, s). <sup>13</sup>C NMR (126 MHz, acetone-d<sub>6</sub>)  $\delta$  ppm 13.47 (s), 22.45 (s), 26.59 (s), 27.31 (s), 27.33 (s), 29.04 (s), 29.18 (s), 29.20 (s), 29.34 (s), 29.39 (s), 29.41 (s), 29.49 (s), 29.53 (s), 29.54 (s), 31.76 (s), 44.22 (s), 49.45 (s), 102.58 (s), 111.46 (s), 122.44 (s), 125.55 (s), 128.78 (s), 141.00 (s), 142.23 (s), 150.69 (s), 174.68 (s). HRMS (m/z): [M]<sup>+</sup> calcd. for C<sub>59</sub>H<sub>97</sub>N<sub>2</sub>, 833.7646; found 833.7680; [M]<sup>-</sup> calcd. for C<sub>24</sub>BF<sub>20</sub>, 678.9779; found 678.9771.

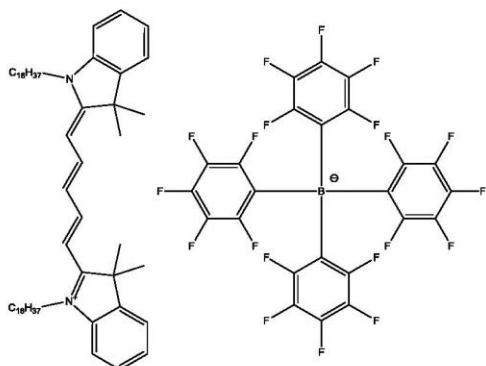


**DiI-F12.** DiI-Cl (1 eq., 10 mg, 0.0104 mmol) and sodium tetrakis[3,5-bis(1,1,1,3,3,3-hexafluoro-2-methoxy-2-propyl)phenyl]borate trihydrate (F12) (2 eq., 38.2 mg, 0.0208 mmol) were mixed in 0.5 ml of dichloromethane, TLC has shown instant conversion. Product was purified by TLC using dichloromethane/methanol 95/5 as eluent. After evaporation of solvents 22 mg of DiI-F12 was obtained (82 % yield). <sup>1</sup>H NMR (500 MHz, acetone-d<sub>6</sub>)  $\delta$  ppm

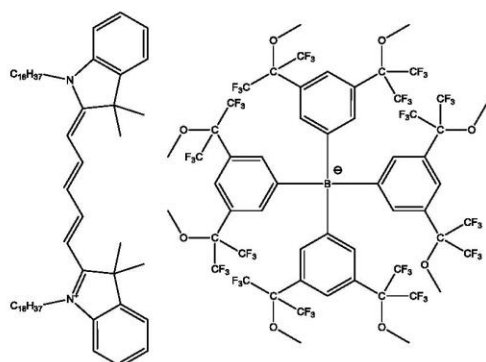
0.84 - 0.90 (6 H, m) 1.25 - 1.32 (52 H, m) 1.37 - 1.44 (4 H, m) 1.47 - 1.53 (4 H, m) 1.84 (12 H, s) 1.89 (4 H, quin,  $J=7.63$  Hz) 3.30 (24 H, s) 4.24 (4 H, t,  $J=7.48$  Hz) 6.59 (2 H, d,  $J=13.43$  Hz) 7.34 (2 H, t,  $J=6.71$  Hz) 7.41 - 7.50 (8 H, m) 7.57 - 7.65 (10 H, m) 8.62 (1 H, t,  $J=13.43$  Hz). <sup>19</sup>F NMR (376 MHz, acetone-d<sub>6</sub>)  $\delta$  ppm -71.69 (48 F, s). <sup>11</sup>B NMR (128 MHz, acetone-d<sub>6</sub>)  $\delta$  ppm -5.85 (1 B, s). <sup>13</sup>C NMR (126 MHz, acetone-d<sub>6</sub>)  $\delta$  ppm 13.46 (s), 22.44 (s), 26.58 (s), 27.31 (s), 27.34 (s), 29.04 (s), 29.18 (s), 29.19 (s), 29.34 (s), 29.35 (s), 29.39 (s), 29.48 (s), 29.52 (s), 29.53 (s), 31.76 (s), 44.22 (s), 49.46 (s), 53.23 (s), 83.33 (sept,  $J=28$  Hz), 102.60 (s), 111.48 (s), 119.21 (s), 121.51 (s), 122.66 (q), 122.45 (s), 122.83 (s), 123.81 (s), 125.29 (dd), 125.56 (s), 126.11 (s), 128.80 (s), 136.98 (s), 141.01 (s), 142.24 (s), 150.69 (s), 162.13 (dd), 174.68 (s). HRMS (m/z): [M]<sup>+</sup> calcd. for C<sub>59</sub>H<sub>97</sub>N<sub>2</sub>, 833.7646; found 833.7641; [M]<sup>-</sup> calcd. for C<sub>56</sub>H<sub>36</sub>BF<sub>48</sub>O<sub>8</sub>, 1759.1742; found 1759.1754.



**DiD-F0.** DiD-Cl (1 eq., 10 mg, 0.0101 mmol) and sodium tetraphenylborate (F0) (3 eq., 10.4 mg, 0.0304 mmol) were mixed in 0.5 ml of dichloromethane, TLC has shown instant conversion. Product was purified by TLC using dichloromethane/methanol 95/5 as eluent. After evaporation of solvents 10 mg of DiD-F0 was obtained (84% yield).



**DiD-F5.** DiD-Cl (1 eq., 12 mg, 0.011 mmol) and lithium tetrakis(pentafluorophenyl)borate (F5) (3 eq., 22.7 mg, 0.0331 mmol) were mixed in 0.5 ml of dichloromethane, TLC has shown instant conversion. Product was purified by TLC using dichloromethane/methanol 95/5 as eluent. After evaporation of solvents 15 mg of DiD-F5 was obtained (83% yield).  $^1\text{H}$  NMR (500 MHz, acetone- $d_6$ )  $\delta$  ppm 0.87 (6 H, t,  $J=6.71$  Hz) 1.25 - 1.31 (52 H, m) 1.37 - 1.43 (4 H, m) 1.49 (4 H, quin,  $J=7.48$  Hz) 1.73 (12 H, s) 1.86 (4 H, quin,  $J=7.55$  Hz) 4.20 (4 H, t,  $J=7.63$  Hz) 6.40 (2 H, d) 6.65 (1 H, t,  $J=12.51$  Hz) 7.28 (2 H, t,  $J=7.04$  Hz) 7.39 - 7.45 (4 H, m) 7.57 (2 H, d,  $J=7.32$  Hz) 8.42 (2 H, t,  $J=13.05$  Hz).  $^{19}\text{F}$  NMR (376 MHz, acetone- $d_6$ )  $\delta$  ppm -168.31 (8 F, br t,  $J=17.17$  Hz) -164.39 (4 F, br t,  $J=20.03$  Hz) -133.00 (8 F, s).  $^{11}\text{B}$  NMR (128 MHz, acetone- $d_6$ )  $\delta$  ppm -16.61 (1 B, s).  $^{13}\text{C}$  NMR (126 MHz, acetone- $d_6$ )  $\delta$  ppm 13.47 (s), 22.45 (s), 26.56 (s), 26.92 (s), 27.22 (s), 29.05 (s), 29.15 (s), 29.20 (s), 29.33 (s), 29.35 (s), 29.37 (s), 29.47 (s), 29.49 (s), 29.50 (s), 29.52 (s), 29.53 (s), 31.76 (s), 43.91 (s), 49.28 (s), 103.21 (s), 111.07 (s), 122.32 (s), 125.05 (s), 125.30 (s), 128.59 (s), 141.35 (s), 142.37 (s), 154.04 (s), 173.29 (s). HRMS ( $m/z$ ):  $[\text{M}]^+$  calcd. for  $\text{C}_{61}\text{H}_{99}\text{N}_2$ , 859.7803; found 859.7834;  $[\text{M}]^-$  calcd. for  $\text{C}_{24}\text{BF}_{20}$ , 678.9779; found 678.9766.



**DiD-F12.** DiD-Cl (1 eq., 8 mg, 0.0081 mmol) and sodium tetrakis[3,5-bis(1,1,1,3,3,3-hexafluoro-2-methoxy-2-propyl)phenyl]borate trihydrate (F12) (2 eq., 29.8 mg, 0.0162 mmol) were mixed in 0.5 ml of dichloromethane, TLC has shown instant conversion. Product was purified by TLC using dichloromethane/methanol 95/5 as eluent. After evaporation of solvents 15 mg of DiD-F12 was obtained (71 % yield).  $^1\text{H}$  NMR (500 MHz, acetone- $d_6$ )  $\delta$  ppm 0.84 - 0.90 (6 H, m) 1.28 (52 H, s) 1.37 - 1.44 (4 H, m) 1.47 - 1.53 (4 H, m) 1.74 (12 H, s) 1.87 (4 H, quin,  $J=7.55$  Hz) 3.30 (24 H, s) 4.20 (4 H, t,  $J=7.48$  Hz) 6.42 (2 H, d,  $J=13.73$  Hz) 6.67 (1 H, t,  $J=12.36$  Hz) 7.28 (2 H, t,  $J=7.21$  Hz) 7.39 - 7.45 (8 H, m) 7.56 - 7.61 (10 H, m) 8.42 (2 H, t,  $J=12.97$  Hz).  $^{19}\text{F}$  NMR (376 MHz, acetone- $d_6$ )  $\delta$  ppm -71.68 (48 F, s).  $^{11}\text{B}$  NMR (128 MHz, acetone- $d_6$ )  $\delta$  ppm -5.85 (1 B, s).  $^{13}\text{C}$  NMR (126 MHz, acetone- $d_6$ )  $\delta$  ppm 13.47 (s), 22.45 (s), 26.56 (s), 26.92 (s), 27.23 (s), 29.04 (s), 29.14 (s), 29.19 (s), 29.33 (s), 29.35 (s), 29.37 (s), 29.47 (s), 29.49 (s), 29.50 (s), 29.52 (s), 29.53 (s), 31.76 (s), 43.91 (s), 49.28 (s), 53.24 (s), 83.33 (sept,  $J=28$  Hz), 103.23 (s), 111.08 (s), 119.22 (s), 121.51 (s), 122.33 (s), 122.83 (s), 123.81 (s), 125.06 (s), 125.29 (dd), 126.11 (s), 128.59 (s), 136.99 (s), 141.35 (s), 142.38 (s), 154.04 (s), 162.13 (dd), 173.30 (s). HRMS ( $m/z$ ):  $[\text{M}]^+$  calcd. for  $\text{C}_{61}\text{H}_{99}\text{N}_2$ , 859.7803; found 859.7840;  $[\text{M}]^-$  calcd. for  $\text{C}_{56}\text{H}_{36}\text{BF}_4\text{O}_8$ , 1759.1742; found 1759.1753.

### 3. Some cellular methods

*Cell culture:* HeLa cells (ATCC® CCL-2™) were grown in DMEM (without phenol red), supplemented with 10 % heat inactivated fetal bovine serum (FBS), L-Glutamine, Penicillin and Streptomycin. KB cells (ATCC® CCL-17™) were first cultured in MEM with Earle's salts, supplemented with 10 % FBS, 1% non-essential amino acids (NEAA), 1 % MEM vitamins, and 40 µg/mL of Gentamicin. For 2 to 5 passages before labeling and testing the KB cells were cultured in DMEM without folic acid, supplemented with 10 % FBS, L-glutamine, sodiumbicarbonate (3.5 g/L), and 40 µg/mL of Gentamicin. Chinese hamster ovary (CHO) cells were cultured in DMEM without phenol red, supplemented with 10 % FBS, L-Glutamine, 1% NEAA, Penicillin and Streptomycin. Human astrocytoma cells U87 (ATCC® HTB-14™) were cultured in MEM with Earle's salts, supplemented with 10 % FBS, 1% NEAA, 1 % sodium pyruvate, Penicillin and Streptomycin. The human embryonic kidney cell line 293T (ATCC® CRL-3216™) was cultured in DMEM with 4.5 g/L glucose, supplemented with 10 % FBS, Penicillin, and Streptomycin. The rat basophilic leukaemia cell line RBL-2H3 (ATCC® CRL-2256™) was cultured in MEM with Earle's salts, supplemented with 15 % FBS, Penicillin and Streptomycin.

*Cytotoxicity:* Cells were seeded in 96-well plates at a density of 1000 cells per well and left to adhere for 18 h. The cells were then rinsed twice with optiMEM and PBS and 80 µL of optiMEM were added to each well. 20 µL of the NP solutions were then added per well, followed by homogenization. After incubation for 3h with the NPs in optiMEM, 100 µL of DMEM media containing 20 % FBS were added to each well without prior rinsing. The cells were then incubated for 72 h, followed by rinsing with PBS. After incubation of the cells in DMEM containing 0.5 gL<sup>-1</sup> of MTT for 4h at 37°C, 80 µL of the medium were removed, 50 µL of DMSO were added, the plates were stirred for 20 min and the absorbance at 540 nm and 570 nm were recorded. For calculating the relative cell viability, the absorbances were corrected by the absorbance of wells containing only the medium, and compared to wells with no added NPs. All experiments were carried out in quintuplicate.

*Doxorubicin and cell competition:* HeLa cells were seeded in 25 cm<sup>2</sup> cell culture flasks (300 000 cells/ flask) and after adhesion for 18 h labeled with 6 different colors using the NPs as described above. After rinsing with Opti-MEM and DMEM, the cells were incubated with different concentration of doxorubicin for 24 h, with one doxorubicin concentration corresponding to one color. Following this incubation the cells were rinsed with PBS and DMEM and left for an additional 24 h. The cells were then rinsed again and detached using trypsin. After counting, the differently treated and colored cells were mixed at equal concentrations (except for the highest doxorubicin concentrations, for which the survival rate was too low to obtain the same total cell number under similar conditions). The cells were incubated for 4 h, rinsed very gently with HBSS, and imaged with a confocal microscope.

#### 4. Tables S1-S2

**Table S1.** Dynamic light scattering data (mean size based on volume statistics, polydispersity) for DiO-series NPs.

Dye	Loading, nM	Size, nm	Stdev, nm	PDI
DiO-CI	5	61.7	1.1	0.02
DiO-F0	5	43.8	0.6	0.15
DiO-F5	5	49.6	1.2	0.18
DiO-F12	5	42.8	0.5	0.03
DiO-CI	20	96.0	2.0	0.07
DiO-F0	20	47.6	1.1	0.12
DiO-F5	20	45.9	0.4	0.16
DiO-F12	20	43.2	0.2	0.06
DiO-CI	50	674	134	0.42
DiO-F0	50	56.5	0.5	0.05
DiO-F5	50	45.0	0.7	0.11
DiO-F12	50	47.2	0.8	0.09

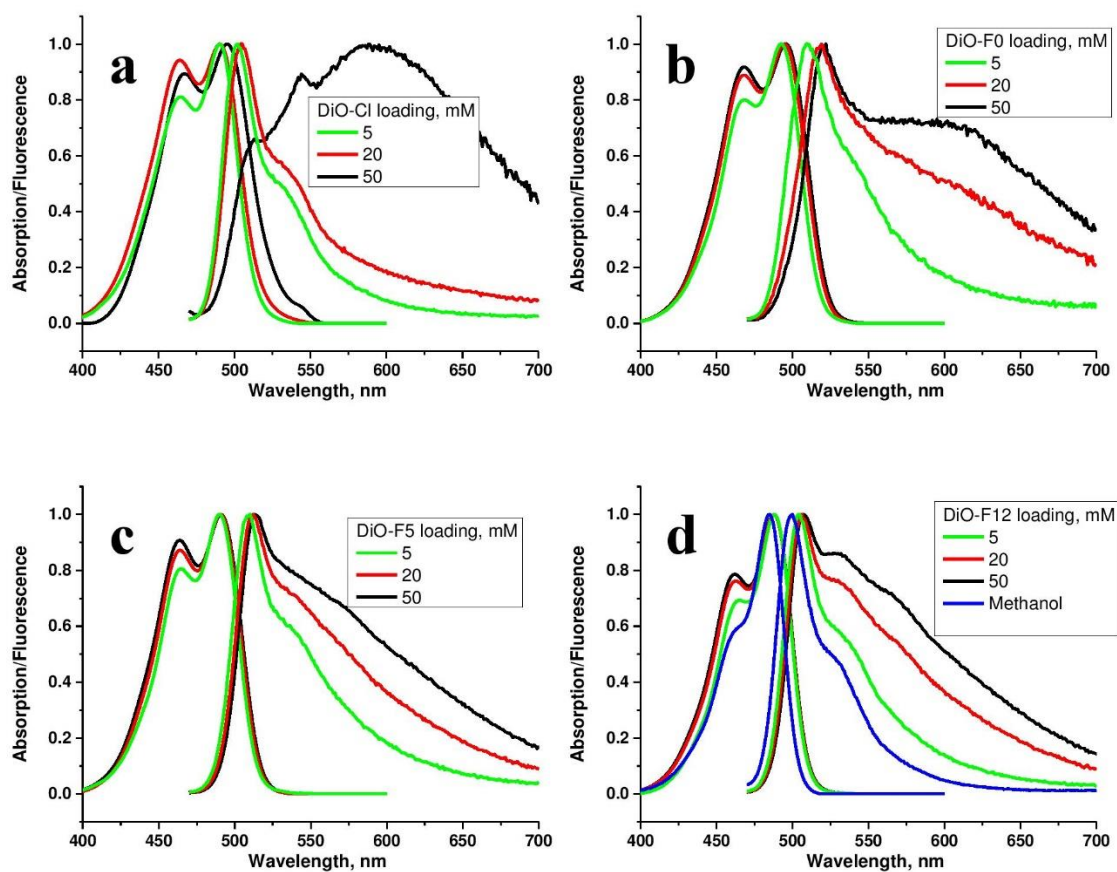
Stdev – standard deviation of the mean (n = 3). PDI – polydispersity index.

**Table S2.** Dynamic light scattering data (mean size based on volume statistics, polydispersity) for DiI-series NPs.

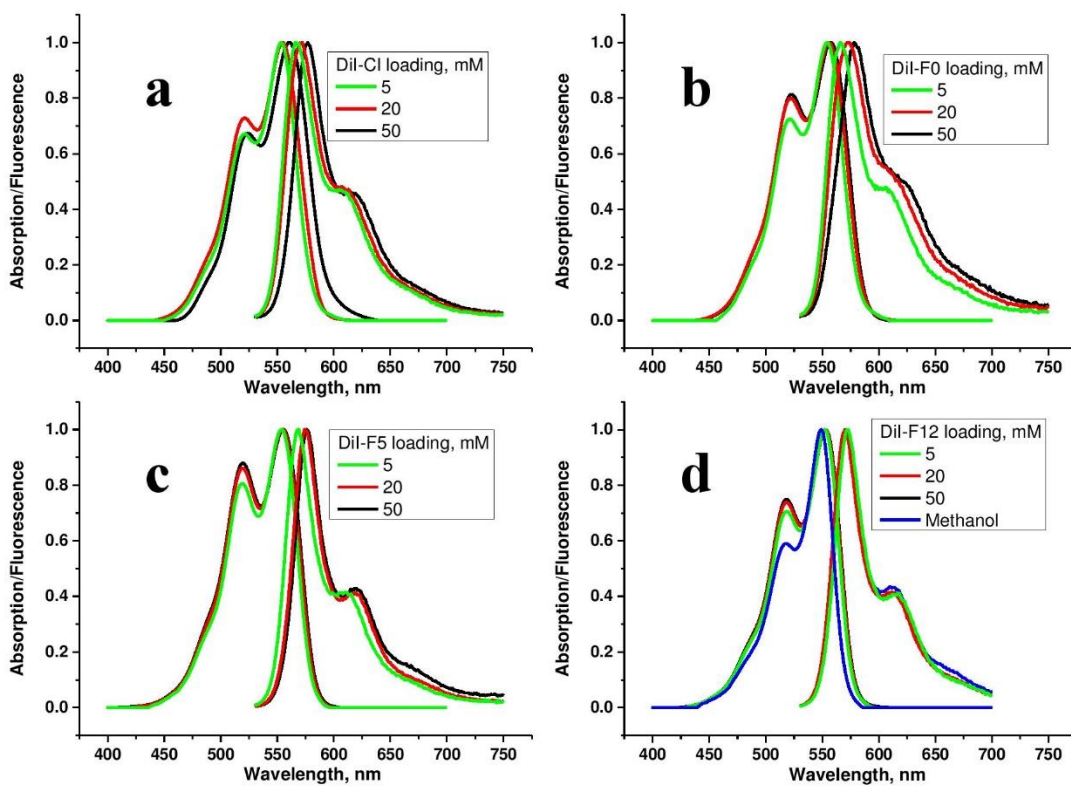
Dye	Loading, nM	Size, nm	Stdev, nm	PDI
DiI-CI	5	56.3	1.2	0.09
DiI-F0	5	44.3	1.1	0.02
DiI-F5	5	42.8	0.4	0.03
DiI-F12	5	43.8	0.7	0.02
DiI-CI	20	64.2	1.7	0.04
DiI-F0	20	51.1	0.4	0.04
DiI-F5	20	45.4	0.3	0.01
DiI-F12	20	45.1	0.5	0.03
DiI-CI	50	375	27.0	0.20
DiI-F0	50	64.6	0.6	0.02
DiI-F5	50	47.2	0.7	0.07
DiI-F12	50	50.3	0.4	0.14

Stdev – standard deviation of the mean (n = 3). PDI – polydispersity index.

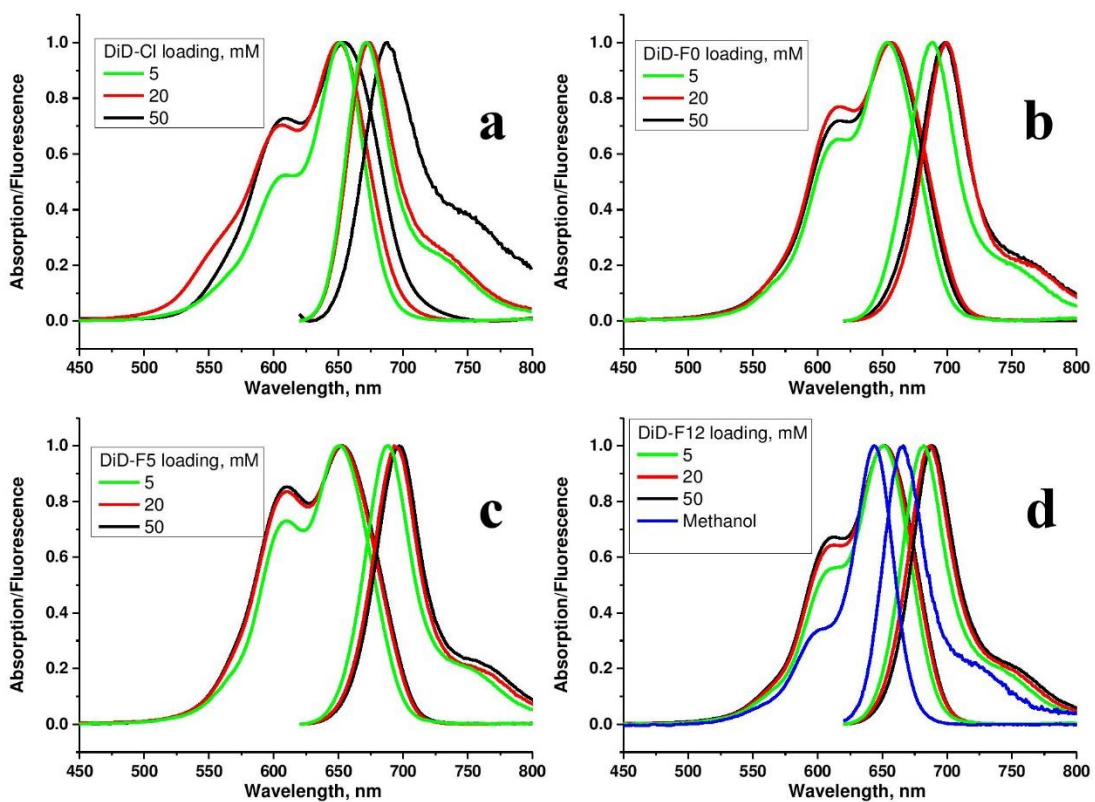
## 5. Figures S1-S19



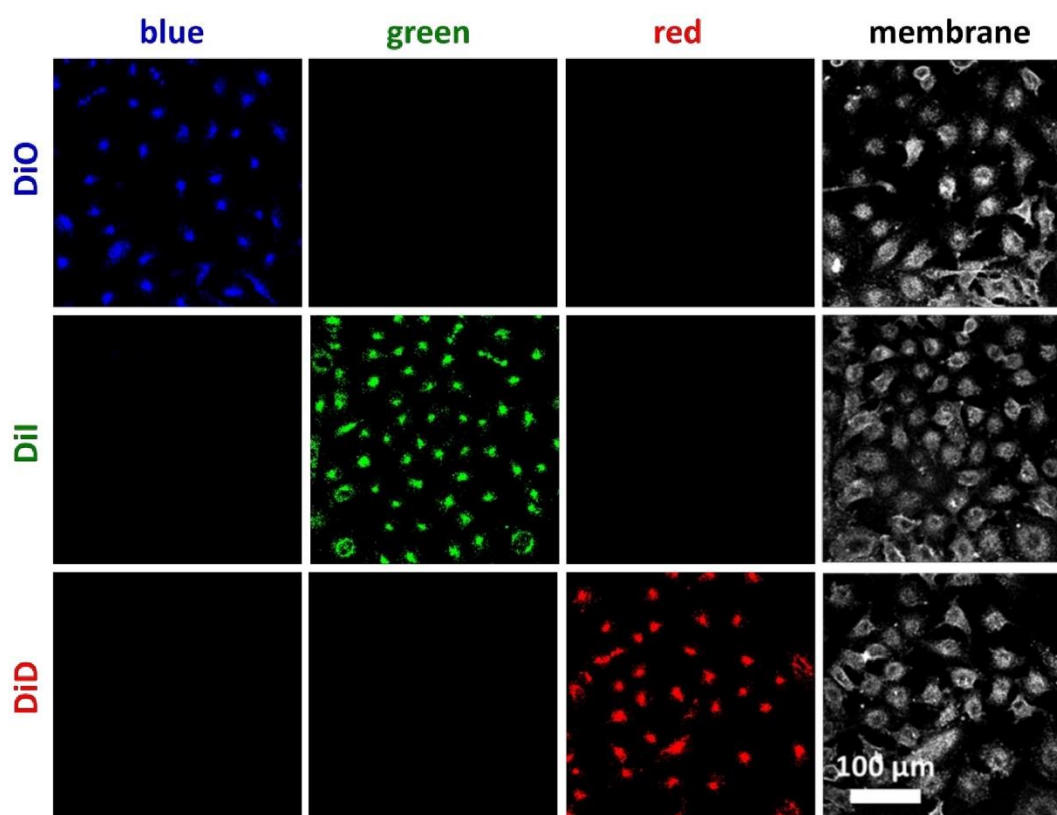
**Figure S1.** Effect of dye loading on spectral properties of DiO-series NPs. Normalized absorption and fluorescence spectra of DiO-Cl (a), DiO-F0 (b), DiO-F5 (c), DiO-F12 (d) at different dye loadings.



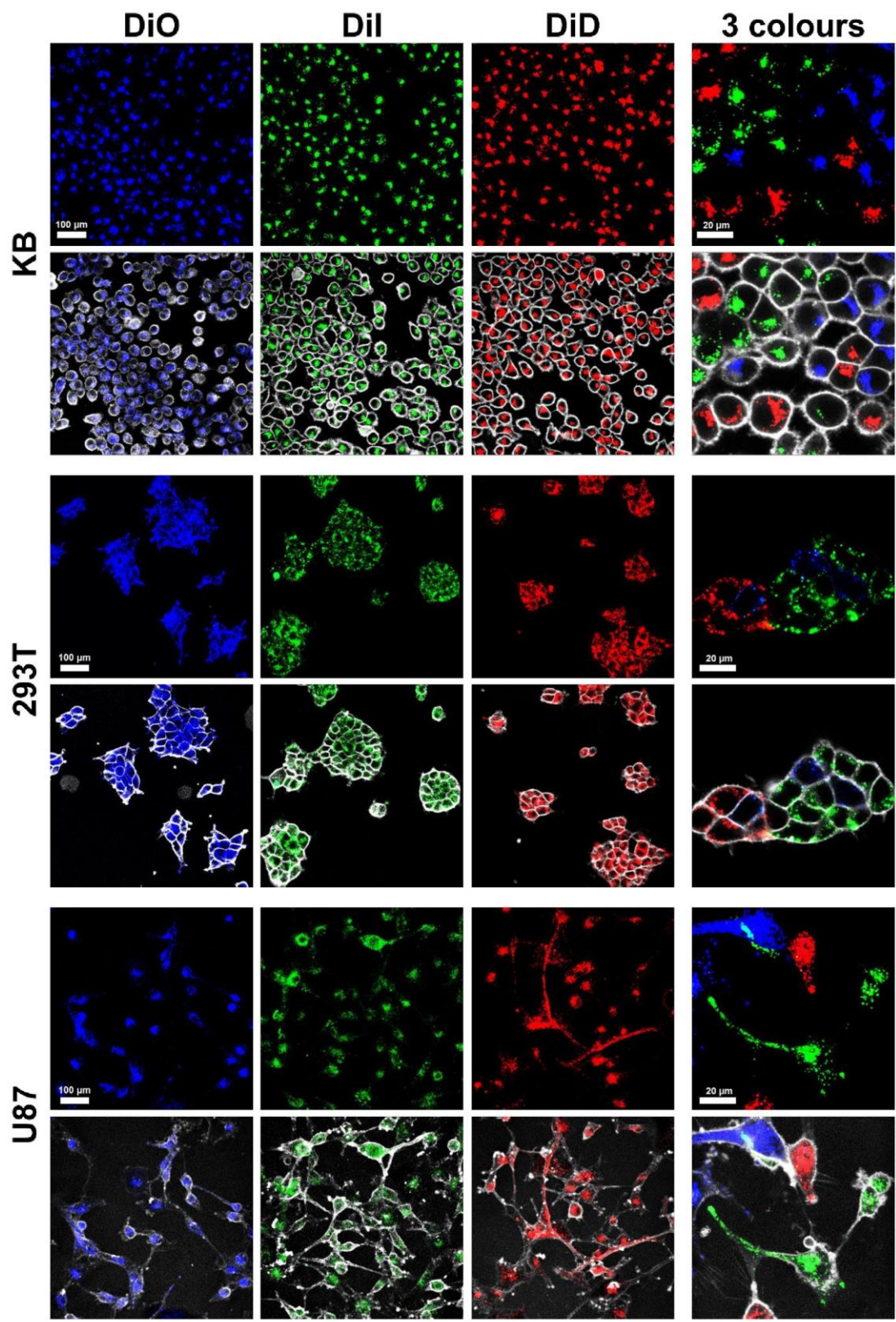
**Figure S2. Effect of dye loading on spectral properties of DiI-series NPs.** Normalized absorption and fluorescence spectra of DiI-C1 (a), DiI-F0 (b), DiI-F5 (c), DiI-F12 (d) at different dye loadings.



**Figure S3. Effect of dye loading on spectral properties of DiD-series NPs.** Normalized absorption and fluorescence spectra of DiD-Cl (a), DiD-F0 (b), DiD-F5 (c), DiD-F12 (d) at different dye loadings.



**Figure S4. Fluorescence confocal images of cells incubated for 3 h with nanoparticles.** HeLa cells labeled with DiO-F12 (top row), DiI-F12 (middle row), and DiD-F12 (bottom row) NPs. The images obtained in the different channels are shown (blue, green and red). Membrane staining by F2N12SM is shown in grey. Before imaging, the cells were incubated with NPs for 3h, rinsed, transferred into microscopy chambers and then incubated for 24h.



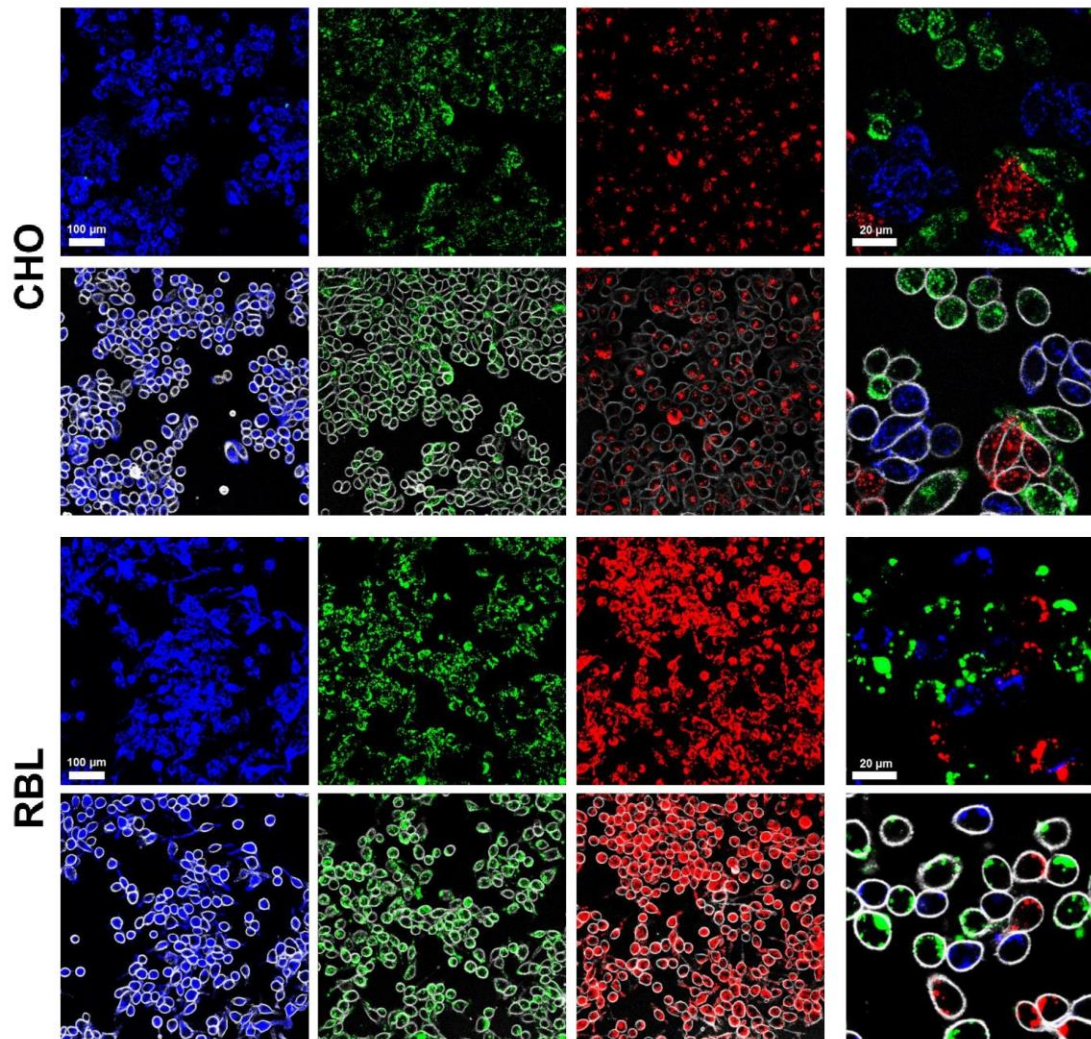


**Figure S5.** Confocal microscopy images of internalization of NPs in different cell types and mixtures of cells stained with three colors. For each cell type the first row represents a superposition of the 3 NP channels set to the same intensities and the second row is a superposition of the NP channels and the channel of the membrane marker (F2N12SM in grey). Columns 1, 2 and 3 correspond to cells labeled with DiO-F12, DiI-F12, and DiD-F12 NPs, respectively recorded with a 20x objective; column 4 corresponds to images of co-cultures of three populations labeled each with one type of NP recorded with a 63x objective.

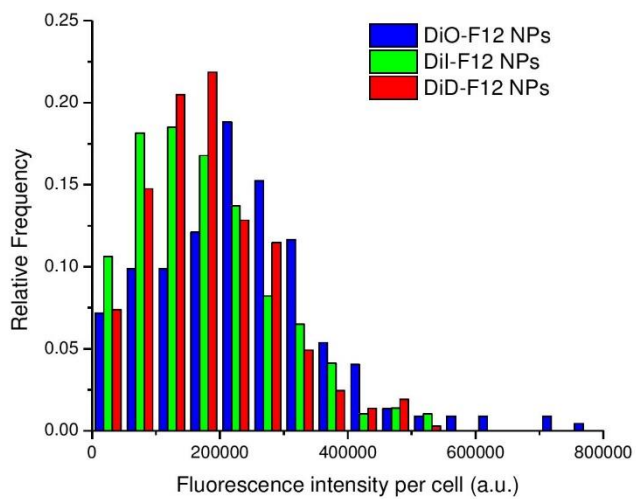


**Figure S6.** Histograms of total fluorescence intensities per cell for HeLa cells labeled with DiO-F12, DiI-F12 and DiD-F12 NPs, respectively, as obtained from confocal microscopy. At least 200 cells were analyzed for each condition.

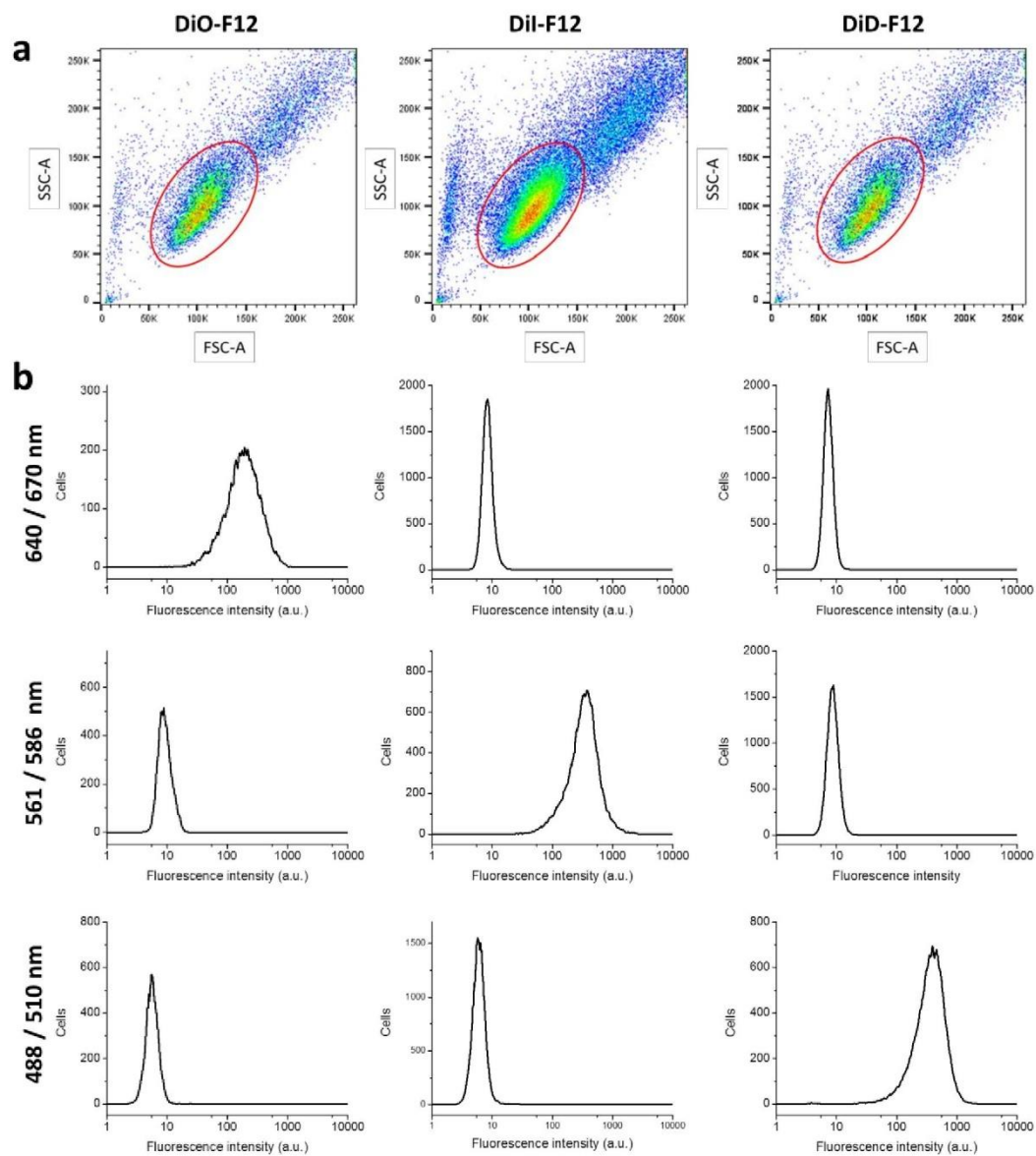


**Figure S7.** Flow cytometry of KB cells labeled with: DiO-F12 NPs (left), DiI-F12 NPs (middle) and DiD-F12 NPs (right). (a) Presentation of side scattering (SSC-A) vs forward scattering (FSC-A) together with the selected region of interest for single-cell analysis. (b) Histograms of the fluorescence intensities for excitation at 488 nm with emission recorded at  $510 \pm 10$  nm (top), excitation at 561 nm with emission recorded at  $586 \pm 7.5$  nm (middle), and excitation at 640 nm with emission recorded at  $670 \pm 15$  nm (bottom). At least 10000 events were recorded for each measurement.

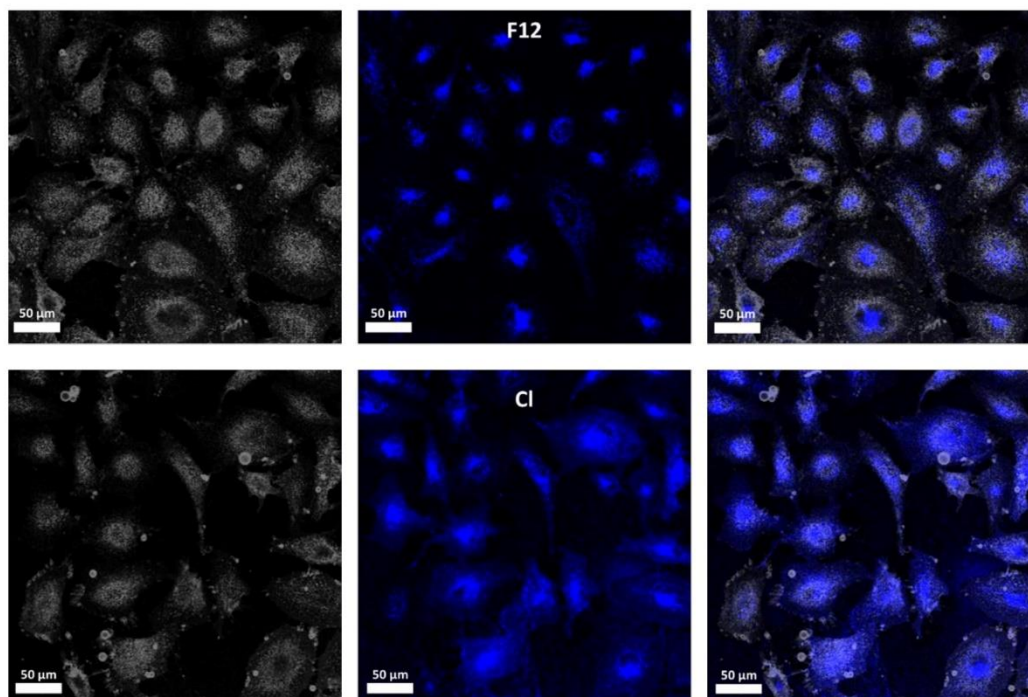


**Figure S8.** HeLa cells incubated with NPs containing DiO with counterions F12 (above) and perchlorate (below). The membrane was labeled with F2N12SM (in grey). On the right side the superposition of the 2 channels is shown.

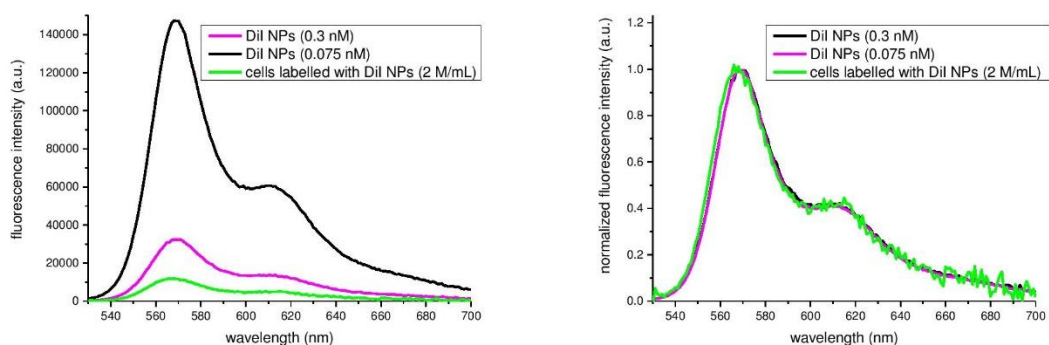


**Figure S9.** Determination of number of NPs per cell using fluorescence spectroscopy of labeled cells in suspension: fluorescence emission spectra of DiI-F12 NP loaded cells at a concentration of 2 000 000 cells per mL and of DiI-F12 NPs at two concentrations. A: at relative scale, B: normalized spectra.

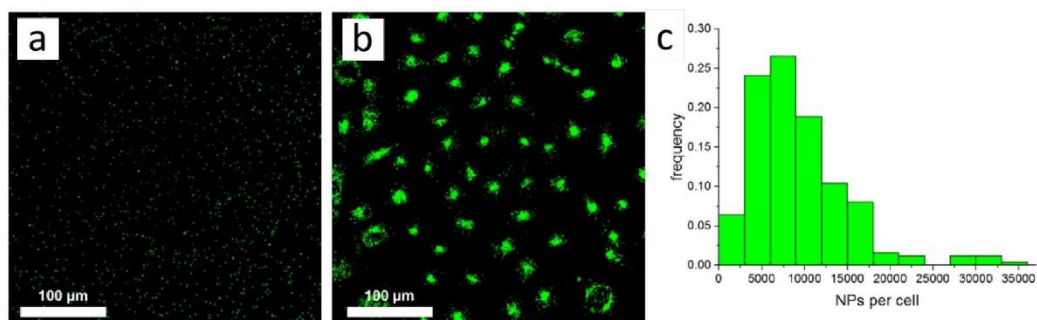
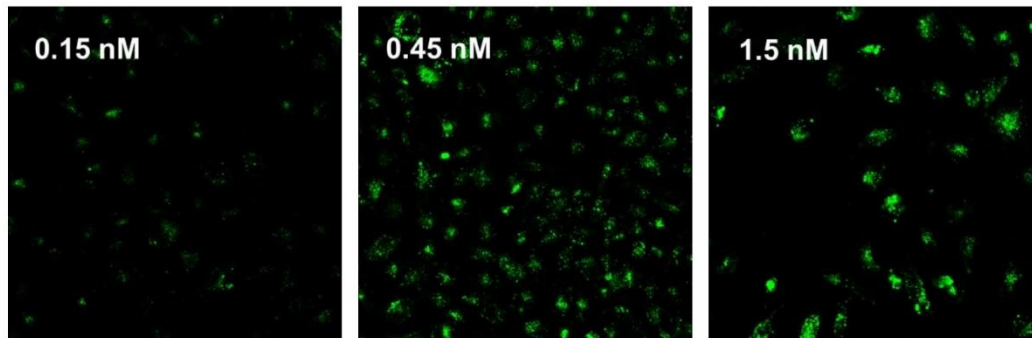


**Figure S10.** Determination of the number of NPs per cell using fluorescence microscopy and comparison with fluorescence beads: A, B: confocal microscopy images of 200 nm Invitrogen Fluospheres 540/560 immobilized on a glass surface and of HeLa cells loaded with DiI-F12 NPs, respectively, at the same conditions for imaging and using the same conditions for representation. C: Corresponding histogram of number of DiI-F12 NPs per cell 24 h after labeling.

A



B

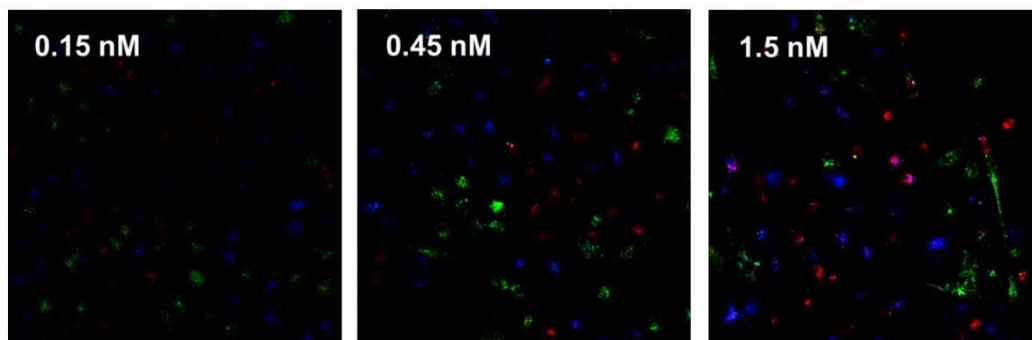


**Figure S11.** Influence of NP concentration. Confocal fluorescence microscopy images of HeLa cells incubated for 3h with different NP concentrations and imaged 24 h after labeling. (a) DiI-F12 NPs only, (b) co-culture of cells labeled with DiO-F12, DiI-F12, and DiD-F12 NPs.

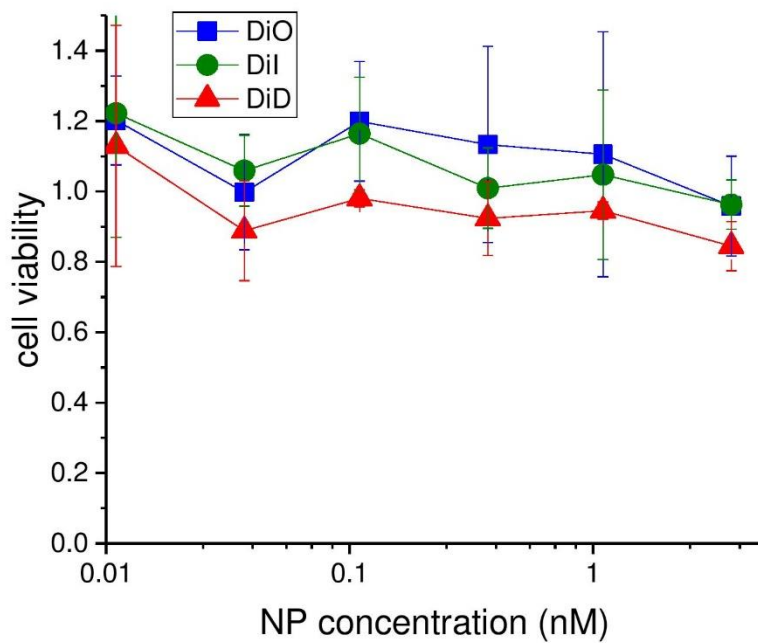


**Figure S12.** Viability of HeLa cells exposed for 72 h to different concentrations of NPs loaded with DiO-F12, DiI-F12, and DiD-F12. Cell viability was tested in quintuplicate using MTT. The error bars correspond to the standard deviation (n = 3).

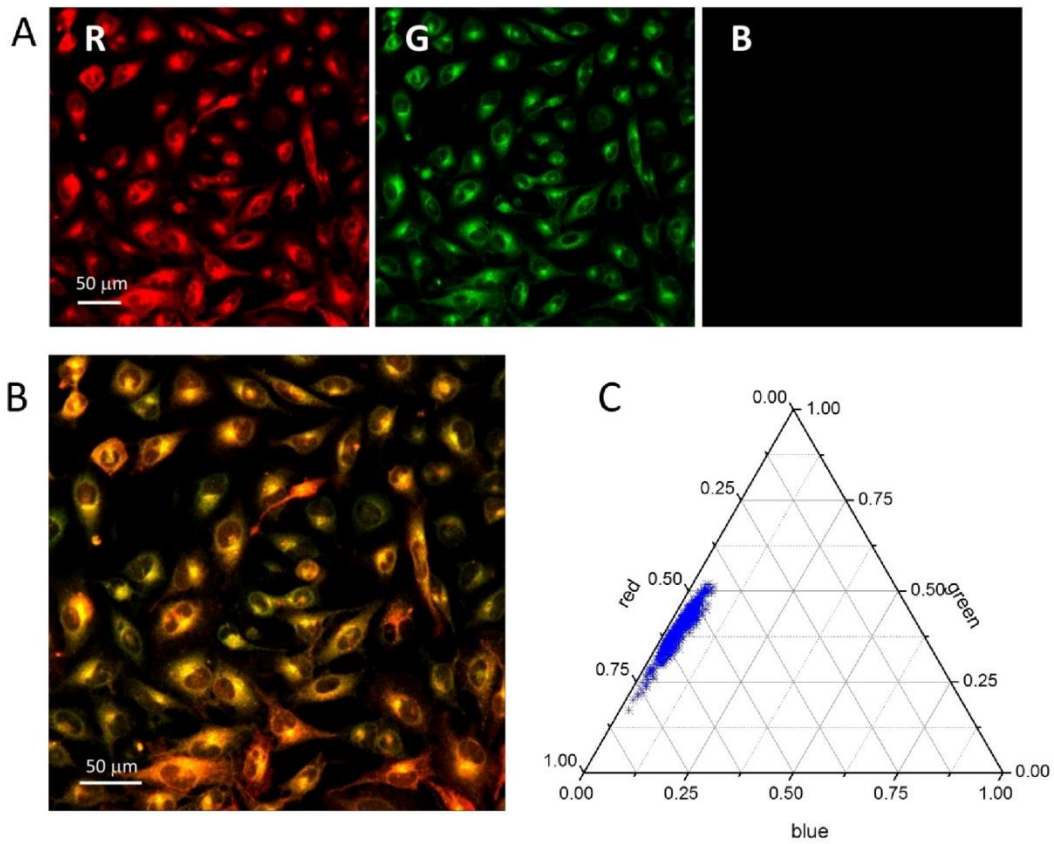


**Figure S13.** Confocal fluorescence microscopy images of HeLa cells incubated with a mixture of DiI (1  $\mu\text{M}$ ) and DiD (1  $\mu\text{M}$ ). In this case, the stock solution in DMSO containing both dyes (1:1 molar ratio) was added Opti-MEM and then immediately transferred to the cells (final DMSO concentration  $<1\%$ ). Before imaging, the cells were incubated with dyes for 3h, rinsed, transferred into microscopy chambers and then incubated for 24h. The images obtained in the different channels are shown: red (R), green (G) and blue (B). (B) Merged image from all three channels. (C) Representation of the relative intensities of DiO, DiI, and DiD channels of individual cells in a ternary diagram. The relative intensities were determined for about 400 cells.

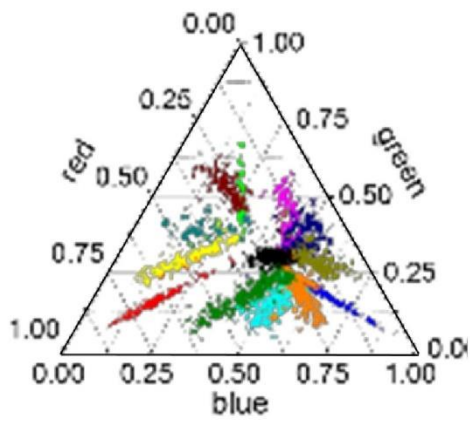


**Figure S14.** Representation of the relative intensities of DiO (blue), DiI (green), and DiD (red) channels of individual cells in a ternary diagram at 8 days after labeling with 13 colors. The relative intensities were determined for about 200 cells per condition.

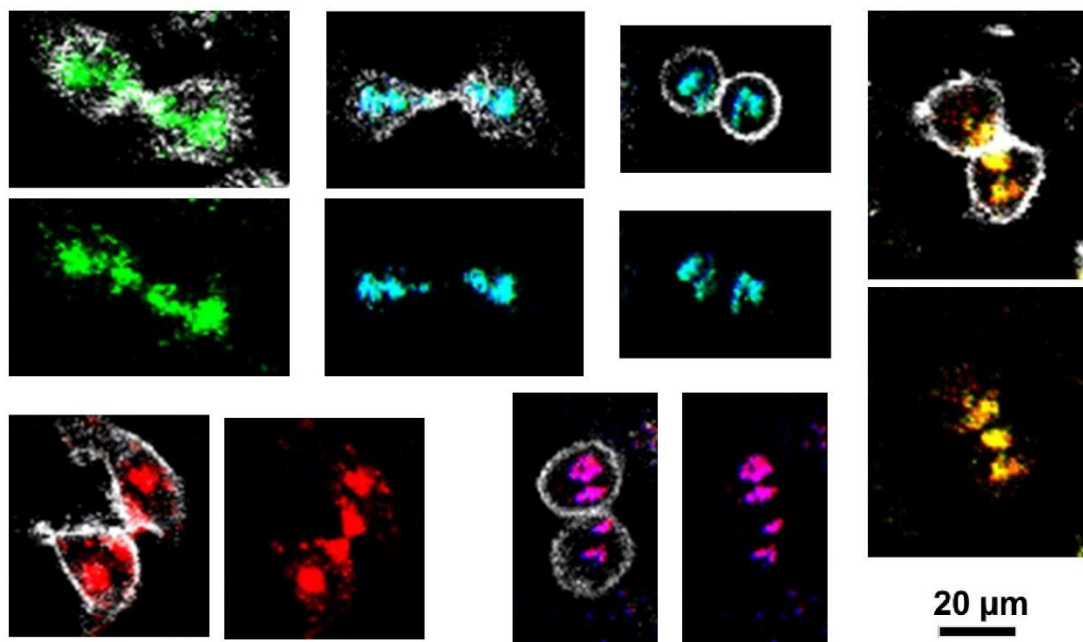


**Figure S15.** Examples of labeled HeLa cells undergoing cell division. Colored part represents NPs, while white part is staining by F2N12SM probe.

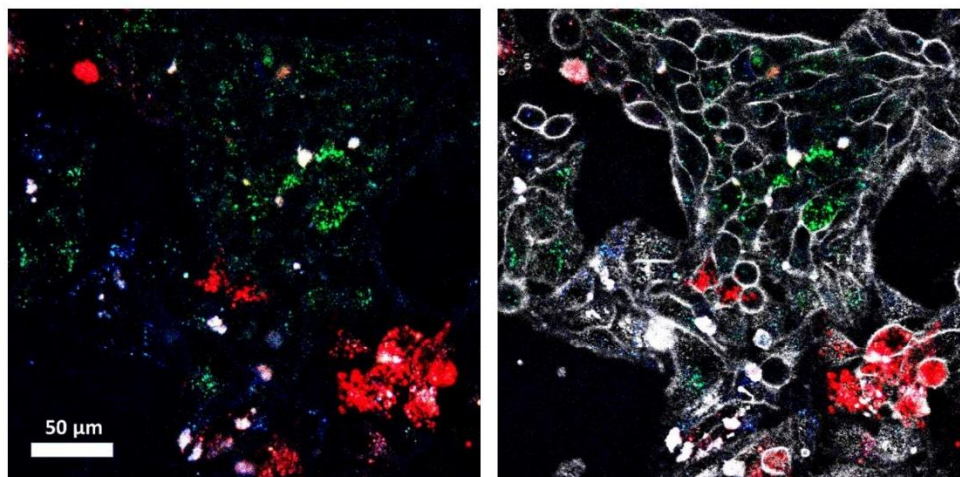


**Figure S16.** Long-term labeling of HeLa cells. Confocal fluorescence microscopy images of a co-culture of HeLa cells labeled with DiO-F12, DiI-F12, and DiD-F12 NPs imaged 19 days after labeling.

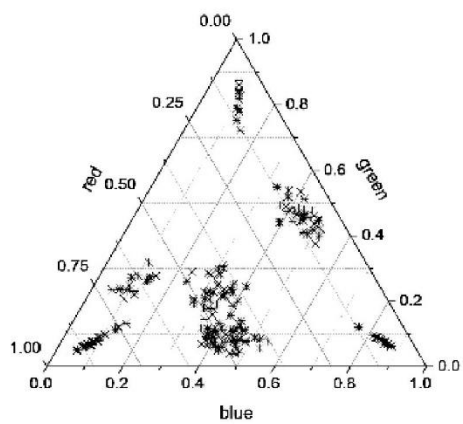


**Figure S17.** Ternary representation of the color analysis of a mixture of seven cell populations labeled with combinations of DiO-F12, DiI-F12, and DiD-F12 NPs in order to achieve seven different colors four days after labeling.

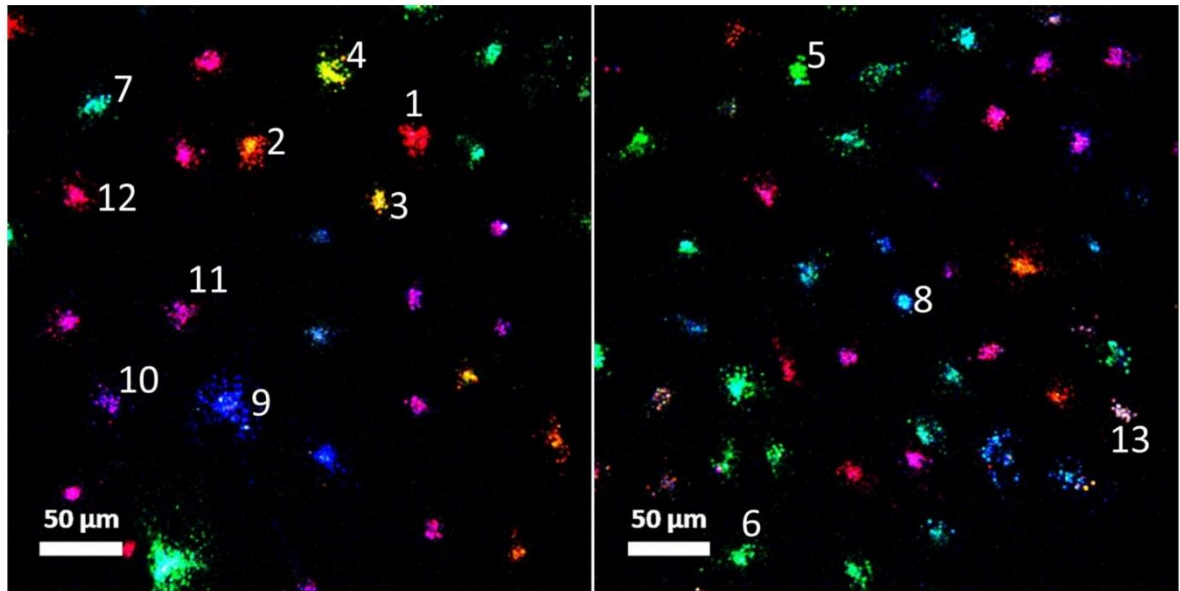


**Figure S18.** Confocal microscope images of co-culture of HeLa cells labeled with 13 colors at 24h after labeling. Numbers correspond to the identified coded colors: 1 – red, 2 – orange, 3 – yellow, 4 – chartreuse, 5 – green, 6 – spring green, 7 – cyan, 8 – turquoise, 9 – blue, 10 – purple, 11 – magenta, 12 – pink, 13 – white.

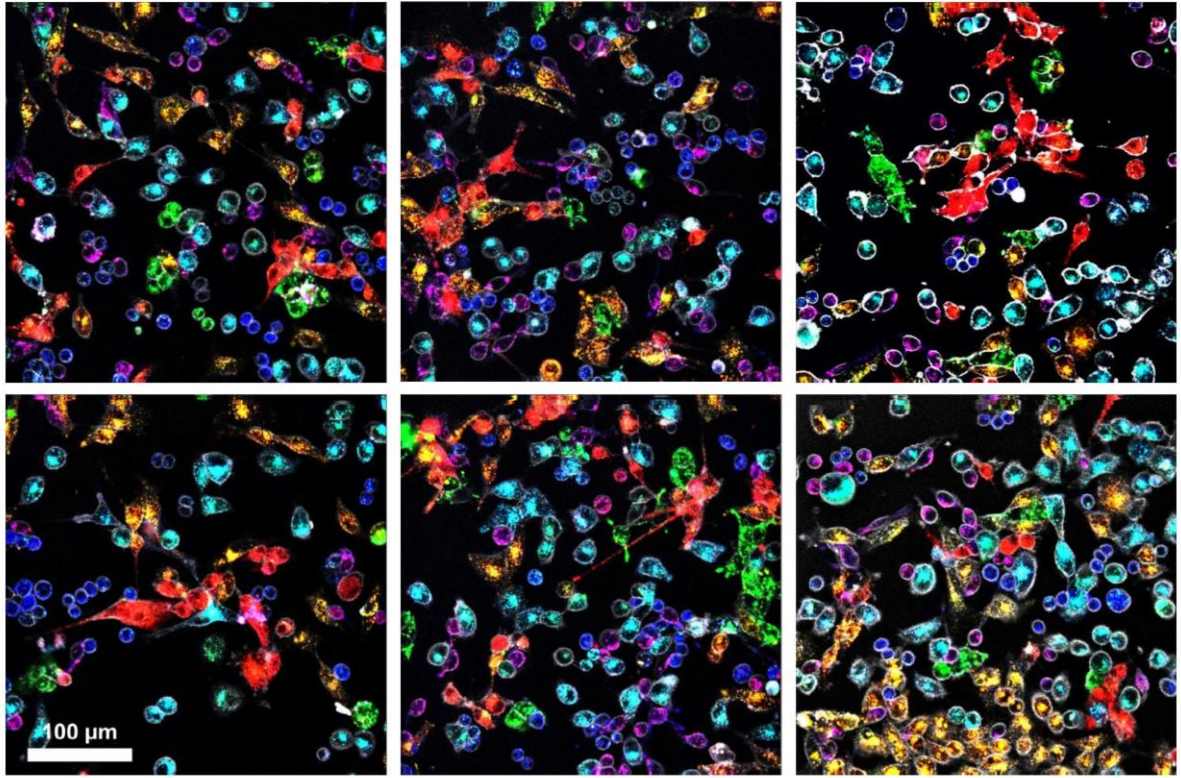


**Figure S19.** Confocal microscopy images of mixtures of 6 different cell lines labeled with 6 different colors, 24h after labeling.

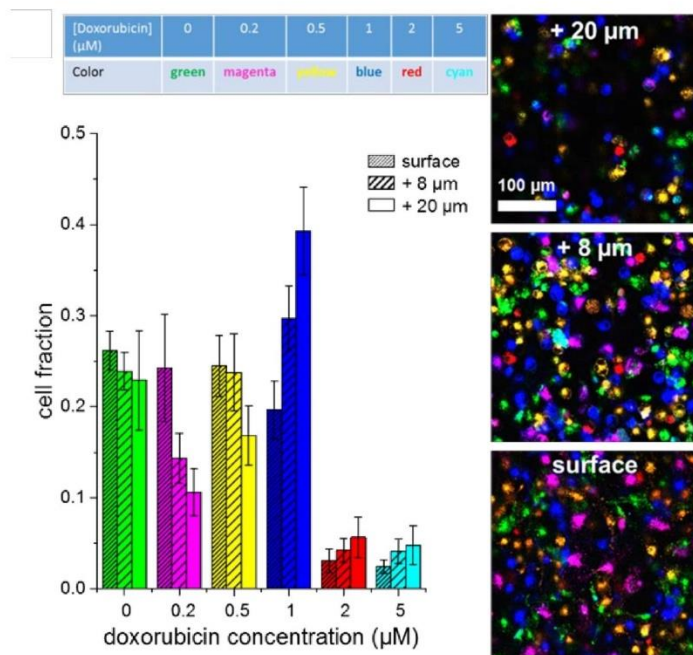


**Figure S20.** Competition of HeLa cells treated with different concentrations of doxorubicin for adhesion onto the surface and their organization: 6 populations of HeLa cells were labeled with distinct colors and each population was treated with a different concentration of doxorubicin during 24 h, followed by 24 h of culture in doxorubicin-free medium. The 6 populations were then mixed in equal concentrations, seeded on a glass surface for 4 h and after gentle rinsing with HBSS were further imaged at three confocal z-levels. The graph represents the relative fractions of each cell population at these different heights measured over 6 regions with at least 330 cells per regions in three experiments. The mean number of cells per region were, respectively, 130, 140, and 75 at the surface, 8  $\mu\text{m}$  and 20  $\mu\text{m}$  above the surface. Error-bars correspond to the standard deviation over all regions.

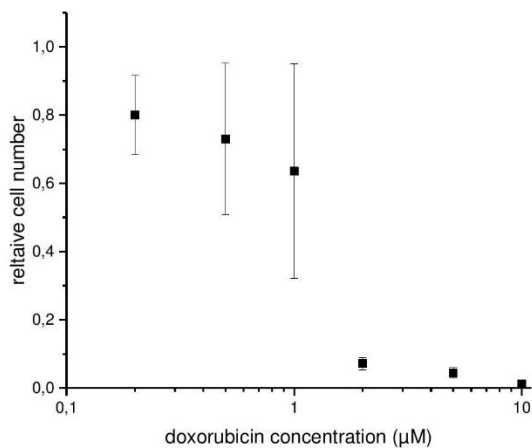


**Figure S21.** Relative number of recovered HeLa cells treated with different doxorubicin concentrations. After 24 h of treatment with the corresponding doxorubicin concentration and rinsing, the cells were left in normal medium for an additional 24 h. Then the cells were detached and counted. The relative cell numbers given here are the ratio of the number of recovered cells to the number of recovered cells for the untreated control. This does not directly correspond to cell viability, as several washing steps are included, which probably removed weakly adhering cells. The error bars correspond to the standard deviation ( $n = 3$ ).

## 6. References

- [1] X. J. Peng, Z. G. Yang, J. Y. Wang, J. L. Fan, Y. X. He, F. L. Song, B. S. Wang, S. G. Sun, J. L. Qu, J. Qi, M. Yang, *J. Am. Chem. Soc.* **2011**, *133*, 6626-6635.

## **2.2. Investigating the effect of a counterion structure on fluorescent NPs properties.**

### **2.2.1. Counterion-enhanced encapsulation and emission of cationic dyes in polymeric nanoparticles: the role of counterion nature.**

Dye-loaded fluorescent polymer nanoparticles, possessing high brightness and potential biodegradability, are becoming a strong rival of quantum dots in bioimaging applications. Recently we reported<sup>135, 136</sup>, that using bulky hydrophobic anions as counterions for cationic dyes can strongly decrease their aggregation-caused quenching upon encapsulation inside nanoparticles. However, these results were validated for only one counterion, perfluorinated tetraphenylborate. Herein, we tested the limits of *counterion-enhanced emission* approach. We prepared ten ion pairs of R18 with different counterions of different sizes and hydrophobicities, from inorganic perchlorate to fluorinated tetraphenylborate derivatives, and encapsulated them inside biodegradable PLGA (poly(lactide-co-glycolide)) nanoparticles of ~ 40 nm size.

#### **Selection of counterions and characterization of their dye salts.**

The counterions were selected to achieve maximal variability in terms of size and hydrophobicity. Thus, our smallest counterions ( $\text{ClO}_4$  and  $\text{BF}_4$ ) were ~0.33 nm in diameter, whereas the largest one (F12-TPB) was ~1.6 nm (Figure 1). We used 10 counterions in order to achieve gradual variation of the size. As the size was systematically increased using fluorinated groups (except  $\text{B}_{21}\text{H}_{18}$ ), we could consider that increase in the size (i.e. increase in the fluorination level) should directly increase hydrophobicity of the counterion.

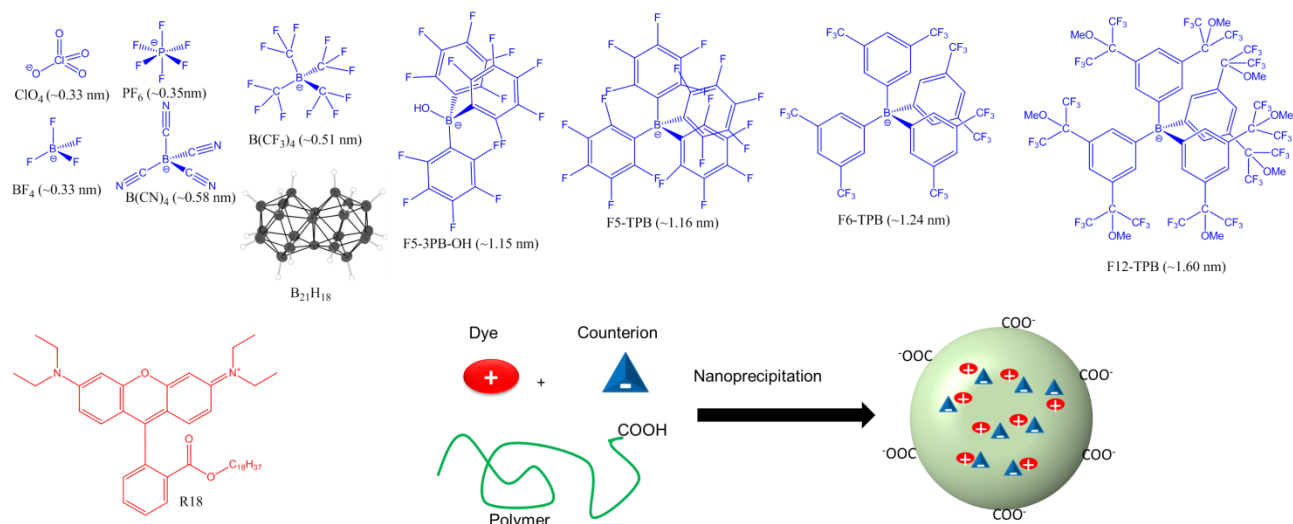


**Figure 1.** Counterions studied for preparation of dye-loaded fluorescent polymeric nanoparticles.

Using these counterions, we prepared the corresponding 10 salts with cationic rhodamine B octadecyl ester (R18). The synthesis of these salts was based on ion exchange, where starting material, R18 salt with  $\text{ClO}_4^-$  anion (R18/ $\text{ClO}_4^-$ ), was mixed in organic solvent (dichloromethane) with excess of an anion of interest. Thin layer chromatography of these salts in dichloromethane revealed remarkable variation of their mobility on silica gel. While R18 salts with  $\text{ClO}_4^-$  and  $\text{BF}_4^-$  did not move on TLC at all,  $\text{PF}_6^-$ ,  $\text{B}(\text{CN})_4^-$  and F5-3PB-OH showed some non-negligible  $R_f$  values (Figure 2A). Much higher mobility was observed for all other studied counterions with  $R_f$  increasing in the following order:  $\text{B}(\text{CF}_3)_4^- < \text{B}_{21}\text{H}_{18} \sim \text{F5-TPB} < \text{F6-TPB} < \text{F12-TPB}$ . Thus, as a general trend, the salts having larger anions and higher values of fluorination showed higher mobility, which could be explained by higher hydrophobicity of these salts. To verify the variation in hydrophobicity of these salts, we studied distribution of the dye salts in a two-phase system composed of three solvents: heptane, acetonitrile and water. In this case heptane and water form, respectively, highly apolar and polar phases, whereas acetonitrile was used to improve the solubility of the dyes salts in water. The obtained logarithm of partitioning constants in this ternary solvent mixture ( $\text{Log}P_{\text{HWA}}$ ) showed gradual changes as a function of counterion (Figure 2B, Table S3). The lowest values were observed for small hydrophilic anions  $\text{ClO}_4^-$  and  $\text{BF}_4^-$ , whereas the highest values were observed for the largest and most fluorinated anions F6-TPB and F12-TPB. Remarkably, for all other anions (excluding  $\text{B}_{21}\text{H}_{18}$ ), the  $\text{Log}P_{\text{HWA}}$  increased gradually with the size and fluorination level of the counterion. We should

note that  $B_{21}H_{18}$ , which does not have fluorines at all, also showed relatively high values of  $\text{Log}P_{\text{HWA}}$ , between those of F5-TPB and F5-3PB-OH, which shows that these boron clusters are also remarkably hydrophobic. The  $\text{Log}P_{\text{HWA}}$  values correlated well with the  $R_f$  values obtained from TLC, namely higher  $R_f$  values usually corresponded to higher values of  $\text{Log}P_{\text{HWA}}$ . The only exception was F5-3PB-OH, which showed unexpectedly low  $R_f$  values, probably due to chemical interactions with OH groups of silica. Overall, our TLC and two-phase distribution studies showed that larger and more fluorinated counterions form significantly more hydrophobic salts with R18 dye, which should affect their further encapsulation into hydrophobic polymer matrix of nanoparticles.

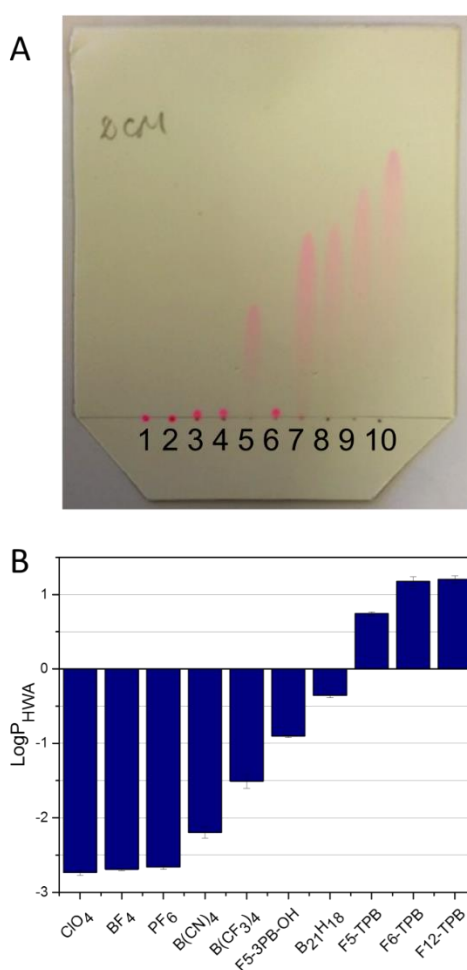


**Figure 2.** (A) Thin layer chromatography plate of all tested ion pairs, run with DCM as eluent. 1) R18/ClO<sub>4</sub>, 2) R18/BF<sub>4</sub>, 3) R18/PF<sub>6</sub>, 4) R18/B(CN)<sub>4</sub>, 5) R18/B(CF<sub>3</sub>)<sub>4</sub>, 6) R18/F5-3PB-OH, 7) R18/B<sub>21</sub>H<sub>18</sub>, 8) R18/F5-TPB, 9) R18/F6-TPB, 10) R18/F12-TPB.  
(B)  $\text{Log}P_{\text{HWA}}$  values of the tested ion pairs.

## Dye-loaded NPs and their properties

On the next step we performed encapsulation of all 10 dye salts into PLGA polymer nanoparticles. As we showed earlier, relatively small PLGA NPs can be obtained by precipitating an organic solvent solution of hydrophobic polymer with one or several charged groups into an aqueous phase<sup>135, 136</sup>. In this case, the charged groups on the polymer chains (carboxylate in case of PLGA) drive the formation of stable NPs suspension with negative surface charge. Adding a hydrophobic dye to a solution of polymer in acetonitrile leads to dye encapsulation inside polymer NPs during nanoprecipitation. The PLGA particles were formulated with different R18 dye salts at 5 and 50 mM loading with respect to the polymer. Size of the particles, loaded at 50 mM, as estimated by DLS, was relatively large for all small hydrophilic counterions (such as ClO<sub>4</sub>, BF<sub>4</sub>, PF<sub>6</sub> and B(CN)<sub>4</sub>), ranging from 100 to 400 nm (Figure 3, Table S2). In sharp contrast, all other counterions showed much smaller particle sizes around 40-50 nm, with some deviation for F5-3PB-OH, showing somewhat larger particle size (~60 nm). Remarkably, for much lower dye loading (5 mM), the sizes of NPs remained small for all the studied counterions (Table S1). These data suggest that high loading of dyes salts with small hydrophilic counterions produces aggregation of NPs. Previously, we showed this phenomenon only for R18/ClO<sub>4</sub> salt. That time it was hypothesized that R18, having a cationic centre and a long hydrocarbon chain, is amphiphilic and therefore may partially adsorb to the particles surface and neutralize their negative charge, which results in aggregation of NPs. Here, similar phenomenon is probably observed for all four small hydrophilic anions. To clarify this issue, we studied encapsulation efficiency of dye salts inside NPs. However, dialysis of all 50 mM dye-loaded NPs in milli-Q water did not produce any change in the dye content in the NPs suspension (not shown). This was expected, because independently of the anion, R18 salt is poorly soluble in water and would probably remain adsorbed to the NPs surface even in the cases of poor encapsulation. As it is well-known that cyclodextrins can encapsulate hydrophobic molecules into their hydrophobic inner cavity, we tested the ability of beta-cyclodextrin to dissolve aggregates of pure R18/ClO<sub>4</sub> in water. We found that in the presence of 1 mM concentration of cyclodextrin the absorption spectra of ~2 μM solution of R18/ClO<sub>4</sub> in water loses its usual shape, typical for aggregates, and becomes that of a dye in molecular form. Therefore, we used aqueous beta-cyclodextrin solution as a recipient medium to

effectively complex nonencapsulated R18, detaching it from particles surface and transferring to aqueous phase. In this case we could see, that after dialysis the amount of the remaining dye fraction (encapsulation efficiency) depended strongly on the nature of the counterion. Indeed, the lowest dye loading was observed for the small hydrophilic counterions  $\text{ClO}_4$ ,  $\text{BF}_4$ ,  $\text{PF}_6$  and  $\text{B}(\text{CN})_4$ , whereas the best loading was observed for the most hydrophobic bulky counterions (Figure 3, Table S2). These results confirm our hypothesis about the adsorption of R18 ion pairs with hydrophilic counterion on the particles surface, which could be the main reason for NPs aggregation, observed in DLS measurements as enlargement of particles sizes. On the other hand, it becomes clear that counterion hydrophobicity plays a crucial role in the encapsulation of the cationic dye inside PLGA NPs, because high loading correlates well with high values of  $\text{LogP}_{\text{HWA}}$  and  $R_f$  of the most hydrophobic anions.

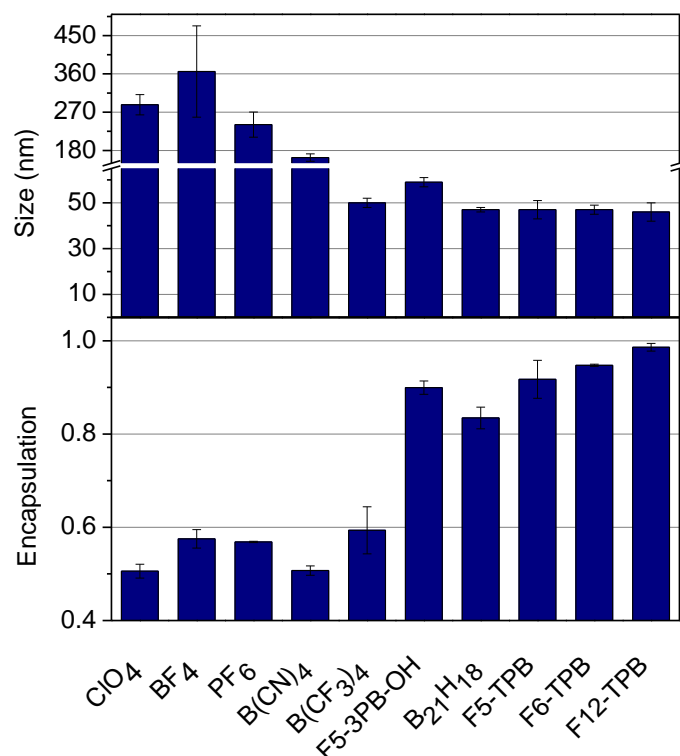


**Figure 3.** Size of dye-loaded PLGA NPs and encapsulation efficiency of R18 salts with different counterions. Both correspond to 50 mM dye loading.

Then we studied the fluorescence properties of the obtained dye-loaded NPs. Despite the quantum yield was high for 5mM-loaded NPs independently on counterion (Table S1), a clear dependence of the fluorescence quantum yield on the counterion

nature was observed for 50 mM-loaded NPs (Figure 4, Table S2). The lowest values of QY were observed for small hydrophilic anions, whereas the highest values corresponded to the most hydrophobic and bulky anions, namely B<sub>21</sub>H<sub>18</sub>, F5-TPB, F6-TPB, F12-TPB. These results corroborate with our earlier report showing that R18 salt with F5-TPB counterion is much less quenched in PLGA NPs than R18 salt with ClO<sub>4</sub>. Here, we show this tendency for a large range of anions, which suggests that bulky and hydrophobic nature is a key to high fluorescence quantum yield of the encapsulated dye. It is clear that bulky hydrophobic counterion plays a role of spacer for the cationic rhodamine dye, thus preventing formation of non-fluorescent aggregates due to pi-pi stacking. On the other hand, these results also suggest that fluorination of the counterion is important, but not absolutely required condition, because very good quantum yields were also obtained for B<sub>21</sub>H<sub>18</sub> anion, which has no fluorines at all. Based on its high LogP<sub>HWA</sub> and R<sub>f</sub> values, we could speculate that its combination of high hydrophobicity and large size are crucial to achieve effective prevention of aggregation-caused quenching. In this respect, B(CF<sub>3</sub>)<sub>4</sub> anions exhibits intermediate values of QY, probably due to intermediate values of size and hydrophobicity in comparison to other studied anions. It is important to note that purification of these NPs by dialysis in the presence of beta-CD improves quantum yields for all small hydrophilic anions, although the obtained QY values never reached those for the best counterions (Figure 4, Table S2). We expect that poorly encapsulated fraction of dyes, which is probably located at the NPs surface, exists in aggregated, weakly emissive state and can further quench the rest of the particle. Therefore, removal of this dark fraction of the dyes improves QY of NPs. Importantly, this purification procedure does not change QY values of bulky hydrophobic anions, probably because the fraction of poorly encapsulated dyes is too small, as suggested by the encapsulation efficiency data.

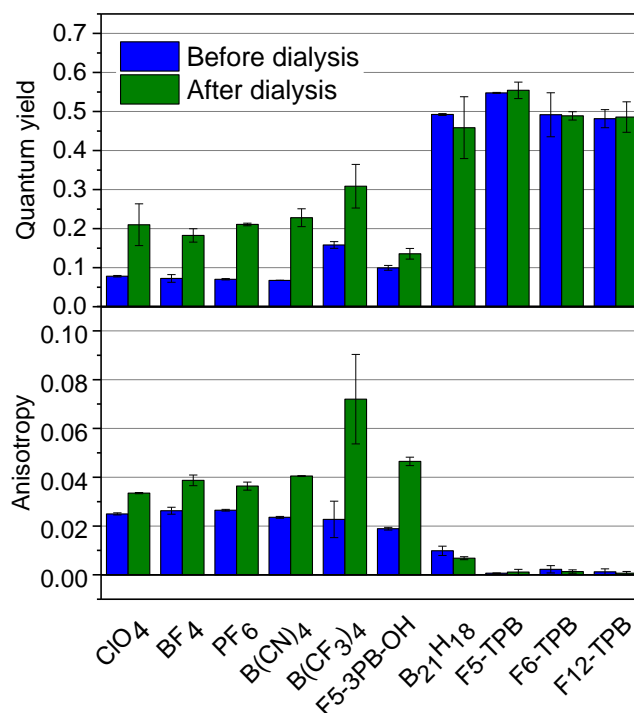


**Figure 4.** Quantum yield and fluorescence anisotropy of the tested dye-loaded PLGA NPs at 50 mM dye loading.

When dyes are localized in a close proximity within the polymer, they may start communicating through energy transfer between the same fluorophores, which is called excitation energy transfer (EET). This process can be readily monitored by fluorescence anisotropy, because EET leads to loss of anisotropy<sup>135</sup>. In the rigid polymer matrix, where fluorophores do not undergo molecular rotation, EET is the only mechanism of the anisotropy loss. The lower are the values of anisotropy, the larger population of dyes is involved in EET. Our data show that extremely low values of anisotropy were observed only for four counterions: F6-TPB, F6-TPB and F12-TPB and B<sub>21</sub>H<sub>18</sub> (Figure 4, Table S2). For all other counterions, the anisotropy value was an order of magnitude higher. Moreover, for these anions the purification by dialysis further increased the anisotropy. This effect was especially pronounced for B(CF<sub>3</sub>)<sub>4</sub>, so that the value reached 0.071, which was ~100-fold higher than those observed for three fluorinated tetraphenylborate counterions. This result underlines that the counterion can strongly alter organization of dyes inside polymer matrix. Thus, for tetraphenylborate counterions, in line with our original work on F5-TPB<sup>135</sup>, the counterions tend to organize the dyes in form of clusters where the dyes undergo very

fast EET. Our recent work suggested, that with F5-TPB EET can undergo on the time scale  $\leq 30$  fs. In sharp contrast, less hydrophobic anions, including  $B(CF_3)_4$ , tend more to disperse dyes within the matrix in molecular form, which decreases their interfluorophore communication, thus explaining the observed much higher anisotropy values.

### **Single-particle emission properties**

On the next step we deposited the dye-loaded NPs onto a glass surface and studied their fluorescence at the single molecule level using wide-field fluorescence microscopy. NPs with small hydrophilic anions as counterions were not tested because they produced particle aggregation. Fluorescent particles were observed as bright spots, distributed randomly within an image (Figure 5A). The best quality images were obtained for  $B_{21}H_{18}$ , F5-TPB, F6-TPB and F12-TPB (Figure 5A and Figure S1), where particles appeared bright on a relatively dark background. By contrast, for  $B(CF_3)_4$  the background signal was significantly higher, probably because some fraction of poorly encapsulated dyes desorbed from particles, producing some background noise. Moreover, the images of quantum dots remained relatively dim despite the use of even higher excitation power, showing that all our NPs are much brighter than QDs. Analysis of single particle brightness revealed that at two different excitation power densities, the brightest particles were those containing F5-TPB and F12-TPB counterions, whereas the lowest brightness corresponded to F5-3PB-OH. All these NPs were 20-40 fold brighter than QD585 particles at the same instrumental settings. Previous studies showed, that high brightness of NPs was achieved using R18 salt with F5-TPB counterion. Here, we show that other counterions can operate similarly to F5-TPB. Particularly interesting are  $B_{21}H_{18}$  and  $B(CF_3)_4$ . The former is an example of a non-fluorinated anion, while the latter is a fluorinated anion of much smaller size compared to F5-TPB. These results show that variety of hydrophobic anions could be used in preparation of bright dye-loaded NPs.

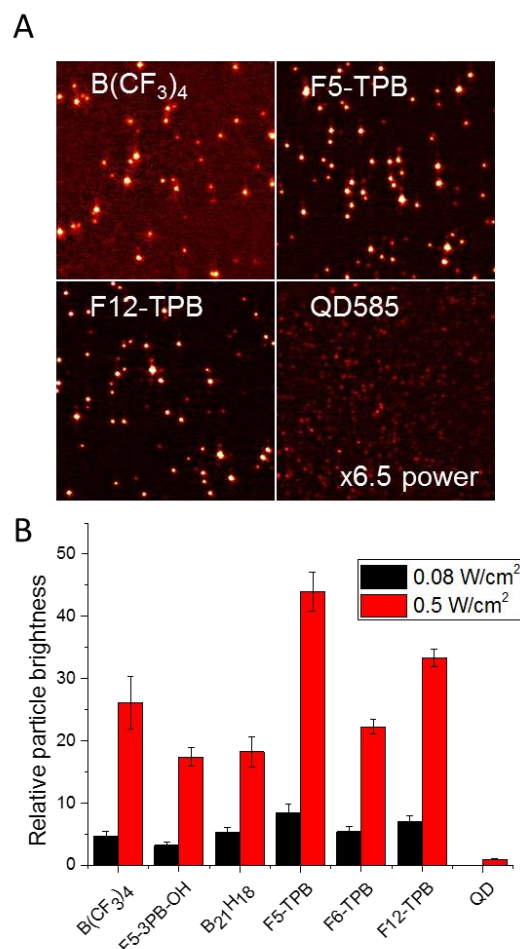


**Figure 5.** Single-particle characterization of dye-loaded polymer NPs by wide-field fluorescence microscopy. (A) Microscopy images of some of the dye-loaded polymer NPs in comparison to quantum dots QD585. Excitation wavelength was 532 nm with power density of 0.08 W/cm<sup>2</sup> (0.5 W/cm<sup>2</sup> for QDs). Integration time was 305 ms. (B) Single-particle brightness dye-loaded polymer NPs measured from microscopy images for two different excitation power densities. The values are relative to the brightness of a single QD585 at 0.5 W/cm<sup>2</sup>. Errors are standard deviation of the mean for 3 images. At least 200 particles per image were analysed in each condition.

Next, we analysed the fluorescence intensity of single particles as a function of time. With some counterions, such as B(CF<sub>3</sub>)<sub>4</sub> and F5-3PB-OH, NPs showed stable fluorescence, whereas for all others a complete ON/OFF switching was observed (Figure 6). The latter was previously reported for F5-TPB, and was assigned to unprecedented communication of R18 dyes, assembled inside polymer matrix by F5-TPB counterion. The counterion plays a role of both a spacer, which prevents dyes from ACQ, and a glue, which brings the dyes together and ensures fast EET. In these conditions any transient dark species inside a particle can quench the entire particle.

Here, we showed that this unique ON/OFF switching behaviour of a large dye ensemble is realized for different types of counterions: three from fluorinated tetraphenylborate family and one is a borohydride cluster. Even more important is the observation of complete absence of the ON/OFF switching behaviour for  $B(CF_3)_4$  and F5-3PB-OH. In both cases, the size of these anions is significantly smaller and they are significantly less hydrophobic (i.e. lower  $\text{Log}P_{\text{HWA}}$  and  $R_f$  values) compared to the tetraphenylborates. The absence of blinking also matches well with the high values of fluorescence anisotropy observed for these two counterions (Figure 4, Table S2), confirming that for these anions the dye-dye communication through EET is clearly less efficient as compared to the fluorinated TPBs. Thus, by varying the counterion nature we could tune the stability of the NPs emission from complete ON/OFF switching to stable emission.

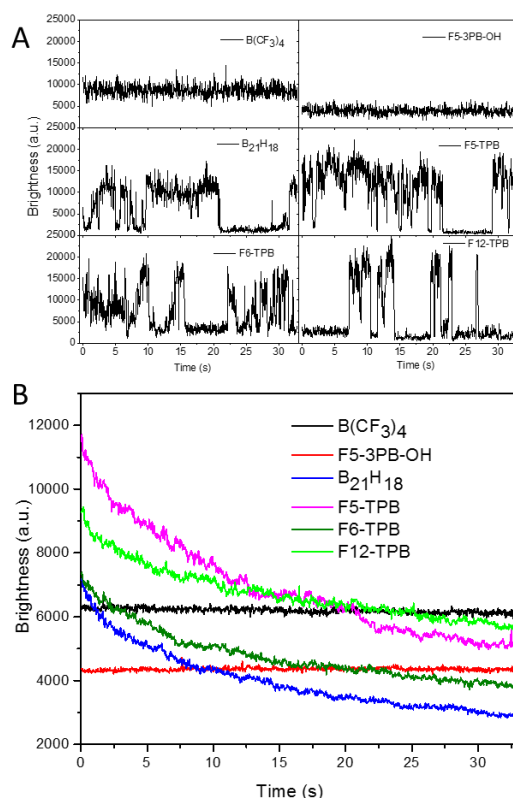


**Figure 6.** Single particle emission traces (A) and photostability (B) of dye-loaded NPs containing R18 dye salts with different counterions, studied under wide-field microscopy.

(A) Fluorescence intensity traces of representative single NPs recorded at integration time of 30.5 ms. Excitation wavelength was 532 nm with power density of  $0.08 \text{ W/cm}^2$ . (B) Fluorescence intensity recorded for all particles within an image as a function of time.

Photostability of these NPs was also monitored with the same wide-field setup by recording the average fluorescence intensity of all detected NPs as a function of time (Figure 6). These studies revealed that all NPs, demonstrating ON/OFF switching behaviour, showed continuous decay of fluorescence, clearly due conversion of the NPs into the dark state. In all these cases, dark species accumulate within the particles, which further leads to complete loss of their fluorescence. In sharp contrast, NPs containing  $B(CF_3)_4$  and F5-3PB-OH that did not show any ON/OFF switching behaviour, but showed stable fluorescence without clear signs of fluorescence decay. These results show that the less hydrophobic counterions do not favour dye-dye energy transfer and ensure higher photostability for their NPs.

### **Cellular studies**

Finally, we incubated our NPs with living cells in order to evaluate their compatibility with cell imaging applications. In this case we tested NPs with all the counterions, including small hydrophilic ones, to see if their poor encapsulation capacity would influence the cell staining profile. Fluorescence confocal images of KB cells, incubated with NPs, showed dramatic difference for NPs containing different counterions and dye loading (Figure 7, Figure S2). Indeed, for NPs containing bulky hydrophobic perfluorinated TPBs, dotted fluorescence of NPs was observed inside the cells. However, for F5-TPB NPs at high loading some background fluorescence could also be observed, probably because some small fraction of poorly encapsulated dyes could be released from NPs into cell interior. On the other hand, for all other counterions the situation was much more dramatic. It concerned especially small hydrophilic anions where continuous fluorescence was observed all over cells without any signs of particle fluorescence. For the intermediate case of NPs containing  $B(CF_3)_4$ , F5-3PB-OH and  $B_{21}H_{18}$ , both continuous fluorescence and dotted fluorescence from NPs were observed. These results show that only in the case of perfluorinated TPBs, especially F6-TPB and F12-TB, no leakage was detected, whereas in all other cases, a significant fraction of the dyes was released from NPs inside the cells in form of free dye. This conclusion is in line with our encapsulation studies showing that only fluorinated TPBs exhibit the capacity to encapsulate the cationic R18 dye with nearly quantitative efficiency. Remarkably, encapsulation efficiency of 0.92 in case of F5-TPB was still not enough, as for high loading some dye

release was observed. We further performed the same cell imaging studies using  $B(CF_3)_4$  (Figure S3) and F5-TPB (Figure S4) NPs after purification by dialysis. It could be seen that purification drastically decreased background intracellular emission of the free dye. These results show, that removal of poorly encapsulated fraction of the dyes from NPs can strongly decrease the amount of released dye in biological media.

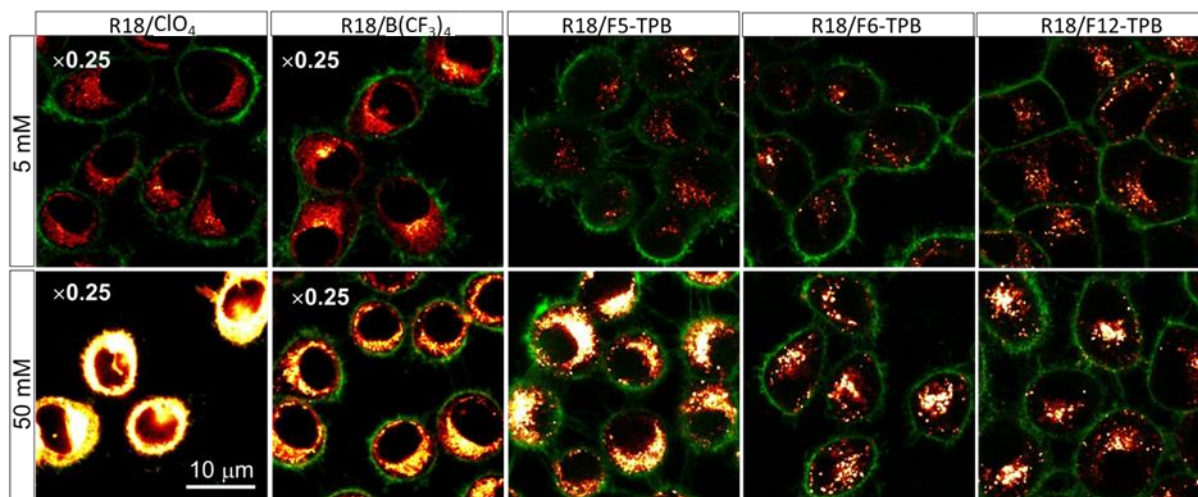


**Figure 7.** Confocal images of KB cells, incubated for 3h with dye-loaded PLGA NPs. NPs were loaded at the concentration of 5 and 50 mM with R18 salts with different counterions. Excitation was done with 561 nm laser, emission was collected from 570 to 650 nm. For R18/ $CIO_4$  and R18/ $B(CF_3)_4$  NPs at both loadings the brightness was decreased 4 times for better visibility. Membranes were stained with wheat-germ agglutinin-Alexa488 (in green). The excitation was done at 488 nm, emission was collected from 500 to 550 nm.

### Role of a counterion in dye encapsulation and emission

Based on all these results we developed a hypothesis about the role of different counterions in the enhanced encapsulation and emission of cationic dye R18 in polymer NPs. During nanoprecipitation of the polymer, encapsulation of dyes is driven by hydrophobic forces that induce dye-polymer and dye-dye association. In case of the more hydrophobic counterions, the obtained salts have higher hydrophobicity, as evidenced from the high values of their  $\text{LogP}_{\text{HWA}}$  and  $R_f$ . These salts will have the strongest tendency to interact with hydrophobic matrix of PLGA polymer, thus explaining their better encapsulation. However, as shown in our recent work, R18/F5-TPB is so hydrophobic that it might precipitate even faster than PLGA, which may result in formation of clusters of this dye salt, followed by formation of the polymer matrix around this cluster. In the present study this is probably the case for the four most hydrophobic and bulky anions, namely  $B_{21}H_{18}$ , F5-TPB, F6-TPB and F12-TPB.

Formation of dye clusters is supported by a remarkably low fluorescence anisotropy and ON/OFF switching, which shows very efficient dye-dye communication. Moreover, nearly quantitative encapsulation and drastically decreased release in cells show that these dye salts are deeply embedded inside the particle core, in line with our assumption of the core-shell organization of these NPs (Figure 8). On the other hand, for all other counterions, the dye salts are much less hydrophobic, as could be seen from the  $\text{LogP}_{\text{HWA}}$  and  $R_f$  data. In these cases, polymer could precipitate at the same time or even faster than the dye salt, thus resulting in some fraction of the dyes being located at the surface of polymer NPs. In case of the smallest and most hydrophilic dye salts, this resulted in a large fraction of dyes being at the NPs surface, decreasing surface charge and NPs colloidal stability (Figure 8). The latter leads to aggregation of NPs, as was evidenced by DLS.

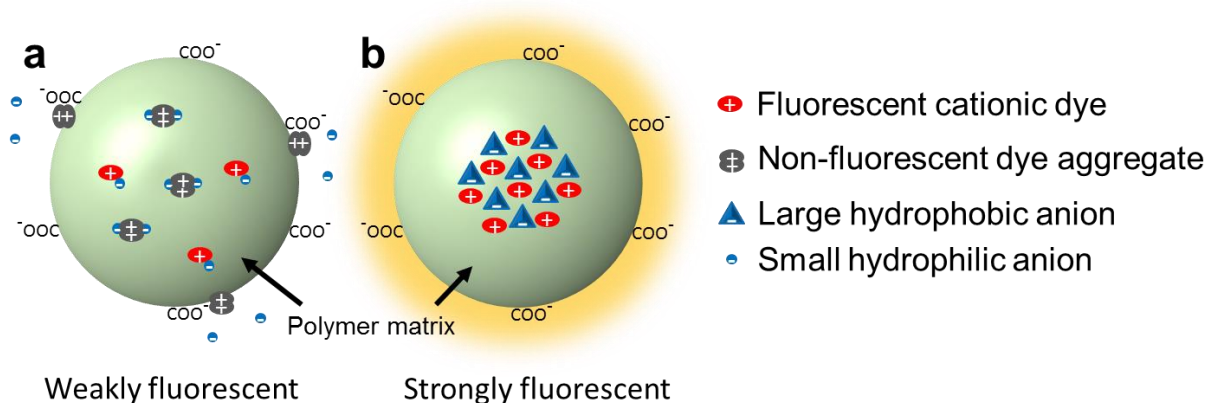


**Figure 8.** Scheme of proposed models of R18 dye distribution inside PLGA NPs for a) for ion pairs with small hydrophilic counterions, like  $\text{ClO}_4$  and b) ion pairs with large hydrophobic counterions, like fluorinated tetraphenylborates.

For other counterions with intermediate properties, such as  $\text{B}(\text{CF}_3)_4$  and F5-3PB-OH, despite not perfect encapsulation, the hydrophobicity of counterion was enough to create stable ion pairs with cationic R18 dye. This stability of the formed ion pairs prevents R18 from associating with surface carboxylates and thus decreasing surface charge, which ensures formation of small and stable nanoparticles. Moreover, for these salts of intermediate hydrophobicity, nanoprecipitation of polymer was probably going with similar speed as encapsulation of the dye, so that in these cases the dyes could be well dispersed inside the polymer matrix (Figure 8). This hypothesis is confirmed by relatively high fluorescence anisotropy as well as total absence of

fluorescence ON/OFF switching. This dispersed distribution ensured maximal dye-dye separation inside the polymer matrix, thus ensuring minimal communication through EET. We could conclude that dispersion of the dye inside the polymer can prevent ON/OFF switching of NPs and ensure their high photostability. Therefore, counterion nature can tune organization of dyes inside the polymer matrix of NPs and thus change their emission from intermittent to stable and continuous. This tuning will help in future to design nanomaterials with desired optical properties. On one hand, NPs with clustered dyes and high EET will be of high interest for superresolution imaging, light harvesting and FRET-based sensing applications. On the other hand, NPs with dispersed dye distribution, showing stable emission, will be of high interest as robust labels for single molecule and single particle tracking and imaging applications.

#### 2.2.1.1 Annex 1: Supplementary information for “Counterion-enhanced encapsulation and emission of cationic dyes in polymeric nanoparticles: the role of counterion nature”.

##### *Supplementary figures*

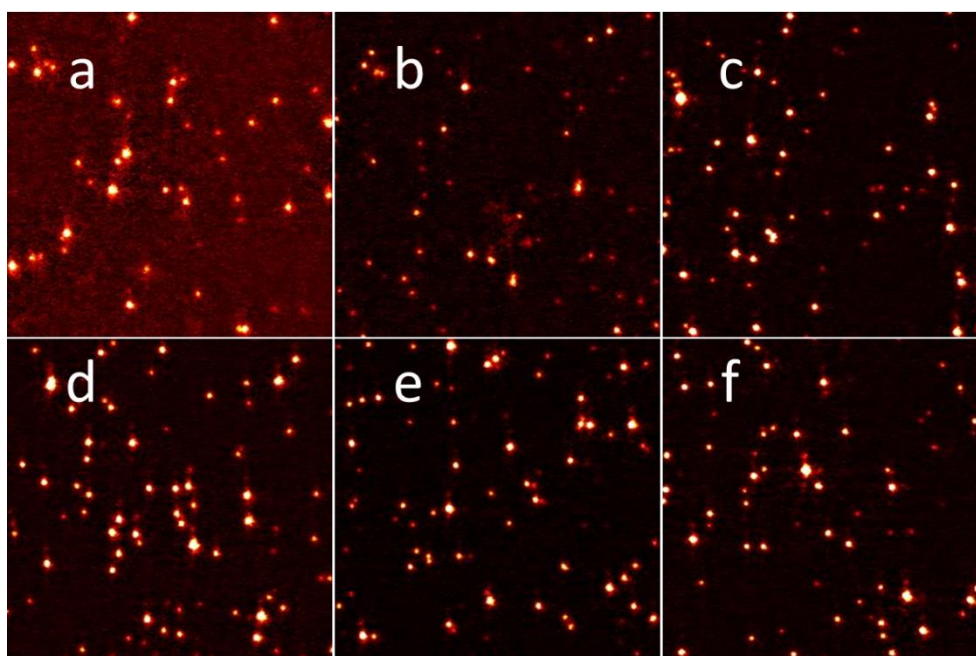


**Figure S1** – Wide-field fluorescence images of 50mM-loaded NPs with R18/B(CF<sub>3</sub>)<sub>4</sub> (a), R18/F5-3PB-OH (b), R18/B<sub>21</sub>H<sub>18</sub> (c), R18/F5-TPB (d), R18/F6-TPB (e), R18/F12-TPB (f). Excitation was done by 532 nm laser at 0.08 W/cm<sup>2</sup> power density. Image size is 27x27 microns.

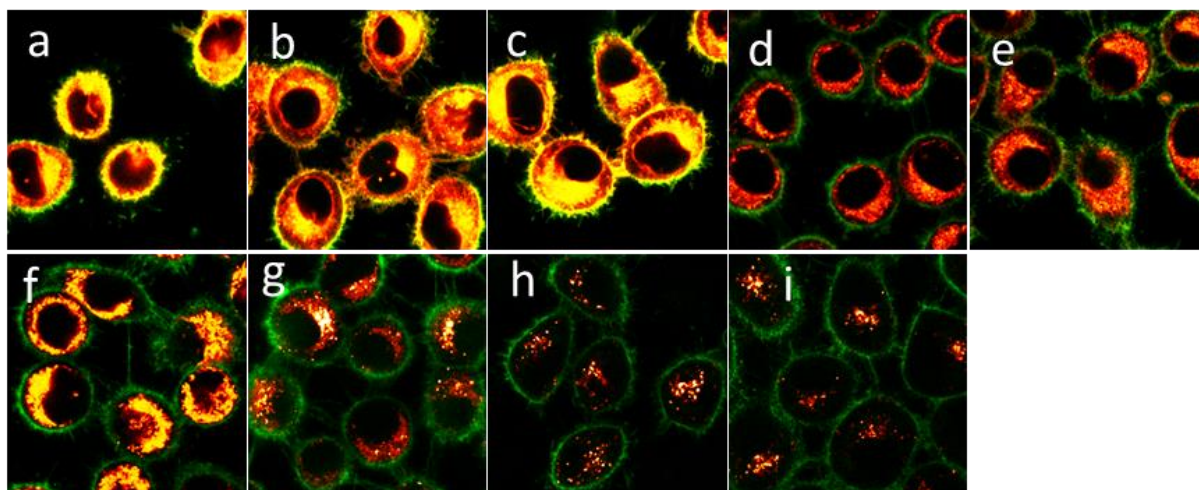


**Figure S2** – Confocal images of KB cells, incubated for 3h with dye-loaded PLGA NPs. NPs were loaded at the concentration of 50 mM with R18/CIO<sub>4</sub> (a), R18/BF<sub>4</sub> (b), R18/PF<sub>6</sub> (c), R18/B(CF<sub>3</sub>)<sub>4</sub> (d), R18/F5-3PB-OH (e), R18/B<sub>21</sub>H<sub>18</sub> (f), R18/F5-TPB (g), R18/F6-TPB (h), R18/F12-TPB (i). Excitation was done with 561 nm laser, emission collected from 570 to 650 nm. For images (a-f) the intensity of NPs channel was divided by two for better visibility. Membranes were stained with wheat-germ agglutinin-Alexa488. The excitation was done at 488 nm, emission was collected from 500 to 550 nm.

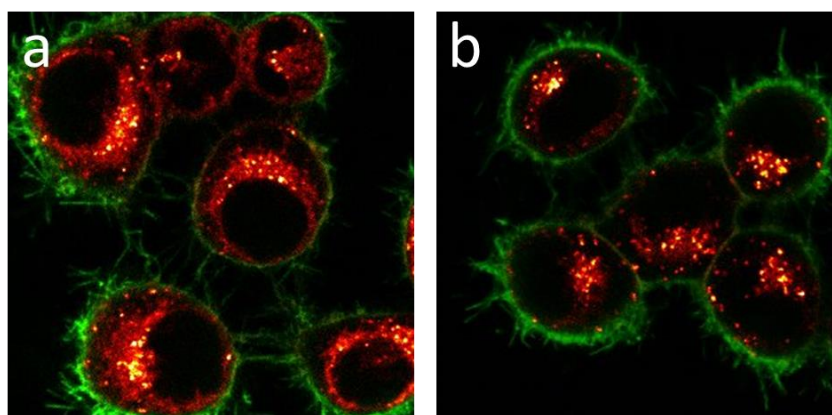


**Figure S3** - Confocal images of KB cells, incubated for 3h with 50 mM R18/B(CF<sub>3</sub>)<sub>4</sub>-loaded PLGA NPs before dialysis with 1mM cyclodextrin (a) and after dialysis (b). Excitation was done with 561 nm laser, emission collected from 570 to 650 nm. Membranes were stained with wheat-germ agglutinin-Alexa488.

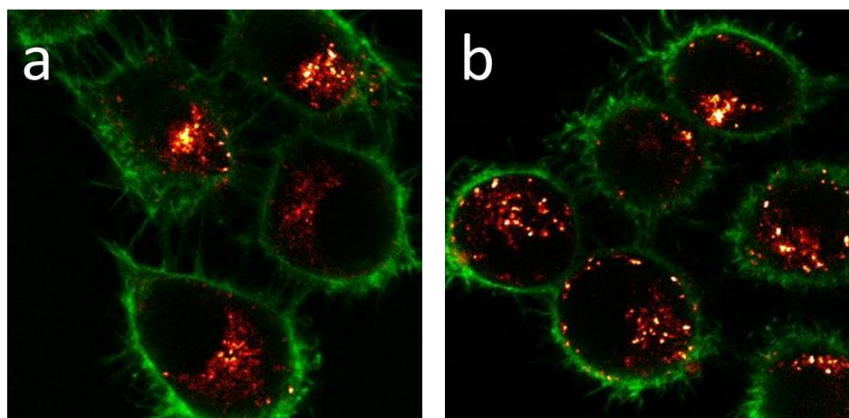


**Figure S4** - Confocal images of KB cells, incubated for 3h with 50 mM R18/F5-TPB-loaded PLGA NPs before dialysis with 1mM cyclodextrin (a) and after dialysis (b). Excitation was done with 561 nm laser, emission collected from 570 to 650 nm. Membranes were stained with wheat-germ agglutinin-Alexa488.

### Supplementary tables

Counterion used in NP preparation	Quantum yield before dialysis	Stdev	Size (nm)	Stdev (nm)	PDI	Stdev
ClO <sub>4</sub>	0.81	0.01	48	1	0.05	0.02
BF <sub>4</sub>	0.66	0.06	42	1	0.05	0.04
PF <sub>6</sub>	0.70	0.05	43	1	0.03	0.03
B(CN) <sub>4</sub>	0.76	0.01	44	1	0.06	0.02
B(CF <sub>3</sub> ) <sub>4</sub>	0.51	0.01	42	1	0.02	0.01
F5-3PB-OH	0.43	0.01	45	1	0.14	0.01
B <sub>21</sub> H <sub>18</sub>	0.78	0.01	43	1	0.21	0.01
F5-TPB	0.94	0.03	47	1	0.15	0.03
F6-TPB	0.91	0.02	44	1	0.13	0.03
F12-TPB	0.87	0.01	42	1	0.03	0.02

**Table S1** – Properties of 5 mM loaded NPs of R18 with different counterions. PDI – polydispersity index.

Counterion used in NP preparation	ClO <sub>4</sub>	BF <sub>4</sub>	PF <sub>6</sub>	B(CN) <sub>4</sub>	B(CF <sub>3</sub> ) <sub>4</sub>	F5-3PB-OH	B <sub>21</sub> H <sub>18</sub>	F5-TPB	F6-TPB	F12-TPB
Quantum yield before dialysis	0.08	0.07	0.07	0.07	0.16	0.1	0.49	0.55	0.49	0.48
Stdev	0.01	0.01	0.01	0.01	0.01	0.01	0.01	0.01	0.06	0.02
Quantum yield after dialysis	0.21	0.18	0.21	0.23	0.31	0.14	0.46	0.55	0.49	0.49
Stdev	0.05	0.02	0.01	0.02	0.06	0.01	0.08	0.02	0.01	0.04
Fluorescence anisotropy before dialysis	0.025	0.026	0.026	0.024	0.023	0.019	0.010	0.001	0.002	0.001
Stdev	0.000	0.001	0.000	0.000	0.007	0.001	0.002	0.000	0.001	0.001
Fluorescence anisotropy after dialysis	0.033	0.039	0.036	0.040	0.072	0.047	0.007	0.001	0.001	0.001
Stdev	0.000	0.002	0.002	0.000	0.018	0.002	0.001	0.001	0.001	0.001
Size (nm)	288	366	241	163	50	59	47	47	47	46
Stdev (nm)	24	107	29	9	2	2	1	4	2	4
PDI	0.14	0.2	0.12	0.04	0.06	0.06	0.09	0.08	0.08	0.08
Stdev	0.04	0.04	0.02	0.03	0.01	0.04	0.03	0.03	0.05	0.03
Dye encapsulation	0.51	0.58	0.57	0.51	0.59	0.9	0.83	0.92	0.95	0.99
Stdev	0.01	0.02	0	0.01	0.05	0.01	0.02	0.04	0	0.01

**Table S2** – Properties of 50 mM loaded NPs of R18 with different counterions. PDI – polydispersity index.

Ion pair	LogP <sub>HWA</sub>	Stdev
R18/CIO <sub>4</sub>	-2.74	0.03
R18/BF <sub>4</sub>	-2.69	0.02
R18/PF <sub>6</sub>	-2.66	0.03
R18/B(CN) <sub>4</sub>	-2.20	0.07
R18/B(CF <sub>3</sub> ) <sub>4</sub>	-1.51	0.09
R18/F5-3PB-OH	-0.90	0.02
R18/B <sub>21</sub> H <sub>18</sub>	-0.36	0.03
R18/F5-TPB	0.74	0.03
R18/F6-TPB	1.18	0.06
R18/F12-TPB	1.21	0.05

**Table S3** – LogP<sub>HWA</sub> of the tested R18 ion pairs

Counterion used in NP preparation	Absorption maximum (nm)	Fluorescence maximum (nm)
CIO <sub>4</sub>	568	587
BF <sub>4</sub>	568	587
PF <sub>6</sub>	565	587
B(CN) <sub>4</sub>	564	587
B(CF <sub>3</sub> ) <sub>4</sub>	559	587
F5-3PB-OH	559	587
B <sub>21</sub> H <sub>18</sub>	560	587
F5-TPB	557	581
F6-TPB	555	580
F12-TPB	555	579
CIO <sub>4</sub> in MeOH	556	577
CIO <sub>4</sub> in phosphate buffer	568	589

**Table S4** – Spectral properties of 50 mM loaded NPs of R18 with different counterions

## 2.2.2. Article 2: Aluminium-based fluorinated counterion for enhanced encapsulation and emission of dyes in biodegradable polymer nanoparticles

Despite high performance of fluorinated derivatives of tetraphenylborates in *counterion-enhanced encapsulation and emission* approach, it is of high interest to substitute them with other counterions, which are simpler in synthesis, cheaper and more bio- and eco-friendly. However, they also must have sufficiently high hydrophobicity and large size to ensure efficient encapsulation of dyes inside nanoparticles and prevent ACQ.

One of the promising candidates was tetrakis[perfluoro-*tert*-butoxy]aluminate (noted **F9-AI**) (Figure 1), which is highly hydrophobic and has similar size with **F5-TPB**. It was synthesized in one step according to a known protocol from inexpensive lithium aluminium hydride and perfluorinated *tert*-butanol.

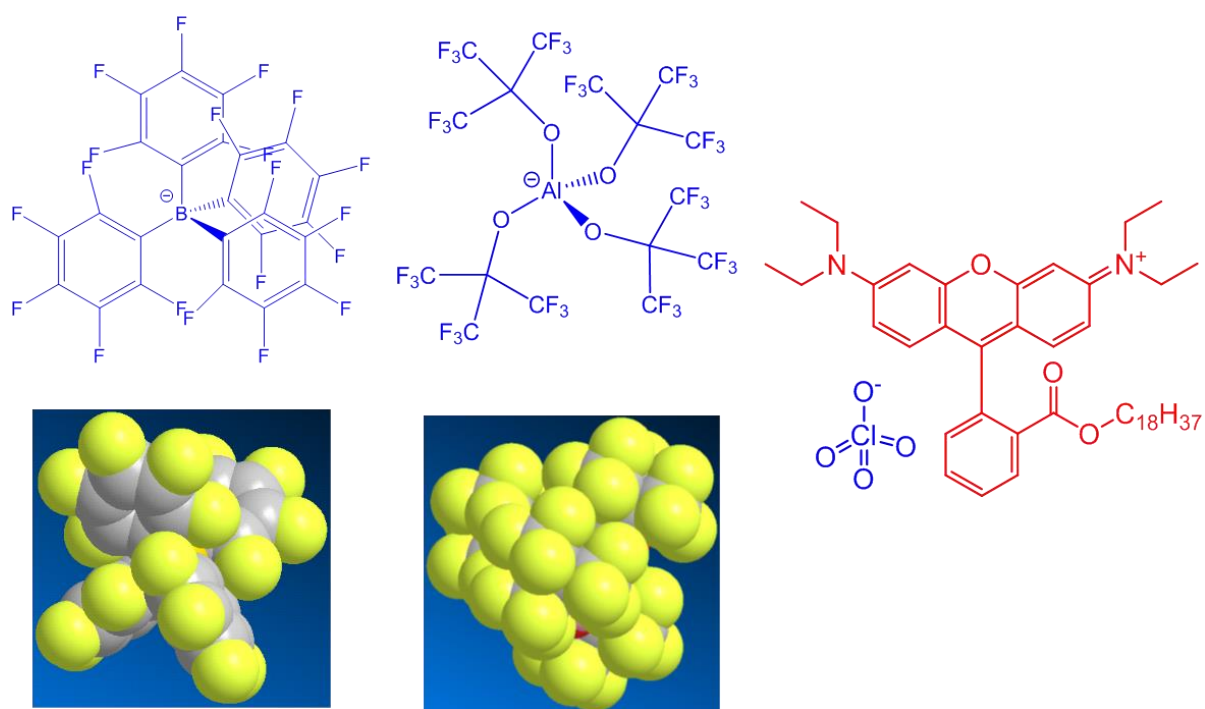


**Figure 1.** Chemical structures and molecular models of counterions used in this study to encapsulate R18 dye inside polymer nanoparticles.

After comparison of nanoparticles, loaded with **R18/F9-AI**, with the ones, loaded with **R18/F5-TPB**, it was found that they have similar size (Figure 2A), quantum yields (Figure 2B), absorption and fluorescence bands, fluorescence anisotropy (Figure 2C),

single particle brightness and they both blink under laser illumination. The only significant difference was observed in encapsulation efficiency of the two ion pairs inside nanoparticles - ~96% for **R18/F9-AI** versus ~92% for **R18/F5-TPB**. This difference becomes important during cell labelling: even at 50 mM loading, particles, loaded with **R18/F9-AI**, demonstrate no dye leaching inside the cells (Fig. 2E), while their **R18/F5-TPB** rivals do show some leaching (Fig. 2D).

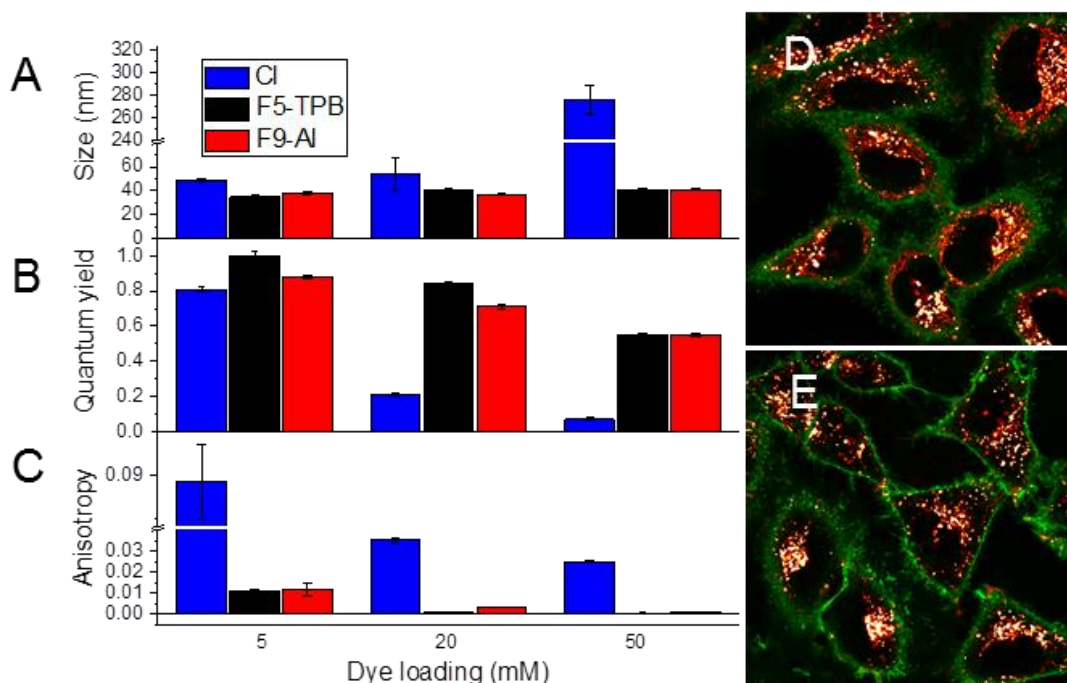


**Figure 2.** (A) Hydrodynamic diameter of NPs loaded with R18 dye and different counterions. (B) Quantum yield of NPs. (C) Anisotropy of NPs. (D,E) Confocal images of HeLa cells, incubated with **R18/F5-TPB**, and **R18/F9-AI** loaded nanoparticles, respectively. Dye loading was 50 mM.

Taking to account all the aforementioned, we can conclude that *counterion-enhanced encapsulation and emission* approach is not limited only to fluorinated derivatives of tetraphenylborate, but can be extended to other types of anions that can even exceed them in properties. Results of the project are under revision in *Materials Chemistry Frontiers* (minor revisions). The manuscript is enclosed below.



## Aluminium-based fluorinated counterion for enhanced encapsulation and emission of dyes in biodegradable polymer nanoparticles

Received 00th January 20xx,  
Accepted 00th January 20xx

DOI: 10.1039/x0xx00000x

www.rsc.org/

Bohdan Andreiuk,<sup>a,b</sup> Andreas Reisch,<sup>a</sup> Vasyl G. Pivovarenko,<sup>b</sup> Andrey S. Klymchenko<sup>\*,a</sup>

Dye-loaded polymer nanoparticles, due to high brightness and potential biodegradability, emerge as a powerful alternative to quantum dots in bioimaging applications. To minimize aggregation-caused quenching of the loaded dyes, we proposed recently to use cationic dyes with bulky hydrophobic counterions (also known as weakly coordinating anions), which serve as spacers preventing dye pi-stacking inside nanoparticles. However, so far this approach of counterion-enhanced emission inside polymer NPs has been limited to one fluorinated tetraphenylborate (tetrakis(pentafluorophenyl)borate, F5-TPB). Herein, we show that the counterion-enhanced emission approach is not limited to tetraphenylborates and can be extended to other types of anions, as the aluminium-based anion Al[OC(CF<sub>3</sub>)<sub>3</sub>]<sub>4</sub><sup>-</sup> (F9-Al), which is much easier to scale up, compared to F5-TPB. It was found that F9-Al strongly improved encapsulation efficiency of rhodamine dye compared to perchlorate as counterion (97±2 vs 51±2 %) and was also slightly better than F5-TPB (92±4 %). Similarly to F5-TPB, F9-Al can effectively prevent aggregation-caused quenching of rhodamine inside NPs made of the biodegradable polymer poly(lactide-co-glycolide) (PLGA) even at 50 mM dye loading. According to single-particle microscopy, the obtained NPs are 33-fold brighter than commercial quantum dots QD585 at 532 nm excitation and exhibit complete ON/OFF switching (blinking), as originally observed for NPs based on F5-TPB. Importantly, NPs loaded with rhodamine/F9-Al ion pair entered the cells by endocytosis, showing no signs of dye leaching, in contrast to rhodamine perchlorate, which exhibits severe leakage from NPs with characteristic accumulation inside mitochondria. Moreover, F9-Al surpassed F5-TPB anion in stability of dye-loaded NPs against leaching, which can be attributed to higher hydrophobicity of the former. Overall, this work shows that counterion-enhanced encapsulation and emission of cationic dyes inside polymer NPs is a general approach for the preparation of stable and highly fluorescent nanomaterials for bioimaging applications.

### Introduction

Fluorescent nanoparticles (NPs) attract strong attention in biological and biomedical research, as they are much brighter than organic dyes and can serve as multifunctional platforms for theranostics. The interest in fluorescent nanoparticles grows rapidly,<sup>1</sup> the most representative ones being quantum dots,<sup>2</sup> dye-doped silica NPs,<sup>3</sup> carbon nanostructures<sup>4</sup> and NPs based on organic materials. Fluorescent organic NPs are an emerging class of functional nanomaterials, which includes conjugated polymer NPs,<sup>5</sup> dye-loaded polymer<sup>6, 7</sup> and lipid<sup>8</sup> NPs, as well as dye-based NPs, notably using aggregation-induced emission dyes.<sup>7, 9</sup> Dye-loaded polymer NPs present several key features, attractive for biological applications.<sup>6</sup> Their polymer matrix can be biodegradable and can serve for

encapsulation of other contrast agents and drugs. The rich variety of available organic dyes makes it possible to prepare dye-loaded NPs of almost any desired spectroscopic characteristics.<sup>10, 11, 12</sup> However, two key challenges remain in the field of dye-loaded NPs. First, at high loading dyes tend to self-quench, which results in poor particle brightness.<sup>6</sup> Second, dye encapsulation can be inefficient and the dye may simply adsorb at the surface of NPs. The latter leads to dye leaching in biological medium, which is detrimental for signal-to-noise ratio in fluorescence microscopy imaging.<sup>13, 14</sup> Several approaches were developed to fight these two problems. The use of long hydrocarbon chains in case of cyanine dyes allowed their efficient encapsulation into polymer NPs and minimal leaching inside cells, although relatively high self-quenching was observed at high dye loading.<sup>15</sup> The use of bulky side groups can significantly decrease self-quenching, as exemplified in the case of BODIPY<sup>16</sup> and perylenediimide<sup>11, 17</sup> derivatives. Aggregation-induced emission (AIE) is a highly popular approach,<sup>9</sup> which gave a variety of examples of organic NPs in recent years.<sup>7, 18, 19</sup> In this case, the dyes are often not dispersed inside the polymer matrix, but form a core, built from pure dyes or their polymerized monomers

<sup>a</sup> Laboratoire de Biophotonique et Pharmacologie, UMR CNRS 7213, University of Strasbourg, 74 route du Rhin, 67401 Illkirch Cedex, France

<sup>b</sup> Organic Chemistry Department, Chemistry Faculty, Taras Shevchenko National University of Kyiv, 01601 Kyiv, Ukraine.

<sup>†</sup> Electronic Supplementary Information (ESI) available: See DOI: 10.1039/x0xx00000x

which is further stabilized by polymeric amphiphiles.<sup>7, 18</sup> A relatively recent approach to prevent aggregation-caused quenching is to use bulky hydrophobic counterions.<sup>6, 10</sup> Many of them belong to the class of weakly coordinating (also called non-coordinating) anions<sup>20</sup> because of their large radius and charge delocalization. The typical examples are derivatives of tetraphenylborate (TPB), tetraalkoxyaluminates, bis(alkylsulfonyl)imides etc. Weakly coordinating anions have been successfully used in catalysis,<sup>21</sup> electrochemistry,<sup>22</sup> stabilization of reactive cations,<sup>23</sup> as components of ionic liquids,<sup>24</sup> microporous materials,<sup>25</sup> lithium batteries,<sup>26</sup> ion-selective electrodes,<sup>27</sup> ion sensors,<sup>28</sup> solar cells<sup>29</sup> and organic light-emitting diodes.<sup>30</sup> Recently, they were proposed for assembly of cationic dyes into fluorescent nanoparticles<sup>31, 32, 33</sup> and ultra-small fluorescent micelles.<sup>34</sup>

However, in biological media these nanomaterials tend to disassemble,<sup>33</sup> which is a strong limitation for their bioimaging applications. Encapsulation of the ion pairs of cationic dyes with such counterions inside a polymer matrix ensures both efficient fluorescence and high stability against dye leaching.<sup>10</sup> Indeed, we recently showed, that fluorinated derivatives of tetraphenylborate, due to their high hydrophobicity, ensured efficient encapsulation of the cationic dye rhodamine inside polymer NPs.<sup>10, 35</sup> Remarkably, only a perfluorinated analogue of TPB, tetrakis(pentafluorophenyl)borate (**F5-TPB**), could efficiently prevent dye self-quenching inside polymer NPs, which allowed preparation of 40-nm NPs that were ~6-fold brighter than quantum dots (QD605) and showed excellent signal-to-noise ratio after entering living cells. Moreover, the obtained NPs showed unprecedented ON/OFF switching (blinking) due to collective behaviour of the dyes, assembled by F5-TPB inside the polymer matrix.<sup>10</sup> This collective behaviour enabled controlled photoswitching of dye-loaded NPs.<sup>36</sup> However, at the moment the approach of *counterion-enhanced encapsulation and emission* of dyes inside polymer NPs is still in its infancy, and it relies exclusively on one

counterion, F5-TPB. The reason is that fluorination in TPB ions is essential for preventing self-quenching of cationic dyes.<sup>31, 33</sup> So, the key question is whether it is possible to extend this unique approach to other anions. The key to broad applications is an easy scale up of the counterion through a straightforward synthesis from inexpensive materials, which is not the case for F5-TPB. Finally, it is also important to replace the aromatic pentafluorophenyl groups of F5-TPB with aliphatic perfluorinated groups in order to understand, whether the aromatic residues are absolutely required to achieve efficient encapsulation and prevent self-quenching of dyes inside NPs.

Herein, we explored the Al-based anion tetrakis[perfluoro-*tert*-butoxy]aluminate (noted **F9-Al**), as potential replacement of F5-TPB. In this anion, four perfluorinated *tert*-butylate groups are coordinated to central aluminium ion (Fig. 1). This anion was described in the literature as a weakly coordinating anion,<sup>37</sup> similarly to F5-TPB.<sup>20</sup> Importantly, this anion can be synthesized in large quantities in one step from inexpensive materials, namely LiAlH<sub>4</sub> and perfluorinated *tert*-butyl alcohol.<sup>38</sup> Our results show that F9-Al perfectly replaces F5-TPB. It ensures more effective encapsulation of rhodamine dyes inside polymer NPs and prevents their self-quenching, especially in comparison with perchlorate, a small inorganic counterion. The obtained NPs are much brighter than reference quantum dots of the same emission colour. Moreover, cellular studies revealed, that at high dye loading Al-based counterion prevents dye leakage better than F5-TPB, indicating that it encapsulates dyes more efficiently. Finally, obtained fluorescent NPs showed minimal cytotoxicity for both F9-Al and F5-TPB counterions. The obtained results propose an easy to scale-up aluminium-based weakly coordinating anion as a highly efficient agent for preparation of bright dye-loaded polymer NPs exhibiting minimized dye self-quenching and leaching.

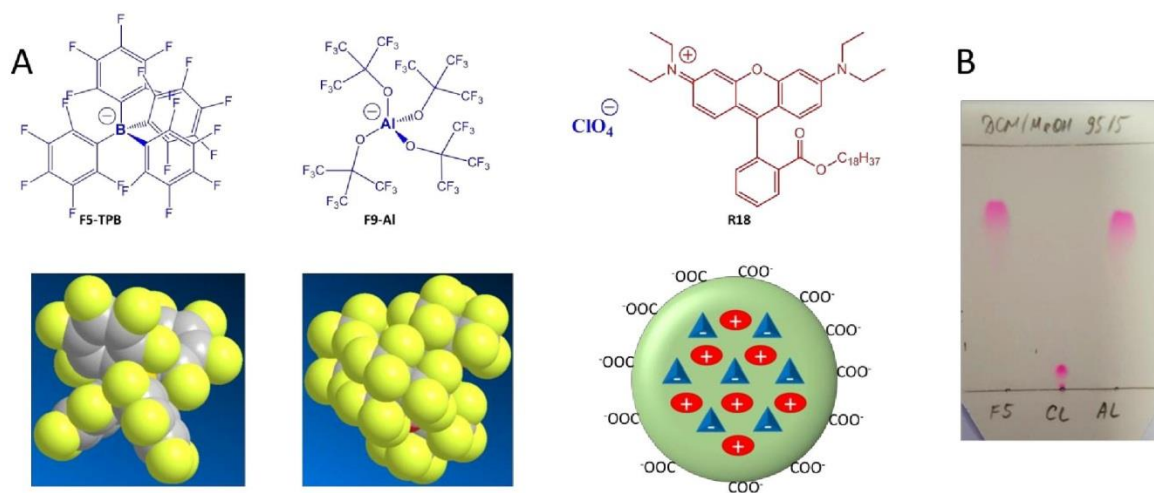


**Fig. 1.** (A) Chemical structures and molecular models of counterions used in this study to encapsulate R18 inside polymer nanoparticles. (B) Thin layer chromatography of R18 dye salts with different counterions: F5-TPB (F5), perchlorate (Cl) and F9-Al (Al). The eluent was dichloromethane/methanol, 95/5.

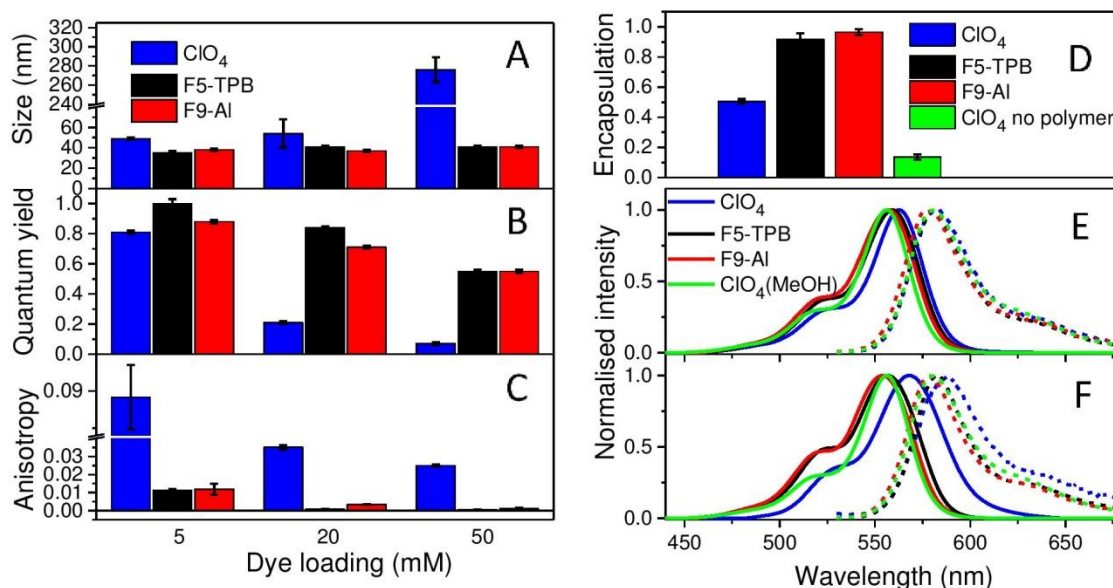


Fig. 2. Characterization of PLGA NPs loaded with R18 and different counterions. Hydrodynamic diameter (A), fluorescence quantum yield (B), fluorescence anisotropy (C) and encapsulation efficiency (D) of NPs. (E,F) Absorption and fluorescence spectra of NPs at 5 (E) and 50 mM (F) dye loading.

## Results and discussion

### Synthesis of dye salts

Basic optimization of the geometry of F9-AI showed that this anion is close in effective diameter to F5-TPB (1.04 vs 1.13 nm). However, F9-AI contains 36 fluorine atoms vs 20 in case of F5-TPB, which leads to their higher density at the surface of F9-AI (Fig. 1A). Li[F9-AI] was synthesized similarly to previous protocols, which consist of reacting LiAlH<sub>4</sub> and perfluorinated *tert*-butyl alcohol.<sup>38, 39</sup> The procedure required gradual increase in temperature to ensure a controlled reaction without rapid evaporation of perfluorinated *tert*-butyl alcohol. Then, the ion pair of Rhodamine B octadecyl ester (**R18**) with F9-AI was prepared similarly to that of F5-TPB: R18 perchlorate (R18/ClO<sub>4</sub>) was mixed with the lithium salt of F9-AI in dichloromethane and the product of the ion exchange was purified by column chromatography. It should be noted, that on thin layer chromatography the ion pair R18/F9-AI showed a much higher R<sub>f</sub> compared to the parent R18/ClO<sub>4</sub>, but nearly the same as R18/F5-TPB (Fig. 1B). According to these results, F9-AI formed stable and highly apolar ion pair with R18 in organic solvents, similarly to F5-TPB.

### Preparation and characterization of NPs

The three different R18 salts with ClO<sub>4</sub>, F5-TPB and F9-AI anions were encapsulated into PLGA NPs. To this end, acetonitrile solutions of PLGA and R18 salts were nanoprecipitated in phosphate buffer (pH 7.4). According to our earlier studies, nanoprecipitation of PLGA at neutral pH should result in small NPs, stabilized by negative charges of deprotonated carboxylate groups of PLGA at the NP's

surface.<sup>10, 35</sup> Indeed, as expected, at low dye loading (5 mM of dye salt with respect to the polymer), small NPs with hydrodynamic diameters of around 40-nm and low polydispersity (~0.1) were obtained according to dynamic light scattering (DLS) for all three dye salts (Fig. 2A, Table S1 in SI). Nevertheless, R18/ClO<sub>4</sub> NPs were slightly larger. Further increase in R18/ClO<sub>4</sub> dye loading significantly increased the size of NPs, reaching ~300 nm at 50 mM loading. Colloidal stability of these NPs was poor, as they precipitated overnight. This is in line with our earlier studies, which suggested that R18 salts with small inorganic counterions, being of amphiphilic nature, tend to accumulate at the NPs surface, where cationic R18 neutralizes negative charges of PLGA carboxylates, thus resulting in NPs aggregation. In sharp contrast, NPs loaded with R18/F5-TPB and R18/F9-AI ion pairs were small independently of dye loading (Fig. 2A). Zeta potential also showed relatively stable negative values for all dye loadings with both F9-AI and F5-TPB anions (Table S1 in SI), indicating that in these cases dye encapsulation did not influence the particle surface properties. These results show that, similarly to F5-TPB, the aluminium-based anion F9-AI is capable of encapsulating dyes without interference with the nanoprecipitation process.

To evaluate quantitatively the efficiency of dye encapsulation into NPs, we developed a protocol to distinguish between encapsulated and adsorbed dyes. In this protocol, the dye-loaded NPs were dialyzed using solution of  $\beta$ -cyclodextrin as recipient medium. As R18 is a hydrophobic molecule poorly soluble in water,  $\beta$ -cyclodextrin, which is known to solubilize hydrophobic molecules,<sup>40</sup> was essential to ensure transfer of poorly encapsulated dyes (i.e. those adsorbed to the NP surface) to the aqueous phase during dialysis. Absorption spectroscopy confirmed that 1 mM  $\beta$ -cyclodextrin can

effectively solubilize R18/CIO<sub>4</sub> in water at micromolar concentration, as the initially broadened absorption band of aggregates of the free dye in water was converted into a narrow band similar to that in organic solvents (Fig. S7 in SI). The dialysis membrane was chosen to be permeable for small molecules, like R18 and  $\beta$ -cyclodextrin, but impermeable for our NPs (MWCO 14000). Then, using absorption measurements of R18 after 24h of dialysis (see Materials and methods for details), we found that both R18/F5-TPB and R18/F9-AI were encapsulated almost quantitatively for the highest (50 mM) loading, with slightly higher efficiency for F9-AI, whereas R18/CIO<sub>4</sub> was encapsulated at only about 50% (Fig. 2D, Table S4 in SI). This result is in good agreement with observations on the NPs size, confirming that a large part of R18/CIO<sub>4</sub> is simply adsorbed at the particle surface. In a control experiment, we used R18/CIO<sub>4</sub> without polymer, and only 13% of remaining dye was observed using the same dialysis protocol (Fig. S8 in SI). To understand the role of the counterion hydrophobicity in the encapsulation of dyes, we studied their partition behaviour in two-phase system formed by heptane/acetonitrile/water mixture. In this case heptane and water form respectively highly apolar and polar phases, whereas acetonitrile was used to improve the solubility of the dyes salts in water. The obtained partitioning constants values for R18/AI-F9, R18/F5-TPB and R18/CIO<sub>4</sub> in this ternary solvent mixture (LogP<sub>HWA</sub>) were 1.43, 0.74 and -2.74, respectively. These differences in hydrophobicity of dyes salts correlate well with encapsulation efficiency, where the most hydrophobic salt R18/AI-F9 shows the most efficient encapsulation. Thus, the encapsulation efficiency of dyes is directly linked to the counterion hydrophobicity.

The fluorescence quantum yield, which is the key parameter of NP brightness, was then evaluated for the obtained NPs (Fig. 2B and Table S2 in SI). As expected, NPs loaded with R18/CIO<sub>4</sub>

displayed a drop in quantum yield from 0.8 to 0.07 on increase in the dye loading from 5 to 50 mM, demonstrating the classical phenomenon of aggregation-caused quenching of rhodamine dyes.<sup>10</sup> This conclusion is also supported by the red-shifted absorption and fluorescence spectra, observed for R18/CIO<sub>4</sub> NPs at 50 mM loading compared to NPs at low loading and the dye in methanol (Fig. 2E,F and Fig. S5 in SI). In sharp contrast, the dye salts R18/F5-TPB and R18/F9-AI displayed significantly lower self-quenching behaviour. Indeed, at the highest dye loading (50 mM) the QY value was 0.55 for both salts. Moreover, the absorption and emission spectra of these NPs were almost the same, and the positions of their maxima were close to those of R18/CIO<sub>4</sub> in methanol (Fig. 2E). These results suggest that the AI-based counterion F9-AI prevents effectively R18 from aggregation-caused quenching, similarly to the boron-based anion F5-TPB. We can conclude that, being close in size to F5-TPB and having even higher fluorination, F9-AI can also serve as a spacer between the cationic rhodamine dyes, thus preventing their  $\pi$ -stacking. It should be noted that so far, only aromatic F5-TPB has been reported to prevent dye self-quenching in polymer NPs.<sup>10, 35</sup> The present result shows that the phenomenon of counterion-enhanced emission in polymer NPs is more general and can be extended to perfluorinated aliphatic AI-based ions.

The other important point is that at high loading dyes may start communicating through excitation energy transfer (EET).<sup>10, 36</sup> The diffusion of energy within randomly oriented fluorophores leads to a loss of fluorescence anisotropy. Earlier, we showed that R18/F5-TPB inside PLGA NPs displayed very low anisotropy even for relatively low dye loading, which suggested that F5-TPB brings dyes in close proximity in the PLGA matrix and thus ensures fast EET.<sup>10</sup> Similarly to R18/F5-TPB, R18/F9-AI displayed much lower anisotropy values inside PLGA NPs in comparison to R18/CIO<sub>4</sub>, a dye salt with small inorganic anion (Fig. 2C, Table S3 in SI). The anisotropy values for R18/F9-AI NPs decreased with dye loading and they were almost the same as for R18/F5-TPB NPs. Thus, the AI-based anion also brings dyes in close proximity within the polymer matrix, which ensures fast EET.

### Single-particle fluorescence

PLGA NPs with the highest tested loading were then deposited on glass surface and further characterized by wide-field fluorescence microscopy. NPs loaded with R18/F5-TPB and R18/F9-AI appeared as dots and their intensities were similar (Fig. 3A,B). NPs loaded with R18/CIO<sub>4</sub> were not tested because of their poor colloidal stability. Remarkably, the mean intensities of R18/F9-AI NPs and of R18/F5-TPB NPs were, respectively, 33-fold and 34-fold higher than that of commercial quantum dots QD585 (Fig. 3A,B). Thus, the F9-AI counterion also enables preparation of NPs that are much brighter than QDs of comparable size, which is an attractive property for bioimaging applications. A remarkable feature of polymer NPs, loaded with R18/F5-TPB, is the ON/OFF switching of the whole particle, caused by collective behaviour of the encapsulated dyes.<sup>10</sup> In the present work, we confirmed the previous data for R18/F5-TPB NPs, as it can be seen from

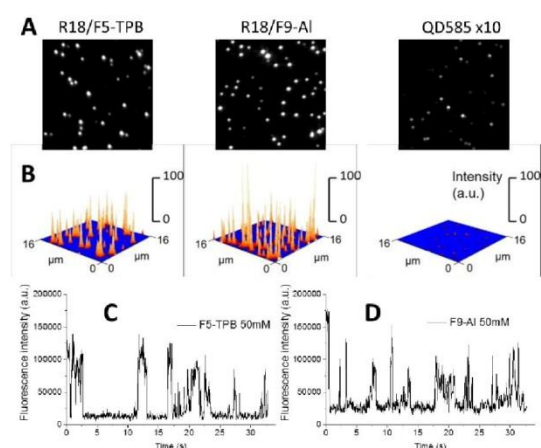


**Fig. 3.** Single-particle fluorescence properties of dye-loaded PLGA NPs. (A,B) Wide-field fluorescence images of different NPs in form of 2D (A) and 3D (B) graphs. In case of 2D image of quantum dots, the intensity was multiplied 10-fold to make the signal visible. All imaging conditions were identical for dye-loaded NPs and QDs. Excitation power density at 532 nm was 0.6 W cm<sup>-2</sup>. (C,D) Representative single-particle traces of NPs loaded with R18/F5-TPB (C) and R18/F9-AI (D), recorded under wide-field microscope. Excitation power density at 532 nm was 0.6 W cm<sup>-2</sup>.

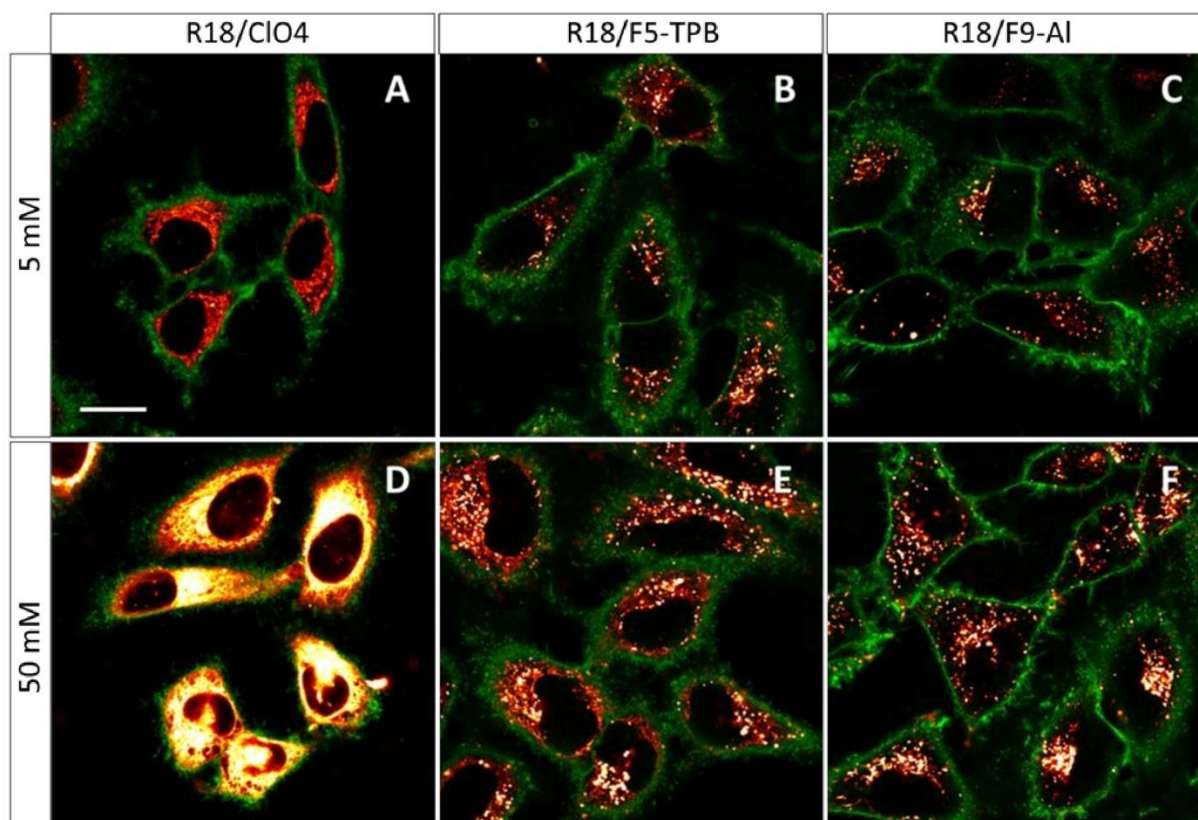


Fig. 4. Laser scanning confocal images of HeLa cells incubated for 3h with dye-loaded PLGA NPs. NPs were loaded with R18/CIO<sub>4</sub>, R18/F5-TPB and R18/F9-AI at 5 and 50 mM concentrations. Excitation wavelength was 561 nm, while the emission was collected from 570 till 650 nm. Image size was 116.8x116.8  $\mu\text{m}$ .

the intensity traces of individual particles (Fig. 3C and Fig. S6 in SI). Importantly, very similar ON/OFF switching was also observed for F9-AI NPs (Fig. 3D and Fig. S6 in SI). Together with the low anisotropy values, observed for this counterion at high dye loading, the switching behaviour of NPs suggests that F9-AI also induces collective behaviour of hundreds of dyes coupled by EET. In this case, a single dark species of encapsulated dyes (*e.g.* their triplet or radical state) within NP can quench all encapsulated dyes within a particle.

#### Cellular data

The obtained NPs at the lowest and highest dye loading were incubated with HeLa cells for 3h. NPs loaded with 5 mM R18/CIO<sub>4</sub> showed continuous fluorescent structures inside the cells, delimited by the membrane marker (WGA-Alexa488 in green, Fig. 4). Very similar images were observed earlier with HeLa cells, stained with free R18 dye, where this cationic dye accumulated inside mitochondria.<sup>33</sup> Thus, without bulky hydrophobic counterions, the dye is not well-encapsulated inside NPs, and therefore upon contact with the cells it is readily released into the cytoplasm. This result is in agreement with our dialysis data, which shows that only 50% of dye is efficiently encapsulated. In sharp contrast, PLGA NPs, containing 5 mM of R18/F5-TPB or R18/F9-AI, appeared in form of bright dots, located inside the cells (Fig. 4). This result is in agreement with our previous work, where PLGA NPs containing 1 wt% R18/F5-TPB (6.3 mM) exhibited minimal dye

leakage after entering cells by endocytosis.<sup>10</sup> The present data suggest that R18/F9-AI also prevents dyes from leakage in the biological medium. Importantly, high dye loading (50 mM) revealed additional differences among the counterions used. While R18/CIO<sub>4</sub> NPs again showed strong dye leaching, observed as continuous intracellular fluorescence, for R18/F5-TPB NPs both particles and continuous extended fluorescent structures were observed (Fig. 4E). This result suggested that at the highest dye loading encapsulation is not complete for R18/F5-TPB ion pair and even the tiny fraction of dye, that is adsorbed to NP surface can lead to significant amounts of nonencapsulated dyes entering the cells. The probable reason here is contact-mediated dye transfer from NP surface to cell membrane, which occurs more effectively than endocytosis of NPs.<sup>14</sup> Remarkably, despite high loading, R18/F9-AI NPs displayed exclusively dotted fluorescence of endocytosed NPs without signs of continuous extended structures. Thus, F9-AI is advantageous over F5-TPB in terms of stability of dye loading against leaching inside the cells, which corroborates with the encapsulation efficiency studies based on dialysis. This property could be attributed to the higher hydrophobicity of R18/F9-AI dye salt vs R18/F5-TPB, which was confirmed in our two-phase partition experiments in the ternary mixture of solvents (see above). It can be explained by higher level of fluorination of F9-AI vs F5-TPB with the “teflon-coated”, extremely hydrophobic surface of the former.<sup>37, 41</sup>

### Cytotoxicity

Finally, we verified the cytotoxicity of our dye-loaded NPs. As R18/CIO<sub>4</sub> NPs were not suitable for bioimaging because of the strong leakage, we did not further study them. All dye-loaded NPs at the highest dye loading showed the same low cytotoxicity as the blank NPs without dye (Fig. 5). Importantly, low values of cytotoxicity were observed even for 0.05 mg/ml of polymer, which is 25-fold higher than the concentration used for cell imaging experiments. Increased cytotoxicity of the highest concentration of polymer (0.084 mg/ml) for both blank and dye-loaded particles could be explained by a significant increase in the concentration of low-salt phosphate buffer (used for NPs preparation) in the growth medium, as compared to cases with lower concentration (0.0005 – 0.05 mg/ml) (see Materials and methods for protocol).

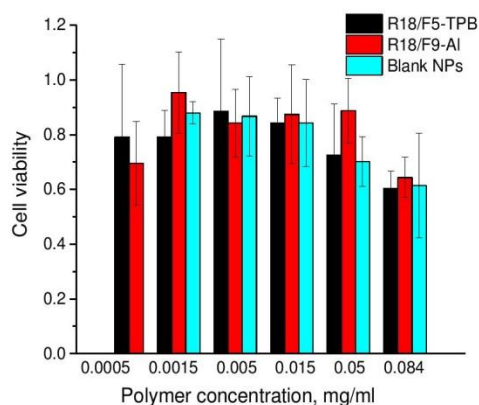


Fig. 5. Viability of HeLa cells incubated with blank and dye-loaded NPs for 24h according to MTT assay. The dye/counterion pairs were loaded at 50 mM concentration.

### Materials and methods

PLGA (lactide 50 mole%, glycolide 50 mole%, Mn 24,000; PDI 1.7), rhodamine B octadecyl ester perchlorate, Lithium aluminium hydride solution (1.0 M in diethyl ether) were purchased from Sigma-Aldrich and used as received. Lithium Tetrakis(pentafluorophenyl)borate-Ethyl Ether Complex (Li/F5-TPB) was purchased from TCI and used as received. Perfluoro-tert-butanol was purchased from Fluorochem and used as received. Toluene was purchased from Alfa Aesar. Sodium phosphate monobasic (99.0%, Sigma-Aldrich) and sodium phosphate dibasic dihydrate (99.0%, Sigma-Aldrich) were used to prepare 20 mM phosphate buffer solutions at pH 7.4. MilliQ-water (Millipore) was used in all experiments. NMR spectra were recorded at 20 °C on Bruker Avance III 400 MHz and Bruker Avance III 500 MHz spectrometers. Mass spectra were obtained using an Agilent Q-TOF 6520 mass spectrometer.

For details of chemical synthesis, see Supporting information.

### Preparation of fluorescent NPs.

PLGA was dissolved at 2 mg/ml concentration in acetonitrile containing different concentrations of dyes. The solutions were rapidly added with a micropipette to a tenfold volume excess of 20 mM phosphate buffer at pH 7.4 and under stirring. The obtained suspension of NPs was then quickly diluted fivefold with the same buffer.

### Characterization of NPs.

DLS measurements were performed on a Zetasizer Nano series DTS 1060 (Malvern Instruments S.A.). Absorption and emission spectra were recorded on a Cary 400 Scan ultraviolet-visible spectrophotometer (Varian) and FluoroMax-4 spectrofluorometer (Horiba Jobin Yvon) equipped with a thermostated cell compartment, respectively. QYs were calculated using rhodamine B in methanol (QY = 0.7)<sup>42</sup> as a reference.

Encapsulation efficiency of dyes inside NPs was measured as the ratio of dye quantity (in moles) in the sample after and before dialysis (MEMBRA-CEL MD34 14x100 membrane, MWCO 14000) in 1 mM beta-cyclodextrin solution according to the following protocol:

450  $\mu$ L of freshly prepared NPs solution was added to 550  $\mu$ L of 1 mM beta-cyclodextrin solution, and the resulting mixture was dialysed for 24 hours with 1 mM beta-cyclodextrin solution as a recipient medium. The mole quantities of the dye inside NPs before and after dialysis were measured using absorption spectroscopy taking into account the volume change during the dialysis.

For control experiment, 20  $\mu$ L of acetonitrile solution of R18/CIO<sub>4</sub> dye were added to 1 ml of 1 mM solution of beta-cyclodextrin in 20 mM phosphate buffer (pH 7.4), and this sample was treated according to the protocol above, showing that 87% of dye gets washed out after 24h dialysis, rest probably being too large aggregates of dye to pass through membrane (see Fig. S8).

### Determination of the partitioning coefficient

To compare hydrophobicities of the ion pairs, a characteristic, similar to conventional LogP (which is applied for octanol/water partition), was introduced. It is a logarithm of the partition of a substance between two phases, heptane as the non-aqueous phase and water / acetonitrile 50/50 as the aqueous phase. It was named LogP<sub>HWA</sub>. In this method, mutually presaturated phases A (heptane), 1 ml, and B (water/acetonitrile 50/50), 1 ml, were placed into an Eppendorf tube, and 10-25  $\mu$ L of acetonitrile solution of a R18-counterion ion pair was added to the mixture. The mixture was vigorously vortexed and then centrifuged to ensure complete phase partition. Then 50  $\mu$ L of each phase was added to 1 ml of ethanol and concentrations of R18 dye in the resulting solutions were measured. In case of R18/CIO<sub>4</sub>, which showed very poor partition into the heptane phase, the absorbance was measured without dilution. LogP<sub>HWA</sub> was calculated as a logarithm of the ratio of dye concentration in phase A to dye concentration in phase B.

**Cellular studies**

**Cell imaging.** HeLa cells (ATCC CCL-2) were grown in DMEM (Gibco–Invitrogen), supplemented with 10% fetal bovine serum (Dominique Dutscher) and 1% antibiotic solution (penicillin–streptomycin, Lonza) at 37 °C in humidified atmosphere containing 5% CO<sub>2</sub>. Cells were seeded onto 8-chambered LabTek at a density of  $2 \times 10^4$  cells per well 24 h before the microscopy measurement. For imaging, the culture medium was removed and the attached cells were washed with Opti-MEM (Gibco–Invitrogen). Next, a freshly prepared solution of 5 and 50 mM loaded NPs of R18/F5-TPB, R18/F9-AI and R18/CIO<sub>4</sub>, prepared as described above, were diluted 20 times in Opti-MEM, added to the cells and incubated for 3 hours. Cell membrane staining with wheat-germ agglutinin–Alexa488 was done for 5 min at room temperature before the measurements.

**Cytotoxicity.** HeLa cells (ATCC CCL-2) were grown in DMEM (Gibco–Invitrogen, without phenol red), supplemented with 10% fetal bovine serum (Lonza), L-glutamine (Gibco–Invitrogen), and 1% antibiotic solution (penicillin–streptomycin, Gibco–Invitrogen) at 37 °C in humidified atmosphere containing 5% CO<sub>2</sub>. For cytotoxicity studies, HeLa cells were seeded in 96-well plates at a concentration of 2000 cells per well in 100 µl of the DMEM growth medium and then incubated overnight. Solutions of NPs for incubation were prepared as follows: NPs in phosphate buffer were diluted to desired concentrations with phosphate buffer, and 20 µl of these solutions were added to 80 µl of Opti-MEM in all cases except the one for the highest polymer concentration (0.084mg/ml). In that case 33 µl of NPs in phosphate buffer were added to 67 µl of Opti-MEM. The NPs were then added by substituting the culture medium with 100 µl of Opti-MEM containing the desired NP concentrations. After 3 h of incubation 100 µl of the DMEM culture medium supplemented with 20% fetal bovine serum were added. The cells were incubated for 48 h in total with the NP solutions. Then the medium was removed and the adherent cell monolayers were washed with PBS. The wells were then filled with cell culture medium containing 1.2 mM MTT (3-(4,5-dimethylthiazol-2-yl)-2,5-diphenyltetrazolium bromide), incubated for 4 h at 37 °C, and the formazan crystals formed were dissolved by removing 85 µl of culture medium per well and adding 50 µl of dimethylsulfoxide followed by shaking for 15 min. The absorbance was then measured at 540 nm and 570 nm with a microplate reader (FLX-Xenius, Safas). Experiments were carried out in triplicate and expressed as the percentage of viable cells compared with the control group that was treated in the same way but not exposed to NPs.

**Conclusions**

Recently, we introduced a concept of *counterion-enhanced emission* of dyes inside polymer nanoparticles using perfluorinated tetraphenylborate (F5-TPB), which enables preparation of ultrabright switchable fluorescent NPs. Here, we show that this concept can be extended to another type of

anions, based on aluminate of aliphatic fluorinated alcohol. In comparison to F5-TPB, the AI-based counterion (F9-AI) is much easier to prepare. Our results show that F9-AI can perfectly replace F5-TPB for dye encapsulation, because it effectively prevents the aggregation-caused quenching and ensures high brightness of NPs and collective behaviour of encapsulated dyes. Importantly, F9-AI enhances encapsulation of rhodamine dyes into PLGA NPs, as they did not show any sign of leakage after entering living cells, in contrast to NPs, loaded with the dye perchlorate salt. Moreover, cellular imaging data suggested that F9-AI encapsulates cationic rhodamine even more efficiently than F5-TPB, which can be assigned to higher hydrophobicity of F9-AI comparing to F5-TPB.

This work proposes an efficient methodology for preparation of highly fluorescent nanomaterials and it opens an important direction in the application of AI-based counterions. Moreover, this work shows, that *counterion-enhanced encapsulation and emission* of cationic dyes inside polymer nanoparticles is a universal approach, extendable to other families of counterions beyond fluorinated tetraphenylborates.

**Conflict of interest**

There are no conflicts of interest to declare.

**Acknowledgements**

This work is supported by the European Research Council ERC Consolidator grant BrightSens 648528. BA is supported by LabEx Chimie des Systèmes Complexes. Prof. Yves Mely and Dr. Pascal Didier are acknowledged for providing access to wide-field microscopy.

**References**

- O. S. Wolfbeis, *Chem. Soc. Rev.*, 2015, **44**, 4743–4768.
- X. Michalet, F. F. Pinaud, L. A. Bentolila, J. M. Tsay, S. Doose, J. J. Li, G. Sundaresan, A. M. Wu, S. S. Gambhir and S. Weiss, *Science*, 2005, **307**, 538–544.
- M. Montalti, L. Prodi, E. Rampazzo and N. Zaccheroni, *Chem. Soc. Rev.*, 2014, **43**, 4243–4268.
- V. N. Mochalin, O. Shenderova, D. Ho and Y. Gogotsi, *Nat. Nanotechnol.*, 2012, **7**, 11–23; P. J. G. Luo, S. Sahu, S. T. Yang, S. K. Sonkar, J. P. Wang, H. F. Wang, G. E. LeCroy, L. Cao and Y. P. Sun, *J. Mater. Chem. B*, 2013, **1**, 2116–2127.
- C. Wu and D. T. Chiu, *Angew. Chem. Int. Ed.*, 2013, **52**, 3086–3109.
- A. Reisch and A. S. Klymchenko, *Small*, 2016, **12**, 1968–1992.
- K. Li and B. Liu, *Chem. Soc. Rev.*, 2014, **43**, 6570–6597.
- V. N. Kilin, H. Anton, N. Anton, E. Steed, J. Vermot, T. E. Vandamme, Y. Mely and A. S. Klymchenko, *Biomaterials*, 2014, **35**, 4950–4957.
- Y. N. Hong, J. W. Y. Lam and B. Z. Tang, *Chem. Soc. Rev.*, 2011, **40**, 5361–5388; J. Mei, N. L. C. Leung, R. T.

- K. Kwok, J. W. Y. Lam and B. Z. Tang, *Chem. Rev.*, 2015, **115**, 11718-11940.
10. A. Reisch, P. Didier, L. Richert, S. Oncul, Y. Arntz, Y. Mely and A. S. Klymchenko, *Nat. Commun.*, 2014, **5**, 4089.
  11. K. Trofymchuk, A. Reisch, I. Shulov, Y. Mely and A. S. Klymchenko, *Nanoscale*, 2014, **6**, 12934-12942.
  12. A. Wagh, F. Jyoti, S. Mallik, S. Qian, E. Leclerc and B. Law, *Small*, 2013, **9**, 2129-2139.
  13. S. Snipstad, S. Hak, H. Baghirov, E. Sulheim, Y. Morch, S. Lelu, E. von Haartman, M. Back, K. P. Nilsson, A. S. Klymchenko, C. de Lange Davies and A. K. Aslund, *Cytometry A*, doi: 10.1002/cyto.a.22853.
  14. H. T. Chen, S. W. Kim, L. Li, S. Y. Wang, K. Park and J. X. Cheng, *Proc. Natl. Acad. Sci. U.S.A.*, 2008, **105**, 6596-6601.
  15. A. Wagh, S. Y. Qian and B. Law, *Bioconjugate Chem.*, 2012, **23**, 981-992.
  16. R. Méallet-Renault, A. Hérault, J.-J. Vachon, R. B. Pansu, S. Amigoni-Gerbier and C. Larpent, *Photochem. Photobiol. Sci.*, 2006, **5**, 300-310; C. Gazon, J. Rieger, R. Méallet-Renault, B. Charleux and G. Clavier, *Macromolecules*, 2013, **46**, 5167-5176.
  17. Z. Tian, A. D. Shaller and A. D. Q. Li, *Chem. Commun.*, 2009, 180-182.
  18. X. Y. Zhang, K. Wang, M. Y. Liu, X. Q. Zhang, L. Tao, Y. W. Chen and Y. Wei, *Nanoscale*, 2015, **7**, 11486-11508.
  19. X. Zhang, L. Tao, Z. Chi, J. Xu and Y. Wei, *J. Mater. Chem. B*, 2014, **2**, 4398-4414; W. Qin, D. Ding, J. Z. Liu, W. Z. Yuan, Y. Hu, B. Liu and B. Z. Tang, *Adv. Funct. Mater.*, 2012, **22**, 771-779; P. Zhang, X. Nie, M. Gao, F. Zeng, A. Qin, S. Wu and B. Z. Tang, *Mater. Chem. Front.*, 2017, **1**, 838-845.
  20. I. Krossing and I. Raabe, *Angew. Chem. Int. Ed.*, 2004, **43**, 2066-2090.
  21. M. Q. Jia and M. Bandini, *Acs Catalysis*, 2015, **5**, 1638-1652.
  22. W. E. Geiger and F. Barriere, *Acc. Chem. Res.*, 2010, **43**, 1030-1039.
  23. T. A. Engesser, M. R. Lichtenthaler, M. Schleep and I. Krossing, *Chem. Soc. Rev.*, 2016, **45**, 789-899.
  24. A. B. A. Rupp and I. Krossing, *Acc. Chem. Res.*, 2015, **48**, 2537-2546; M. Kaliner and T. Strassner, *Tetrahedron Lett.*, 2016, **57**, 3453-3456; I. Raabe, K. Wagner, K. Guttsche, M. K. Wang, M. Gratzel, G. Santiso-Quinones and I. Krossing, *Chem. Eur. J.*, 2009, **15**, 1966-1976.
  25. S. Fischer, J. Schmidt, P. Strauch and A. Thomas, *Angew. Chem. Int. Ed.*, 2013, **52**, 12174-12178.
  26. A. Rupp, N. Roznyatovskaya, H. Scherer, W. Beichel, P. Klose, C. Sturm, A. Hoffmann, J. Tubke, T. Koslowski and I. Krossing, *Chem. Eur. J.*, 2014, **20**, 9794-9804; W. Xu and C. A. Angell, *Electrochem. Solid State Lett.*, 2001, **4**, E1-E4; M. L. Aubrey and J. R. Long, *J. Am. Chem. Soc.*, 2015, **137**, 13594-13602.
  27. E. Bakker, P. Buhlmann and E. Pretsch, *Chem. Rev.*, 1997, **97**, 3083-3132.
  28. X. J. Xie, A. Gutierrez, V. Trofimov, I. Szilagy, T. Soldati and E. Bakker, *Anal. Chem.*, 2015, **87**, 9954-9959.
  29. L. E. Chen, Y. Tan, X. F. Liu and Y. W. Chen, *Nano Energy*, 2016, **27**, 492-498; A. C. Veron, H. Zhang, A. Linden, F. Nuesch, J. Heier, R. Hany and T. Geiger, *Org. Lett.*, 2014, **16**, 1044-1047.
  30. D. X. Ma, C. Zhang, Y. Qiu and L. Duan, *J. Mater. Chem. C*, 2016, **4**, 5731-5738; D. X. Ma, L. Duan and Y. Qiu, *J. Mater. Chem. C*, 2016, **4**, 5051-5058.
  31. H. Yao and K. Ashiba, *RSC Adv.*, 2011, **1**, 834-838.
  32. D. K. Bwambok, B. El-Zahab, S. K. Challa, M. Li, L. Chandler, G. A. Baker and I. M. Warner, *ACS Nano*, 2009, **3**, 3854-3860; A. N. Jordan, S. Das, N. Siraj, S. L. de Rooy, M. Li, B. El-Zahab, L. Chandler, G. A. Baker and I. M. Warner, *Nanoscale*, 2012, **4**, 5031-5038; M. Soulie, C. Frongia, V. Lobjois and S. Fery-Forgues, *RSC Adv.*, 2015, **5**, 1181-1190; W. I. S. Galpothdeniya, F. R. Fronczek, M. Y. Cong, N. Bhattarai, N. Siraj and I. M. Warner, *J. Mater. Chem. B*, 2016, **4**, 1414-1422.
  33. I. Shulov, S. Oncul, A. Reisch, Y. Arntz, M. Collot, Y. Mely and A. S. Klymchenko, *Nanoscale*, 2015, **7**, 18198-18210.
  34. I. Shulov, Y. Arntz, Y. Mely, V. G. Pivovarenko and A. S. Klymchenko, *Chem. Commun.*, 2016, **52**, 7962-7965.
  35. A. Reisch, A. Runser, Y. Arntz, Y. Mély and A. S. Klymchenko, *ACS Nano*, 2015, **9**, 5104-5116.
  36. K. Trofymchuk, L. Prodi, A. Reisch, Y. Mély, K. Altenhöner, J. Mattay and A. S. Klymchenko, *J. Phys. Chem. Lett.*, 2015, **6**, 2259-2264.
  37. I. Krossing and A. Reisinger, *Coord. Chem. Rev.*, 2006, **250**, 2721-2744.
  38. S. M. Ivanova, B. G. Nolan, Y. Kobayashi, S. M. Miller, O. P. Anderson and S. H. Strauss, *Chem. Eur. J.*, 2001, **7**, 503-510.
  39. I. Krossing, *Chem. Eur. J.*, 2001, **7**, 490-502.
  40. E. M. M. Del Valle, *Process Biochem.*, 2004, **39**, 1033-1046.
  41. M. Cametti, B. Crousse, P. Metrangolo, R. Milani and G. Resnati, *Chem. Soc. Rev.*, 2012, **41**, 31-42.
  42. R. A. Velapoldi and H. H. Tonnesen, *J. Fluorescence*, 2004, **14**, 465-472.

## Supporting information

### Aluminium-based fluorinated counterion for enhanced encapsulation and emission of dyes in biodegradable polymer nanoparticles

Bohdan Andreiuk, Andreas Reisch, Vasyl G. Pivovarenko, Andrey S. Klymchenko

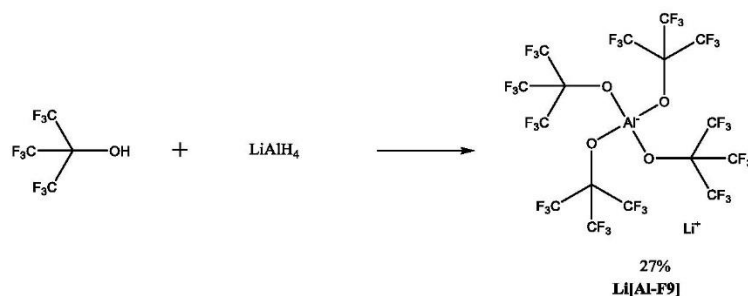
## Chemical synthesis

### R18/F5-TPB

Synthesis of Rhodamine B octadecyl ester tetrakis(pentafluorophenyl)borate (**R18/F5-TPB**) was described previously.<sup>1</sup>

### Li[F9-Al]

Compound was prepared according to a modified protocol.<sup>2</sup>



An oven-dried 250 ml 3-necked flask with a stirring bar was vacuumated and argonated several times, afterwards 1M LiAlH<sub>4</sub> solution in ether (1 eq., 20 mL, 20 mmol) was added through a syringe and the flask was put on a rotavap to evaporate ether. After the liquid was evaporated, temperature of the bath was increased to 80 °C and LAH was left do dry for 2,5 hours more at this temperature. After drying and cooling, the flask was argonated and put to an oil bath on the stirring plate; a reflux condenser and a bubbler outlet were attached. The system was vacuumated and argonated 3 times, and dry toluene (70 mL) was added through a syringe. 3 ml of perfluoro-tert-butanol were added while stirring, but no gas evolution was observed, and reaction mixture was heated to 80°C, when the strong gas evolution started and reaction mixture began to warm itself, so it was taken out of the bath until the reaction mixture calmed down. Afterwards, the flask was put back into an oil bath, and the rest of perfluoro-tert-butanol (11 ml, 5eq in total) was added dropwise.

Reaction mixture was left for 2 hrs at 80 °C and then temperature was risen to 100°C for one hour, afterwards the reaction was left at 50 °C over the weekend.

Afterwards, the reaction mixture was heated up to reflux and hot filtration was performed, separating greyish insoluble powder from toluene solution. Solution was let to cool down, put to freezer, and precipitated white crystals were filtered and washed with cold toluene and dried under vacuum, which yielded 5.23 g (5.37 mmol, 27 %) of **Li[F9-AI]**.

Decreased product yields and weaker reactivity of LAH comparing to original protocol could be explained by insufficiently dry toluene and/or argon.

$^{19}\text{F}$  NMR (376 MHz, DMSO- $d_6$ )  $\delta$  ppm -75.10 (s)

MS (m/z): [M]<sup>-</sup> calcd. for C<sub>16</sub>AlF<sub>36</sub>O<sub>4</sub>, 966.904; found 966.815

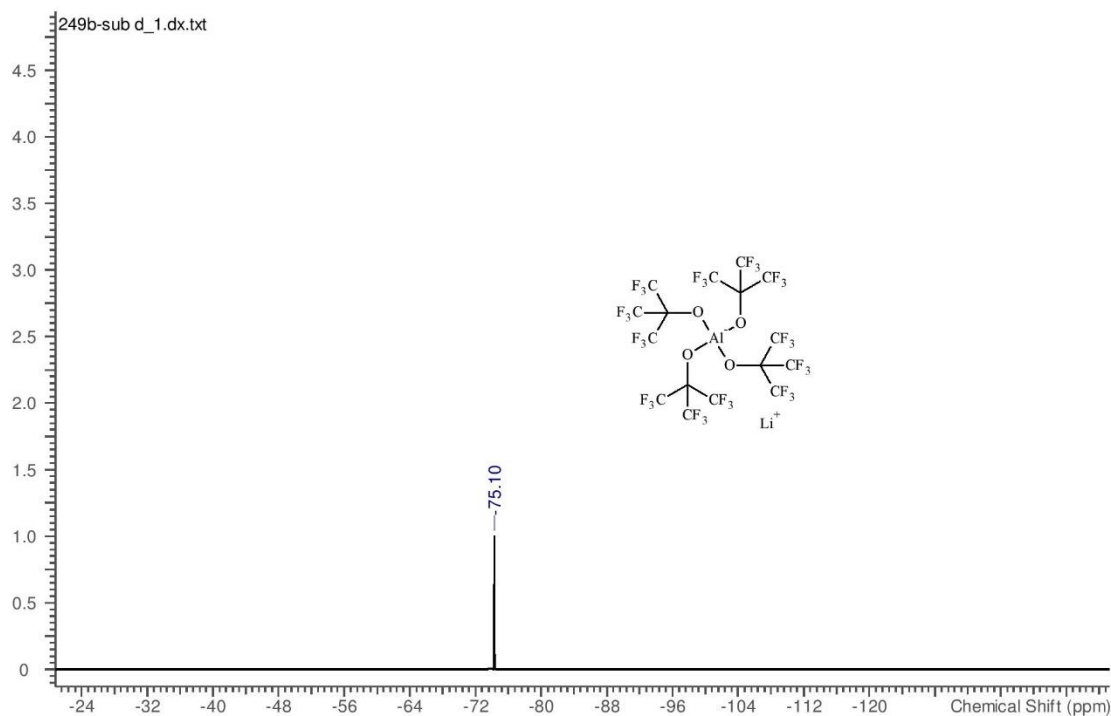
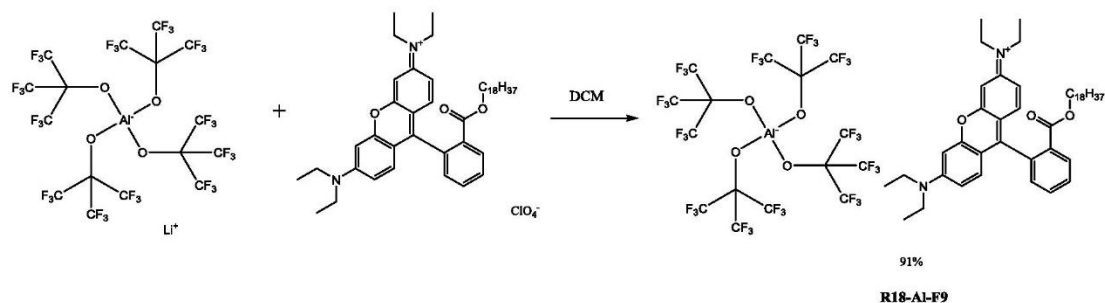


**Figure S1** - FNMR of **Li[F9-AI]** in DMSO- $d_6$

## R18/F9-AI



Rhodamine B octadecyl ester perchlorate (1 eq., 8 mg, 0.0101 mmol) and Li[F9-AI] (3 eq., 29.4 mg, 0.0302 mmol) were mixed in DCM and sonicated for 20 sec, TLC (MeOH/DCM 5/95) has shown full conversion. Product was purified by column chromatography on silica, using DCM/MeOH 98/2 as eluent. After evaporation of solvents purple viscous oil of **R18/F9-AI** was obtained (15.2 mg, 0.00915 mmol, 91 %)

$^1\text{H}$  NMR (500 MHz, ACETONITRILE- $d_3$ )  $\delta$  ppm 8.30 (1 H, d,  $J=7.7$  Hz), 7.80 - 7.87 (2 H, m), 7.40 (1 H, d,  $J=7.4$  Hz), 7.11 (2 H, d,  $J=9.5$  Hz), 6.97 (2 H, dd,  $J=9.6, 2.6$  Hz), 6.86 (2 H, d,  $J=2.4$  Hz), 3.94 (2 H, t,  $J=6.4$  Hz), 3.64 (8 H, q,  $J=7.3$  Hz), 1.23 - 1.30 (40 H, m), 1.09 - 1.16 (4 H, m), 0.94 - 0.97 (2 H, m), 0.89 - 0.92 (3 H, m)

$^{13}\text{C}$  NMR (126 MHz, ACETONITRILE- $d_3$ )  $\delta$  ppm 166.07 (s), 163.53 (s), 159.30 (s), 158.42 (s), 156.28 (s), 133.73 (s), 133.34 (s), 131.87 (s), 131.66 (s), 131.21 (s), 130.87 (s), 130.75 (s), 121.78 (q,  $J=288\text{Hz}$ ), 114.90 (s), 114.08 (s), 96.49 (s), 66.05 (s), 46.25 (s), 32.25 (s), 29.99 (s), 29.98 (s), 29.97 (s), 29.96 (s), 29.89 (s), 29.87 (s), 29.68 (s), 29.68 (s), 29.47 (s), 28.60 (s), 26.13 (s), 23.00 (s), 13.99 (s), 12.39 (s)

$^{19}\text{F}$  NMR (471 MHz, ACETONITRILE- $d_3$ )  $\delta$  ppm -75.98 (s)

HRMS (m/z): [M]<sup>+</sup> calcd. for  $\text{C}_{46}\text{H}_{67}\text{N}_2\text{O}_3^+$ , 695.51517; found 695.51376  
[M]<sup>-</sup> calcd. for  $\text{C}_{16}\text{AlF}_{36}\text{O}_4$ , 966.90371; found 966.89781

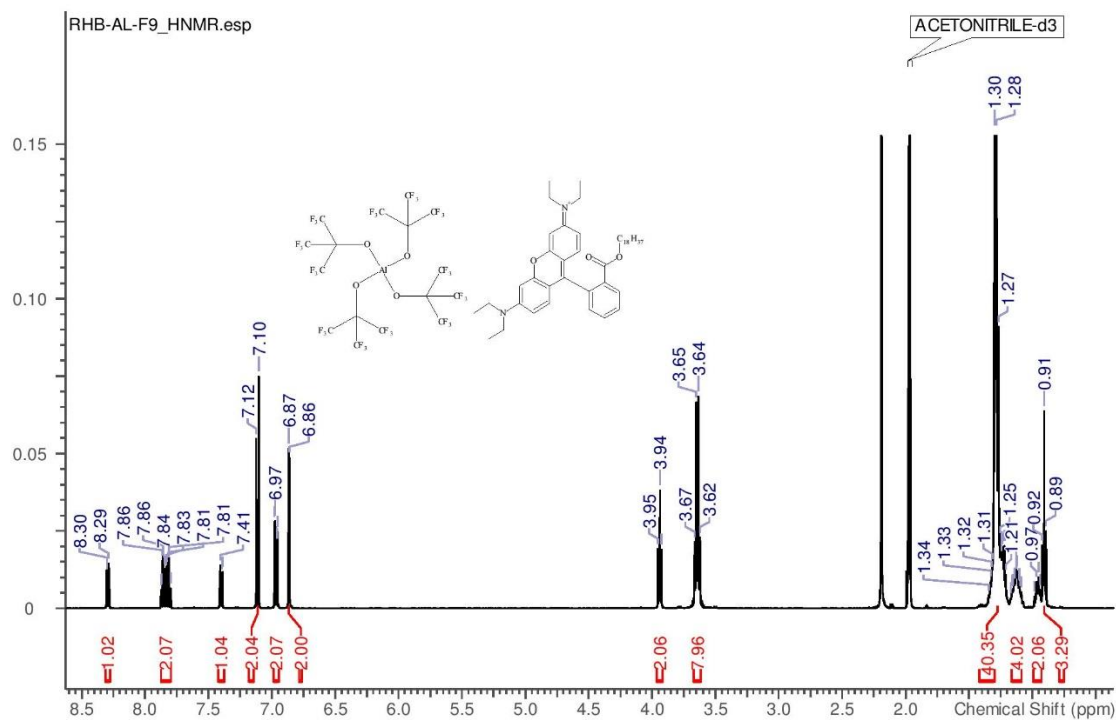


Figure S2 -  $^1\text{H}$ NMR of R18/F9-Al in MeCN-d3

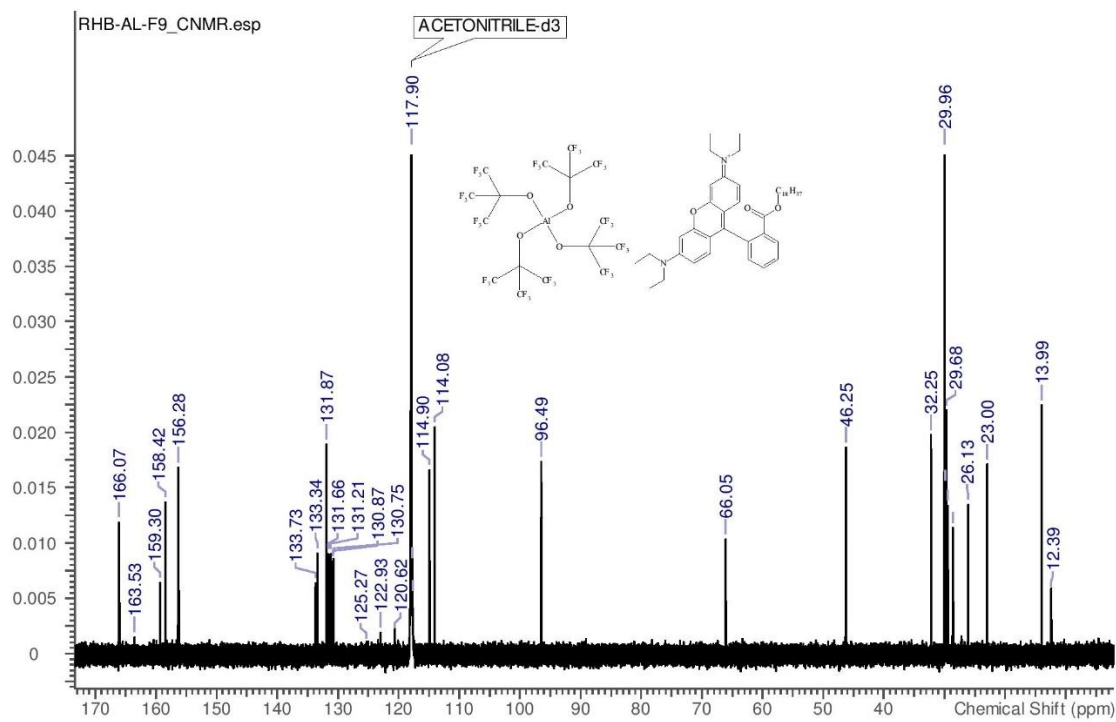
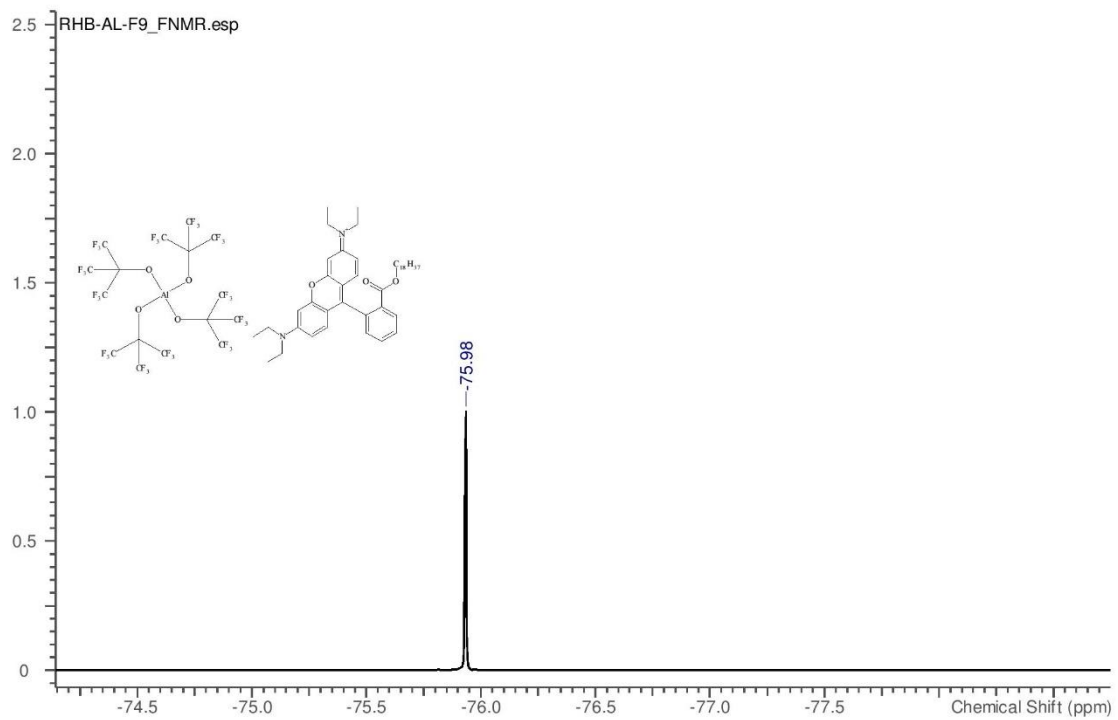
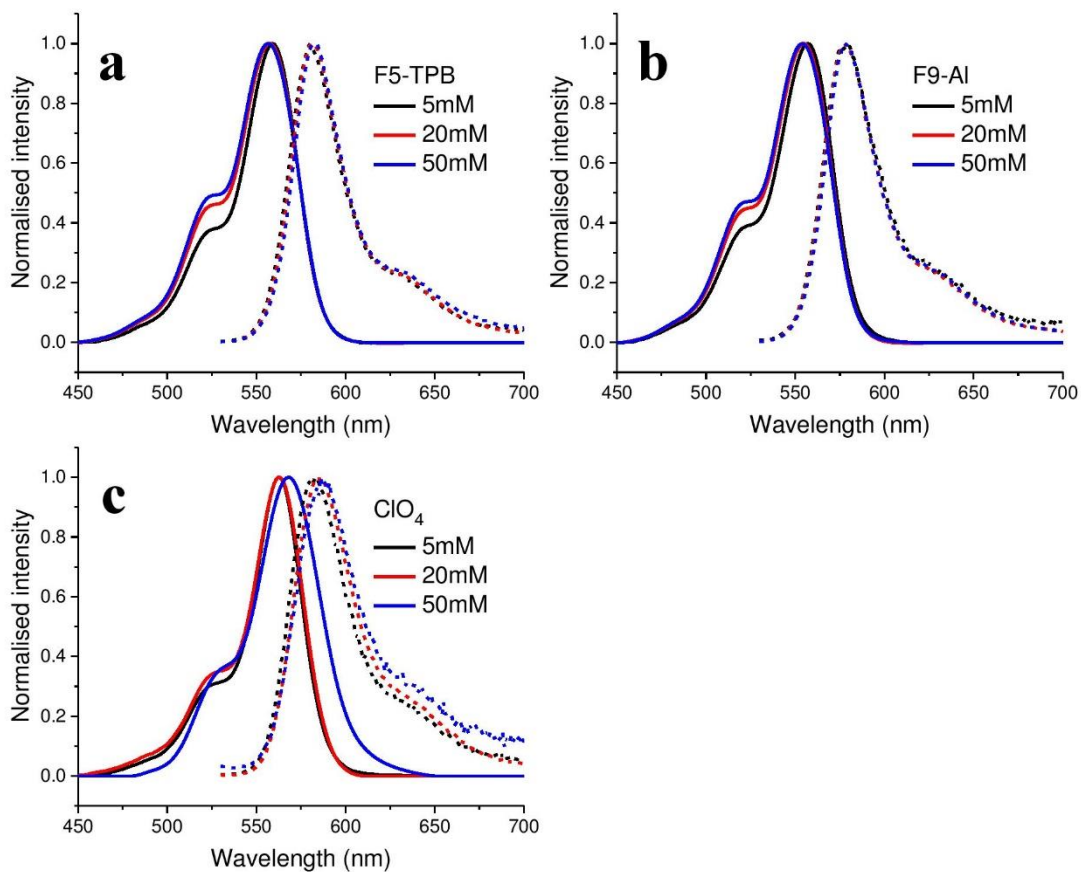


Figure S3 -  $^{13}\text{C}$ NMR of R18/F9-Al in MeCN-d3



**Figure S4** - FNMR of **R18/F9-Al** in MeCN-d3

## Supplementary figures



**Figure S5 – Effect of dye loading on spectral properties of R18 NPs.** Normalised absorption and fluorescence spectra of R18/F5-TPB (a), R18/F9-Al (b), R18/ClO<sub>4</sub> (c) at different dye loadings.

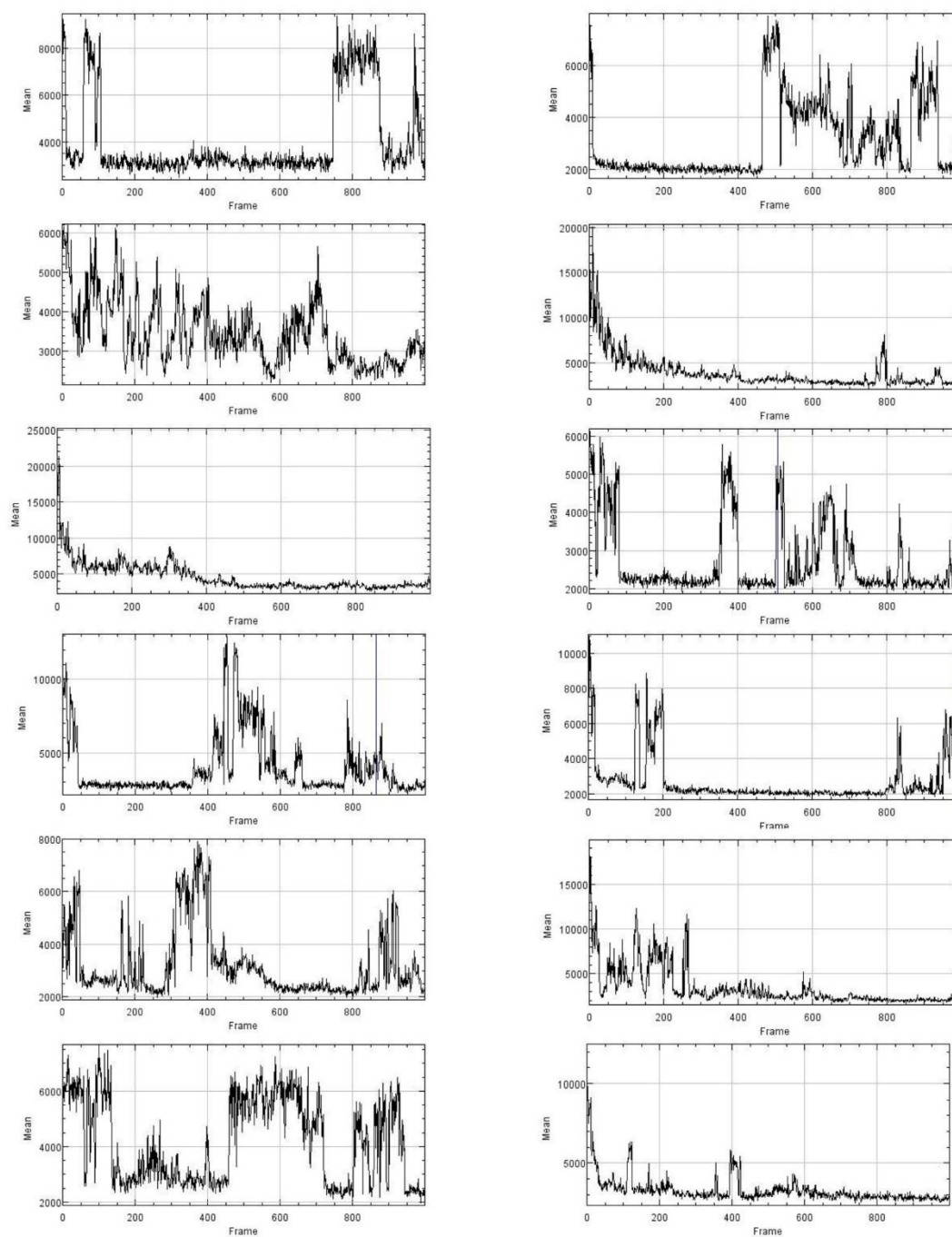


**Figure S6 – Single particle blinking.** Different emission transients of 50mM-loaded R18/F5-TPB (right) and R18/F9-Al (left) NPs under  $0.6\text{W}/\text{cm}^2$  532nm laser illumination. Recording speed was 33 frames per second. No significant difference in blinking behaviour was observed.

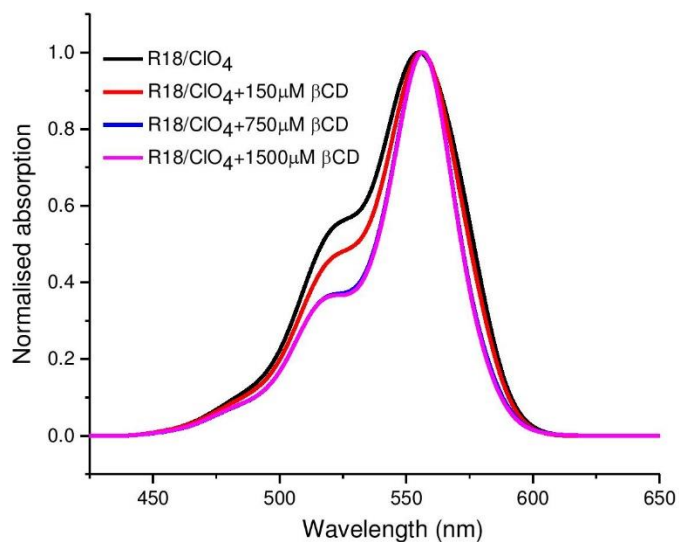


**Figure S7 – Effect of β-cyclodextrin on absorption spectra of R18/C10<sub>4</sub> in water.** Approximately 2 μM solution of R18/C10<sub>4</sub> dye in water was treated with different amounts of β-cyclodextrin. Spectra demonstrate that β-cyclodextrin can help to dissolve aggregates of R18/C10<sub>4</sub> dye in water, and its sufficient concentration is about 1mM. Dilution due to addition of β-cyclodextrin was less than 10%.

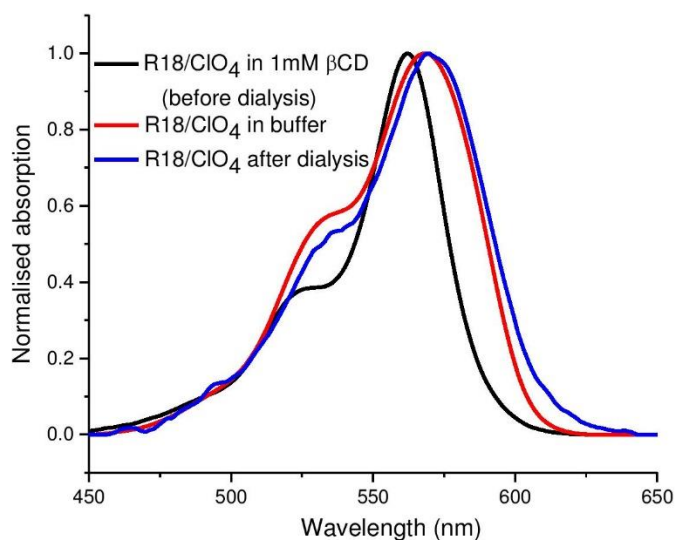


**Figure S8 – Absorption spectra of R18/ClO<sub>4</sub> dye in buffer and β-cyclodextrin solution before and after dialysis.** The figure shows, that absorption spectrum of R18/ClO<sub>4</sub> dye after dialysis (blue line) is significantly different from its absorption spectra before dialysis (black line), but very similar to a spectrum of R18/ClO<sub>4</sub> dye in 20 mM phosphate buffer (pH 7.4) (red line). As R18/ClO<sub>4</sub> dye in buffer exists as irregular dye aggregates of different sizes, we can assume that after dialysis of R18/ClO<sub>4</sub> dye solution, remaining dye is in aggregated state, probably in aggregates too large to pass through membrane and stabilised by β-cyclodextrin coating.

## Supplementary tables

**Table S1** - Dynamic light scattering data (mean size based on volume statistics, polydispersity, zeta potential) for tested NPs.

NPs	Loading (mM)	Size (nm)	Size SD (nm)	PDI	Zeta potential (mV)	Zeta potential SD (mV)
ClO <sub>4</sub>	5	49	1	0.05	-28	1
F5-TPB	5	35	2	0.07	-31	2
F9-AI	5	38	1	0.09	-29	3
ClO <sub>4</sub>	20	54	14	0.09	-20	6
F5-TPB	20	41	1	0.12	-31	2
F9-AI	20	37	1	0.07	-31	2
ClO <sub>4</sub>	50	276	13	0.12	*	*
F5-TPB	50	41	1	0.08	-33	3
F9-AI	50	41	1	0.08	-34	3
Blank	0	37	1	0.16	-29	3

SD – standard deviation of the mean, PDI – polydispersity index.

\*Zeta potential for 50mM R18/ClO<sub>4</sub> NPs could not be measured due to NPs aggregation.

**Table S2** - Quantum yield data of tested dye-loaded NPs.

NPs	Loading (mM)	Quantum yield	SD
ClO <sub>4</sub>	5	0.81	0.01
F5-TPB	5	1.0	0.03
F9-AI	5	0.88	0.01
ClO <sub>4</sub>	20	0.21	0.01
F5-TPB	20	0.84	0.01
F9-AI	20	0.71	0.01
ClO <sub>4</sub>	50	0.07	0.01
F5-TPB	50	0.55	0.01
F9-AI	50	0.55	0.01

SD – standard deviation of the mean.

**Table S3** - Anisotropy of tested dye-loaded NPs.

NPs	Loading (mM)	Anisotropy	SD
ClO <sub>4</sub>	5	0.0892	0.0043
ClO <sub>4</sub>	20	0.0351	0.0012
ClO <sub>4</sub>	50	0.0250	0.0004
F5-TPB	5	0.0114	0.0006
F5-TPB	20	0.0008	0.0001
F5-TPB	50	0.0007	0.0001
F9-AI	5	0.0119	0.0030
F9-AI	20	0.0035	0.0001
F9-AI	50	0.0013	0.0002

SD – standard deviation of the mean.

**Table S4** – Encapsulation efficiency of 50 mM dye-loaded NPs.

NPs	Encapsulation (%)	SD (%)
F9-AI	96.5	2.0
F5-TPB	91.7	4.1
ClO <sub>4</sub>	50.6	1.5
ClO <sub>4</sub> no polymer	*13.5	1.8

SD – standard deviation of the mean.

\*amount of dye left inside dialysis membrane, probably as large aggregates of pure dye.

## Supplementary references

1. A. Reisch, P. Didier, L. Richert, S. Oncul, Y. Arntz, Y. Mely and A. S. Klymchenko, *Nat. Commun.*, 2014, **5**, 4089.
2. I. Crossing, *Chem. Eur. J.*, 2001, **7**, 490-502.

### 2.2.3. Bulky hydrophobic barbiturates for enhanced encapsulation and emission of cationic dyes inside polymer nanoparticles

Already knowing that size and hydrophobicity of a counterion are crucial in *counterion-enhanced emission* approach, we set a goal to find an organic scaffold, which would allow us to create customisable anions of varying size and hydrophobicity. Classical examples of hydrophobic anions are anionic dyes, in which a single negative charge is delocalised over a long conjugation system.

Here, oxonol should be mentioned (Figure 1, top), a dye based on a barbituric acid scaffold, which is a strong electron-withdrawing cycle capable of charge delocalisation. However, oxonol itself is coloured, which will alter the emission of the cationic dye in the counterion-based approach. Therefore, it was decided to take the barbituric scaffold of this dye, but substitute chromophoric polymethine chain with an electron-withdrawing acyl group. Such C-acylbarbiturates should also have high charge delocalisation (Figure 1, bottom), similarly to oxonols, but no absorption of light in the visible region. We hypothesized, that C-acylbarbiturates may exhibit properties similar to fluorinated tetraphenylborates in the *counterion-enhanced emission* approach. In this work, we synthesized C-acylbarbiturates bearing various R and R' groups.

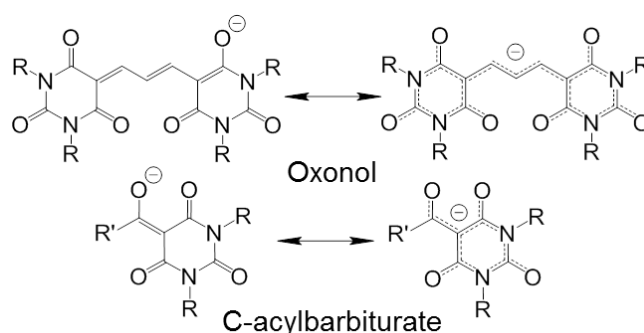


**Figure 1.** Chemical structures of oxonol dyes and C-acylbarbiturates with their resonance structures.

For the first trials we synthesized barbiturates with R = cyclohexyl (Figure 2, Scheme 1) and R' being undecyl (**Compound 1**) or phenyl (**Compound 2**). These molecules were readily obtained from the barbituric acid derivative and the corresponding carboxylic acids. The obtained barbituric acids were mixed with octadecylrhodamine B (R18) in DCM and washed with 10% aqueous potassium carbonate solution for deprotonation of barbiturates and ion exchange. However,

allegedly formed ion pairs of compounds **1** and **2** with cationic dye R18 were not stable on silica. This result could be explained by insufficient electron-withdrawing effect of the used acyl groups, which made possible reprotonation of the formed enolate anion on silica, in line with relatively high calculated pKa of 6.51 and 6.04 for compounds **1** and **2**, respectively. Therefore, to increase the acidity of the counterion's protonated form, R' group was changed to perfluorophenyl in molecule **BarC6** (Figure 2, Scheme 1). The anion of the obtained molecule could form stable enough ion pairs with R18 for purification on silica, probably due to lower calculated pKa values (3.68). Moreover, we changed R groups to diphenylmethyl to obtain even bulkier perfluorophenyl analogue **BarPh2** (Figure 2, Scheme 2). Anionic form of **BarPh2** also appeared to form stable ion pairs with R18, in line similarly low calculated pKa values (3.98).

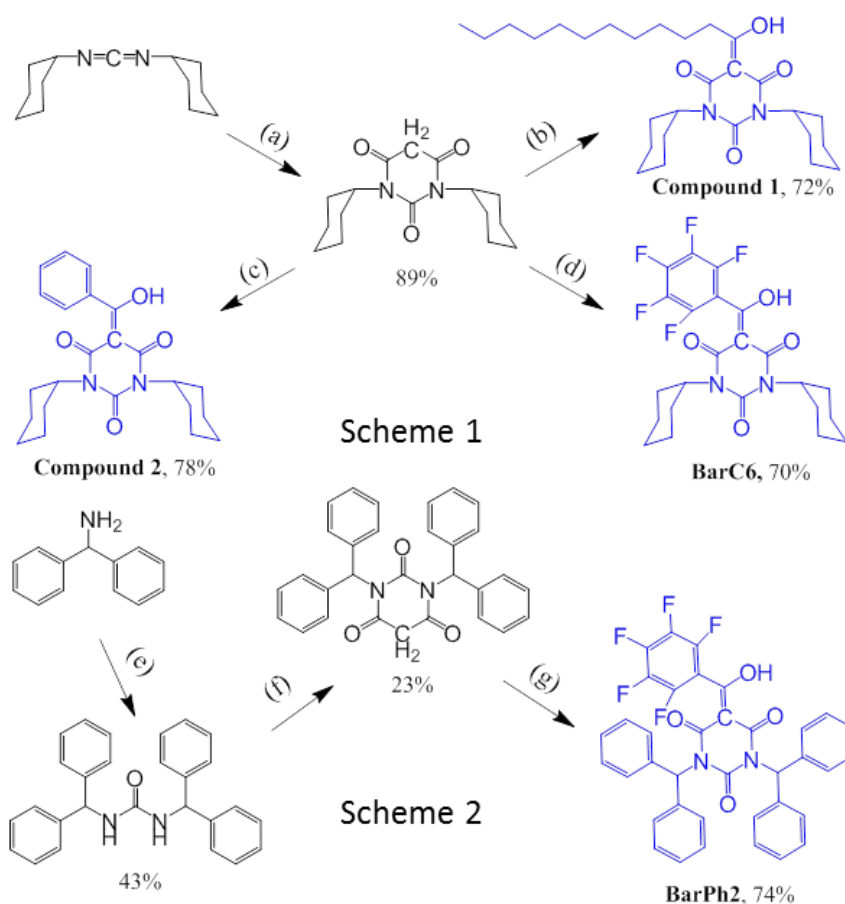


**Figure 2.** Synthesis of target barbiturates: (a) malonic acid, THF; (b) dodecanoic acid, EDC-HCl, DMAP, DCM; (c) benzoic acid, EDC-HCl, DMAP, DCM; (d) perfluorobenzoic acid, EDC-HCl, DMAP, DCM; (e) CDI, THF (f) malonic acid, acetic acid, acetic anhydride; (g) perfluorobenzoic acid, EDC-HCl, DMAP, DCM.

Both ion pairs of novel barbiturate anions with R18 dye, namely R18/BarC6 and R18/BarPh2, alongside with already known R18/F5-TPB and R18/ClO<sub>4</sub> as reference compounds, were encapsulated inside biodegradable PLGA (poly(lactide-co-glycolide)) nanoparticles (Figure 3) using simple nanoprecipitation method from water miscible solvent acetonitrile<sup>135, 136</sup>. The dyes were loaded at 5, 20 and 50 mM concentration (with respect to polymer).

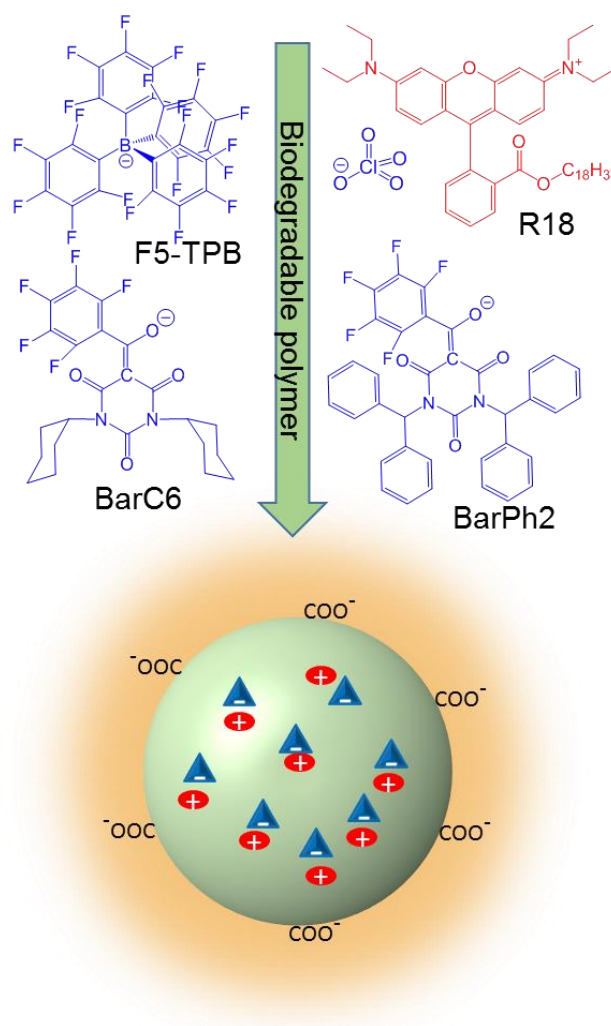


**Figure 3.** Chemical structures of R18 dye and counterions that were used to encapsulate it into polymer nanoparticles.

Size of the obtained nanoparticles was measured by DLS (Figure 4A). For both new barbiturates, similarly to F5-TPB, small (40-50 nm) nanoparticles are formed independently on dye loading. In contrast, ion pairs with more hydrophilic perchlorate counterion induce formation of much larger (>500 nm) and colloiddally unstable nanoparticles at 50 mM dye loading, which is in line with our previous reports. This is explained by cationic dye adsorption at the anionic nanoparticles surface, which leads

to decrease of surface charge and further NPs aggregation. To evaluate quantitatively the dyes encapsulation efficiency in NPs, we used our previously developed protocol – dialysis of NPs solutions versus 1 mM beta-cyclodextrin. During this procedure all the non-encapsulated/adsorbed dye gets washed off, and the comparison of dye concentration before and after dialysis gives us the encapsulation efficiency. The obtained results (Figure 4D) show poor encapsulation of R18/CIO<sub>4</sub> (~50%) and almost quantitative encapsulation of R18/F5-TPB. Ion pair with bulkier barbiturate, R18/BarPh2, also showed nearly quantitative encapsulation, while for the less bulky of two, R18/BarC6, encapsulation efficiency was about 70%. This signifies, that R18/BarC6, despite similar size of the formed NPs, probably has lower hydrophobicity comparing to its biphenylmethyl-substituted rival.

At 5 mM dye loading, independently on counterion, the quantum yields of all NPs were high (Figure 4B). However upon increase of loading to 20 and 50 mM, perchlorate demonstrated its inability to prevent dye self-quenching (quantum yield 4%), in contrast to R18/F5-TPB loaded NPs, displaying quantum yield of 55% at 50 mM loading. Remarkably, for bulky barbiturate-based ion pair R18/BarPh2, the quantum yield value is also high (52%), suggesting that BarPh2 is as effective in preventing ACQ as the current leader, F5-TPB. Ion pair R18/BarC6 demonstrate quantum yields of about 20% at 50 mM loading, which is 5 times higher than for perchlorate, but still not as high as for F5-TPB. These results show that quantum yield and encapsulation efficiency of dye-loaded NPs correlate directly with bulkiness and/or hydrophobicity of the barbiturates. Both BacC6 and BarPh2 are much more effective than relatively hydrophilic anion perchlorate, but only the bulkiest anion BarPh2 performs as effectively as F5-TPB.

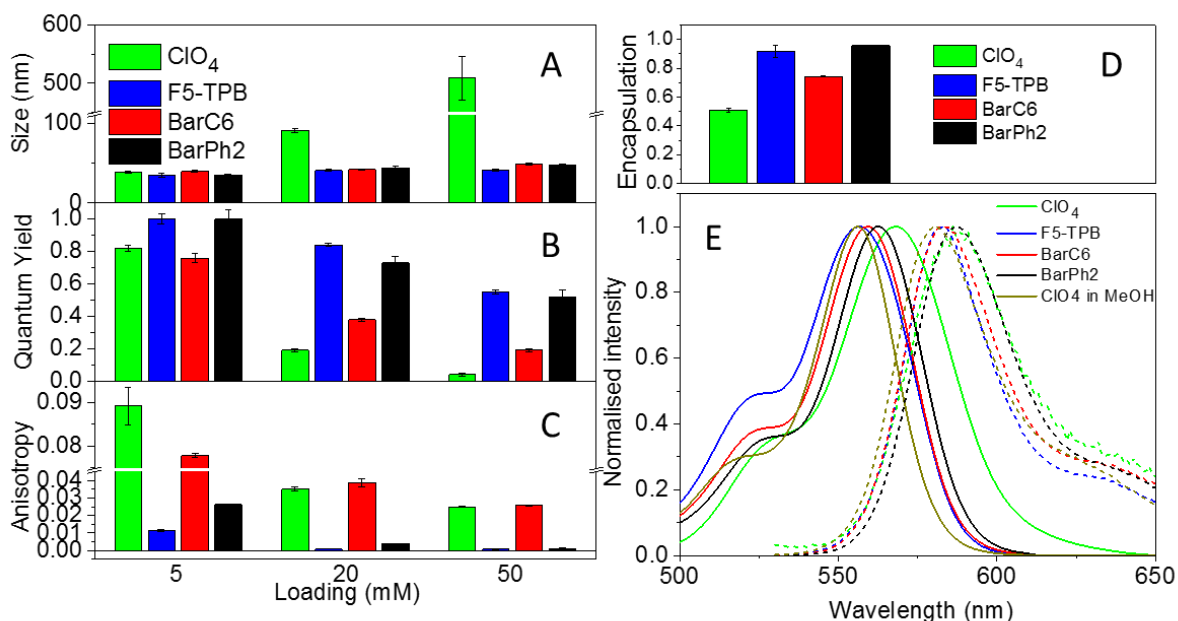


**Figure 4.** Properties of the developed NPs, loaded with ion pairs of R18 dye with different counterions. (A) Hydrodynamic diameter according to DLS, (B) fluorescence quantum yield, (C) fluorescence anisotropy and (D) encapsulation efficiency. (E) Absorption and fluorescence spectra of NPs at 50 mM dye loading and solution of R18/ClO<sub>4</sub> in methanol. Excitation wavelength was 520 nm.

Fluorescence anisotropy measurement is one of the ways to study dye communication inside NPs – energy transfer from dye to dye leads to loss of fluorescence anisotropy<sup>135</sup>. According to our results, in case of F5-TPB and, to less extent, BarPh2 as counterions, dye communication is observed even at relatively low loading of 5 mM (Figure 4C). At 50 mM loading their fluorescence anisotropy values become low enough to signify ultrafast excitation energy transfer. In case of perchlorate or BarC6 as counterions, the anisotropy values are quite high at all loadings, therefore dyes communication inside NPs is weak. Such difference in fluorescence anisotropy values for the two cases with barbiturate counterions suggests different types of organisation of their R18 cationic partners inside NPs.

Structure of counterion affects spectral properties of encapsulated R18 dye, and though at 5 mM loading the effect is minor, at 50 mM dye loading it becomes much more pronounced (Figure 4E). In line with previous studies, NPs loaded with R18/F5-TPB have the most blue-shifted absorption maximum, while R18/ClO<sub>4</sub>-loaded NPs – the most red-shifted maximum and the broadest spectrum. Surprisingly, despite having almost the same quantum yield as R18/F5-TPB, R18/BarPh2-loaded NPs display significantly red-shifted absorption maximum and lower short-wavelength

absorption shoulder. Taking to account their similar fluorescence anisotropy and encapsulation efficiency values, we can assume that this difference in absorption properties comes directly from the structure of the counterions, not the general difference in dye organisation within NPs. Being intermediate in quantum yields and encapsulation efficiency, NPs, loaded with R18/BarC6, display intermediate position of absorption maximum between R18/CIO<sub>4</sub> and R18/F5-TPB dye-loaded NPs. Similar bathochromic and hypsochromic shifts are observed in fluorescence spectra.

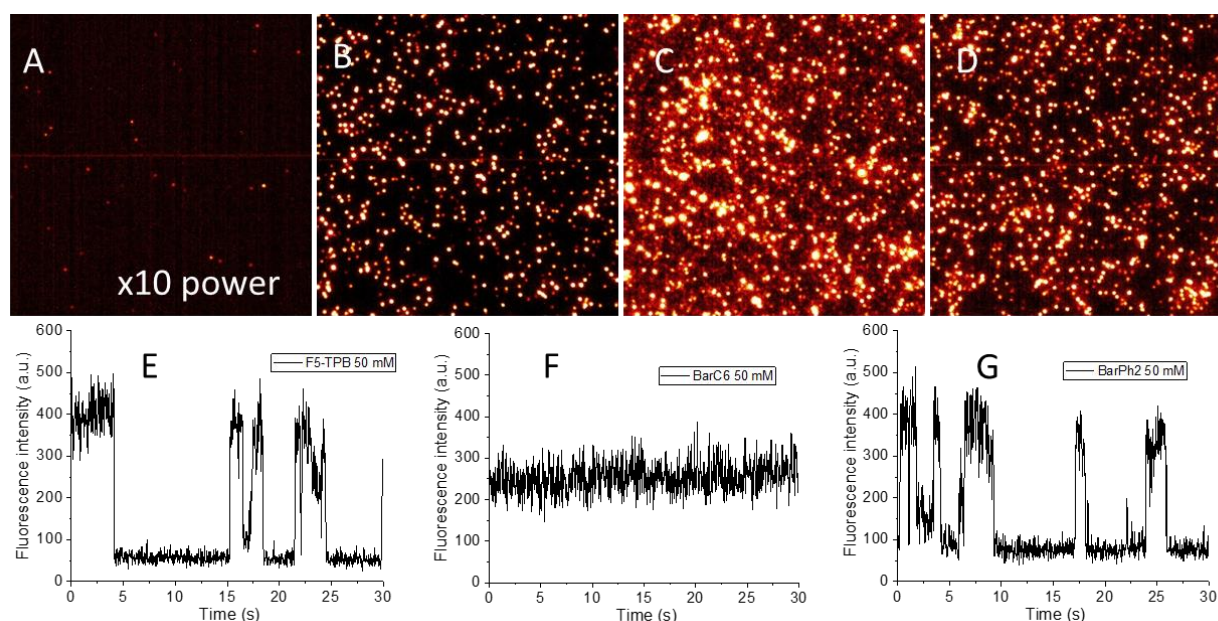


**Figure 5.** Single-particle fluorescence properties of the tested dye-loaded PLGA NPs. **Top:** Wide-field fluorescence images of QD585 (A), R18/F5-TPB (B), R18/BarC6 (C) and R18/BarPh2 (D) NPs at 50 mM dye loading. Identical imaging conditions were applied for dye-loaded NPs (excitation power density of 1.6 W/cm<sup>2</sup> at 550 nm), ten times higher illumination power was used for QDs. **Bottom:** Typical single-particle fluorescence traces of NPs loaded with R18/F5-TPB (E), R18/BarC6 (F) and R18/BarPh2 (G), recorded at the same conditions.

Single particle brightness was tested by wide-field microscopy. 50 mM loaded NPs of R18/BarPh2, R18/BarC6 and R18/F5-TPB were illuminated by LED at 550 nm and compared with commercial quantum dots of the same emission region, QD585 (Figure 5, top). All of the tested dye-loaded NPs appear to be much brighter than quantum dots QD585: R18/BarPh2, R18/BarC6 and R18/F5-TPB-loaded NPs are 40, 51 and 45 times brighter, respectively. Brightness of R18/BarC6 (Figure 5C) NPs is surprisingly high, even slightly exceeding the brightness of R18/BarPh2 (Figure 5D) and R18/F5-TPB (Figure 5B) NPs, despite having more than two times lower quantum yield and lower encapsulation efficiency. This peculiar behaviour of NPs can be

explained from single particle fluorescence intensity traces. In the case of R18/BarPh2 (Figure 5G) and R18/F5-TPB (Figure 5E) NPs we can observe the ON/OFF switching of fluorescence of the whole particle (blinking). Statistical analysis based on the mean of three images (>1000 particles per image), suggests that blinking takes place for 95+/-0.5% and 78+/-2% of all recorded R18/F5-TPB and R18/BarPh2 NPs, respectively. Such behaviour is only possible when the dyes are in close proximity inside the nanoparticle, making possible ultrafast energy transfer. Indeed, according to the anisotropy data, F5-TPB and BarPh2 may favour clustering of R18 dyes inside polymer matrix, as proposed in the earlier work<sup>135</sup>. In these conditions the decrease of brightness due to appearance of dark species inside NPs and effects like singlet-singlet annihilation can take place. However, for the case of R18/BarC6 NPs (Figure 5F), only a small fraction of particles is blinking (24+/-6%). This very different behaviour is probably due to more homogeneous distribution of fluorophores within R18/BarC6 NPs and inefficiency of energy transfer, which prevents decrease of brightness due to aforementioned effects. Absence of dyes communication in R18/BarC6 NPs is in line with fluorescence anisotropy measurements, confirming the link between the two.

To test the obtained NPs in biological media, they were incubated with KB cells for 3 hours and then the cells were washed and imaged by confocal microscopy. All four counterions at the highest (50 mM) and lowest (5 mM) loadings were tested (Figure 6). R18/F5-TPB NPs at 5 mM loading (Figure 6B) appeared as bright dots, being localised in endosomes without dye leakage, in line with previous data. R18/BarPh2 and R18/BarC6 NPs at this loading showed similar behaviour (Figure 6C and 6D). Significant degree of leakage can be observed for R18/CIO<sub>4</sub> NPs at 5 mM loading (Figure 6A) as a diffuse fluorescence inside the cells, so that endosomes are practically not visible. This effect becomes much more pronounced at 50 mM loading: due to poor encapsulation of R18/CIO<sub>4</sub>, fluorescence can be observed all over the intracellular compartments (Figure 6E). For both R18/F5-TPB and R18/BarC6 NPs at 50 mM loading diffuse intracellular fluorescence starts to be visible (Figures 6F and 6G, respectively), indicating imperfect encapsulation of these ion pairs at the highest loading. Remarkably, for 50 mM R18/BarPh2 NPs, no diffuse fluorescence could be observed (Figure 6H), indicating absence of dye leakage in biological media and, therefore, highly efficient encapsulation of the dye. These results suggest that novel

BarPh2 counterion outperforms the “golden standard” F5-TPB for bioimaging purposes. In this respect it is close to F9-Al anion described in the earlier chapter.

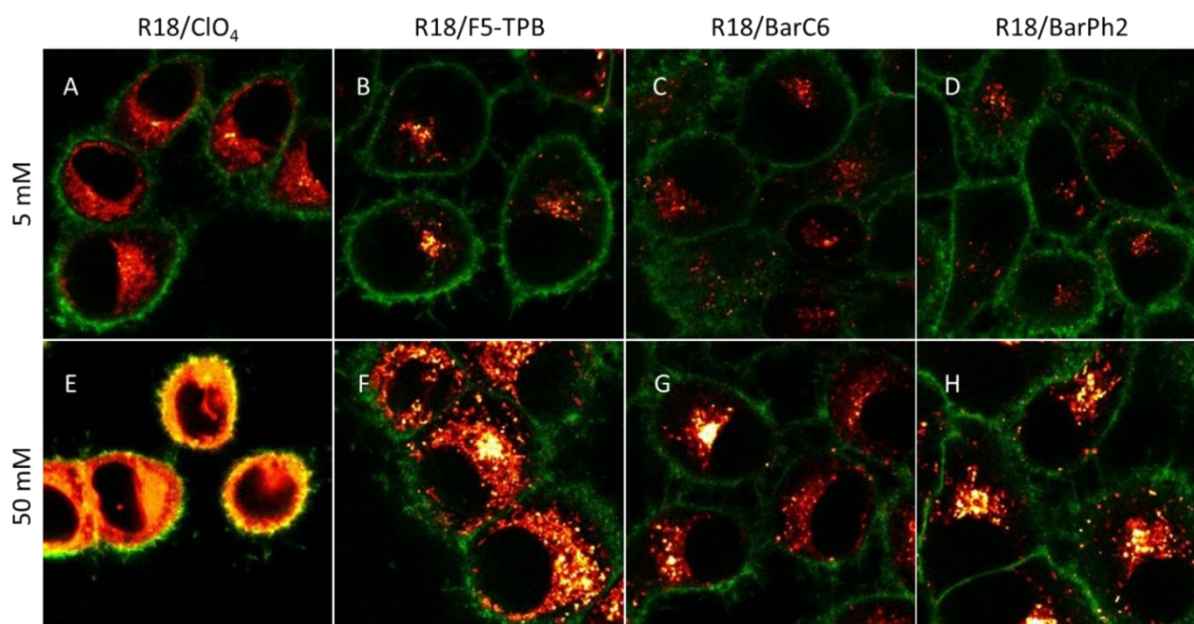


**Figure 6.** Confocal images of KB cells incubated for 3h with dye-loaded PLGA NPs. NPs were loaded with R18/CIO<sub>4</sub>, R18/F5-TPB, R18/BarC6 and R18/BarPh2 at 5 and 50 mM concentrations. Excitation wavelength was 561 nm, emission was collected from 570 to 650 nm. Image size was 58.4x58.4  $\mu$ m.

In conclusion, this work demonstrates that *counterion-enhanced encapsulation and emission* approach is not limited to symmetrical borates or aluminates, but can be extended to easily obtainable and customisable barbiturates. Both new anions BarC6 and BarPh2 can prevent self-quenching of dyes in polymer NPs and ensure small size of NPs without aggregation, unlike small hydrophilic perchlorate. However, the obtained dye-loaded NPs using BarC6 and BarPh2 present quite different fluorescence properties. BarPh2 is very similar to well-described F5-TPB in terms of high fluorescence quantum yield and blinking. BarPh2 even outperforms F5-TPB in cellular studies, where the former ensured no dye leakage inside the cells. By contrast, BarC6 allows obtaining bright and non-blinking nanoparticles, although it shows signs of leakage in biological media. Thus, while BarPh2 favours R18 dye clustering inside PLGA matrix, BarC6 produces more homogeneous distribution of dyes in the polymer and thus non-blinking emission. These results show that fine-tuning of the counterions properties, and thus properties of fluorescent NPs, can be achieved by simply altering substituents in the barbituric scaffold. This opens path to rational design of tailor-made counterions and obtaining ultrabright fluorescent NPs with desired properties.

## Conclusions and perspectives

My PhD project was dedicated to exploring and developing *counterion-enhanced encapsulation and emission* approach, and understanding the role of counterion for assembly of cationic dyes inside polymer nanoparticles. Several key questions about the approach were answered.

In the first project we validated, that bulky hydrophobic counterions, namely fluorinated tetraphenylborates in that case, can decrease self-quenching in cyanine-loaded polymer nanoparticles. However, the efficiency of preventing self-quenching decreases with loading and with moving from visible to NIR spectral region of cyanines. Small (~40 nm) and bright (20x brighter than QDs) NPs were obtained, and they have shown no signs of dye leakage in biological medium. Having bright differently coloured fluorescent NPs, which have the same surface properties, allowed us to develop multicolour cell barcoding system for long-term tracking of living cells.

The next important step of the project was to understand how and why some of the counterions prevent ACQ, and some – do not. Having tested ion pairs of octadecylrhodamine B with ten different counterions of different sizes and hydrophobicities, we have found that there are two main features required from a counterion, compatible with our approach – large size and high hydrophobicity. High hydrophobicity ensures complete dye encapsulation inside the NPs and allows forming clusters of dyes inside NPs with strong dye-dye communication, which is of great importance for FRET-based studies and super-resolution imaging. Hydrophilic counterions do not allow formation of small NPs due to low encapsulation of cationic dyes, which stick to NPs surface, compensate their surface charge and decrease their colloidal stability. Large size of a counterion, on the other hand, is crucial for preventing self-quenching of dyes, acting like a spacer between them. Importantly, we found that counterions of intermediate hydrophobicity and size allow preparation of small and bright NPs, but do not favour dye communication and particle blinking, which can be useful for tracking applications.

Already knowing the requirements for counterions and their role in preparation of dye-loaded NPs, we found several new counterions to substitute fluorinated tetraphenylborates. Tetrakis[perfluoro-*tert*-butoxy]aluminate appeared to perfectly

replace F5-TPB in ultra-bright dye-loaded fluorescent polymer NPs. Particles, based on it, had the same size, brightness and dye communication as the ones, based on F5-TPB. Moreover, due to the higher hydrophobicity of F9-Al, NPs based on it show no leakage in biological environment even at high loadings (50 mM), while their F5-TPB-based rivals demonstrate some dye leakage in these conditions.

Despite working very well, even Al-F9 counterion has a drawback – it has little potential for chemical modification, customisation and, as a result, fine-tuning of properties of NPs. Therefore, we developed two barbiturate-based counterions, both of which are bulky, hydrophobic and capable to decrease ACQ. And while more bulky and hydrophobic of them, BarPh2, resembles F5-TPB in almost everything, it still beats it in cellular imaging, where it shows much less dye leakage. On the other hand, less bulky and hydrophobic BarC6, has significantly lower dye communication and fraction of blinking particles. The most important thing about barbiturate counterions is their potential for chemical modification – the scaffold has three sites for facile and independent modification, providing endless variations of customisable tailor-made counterions. The latter could be used for fine-tuning of fluorescent NPs properties with a high degree of creative freedom.

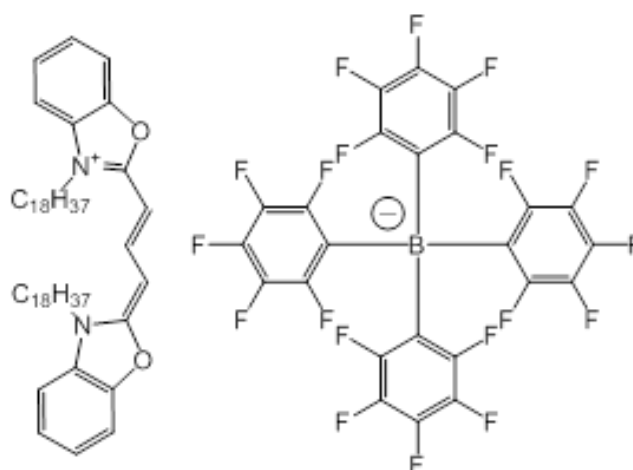
Obtained results provide a solid basis for counterion-enhanced encapsulation and emission concept in preparation of dye-loaded fluorescent NPs. The work revealed that the concept can be extended to a large variety of cationic dyes, notably cyanines and the design of counterion enables fine tuning of optical properties of NPs. We could extend this approach to a number of unexplored counterions, which shows the new attractive research direction on developing novel counterions for precise control of NPs properties. In particular it will be important to obtain counterions that would be compatible with near-infrared dyes, because the currently studied anions are not so effective. It will be also important to further tune counterion properties in order to obtain particles with either perfect ON/OFF switching or stable emission. Finally, surface modification of the polymer would allow to further decrease the NPs size, increase stability, and most importantly – target biomolecules and build sensors and probes based on ultra-bright NPs.

### **3. Materials and Methods**

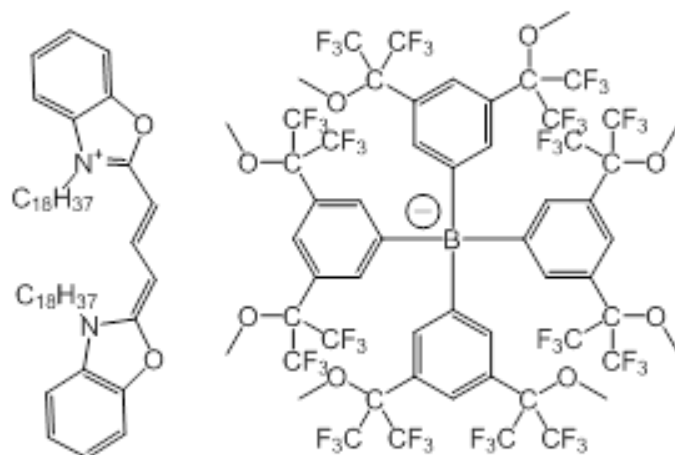
All starting materials for synthesis were purchased from Alfa Aesar, Sigma Aldrich, Fluorochem or TCI Europe and used as received unless stated otherwise. NMR spectra were recorded on a Bruker Avance III 400 MHz and 500 MHz spectrometers. Mass spectra were obtained using an Agilent Q-TOF 6520 mass spectrometer. MilliQ-water (Millipore) was used in all experiments.

## 3.1. Chemical synthesis

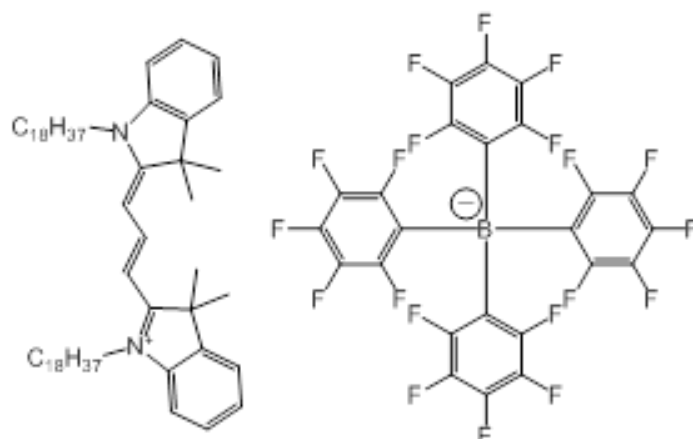
### 3.1.1. Fluorescent Polymer Nanoparticles for Cell Barcoding In Vitro and In Vivo



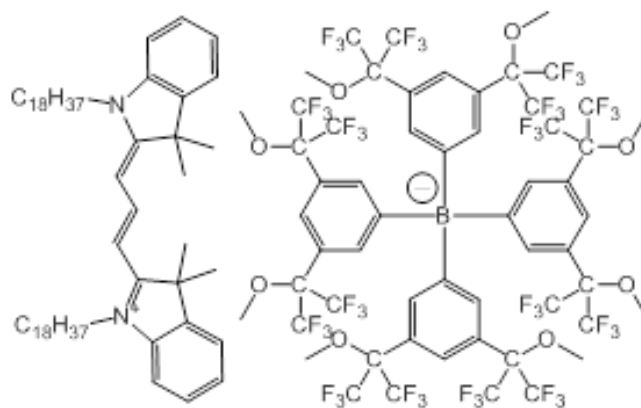
**DiO-F5.** DiO-Cl (1 eq., 8 mg, 0.00907 mmol) and lithium tetrakis(pentafluorophenyl)borate (F5) (3 eq., 26.7 mg, 0.0272 mmol) were mixed in 0.5 ml of dichloromethane, TLC has shown instant conversion. Product was purified by TLC using dichloromethane/methanol 95/5 as eluent. After evaporation of solvents 11 mg of DiO-F5 was obtained (83% yield). <sup>1</sup>H NMR (500 MHz, acetone-d<sub>6</sub>) δ ppm 0.85 - 0.90 (6 H, m) 1.25 - 1.30 (52 H, m) 1.36 - 1.43 (4 H, m) 1.47 - 1.54 (4 H, m) 1.93 - 2.00 (4 H, m) 4.34 (4 H, t, *J*=7.48 Hz) 6.13 (2 H, d) 7.45 - 7.53 (4 H, m) 7.70 (2 H, br d, *J*=7.94 Hz) 7.73 (2 H, br d, *J*=7.94 Hz) 8.56 (1 H, t, *J*=13.25 Hz). <sup>19</sup>F NMR (376 MHz, acetone-d<sub>6</sub>) δ ppm -168.36 (8 F, br t, *J*=17.16 Hz) -164.42 (4 F, br t, *J*=19.45 Hz) -133.03 (8 F, s). <sup>11</sup>B NMR (128 MHz, acetone-d<sub>6</sub>) δ ppm -11.39 (1 B, s). <sup>13</sup>C NMR (126 MHz, acetone-d<sub>6</sub>) δ ppm 13.46 (s), 22.44 (s), 26.46 (s), 27.77 (s), 28.89 (s), 28.95 (s), 29.04 (s), 29.07 (s), 29.19 (s), 29.30 (s), 29.35 (s), 29.45 (s), 29.48 (s), 29.50 (s), 29.51 (s), 29.52 (s), 31.76 (s), 44.29 (s), 85.06 (s), 110.83 (s), 111.19 (s), 125.31 (s), 126.10 (s), 131.63 (s), 147.02 (s), 147.26 (s), 162.46 (s). HRMS (m/z): [M]<sup>+</sup> calcd. 781.6606; found 781.6605; [M]<sup>-</sup> calcd. 678.9779; found 678.9768.



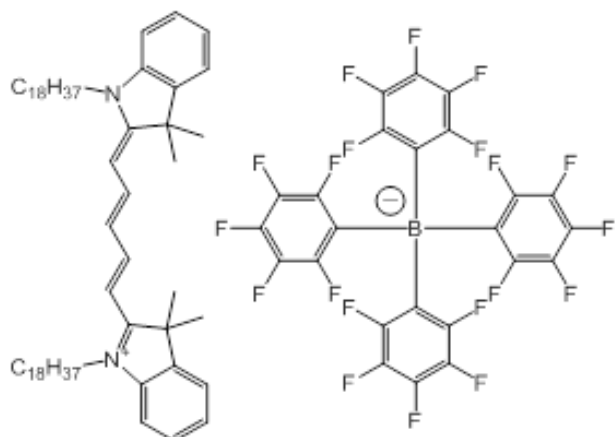
**DiO-F12.** DiO-Cl (1 eq., 8 mg, 0.00907 mmol) and sodium tetrakis[3,5-bis(1,1,1,3,3,3-hexafluoro-2-methoxy-2-propyl)phenyl]borate trihydrate (F12) (2 eq., 33.3 mg, 0.0181 mmol) were mixed in 0.5 ml of dichloromethane, TLC has shown instant conversion. Product was purified by TLC using dichloromethane/methanol 95/5 as eluent. After evaporation of solvents 17 mg of DiO-F12 was obtained (74 % yield).  $^1\text{H}$  NMR (500 MHz, acetone- $d_6$ )  $\delta$  ppm 0.86 - 0.89 (6 H, m) 1.28 (52 H, s) 1.37 - 1.42 (4 H, m) 1.48 - 1.53 (4 H, m) 1.94 - 2.00 (4 H, m) 3.30 (24 H, s) 4.34 (4 H, t,  $J=7.48$  Hz) 6.14 (2 H, d) 7.43 (4 H, s) 7.46 - 7.49 (2 H, m) 7.51 (2 H, dd,  $J=7.78, 1.07$  Hz) 7.59 (8 H, br s) 7.70 (2 H, d,  $J=7.63$  Hz) 7.74 (2 H, d,  $J=7.94$  Hz) 8.56 (1 H, m).  $^{19}\text{F}$  NMR (376 MHz, acetone- $d_6$ )  $\delta$  ppm -71.69 (48 F, s).  $^{11}\text{B}$  NMR (128 MHz, acetone- $d_6$ )  $\delta$  ppm -0.65 (1 B, s).  $^{13}\text{C}$  NMR (126 MHz, acetone- $d_6$ )  $\delta$  ppm 13.46 (s), 22.44 (s), 26.46 (s), 27.77 (s), 29.04 (s), 29.07 (s), 29.19 (s), 29.30 (s), 29.35 (s), 29.45 (s), 29.48 (s), 29.49 (s), 29.50 (s), 29.52 (s), 31.75 (s), 44.29 (s), 53.24 (s), 83.33 (sept,  $J=28$  Hz), 110.84 (s), 111.19 (s), 121.50 (s), 122.83 (s), 123.81 (s), 125.29 (dd), 125.31 (s), 126.10 (s), 131.63 (s), 136.98 (s), 147.03 (s), 147.10 (s), 162.13 (dd), 162.44 (s), 162.46 (s). HRMS ( $m/z$ ):  $[\text{M}]^+$  calcd. 781.6606; found 781.6614;  $[\text{M}]^-$  calcd. 1759.1742; found 1759.1720.



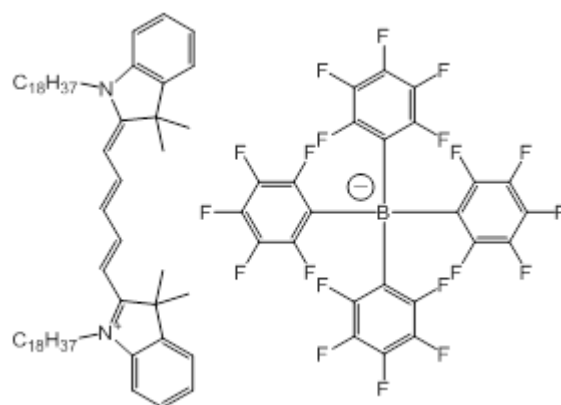
**Dil-F5.** Dil-Cl (1 eq., 10 mg, 0.0104 mmol) and lithium tetrakis(pentafluorophenyl)borate (F5) (3 eq., 30.6 mg, 0.0312 mmol) were mixed in 0.5 ml of dichloromethane, TLC has shown instant conversion. Product was purified by TLC using dichloromethane/methanol 95/5 as eluent. After evaporation of solvents 13 mg of Dil-F5 was obtained (83% yield).  $^1\text{H}$  NMR (500 MHz, acetone- $d_6$ )  $\delta$  ppm 0.84 - 0.89 (6 H, m) 1.25 - 1.33 (52 H, m) 1.36 - 1.43 (4 H, m) 1.46 - 1.52 (4 H, m) 1.83 (12 H, s) 1.86 - 1.92 (4 H, m) 4.23 (4 H, t,  $J=7.63$  Hz) 6.58 (2 H, d,  $J=13.43$  Hz) 7.33 (2 H, t,  $J=6.53$  Hz) 7.45 - 7.49 (4 H, m) 7.63 (2 H, d,  $J=7.63$  Hz) 8.62 (1 H, t,  $J=13.58$  Hz).  $^{19}\text{F}$  NMR (376 MHz, acetone- $d_6$ )  $\delta$  ppm -168.33 (8 F, br t,  $J=18.31$  Hz) -164.40 (4 F, br t,  $J=20.03$  Hz) -133.01 (8 F, s).  $^{11}\text{B}$  NMR (128 MHz, acetone- $d_6$ )  $\delta$  ppm -16.60 (1 B, s).  $^{13}\text{C}$  NMR (126 MHz, acetone- $d_6$ )  $\delta$  ppm 13.47 (s), 22.45 (s), 26.59 (s), 27.31 (s), 27.33 (s), 29.04 (s), 29.18 (s), 29.20 (s), 29.34 (s), 29.39 (s), 29.41 (s), 29.49 (s), 29.53 (s), 29.54 (s), 31.76 (s), 44.22 (s), 49.45 (s), 102.58 (s), 111.46 (s), 122.44 (s), 125.55 (s), 128.78 (s), 141.00 (s), 142.23 (s), 150.69 (s), 174.68 (s). HRMS (m/z):  $[\text{M}]^+$  calcd. 833.7646; found 833.7680;  $[\text{M}]^-$  calcd. 678.9779; found 678.9771.



**Dil-F12.** Dil-Cl (1 eq., 10 mg, 0.0104 mmol) and sodium tetrakis[3,5-bis(1,1,1,3,3,3-hexafluoro-2-methoxy-2-propyl)phenyl]borate trihydrate (F12) (2 eq., 38.2 mg, 0.0208 mmol) were mixed in 0.5 ml of dichloromethane, TLC has shown instant conversion. Product was purified by TLC using dichloromethane/methanol 95/5 as eluent. After evaporation of solvents 22 mg of Dil-F12 was obtained (82 % yield).  $^1\text{H}$  NMR (500 MHz, acetone- $d_6$ )  $\delta$  ppm 0.84 - 0.90 (6 H, m) 1.25 - 1.32 (52 H, m) 1.37 - 1.44 (4 H, m) 1.47 - 1.53 (4 H, m) 1.84 (12 H, s) 1.89 (4 H, quin,  $J=7.63$  Hz) 3.30 (24 H, s) 4.24 (4 H, t,  $J=7.48$  Hz) 6.59 (2 H, d,  $J=13.43$  Hz) 7.34 (2 H, t,  $J=6.71$  Hz) 7.41 - 7.50 (8 H, m) 7.57 - 7.65 (10 H, m) 8.62 (1 H, t,  $J=13.43$  Hz).  $^{19}\text{F}$  NMR (376 MHz, acetone- $d_6$ )  $\delta$  ppm -71.69 (48 F, s).  $^{11}\text{B}$  NMR (128 MHz, acetone- $d_6$ )  $\delta$  ppm -5.85 (1 B, s).  $^{13}\text{C}$  NMR (126 MHz, acetone- $d_6$ )  $\delta$  ppm 13.46 (s), 22.44 (s), 26.58 (s), 27.31 (s), 27.34 (s), 29.04 (s), 29.18 (s), 29.19 (s), 29.34 (s), 29.35 (s), 29.39 (s), 29.48 (s), 29.52 (s), 29.53 (s), 31.76 (s), 44.22 (s), 49.46 (s), 53.23 (s), 83.33 (sept,  $J=28$  Hz), 102.60 (s), 111.48 (s), 119.21 (s), 121.51 (s), 122.66 (q), 122.45 (s), 122.83 (s), 123.81 (s), 125.29 (dd), 125.56 (s), 126.11 (s), 128.80 (s), 136.98 (s), 141.01 (s), 142.24 (s), 150.69 (s), 162.13 (dd), 174.68 (s). HRMS ( $m/z$ ):  $[\text{M}]^+$  calcd. 833.7646; found 833.7641;  $[\text{M}]^-$  calcd. 1759.1742; found 1759.1754.

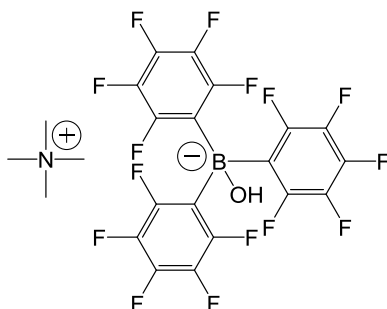


**DiD-F5.** DiD-Cl (1 eq., 12 mg, 0.011 mmol) and lithium tetrakis(pentafluorophenyl)borate (F5) (3 eq., 22.7 mg, 0.0331 mmol) were mixed in 0.5 ml of dichloromethane, TLC has shown instant conversion. Product was purified by TLC using dichloromethane/methanol 95/5 as eluent. After evaporation of solvents 15 mg of DiD-F5 was obtained (83% yield). <sup>1</sup>H NMR (500 MHz, acetone-d<sub>6</sub>) δ ppm 0.87 (6 H, t, *J*=6.71 Hz) 1.25 - 1.31 (52 H, m) 1.37 - 1.43 (4 H, m) 1.49 (4 H, quin, *J*=7.48 Hz) 1.73 (12 H, s) 1.86 (4 H, quin, *J*=7.55 Hz) 4.20 (4 H, t, *J*=7.63 Hz) 6.40 (2 H, d) 6.65 (1 H, t, *J*=12.51 Hz) 7.28 (2 H, t, *J*=7.04 Hz) 7.39 - 7.45 (4 H, m) 7.57 (2 H, d, *J*=7.32 Hz) 8.42 (2 H, t, *J*=13.05 Hz). <sup>19</sup>F NMR (376 MHz, acetone-d<sub>6</sub>) δ ppm -168.31 (8 F, br t, *J*=17.17 Hz) -164.39 (4 F, br t, *J*=20.03 Hz) -133.00 (8 F, s). <sup>11</sup>B NMR (128 MHz, acetone-d<sub>6</sub>) δ ppm -16.61 (1 B, s). <sup>13</sup>C NMR (126 MHz, acetone-d<sub>6</sub>) δ ppm 13.47 (s), 22.45 (s), 26.56 (s), 26.92 (s), 27.22 (s), 29.05 (s), 29.15 (s), 29.20 (s), 29.33 (s), 29.35 (s), 29.37 (s), 29.47 (s), 29.49 (s), 29.50 (s), 29.52 (s), 29.53 (s), 31.76 (s), 43.91 (s), 49.28 (s), 103.21 (s), 111.07 (s), 122.32 (s), 125.05 (s), 125.30 (s), 128.59 (s), 141.35 (s), 142.37 (s), 154.04 (s), 173.29 (s). HRMS (*m/z*): [M]<sup>+</sup> calcd. 859.7803; found 859.7834; [M]<sup>-</sup> calcd. 678.9779; found 678.9766.



**DiD-F12.** DiD-Cl (1 eq., 8 mg, 0.0081 mmol) and sodium tetrakis[3,5-bis(1,1,1,3,3,3-hexafluoro-2-methoxy-2-propyl)phenyl]borate trihydrate (F12) (2 eq., 29.8 mg, 0.0162 mmol) were mixed in 0.5 ml of dichloromethane, TLC has shown instant conversion. Product was purified by TLC using dichloromethane/methanol 95/5 as eluent. After evaporation of solvents 15 mg of DiD-F12 was obtained (71 % yield).  $^1\text{H}$  NMR (500 MHz, acetone- $d_6$ )  $\delta$  ppm 0.84 - 0.90 (6 H, m) 1.28 (52 H, s) 1.37 - 1.44 (4 H, m) 1.47 - 1.53 (4 H, m) 1.74 (12 H, s) 1.87 (4 H, quin,  $J=7.55$  Hz) 3.30 (24 H, s) 4.20 (4 H, t,  $J=7.48$  Hz) 6.42 (2 H, d,  $J=13.73$  Hz) 6.67 (1 H, t,  $J=12.36$  Hz) 7.28 (2 H, t,  $J=7.21$  Hz) 7.39 - 7.45 (8 H, m) 7.56 - 7.61 (10 H, m) 8.42 (2 H, t,  $J=12.97$  Hz).  $^{19}\text{F}$  NMR (376 MHz, acetone- $d_6$ )  $\delta$  ppm -71.68 (48 F, s).  $^{11}\text{B}$  NMR (128 MHz, acetone- $d_6$ )  $\delta$  ppm -5.85 (1 B, s).  $^{13}\text{C}$  NMR (126 MHz, acetone- $d_6$ )  $\delta$  ppm 13.47 (s), 22.45 (s), 26.56 (s), 26.92 (s), 27.23 (s), 29.04 (s), 29.14 (s), 29.19 (s), 29.33 (s), 29.35 (s), 29.37 (s), 29.47 (s), 29.49 (s), 29.50 (s), 29.52 (s), 29.53 (s), 31.76 (s), 43.91 (s), 49.28 (s), 53.24 (s), 83.33 (sept,  $J=28$  Hz), 103.23 (s), 111.08 (s), 119.22 (s), 121.51 (s), 122.33 (s), 122.83 (s), 123.81 (s), 125.06 (s), 125.29 (dd), 126.11 (s), 128.59 (s), 136.99 (s), 141.35 (s), 142.38 (s), 154.04 (s), 162.13 (dd), 173.30 (s). HRMS ( $m/z$ ):  $[\text{M}]^+$  calcd. 859.7803; found 859.7840;  $[\text{M}]^-$  calcd. 1759.1742; found 1759.1753.

### 3.1.2. Counterion-enhanced encapsulation and emission of cationic dyes in polymeric nanoparticles: the role of counterion nature.



**N(Me)<sub>4</sub>/F5-3PB-OH.** Tris(pentafluorophenyl)borane (1 eq., 200 mg, 0.391 mmol) was dissolved in 1 ml of DCM and tetramethylammonium hydroxide solution (25% w/w, aqueous) (10 eq., 1.4 mL, 3.91 mmol) was added. This two-phase system was stirred vigorously for 10 min, then phases were separated and aqueous phase was extracted two times with DCM. All DCM fractions were combined, dried over sodium sulphate, and after solvent evaporation 197 mg (0.328 mmol, 84%) of tetramethylammonium hydroxytris(pentafluorophenyl)borate (**N(Me)<sub>4</sub>/F5-3PB-OH**) was obtained as white crystals.

<sup>19</sup>F NMR (376 MHz, acetonitrile-*d*<sub>3</sub>) δ ppm -136.66 (1 F, d, *J*=23 Hz), -164.15 (1F, br t, *J*=20 Hz), -167.93 (1 F, br t, *J*=19 Hz)

<sup>11</sup>B NMR (128 MHz, acetonitrile -*d*<sub>3</sub>) δ ppm -4.00 (1 B, s)

<sup>1</sup>H NMR (400 MHz, acetonitrile-*d*<sub>3</sub>) δ ppm 3.06 (12 H, br s), 1.50 (1 H, br s)

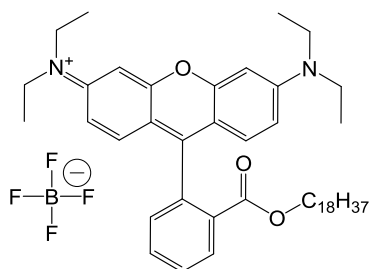
### General protocol for preparation of Rhodamine-counterion pairs

Rhodamine-counterion pairs were obtained according to a following ion exchange general procedure:

10 mg (0.012 mmol) of Rhodamine B octadecyl ester perchlorate (**R18/CIO<sub>4</sub>**) was mixed with 3-10 equivalents of appropriate counterion salt in DCM and the mixture was sonicated for 5 minutes. Products of ion exchange were purified on preparative TLC plates using DCM/MeOH mixtures as eluent. Results are summarised in the table below (Table S1).

**Table S1** – Conditions for ion exchange to obtain R18-counterion pairs.

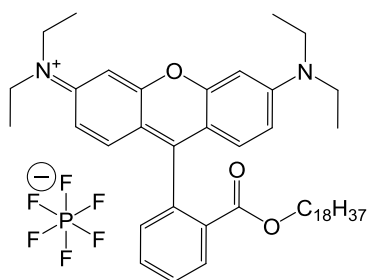
Product	Starting counterion salt	Equivalents of counterion salt	Eluent (DCM/MeOH)	Product yield, %
R18/BF <sub>4</sub>	NaBF <sub>4</sub>	10	90/10	54
R18/PF <sub>6</sub>	KPF <sub>6</sub>	10	90/10	71
R18/B(CN) <sub>4</sub>	KB(CN) <sub>4</sub>	3	90/10	68
R18/B(CF <sub>3</sub> ) <sub>4</sub>	KB(CF <sub>3</sub> ) <sub>4</sub>	3	90/10	78
R18/F5-3PB-OH	N(Me) <sub>4</sub> /F5-3PB-OH	3	90/10	73
R18/B <sub>21</sub> H <sub>18</sub>	KB <sub>21</sub> H <sub>18</sub>	3	95/5	91
R18/F5-TPB	Li/F5-TPB	3	95/5	95
R18/F6-TPB	K/F6-TPB	3	95/5	93
R18/F12-TPB	Na/F12-TPB	3	95/5	96



#### R18/BF<sub>4</sub>

<sup>19</sup>F NMR (376 MHz, acetonitrile-*d*<sub>3</sub>) δ ppm -151.82 (s) (<sup>10</sup>B coupling), -151.87 (s) (<sup>11</sup>B coupling)

<sup>11</sup>B NMR (128 MHz, acetonitrile-*d*<sub>3</sub>) δ ppm -1.18 (s)

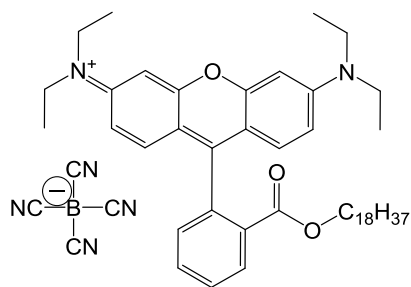


#### R18/PF<sub>6</sub>

<sup>19</sup>F NMR (376 MHz, acetonitrile-*d*<sub>3</sub>) δ ppm -72.93 (d, *J*=706 Hz)

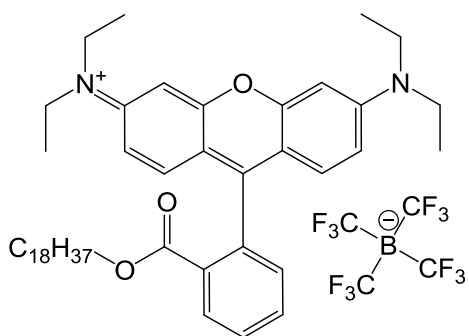
<sup>31</sup>P NMR (162 MHz, acetonitrile-*d*<sub>3</sub>) δ ppm -144.65 (sept, *J*=706 Hz)

HRMS (*m/z*): [M]<sup>-</sup> calcd. 144.9647; found 144.9658.



**R18/B(CN)<sub>4</sub>**

<sup>11</sup>B NMR (128 MHz, acetonitrile-*d*<sub>3</sub>) δ ppm -38.64 (s)

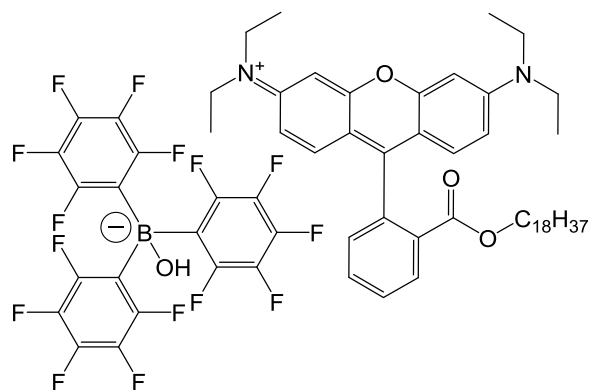


**R18/B(CF<sub>3</sub>)<sub>4</sub>**

<sup>19</sup>F NMR (376 MHz, acetonitrile-*d*<sub>3</sub>) δ ppm -62.91 (q, *J*=26 Hz)

<sup>11</sup>B NMR (128 MHz, acetonitrile-*d*<sub>3</sub>) δ ppm -19.02 (m, *J*=26 Hz)

HRMS (*m/z*): [M]<sup>-</sup> calcd. 285.9938; found 285.9943.

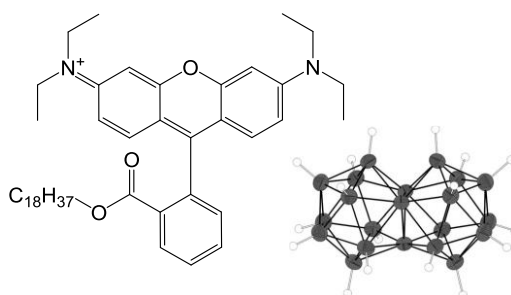


### R18/F5-3PB-OH

$^{19}\text{F}$  NMR (376 MHz, acetonitrile- $d_3$ )  $\delta$  ppm -136.53 (2 F, d,  $J=23$  Hz), -163.95 (1F, br t,  $J=19$  Hz), -167.83 (2 F, br t,  $J=19$  Hz)

$^{11}\text{B}$  NMR (128 MHz, acetonitrile- $d_3$ )  $\delta$  ppm -4.02 (1 B, s)

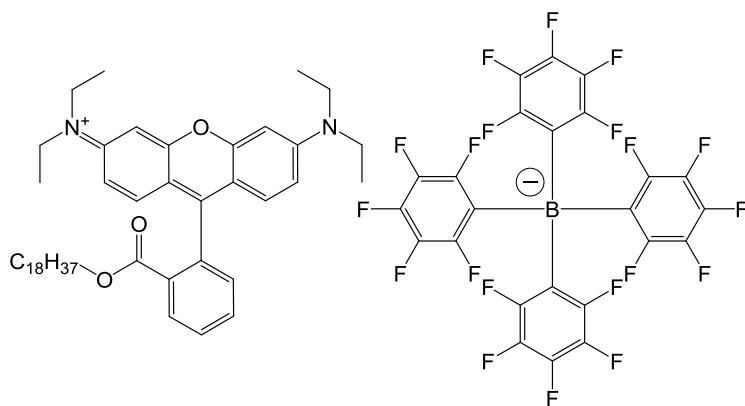
HRMS (m/z):  $[\text{M}]^-$  calcd. 528.9886; found 528.9866.



### R18/B<sub>21</sub>H<sub>18</sub>

$^{11}\text{B}$  NMR (128 MHz, acetonitrile- $d_3$ )  $\delta$  ppm 4.67 (6 B, d,  $J=170$  Hz), 1.83 (6 B, d,  $J=144$  Hz), -18.44 (6 B, d,  $J=144$  Hz), -20.60 (3 B, s)

MS (m/z):  $[\text{M}]^-$  calcd. 245.3513; found 245.36073.

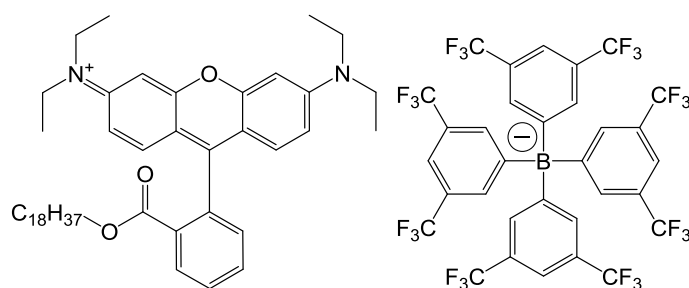


### R18/F5-TPB

$^{19}\text{F}$  NMR (376 MHz, acetonitrile- $d_3$ )  $\delta$  ppm -133.66 (2 F, s), -163.89 (1 F, br t,  $J=19$  Hz), -168.26 (2 F, br t,  $J=17$  Hz)

$^{11}\text{B}$  NMR (128 MHz, acetonitrile- $d_3$ )  $\delta$  ppm -16.70 (1 B, s)

HRMS (m/z): [M]<sup>-</sup> calcd. 678.9779; found 678.97267.

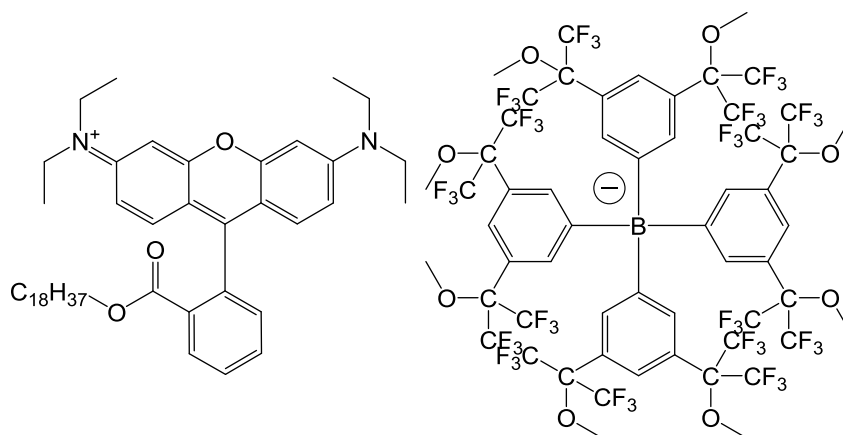


### R18/F6-TPB

$^{19}\text{F}$  NMR (376 MHz, acetonitrile- $d_3$ )  $\delta$  ppm -63.21 (1 F, s)

$^{11}\text{B}$  NMR (128 MHz, acetonitrile- $d_3$ )  $\delta$  ppm -6.66 (1 B, s)

HRMS (m/z): [M]<sup>-</sup> calcd. 863.0654; found 863.0607.



### R18/F12-TPB

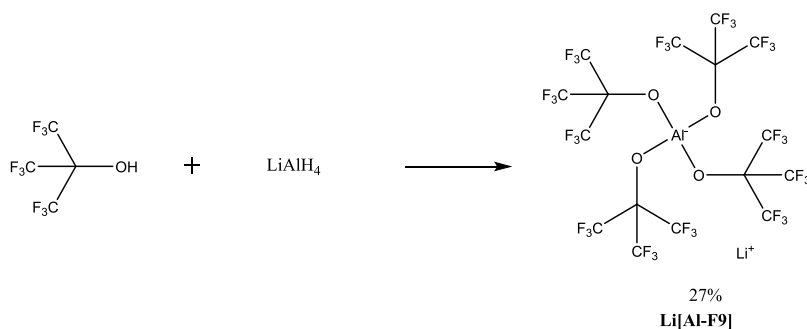
$^{19}\text{F}$  NMR (376 MHz, acetonitrile- $d_3$ )  $\delta$  ppm -71.82 (1 F, s)

$^{11}\text{B}$  NMR (128 MHz, acetonitrile- $d_3$ )  $\delta$  ppm -5.94 (1 B, s)

HRMS (m/z): [M] $^-$  calcd. 1759.1810; found 1759.1742.

### 3.1.3. Aluminium-based fluorinated counterion for enhanced encapsulation and emission of dyes in biodegradable polymer nanoparticles

#### Li[F9-Al]



An oven-dried 250 ml 3-necked flask with a stirring bar was vacuumated and argonated several times, afterwards 1M  $\text{LiAlH}_4$  solution in ether (1 eq., 20 mL, 20 mmol) was added through a syringe and the flask was put on a rotavap to evaporate ether. After the liquid was evaporated, temperature of the bath was increased to 80 °C and LAH was left do dry for 2,5 hours more at this temperature. After drying and cooling, the flask was argonated and put to an oil bath on the stirring plate; a reflux

condenser and a bubbler outlet were attached. The system was vacuumated and argonated 3 times, and dry toluene (70 mL) was added through a syringe. 3 ml of perfluoro-tert-butanol were added while stirring, but no gas evolution was observed, and reaction mixture was heated to 80 °C, when the strong gas evolution started and reaction mixture began to warm itself, so it was taken out of the bath until the reaction mixture calmed down. Afterwards, the flask was put back into an oil bath, and the rest of perfluoro-tert-butanol (11 ml, 5eq in total) was added dropwise.

Reaction mixture was left for 2 hrs at 80 °C and then temperature was risen to 100°C for one hour, afterwards the reaction was left at 50 °C over the weekend.

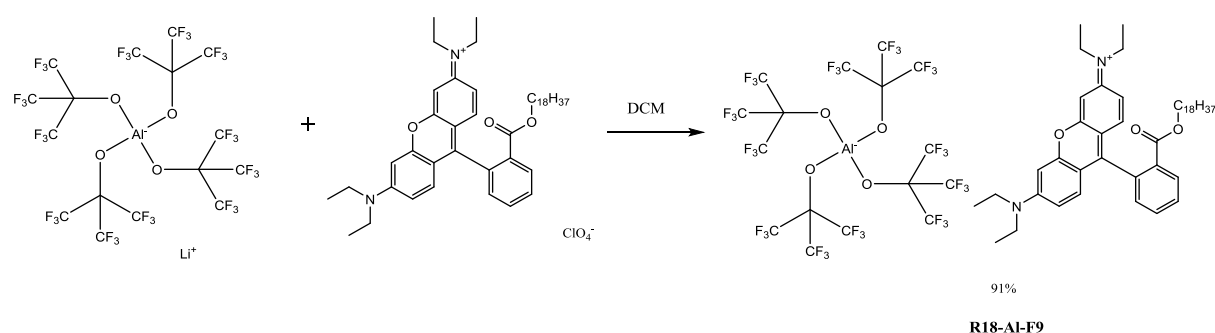
Afterwards, the reaction mixture was heated up to reflux and hot filtration was performed, separating greyish insoluble powder from toluene solution. Solution was let to cool down, put to freezer, and precipitated white crystals were filtered and washed with cold toluene and dried under vacuum, which yielded 5.23 g (5.37 mmol, 27 %) of **Li[F9-AI]**.

Decreased product yields and weaker reactivity of LAH comparing to original protocol could be explained by insufficiently dry toluene and/or argon.

$^{19}\text{F}$  NMR (376 MHz, DMSO- $d_6$ )  $\delta$  ppm -75.10 (s)

MS (m/z): [M]<sup>-</sup> calcd. for C<sub>16</sub>AlF<sub>36</sub>O<sub>4</sub>, 966.904; found 966.815

### R18/F9-AI



Rhodamine B octadecyl ester perchlorate (1 eq., 8 mg, 0.0101 mmol) and Li[F9-AI] (3 eq., 29.4 mg, 0.0302 mmol) were mixed in DCM and sonicated for 20 sec, TLC (MeOH/DCM 5/95) has shown full conversion. Product was purified by column

chromatography on silica, using DCM/MeOH 98/2 as eluent. After evaporation of solvents purple viscous oil of **R18/F9-AI** was obtained (15.2 mg, 0.00915 mmol, 91 %)

$^1\text{H}$  NMR (500 MHz, acetonitrile- $d_3$ )  $\delta$  ppm 8.30 (1 H, d,  $J=7.7$  Hz), 7.80 - 7.87 (2 H, m), 7.40 (1 H, d,  $J=7.4$  Hz), 7.11 (2 H, d,  $J=9.5$  Hz), 6.97 (2 H, dd,  $J=9.6, 2.6$  Hz), 6.86 (2 H, d,  $J=2.4$  Hz), 3.94 (2 H, t,  $J=6.4$  Hz), 3.64 (8 H, q,  $J=7.3$  Hz), 1.23 - 1.30 (40 H, m), 1.09 - 1.16 (4 H, m), 0.94 - 0.97 (2 H, m), 0.89 - 0.92 (3 H, m)

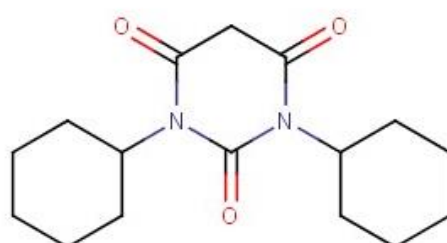
$^{13}\text{C}$  NMR (126 MHz, acetonitrile- $d_3$ )  $\delta$  ppm 166.07 (s), 163.53 (s), 159.30 (s), 158.42 (s), 156.28 (s), 133.73 (s), 133.34 (s), 131.87 (s), 131.66 (s), 131.21 (s), 130.87 (s), 130.75 (s), 121.78 (q,  $J=288$ Hz), 114.90 (s), 114.08 (s), 96.49 (s), 66.05 (s), 46.25 (s), 32.25 (s), 29.99 (s), 29.98 (s), 29.97 (s), 29.96 (s), 29.89 (s), 29.87 (s), 29.68 (s), 29.68 (s), 29.47 (s), 28.60 (s), 26.13 (s), 23.00 (s), 13.99 (s), 12.39 (s)

$^{19}\text{F}$  NMR (471 MHz, acetonitrile- $d_3$ )  $\delta$  ppm -75.98 (s)

HRMS (m/z):  $[\text{M}]^+$  calcd. for  $\text{C}_{46}\text{H}_{67}\text{N}_2\text{O}_3^+$ , 695.51517; found 695.51376

$[\text{M}]^-$  calcd. for  $\text{C}_{16}\text{AlF}_{36}\text{O}_4$ , 966.90371; found 966.89781

### **3.1.4. Bulky hydrophobic barbiturates for enhanced encapsulation and emission of cationic dyes inside polymer nanoparticles**

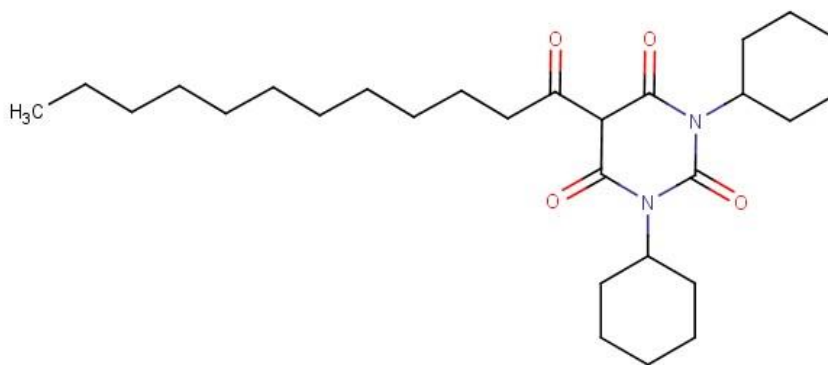


#### ***1,3-dicyclohexyl-1,3-diazinane-2,4,6-trione***

N-(2-cyclohexylethenylidene)cyclohexanamine (2.1 eq., 41.4 g, 201 mmol) and malonic acid (1 eq., 10 g, 96.1 mmol) were mixed in 200 ml of dry THF, slight heating of the system was observed. Reaction was left at stirring for about an hour, during which the precipitate of urea was formed. The precipitate was filtered off, filtrate was

collected, evaporated under reduced pressure and the obtained solid was recrystallized from ethanol. Obtained 1,3-dicyclohexyl-1,3-diazinane-2,4,6-trione (25 g, 85.5 mmol, 89 %) as white solid.

$^1\text{H}$  NMR (400 MHz, chloroform-*d*)  $\delta$  ppm 4.59 (2 H, tt), 3.59 (2 H, s), 2.24 (4 H, dd,), 1.84 (2 H, br s), 1.81 (2 H, br s), 1.58 - 1.67 (6 H, m), 1.14 - 1.40 (6 H, m).

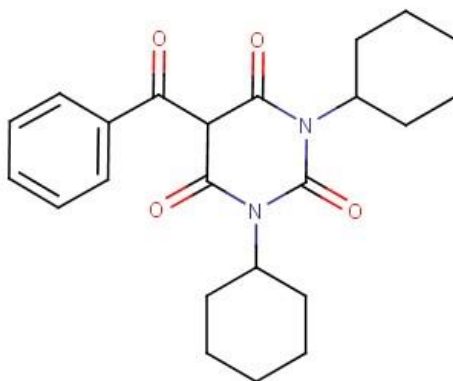


**Compound 1 (1,3-dicyclohexyl-5-dodecanoyl-1,3-diazinane-2,4,6-trione)**

1,3-dicyclohexyl-1,3-diazinane-2,4,6-trione (1 eq., 500 mg, 1.71 mmol), dodecanoic acid (1.3 eq., 445 mg, 2.22 mmol) and DMAP (1.2 eq., 250 mg, 2.05 mmol) were mixed in 10 ml of dry DCM. Afterwards EDCI (1.5 eq., 491 mg, 2.57 mmol) was added to the mixture and reaction was left to stir overnight. The next day the reaction mixture was diluted with 30 ml of ethyl acetate and washed with 1M HCl (2x) and water (2x). Organic layer was dried with magnesium sulphate, filtered and evaporated. Obtained oil was purified by gradient column chromatography using DCM/MeOH 99/1 - 9/1 as eluent. 1,3-dicyclohexyl-5-dodecanoyl-1,3-diazinane-2,4,6-trione (**compound 1**) (583 mg, 1.23 mmol, 72 %) was obtained as a colourless viscous oil.

$^1\text{H}$  NMR (400 MHz, chloroform-*d*)  $\delta$  ppm 4.73 (1 H, tt), 4.70 (1 H, tt), 3.10 (2 H, t), 2.28 - 2.37 (4 H, m), 1.79 - 1.88 (4 H, m), 1.57 - 1.72 (8 H, m), 1.21 - 1.42 (22 H, m) 0.88 (3 H, t).

$^{13}\text{C}$  NMR (101 MHz, chloroform-*d*)  $\delta$  ppm 200.06 (s), 170.30 (s), 161.20 (s), 37.34 (s), 31.93 (s), 29.64 (s), 29.63 (s), 29.61 (s), 29.53 (s), 29.51 (s), 29.39 (s), 29.35 (s), 29.17 (s), 29.05 (s), 26.49 (s), 26.45 (s), 25.67 (s), 25.33 (s), 25.25 (s), 22.70 (s), 14.12 (s)  
HRMS (m/z): [M+H] calcd. 475.3530; found 475.3300.



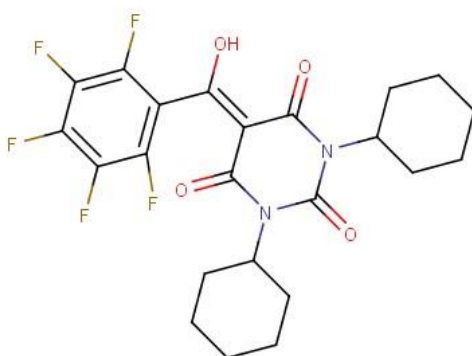
**Compound 2 (5-benzoyl-1,3-dicyclohexyl-1,3-diazinane-2,4,6-trione)**

1,3-dicyclohexyl-1,3-diazinane-2,4,6-trione (1 eq., 500 mg, 1.71 mmol), benzoic acid (1.3 eq., 271 mg, 2.22 mmol) and DMAP (1.2 eq., 250 mg, 2.05 mmol) were mixed in 10 ml of dry DCM. Afterwards EDCI (1.5 eq., 491 mg, 2.57 mmol) was added to the mixture and reaction was left to stir overnight. The next day the reaction mixture was diluted with 30 ml of ethyl acetate and washed with 1M HCl (2x) and water (2x). Organic layer was dried with magnesium sulphate, filtered and evaporated. Obtained oil was purified by gradient column chromatography using DCM/MeOH 99/1 - 9/1 as eluent. 5-benzoyl-1,3-dicyclohexyl-1,3-diazinane-2,4,6-trione (**compound 2**) was obtained as a white solid.

$^1\text{H}$  NMR (400 MHz, chloroform-*d*)  $\delta$  ppm 7.51 - 7.56 (3 H, m), 7.42 - 7.48 (2 H, m), 4.76 (1 H, tt), 4.67 (1 H, tt), 2.22 - 2.46 (4 H, m), 1.90 (1 H, br s), 1.87 (1 H, br s), 1.65 - 1.83 (4 H, m), 1.52 - 1.65 (4 H, m), 1.22 - 1.49 (6 H, m).

$^{13}\text{C}$  NMR (126 MHz, chloroform-*d*)  $\delta$  ppm 191.77 (s), 170.62 (s), 160.33 (s), 149.73 (s), 135.64 (s), 131.57 (s), 128.17 (s), 127.78 (s), 95.75 (s), 55.37 (s), 54.25 (s), 29.23 (s), 28.94 (s), 26.48 (s), 26.37 (s), 25.27 (s), 25.24 (s).

HRMS (m/z): [M+H] calcd. 397.2122; found 397.2126.



### **BarC6**

#### **(1,3-dicyclohexyl-5-(pentafluorophenyl)carbonyl-1,3-diazinane-2,4,6-trione)**

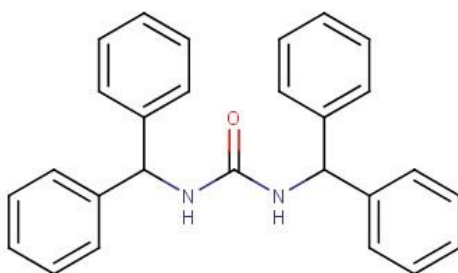
1,3-dicyclohexyl-1,3-diazinane-2,4,6-trione (1 eq., 500 mg, 1.71 mmol), pentafluorobenzoic acid (1.1 eq., 398 mg, 1.88 mmol) and DMAP (1.2 eq., 250 mg, 2.05 mmol) were mixed in 5 ml of dry DCM. Afterwards EDCI (1.5 eq., 491 mg, 2.57 mmol) was added to the mixture and reaction was left to stir overnight. The next day the reaction mixture was diluted with 30 ml of ethyl acetate and washed with 1M HCl (2x) and water (2x). Organic layer was dried with magnesium sulphate, filtered and evaporated. Obtained oil was purified by gradient column chromatography using DCM/MeOH 99/1 - 9/1 as eluent. 1,3-dicyclohexyl-5-(pentafluorophenyl)carbonyl-1,3-diazinane-2,4,6-trione (582 mg, 1.2 mmol, 70 %) (**BarC6**) was obtained as a white-yellowish solid.

$^1\text{H}$  NMR (400 MHz, chloroform-*d*)  $\delta$  ppm 4.75 (1 H, tt), 4.60 (1 H, tt), 2.29 - 2.42 (2 H, m), 2.16 - 2.28 (2 H, m), 1.91 (1 H, b s), 1.88 (1 H, br s), 1.73 - 1.82 (4 H, m), 1.49 - 1.66 (4 H, m), 1.10 - 1.44 (6 H, m).

$^{13}\text{C}$  NMR (126 MHz, chloroform-*d*)  $\delta$  ppm 178.45 (s), 170.00 (s), 165.04 (s), 159.45 (s), 149.04 (s), 143.2 (d), 142.55 (d), 137.48 (d), 111.83 (s), 98.69 (s), 56.07 (s), 54.82 (s), 29.15 (s), 29.14 (s), 28.81 (s), 26.36 (s), 26.38 (s), 26.30 (s), 25.14 (s).

$^{19}\text{F}$  NMR (376 MHz, chloroform-*d*)  $\delta$  ppm -140.65 (2F, d), -150.75 (1F, t), -160.90 (2F, t).

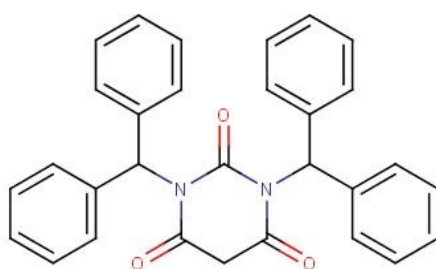
HRMS (m/z): [M+H] calcd. 487.1651; found 487.1654.



### **1,3-bis(diphenylmethyl)urea**

Aminodiphenylmethane (1 eq., 10 g, 9.43 mL, 54.6 mmol) was dissolved in 50 ml of dry THF and cdi (0.7 eq., 6.19 g, 38.2 mmol) was added. Reaction was left to reflux under stirring for 1h, TLC after acidic micro-workup has shown the presence of both urea product and amine reagent, therefore another portion of cdi (0.7 eq., 6.19 g, 38.2 mmol) was added and reflux was continued for another 2 hrs. After cooling of the mixture 10 ml of 1M aqueous HCl was added, left to stir for another 10 mins, white precipitate of urea was filtered off, washed with 1M HCl and cold ethanol. The solid was further recrystallized from ethanol to obtain 1,3-bis(diphenylmethyl)urea (6.5 g, 16.6 mmol, 43 %) as white solid.

$^1\text{H NMR}$  (400 MHz,  $\text{DMSO-}d_6$ )  $\delta$  ppm 7.30 - 7.35 (8 H, m), 7.21 - 7.28 (12 H, m), 6.95 (2 H, d), 5.88 (2 H, d).



### **1,3-bis(diphenylmethyl)-1,3-diazinane-2,4,6-trione**

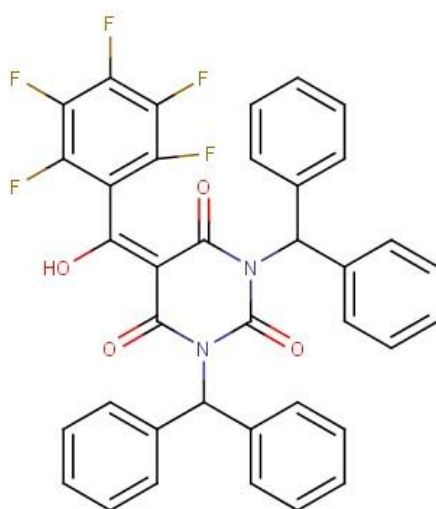
1,3-bis(diphenylmethyl)urea (1 eq., 1000 mg, 2.55 mmol) and malonic acid (1 eq., 265 mg, 2.55 mmol) were mixed in 3 ml of acetic acid. 1 ml of acetic anhydride was added and reaction mixture was stirred at 90 °C for 2h until it became completely homogenous. The TLC has shown presence of the starting urea and another 1 ml of acetic anhydride was added and heating continued for another 2h. After TLC has

shown disappearance of the starting urea, the reaction was cooled down, poured into 5x volume of water and extracted with DCM (x3). DCM fractions were collected, dried with magnesium sulphate, filtered and evaporated. Obtained mixture was purified by gradient column chromatography using DCM/MeOH 99/1 - 9/1 as eluent to obtain 1,3-bis(diphenylmethyl)-1,3-diazinane-2,4,6-trione (269 mg, 0.586 mmol, 23 %) as white solid.

$^1\text{H}$  NMR (400 MHz, chloroform-*d*)  $\delta$  ppm 7.22 - 7.30 (20 H, m), 7.17 (2 H, s), 3.65 (2 H, s).

$^{13}\text{C}$  NMR (126 MHz, chloroform-*d*)  $\delta$  ppm 164.47 (s), 150.88 (s), 137.58 (s), 128.64 (s), 128.34 (s), 127.70 (s), 60.57 (s), 40.94 (s).

HRMS (m/z): [M+H] calcd. 461.1860; found 461.18535.



### **BarPh2**

#### **(1,3-bis(diphenylmethyl)-5-(penta-fluorophenyl)carbonyl-1,3-diazinane-2,4,6-trione)**

1,3-bis(diphenylmethyl)-1,3-diazinane-2,4,6-trione (1 eq., 50 mg, 0.109 mmol) , pentafluorobenzoic acid (1.1 eq., 25.3 mg, 0.119 mmol) and DMAP (1.2 eq., 15.9 mg, 0.13 mmol) were mixed in 0.5 ml of dry DCM. Afterwards EDCI (1.5 eq., 31.2 mg, 0.163 mmol) was added to the mixture and reaction was left to stir overnight. The next day the reaction mixture was diluted with 3 ml of ethyl acetate and washed with 1M HCl and water. Organic layer was dried with magnesium sulphate, filtered and evaporated. Obtained oil was purified by gradient column chromatography using

DCM/MeOH 99/1 - 9/1 as eluent. 1,3-bis(diphenylmethyl)-5-(pentafluorophenyl)carbonyl-1,3-diazinane-2,4,6-trione (52.6 mg, 0.0803 mmol, 74 %) (BarPh2) was obtained as a white solid.

$^1\text{H}$  NMR (400 MHz, acetonitrile- $d_3$ )  $\delta$  ppm 7.14 – 7.40 (22H, m)

$^{19}\text{F}$  NMR (376 MHz, acetonitrile- $d_3$ , drop of TFA)  $\delta$  ppm -141.67 (2 F, d), -152.38 (1 F, t), -163.40 (2 F, t).

HRMS (m/z): [M]<sup>-</sup> calcd. 653.1505; found 653.1496.

## **3.2. Preparation of nanoparticles**

Stock solutions of polymers in acetonitrile were prepared at a concentration of 10 mg/ml. These solutions were then diluted with acetonitrile containing desired amount of dye, to the concentration of 2 mg/ml. 50  $\mu$ L of the polymer solutions were then added rapidly, using a micropipette and under shaking, (Thermomixer comfort, Eppendorf, 1000 rpm) to 450  $\mu$ L of 20 mM phosphate buffer (pH 7.4) at 21°C. The particles solution was then quickly diluted 5-fold with the same buffer

## **3.3. Characterisation of nanoparticles**

Dynamic light scattering measurements were performed on a Zetasizer Nano ZSP (Malvern Instruments S.A.). Electron microscopy was performed on Philips CM120 transmission electron microscope.

Absorption and emission spectra were recorded on a Cary 4000 scan UV-visible spectrophotometer (Varian) and a FluoroMax-4 spectrofluorometer (Horiba Jobin Yvon) equipped with a thermostated cell compartment, respectively. For standard recording of fluorescence spectra, the excitation wavelength was chosen to excite the sample optimally. The fluorescence spectra were corrected for detector response and lamp fluctuations. QY was calculated by comparative method, using appropriate reference sample. Steady-state anisotropy was measured on a Fluorolog (Jobin Yvon, Horiba).

### 3.4. Wide-field microscopy

For single particle fluorescence measurements, the NPs were immobilized on a glass surface with an adsorbed layer of polyethyleneimine (PEI). The solutions of NPs were diluted to a particle concentration of about 6 pM with buffer. 400  $\mu$ L of these solutions were then brought in contact with the PEI-covered glass for 15 min, followed by extensive rinsing with milliQ-water. The surfaces were left in milliQ water during the microscopy measurements. Quantum dots and FluoSpheres® red-orange at 6 pM concentration were immobilized and imaged in the same way as NPs. Single particle measurements were performed in the TIRF (Total Internal Reflection Fluorescence) mode on a homemade wide-field setup based on an Olympus IX-71 microscope with an oil immersion objective (NA = 1.49, 100 $\times$ ). The fluorescence signal was recorded with an EMCCD (ImagEM Hamamatsu). A DPSS (Cobolt) continuous wave (CW) laser emitting at 532 nm was used for excitation NPs loaded R18- and DiI-based NPs. 642 nm diode laser (Spectra-Physics Excelsior 635) was used for excitation DiD-based NPs containing. 488 nm diode laser Spectra-Physics Excelsior) was used for excitation of DiO-based NPs.

Single-particle microscopy experiments with barbiturate-based NPs were performed using another microscope recently installed in our laboratory. It is Nikon Ti-E inverted microscope using CFI Plan Apo 60X oil (NA = 1.4) objective and a Hamamatsu Orca Flash 4 camera. Excitation was realized with Spectra X LED light source centred at 550 nm. Emission was recorded through a 600 nm band-pass filter (50 nm bandwidth, Semrock). Data were recorded using NIS Elements and Fiji software, respectively. Image analysis for both microscopes was performed using the Fiji software.

### 3.5. Cellular studies

**Cell culture:** HeLa cells (ATCC® CCL-2™) were grown in DMEM (without phenol red), supplemented with 10 % heat inactivated fetal bovine serum (FBS), L-Glutamine, Penicillin and Streptomycin. KB cells (ATCC® CCL-17™) were first cultured in MEM with Earle's salts, supplemented with 10 % FBS, 1% non-essential amino acids (NEAA), 1 % MEM vitamins, and 40 µg/mL of Gentamicin. For 2 to 5 passages before labeling and testing the KB cells were cultured in DMEM without folic acid, supplemented with 10 % FBS, L-glutamine, sodium bicarbonate (3.5 g/L), and 40 µg/mL of Gentamicin. Chinese hamster ovary (CHO) cells were cultured in DMEM without phenol red, supplemented with 10 % FBS, L-Glutamine, 1% NEAA, Penicillin and Streptomycin. Human astrocytoma cells U87 (ATCC® HTB-14™) were cultured in MEM with Earle's salts, supplemented with 10 % FBS, 1% NEAA, 1 % sodium pyruvate, Penicillin and Streptomycin. The human embryonic kidney cell line 293T (ATCC® CRL-3216™) was cultured in DMEM with 4.5 g/L glucose, supplemented with 10 % FBS, Penicillin, and Streptomycin. The rat basophilic leukemia cell line RBL-2H3 (ATCC® CRL-2256™) was cultured in MEM with Earle's salts, supplemented with 15 % FBS, Penicillin and Streptomycin.

**Cell labeling:** For labeling, cells were seeded in 6 well plates at 200 000 cells/well (21 000 cells / cm<sup>2</sup>) or at 500 000 cells/well in 25 cm<sup>2</sup> cell culture flasks (20 000 cells / cm<sup>2</sup>). After letting the cells adhere for 18 h, the cell culture medium was removed and the cells were rinsed twice with optiMEM, followed by incubation with a freshly prepared solution of the NPs (0.15 nM in particles, 2.5 mL for 6 well plates, 10 mL for 25 cm<sup>2</sup> cell culture flasks). NP suspensions for cell labeling were prepared

starting from stock solutions in 20 mM phosphate buffer at a pH of 7.4 with a particle concentration of 3 nM (0.04 g/L of polymer). Depending on the desired color the stock solutions were mixed in the needed proportions (e.g. DiO:DiI:DiD 1:0:0 for “blue”, or 0.5:0.5:0 for “cyan”) and diluted in optiMEM to a concentration of 0.15 nM (0.002 g/L of polymer). After 3 h of incubation the NP suspension was removed, the cells were rinsed first with optiMEM, then with PBS, and finally with the corresponding cell culture medium. The resulting cells were then either cultured for longer periods, mixed, or transferred for imaging. For transfer or mixing the wells were rinsed twice with PBS followed by incubation for 2 to 5 min with 0.4 mL of trypsin at 37°C, and collection of the detached cells in 3 mL of the corresponding medium. After centrifugation and redispersion in 1 to 5 mL of medium (depending on the obtained number of cells), the cells were counted. For mixing of different cell populations, equal numbers of cells were combined in a centrifugation tube and thoroughly mixed before further use (for example “blue”, green”, and “red” cells or HeLa, KB, and CHO cells). For imaging, the cells, after the desired labeling, mixing, and time of culture, were seeded in LabTek 8 well plates at 60 000 cells/well and left to adhere for at least 18 h.

**Cytotoxicity:** Cells were seeded in 96-well plates at a density of 1000 cells per well and left to adhere for 18 h. The cells were then rinsed twice with optiMEM and PBS and 80  $\mu$ L of optiMEM were added to each well. 20  $\mu$ L of the NP solutions were then added per well, followed by homogenization. After incubation for 3h with the NPs in optiMEM, 100  $\mu$ L of DMEM media containing 20 % FBS were added to each well without prior rinsing. The cells were then incubated for 72 h, followed by rinsing with PBS. After incubation of the cells in DMEM containing 0.5  $\text{gL}^{-1}$  of MTT for 4h at 37°C, 80  $\mu$ L of the medium were removed, 50  $\mu$ L of DMSO were added, the plates were stirred for 20 min and the absorbance at 540 nm and 570 nm were recorded. For

calculating the relative cell viability, the absorbances were corrected by the absorbance of wells containing only the medium, and compared to wells with no added NPs. All experiments were carried out in quintuplicate.

***Doxorubicin and cell competition:*** HeLa cells were seeded in 25 cm<sup>2</sup> cell culture flasks (300 000 cells/ flask) and after adhesion for 18 h labeled with 6 different colors using the NPs as described above. After rinsing with Opti-MEM and DMEM, the cells were incubated with different concentration of doxorubicin for 24 h, with one doxorubicin concentration corresponding to one color. Following this incubation the cells were rinsed with PBS and DMEM and left for an additional 24 h. The cells were then rinsed again and detached using trypsin. After counting, the differently treated and colored cells were mixed at equal concentrations (except for the highest doxorubicin concentrations, for which the survival rate was too low to obtain the same total cell number under similar conditions). The cells were incubated for 4 h, rinsed very gently with HBSS, and imaged with a confocal microscope.

***Confocal microscopy:*** Fluorescence imaging of the cells in chambered microscope slides (LabTek or Ibidi 8 well plates) was performed on a Leica TSC SPE confocal microscope using either a 20x air objective or a 63x oil immersion objective. For all rhodamine based NPs the excitation wavelength was 561 nm and emission was recorded from 570 nm to 650 nm. The laser power and the sensitivity of detector was adjusted to obtained optimal signal. In case of multicolor cyanine-loaded NPs, different channels were recorded as follows: excitation 405 nm, emission recorded from 430 nm to 480 nm (for membrane probe F2N12SM); excitation 488 nm, emission recorded from 495 nm to 560 nm (for DiO-based NPs); excitation 561 nm, emission recorded from 570 nm to 610 nm (for Dil-based NPs); excitation 635 nm, emission recorded from 650 nm to 750 nm (for DiD-based NPs). The power of the 405 nm laser

was adjusted as needed. The power of the 488, 561, and 635 nm lasers was set either to 10 or to 20 % of the nominal power (same for all three) and the gain and offset were set to the same value for all three. Three successive sequences were recorded for each image.

## References

1. Lakowicz, J. R., *Principles of Fluorescence Spectroscopy*. 3 ed.; Springer US: 2006.
2. Jameson, D. M., *Introduction to Fluorescence*. CRC Press: Boca Raton, 2014.
3. Zhai, D. T.; Xu, W.; Zhang, L. Y.; Chang, Y. T., The role of "disaggregation" in optical probe development. *Chemical Society Reviews* **2014**, *43* (8), 2402-2411.
4. HERZ, A., AGGREGATION OF SENSITIZING DYES IN SOLUTION AND THEIR ADSORPTION ONTO SILVER-HALIDES. *Advances in Colloid and Interface Science* **1977**, *8* (4), 237-298.
5. Wuerthner, F.; Kaiser, T. E.; Saha-Moeller, C. R., J-Aggregates: From Serendipitous Discovery to Supramolecular Engineering of Functional Dye Materials. *Angewandte Chemie-International Edition* **2011**, *50* (15), 3376-3410.
6. Wurth, C.; Grabolle, M.; Pauli, J.; Spieles, M.; Resch-Genger, U., Relative and absolute determination of fluorescence quantum yields of transparent samples. *Nature Protocols* **2013**, *8* (8), 1535-1550.
7. Jelley, E. E., Spectral Absorption and Fluorescence of Dyes in the Molecular State. *Nature* **1936**, *138*, 1009.
8. Einfeld, A.; Briggs, J. S., The J-band of organic dyes: lineshape and coherence length. *Chemical Physics* **2002**, *281* (1), 61-70.
9. LAKOWICZ, J.; BALTER, A., ANALYSIS OF EXCITED-STATE PROCESSES BY PHASE-MODULATION FLUORESCENCE SPECTROSCOPY. *Biophysical Chemistry* **1982**, *16* (2), 117-132.
10. v. Büнау, G., J. B. Birks: Photophysics of Aromatic Molecules. Wiley-Interscience, London 1970. 704 Seiten. Preis: 210s. *Berichte der Bunsengesellschaft für physikalische Chemie* **1970**, *74* (12), 1294--1295.
11. Chudakov, D.; Matz, M.; Lukyanov, S.; Lukyanov, K., Fluorescent Proteins and Their Applications in Imaging Living Cells and Tissues. *Physiological Reviews* **2010**, *90* (3), 1103-1163.
12. Chen, J.; Zhang, P.; Yu, X.; Li, X.; Tao, H.; Yi, P., Fabrication of Novel Polymer Nanoparticle-Based Fluorescence Resonance Energy Transfer Systems and their Tunable Fluorescence Properties. *Journal of Macromolecular Science Part a-Pure and Applied Chemistry* **2011**, *48* (3), 219-226.
13. Frigoli, M.; Ouadahi, K.; Larpent, C., A Cascade FRET-Mediated Ratiometric Sensor for Cu(2+)Ions Based on Dual Fluorescent Ligand-Coated Polymer Nanoparticles. *Chemistry-a European Journal* **2009**, *15* (33), 8319-8330.
14. Ouadahi, K.; Sbagoud, K.; Allard, E.; Larpent, C., FRET-mediated pH-responsive dual fluorescent nanoparticles prepared via click chemistry. *Nanoscale* **2012**, *4* (3), 727-732.
15. Sapsford, K.; Berti, L.; Medintz, I., Materials for fluorescence resonance energy transfer analysis: Beyond traditional donor-acceptor combinations. *Angewandte Chemie-International Edition* **2006**, *45* (28), 4562-4588.
16. LAKOWICZ, J.; GRYCZYNSKI, I.; LACZKO, G.; WICZK, W.; JOHNSON, M., DISTRIBUTION OF DISTANCES BETWEEN THE TRYPTOPHAN AND THE N-TERMINAL RESIDUE OF MELITTIN IN ITS COMPLEX WITH CALMODULIN, TROPONIN-C, AND PHOSPHOLIPIDS. *Protein Science* **1994**, *3* (4), 628-637.

17. Mallick, A.; Haldar, B.; Chattopadhyay, N., Spectroscopic investigation on the interaction of ICT probe 3-acetyl-4-oxo-6,7-dihydro-12H indolo- 2,3-a quinolizine with serum albumins. *Journal of Physical Chemistry B* **2005**, *109* (30), 14683-14690.
18. Yeow, E.; Ghiggino, K.; Reek, J.; Crossley, M.; Bosman, A.; Schenning, A.; Meijer, E., The dynamics of electronic energy transfer in novel multiporphyrin functionalized dendrimers: A time-resolved fluorescence anisotropy. *Journal of Physical Chemistry B* **2000**, *104* (12), 2596-2606.
19. Berberan-Santos, M.; Choppinet, P.; Fedorov, A.; Jullien, L.; Valeur, B., Multichromophoric cyclodextrins. 6. Investigation of excitation energy hopping by Monte-Carlo simulations and time-resolved fluorescence anisotropy. *Journal of the American Chemical Society* **1999**, *121* (11), 2526-2533.
20. Devauges, V.; Matthews, D.; Aluko, J.; Nedbal, J.; Levitt, J.; Poland, S.; Coban, O.; Weitsman, G.; Monypenny, J.; Ng, T.; Ameer-Beg, S., Steady-State Acceptor Fluorescence Anisotropy Imaging under Evanescent Excitation for Visualisation of FRET at the Plasma Membrane. *Plos One* **2014**, *9* (10).
21. EKIMOV, A.; ONUSHCHENKO, A., QUANTUM SIZE EFFECT IN 3-DIMENSIONAL MICROSCOPIC SEMICONDUCTOR CRYSTALS. *Jetp Letters* **1981**, *34* (6), 345-349.
22. Alivisatos, A. P., Semiconductor clusters, nanocrystals, and quantum dots. *Science* **1996**, *271* (5251), 933-937.
23. BRUS, L., ELECTRONIC WAVE-FUNCTIONS IN SEMICONDUCTOR CLUSTERS - EXPERIMENT AND THEORY. *Journal of Physical Chemistry* **1986**, *90* (12), 2555-2560.
24. Alivisatos, A., Semiconductor nanocrystals as fluorescent biological labels. *Abstracts of Papers of the American Chemical Society* **1999**, *218*, U296-U296.
25. Kuno, M.; Fromm, D.; Hamann, H.; Gallagher, A.; Nesbitt, D., Nonexponential "blinking" kinetics of single CdSe quantum dots: A universal power law behavior. *Journal of Chemical Physics* **2000**, *112* (7), 3117-3120.
26. Michalet, X.; Pinaud, F.; Bentolila, L.; Tsay, J.; Doose, S.; Li, J.; Sundaresan, G.; Wu, A.; Gambhir, S.; Weiss, S., Quantum dots for live cells, in vivo imaging, and diagnostics. *Science* **2005**, *307* (5709), 538-544.
27. Hardman, R., A toxicologic review of quantum dots: Toxicity depends on physicochemical and environmental factors. *Environmental Health Perspectives* **2006**, *114* (2), 165-172.
28. Liu, H.; Ye, T.; Mao, C., Fluorescent carbon nanoparticles derived from candle soot. *Angewandte Chemie-International Edition* **2007**, *46* (34), 6473-6475.
29. Zhai, X.; Zhang, P.; Liu, C.; Bai, T.; Li, W.; Dai, L.; Liu, W., Highly luminescent carbon nanodots by microwave-assisted pyrolysis. *Chemical Communications* **2012**, *48* (64), 7955-7957.
30. Dong, Y.; Wang, R.; Li, H.; Shao, J.; Chi, Y.; Lin, X.; Chen, G., Polyamine-functionalized carbon quantum dots for chemical sensing. *Carbon* **2012**, *50* (8), 2810-2815.
31. Sun, Y.; Zhou, B.; Lin, Y.; Wang, W.; Fernando, K.; Pathak, P.; Mezziani, M.; Harruff, B.; Wang, X.; Wang, H.; Luo, P.; Yang, H.; Kose, M.; Chen, B.; Veca, L.; Xie, S., Quantum-sized carbon dots for bright and colorful photoluminescence. *Journal of the American Chemical Society* **2006**, *128* (24), 7756-7757.
32. Lim, S.; Shen, W.; Gao, Z., Carbon quantum dots and their applications. *Chemical Society Reviews* **2015**, *44* (1), 362-381.
33. Zhou, B.; Shi, B.; Jin, D.; Liu, X., Controlling upconversion nanocrystals for emerging applications. *Nature Nanotechnology* **2015**, *10* (11), 924-936.

34. Chen, G.; Qju, H.; Prasad, P.; Chen, X., Upconversion Nanoparticles: Design, Nanochemistry, and Applications in Theranostics. *Chemical Reviews* **2014**, *114* (10), 5161-5214.
35. Bonacchi, S.; Genovese, D.; Juris, R.; Montalti, M.; Prodi, L.; Rampazzo, E.; Zaccheroni, N., Luminescent Silica Nanoparticles: Extending the Frontiers of Brightness. *Angewandte Chemie-International Edition* **2011**, *50* (18), 4056-4066.
36. YAMAUCHI, H.; ISHIKAWA, T.; KONDO, S., SURFACE CHARACTERIZATION OF ULTRAMICRO SPHERICAL-PARTICLES OF SILICA PREPARED BY W/O MICROEMULSION METHOD. *Colloids and Surfaces* **1989**, *37*, 71-80.
37. Rio-Echevarria, I.; Tavano, R.; Causin, V.; Papini, E.; Mancin, F.; Moretto, A., Water-Soluble Peptide-Coated Nanoparticles: Control of the Helix Structure and Enhanced Differential Binding to Immune Cells. *Journal of the American Chemical Society* **2011**, *133* (1), 8-11.
38. Montalti, M.; Prodi, L.; Rampazzo, E.; Zaccheroni, N., Dye-doped silica nanoparticles as luminescent organized systems for nanomedicine. *Chemical Society Reviews* **2014**, *43* (12), 4243-4268.
39. Burns, A.; Ow, H.; Wiesner, U., Fluorescent core-shell silica nanoparticles: towards "Lab on a Particle" architectures for nanobiotechnology. *Chemical Society Reviews* **2006**, *35* (11), 1028-1042.
40. Ow, H.; Larson, D.; Srivastava, M.; Baird, B.; Webb, W.; Wiesner, U., Bright and stable core-shell fluorescent silica nanoparticles. *Nano Letters* **2005**, *5* (1), 113-117.
41. Hormann, K.; Zimmer, A., Drug delivery and drug targeting with parenteral lipid nanoemulsions - A review. *Journal of Controlled Release* **2016**, *223*, 85-98.
42. Singh, Y.; Meher, J. G.; Raval, K.; Khan, F. A.; Chaurasia, M.; Jain, N. K.; Chourasia, M. K., Nanoemulsion: Concepts, development and applications in drug delivery. *Journal of Controlled Release* **2017**, *252*, 28-49.
43. Hippalgaonkar, K.; Majumdar, S.; Kansara, V., Injectable Lipid Emulsions-Advancements, Opportunities and Challenges. *Aaps Pharmscitech* **2010**, *11* (4), 1526-1540.
44. Delmas, T.; Piraux, H.; Couffin, A.; Texier, I.; Vinet, F.; Poulin, P.; Cates, M.; Bibette, J., How To Prepare and Stabilize Very Small Nanoemulsions. *Langmuir* **2011**, *27* (5), 1683-1692.
45. Gravier, J.; Navarro, F.; Delmas, T.; Mittler, F.; Couffin, A.; Vinet, F.; Texier, I., Lipidots: competitive organic alternative to quantum dots for in vivo fluorescence imaging. *Journal of Biomedical Optics* **2011**, *16* (9).
46. Ng, K.; Lovell, J.; Zheng, G., Lipoprotein-Inspired Nanoparticles for Cancer Theranostics. *Accounts of Chemical Research* **2011**, *44* (10), 1105-1113.
47. Cormode, D.; Jarzyna, P.; Mulder, W.; Fayad, Z., Modified natural nanoparticles as contrast agents for medical imaging. *Advanced Drug Delivery Reviews* **2010**, *62* (3), 329-338.
48. Zheng, G.; Chen, J.; Li, H.; Glickson, J., Rerouting lipoprotein nanoparticles to selected alternate receptors for the targeted delivery of cancer diagnostic and therapeutic agents. *Proceedings of the National Academy of Sciences of the United States of America* **2005**, *102* (49), 17757-17762.
49. Cheng, C. C.; Huang, J. J.; Muhale, A. A.; Liao, Z. S.; Huang, S. Y.; Lee, S. C.; Chiu, C. W.; Lee, D. J., Supramolecular fluorescent nanoparticles functionalized with controllable physical properties and temperature-responsive release behavior. *Polymer Chemistry* **2017**, *8* (15), 2292-2298.

50. Shulov, I.; Arntz, Y.; Mely, Y.; Pivovarenko, V.; Klymchenko, A., Non-coordinating anions assemble cyanine amphiphiles into ultra-small fluorescent nanoparticles. *Chemical Communications* **2016**, 52 (51), 7962-7965.
51. Zheng, X.; Xing, D.; Zhou, F.; Wu, B.; Chen, W., Indocyanine Green-Containing Nanostructure as Near Infrared Dual-Functional Targeting Probes for Optical Imaging and Photothermal Therapy. *Molecular Pharmaceutics* **2011**, 8 (2), 447-456.
52. Kirchherr, A.; Briel, A.; Mader, K., Stabilization of Indocyanine Green by Encapsulation within Micellar Systems. *Molecular Pharmaceutics* **2009**, 6 (2), 480-491.
53. Li, S. H.; Johnson, J.; Peck, A.; Xie, Q., Near infrared fluorescent imaging of brain tumor with IR780 dye incorporated phospholipid nanoparticles. *Journal of Translational Medicine* **2017**, 15.
54. Zhou, F.; Li, B., Exonuclease III-Assisted Target Recycling Amplification Coupled with Liposome-Assisted Amplification: One-Step and Dual-Amplification Strategy for Highly Sensitive Fluorescence Detection of DNA. *Analytical Chemistry* **2015**, 87 (14), 7156-7162.
55. Mahrhauser, D. S.; Reznicek, G.; Kotisch, H.; Brandstetter, M.; Nagelreiter, C.; Kwizda, K.; Valenta, C., Semi-solid fluorinated-DPPC liposomes: Morphological, rheological and thermic properties as well as examination of the influence of a model drug on their skin permeation. *International Journal of Pharmaceutics* **2015**, 486 (1-2), 350-355.
56. Deissler, V.; Ruger, R.; Frank, W.; Fahr, A.; Kaiser, W.; Hilger, I., Fluorescent liposomes as contrast agents for in vivo optical imaging of edemas in mice. *Small* **2008**, 4 (8), 1240-1246.
57. Portnoy, E.; Lecht, S.; Lazarovici, P.; Danino, D.; Magdassi, S., Cetuximab-labeled liposomes containing near-infrared probe for in vivo imaging. *Nanomedicine-Nanotechnology Biology and Medicine* **2011**, 7 (4), 480-488.
58. Sou, K.; Goins, B.; Takeoka, S.; Tsuchida, E.; Phillips, W., Selective uptake of surface-modified phospholipid vesicles by bone marrow macrophages in vivo. *Biomaterials* **2007**, 28 (16), 2655-2666.
59. Sandanaraj, B.; Gremlich, H.; Kneuer, R.; Dawson, J.; Wacha, S., Fluorescent Nanoprobes as a Biomarker for Increased Vascular Permeability: Implications in Diagnosis and Treatment of Cancer and Inflammation. *Bioconjugate Chemistry* **2010**, 21 (1), 93-101.
60. Feng, L.; Zhu, C.; Yuan, H.; Liu, L.; Lv, F.; Wang, S., Conjugated polymer nanoparticles: preparation, properties, functionalization and biological applications. *Chemical Society Reviews* **2013**, 42 (16), 6620-6633.
61. Tuncel, D.; Demir, H., Conjugated polymer nanoparticles. *Nanoscale* **2010**, 2 (4), 484-494.
62. Kurokawa, N.; Yoshikawa, H.; Hirota, N.; Hyodo, K.; Masuhara, H., Size-dependent spectroscopic properties and thermochromic behavior in poly(substituted thiophene) nanoparticles. *Chemphyschem* **2004**, 5 (10), 1609-1615.
63. Wu, C.; Jin, Y.; Schneider, T.; Burnham, D.; Smith, P.; Chiu, D., Ultrabright and Bioorthogonal Labeling of Cellular Targets Using Semiconducting Polymer Dots and Click Chemistry. *Angewandte Chemie-International Edition* **2010**, 49 (49), 9436-9440.
64. Rao, J.; Geckeler, K., Polymer nanoparticles: Preparation techniques and size-control parameters. *Progress in Polymer Science* **2011**, 36 (7), 887-913.
65. Tian, Z.; Shaller, A. D.; Li, A. D. Q., Twisted perylene dyes enable highly fluorescent and photostable nanoparticles. *Chemical Communications* **2009**, (2), 180-182.

66. Chen, J.; Zhang, P.; Fang, G.; Yi, P.; Yu, X.; Li, X.; Zeng, F.; Wu, S., Synthesis and Characterization of Novel Reversible Photoswitchable Fluorescent Polymeric Nanoparticles via One-Step Miniemulsion Polymerization. *Journal of Physical Chemistry B* **2011**, *115* (13), 3354-3362.
67. Candau, F.; Pabon, M.; Anquetil, J. Y., Polymerizable microemulsions: some criteria to achieve an optimal formulation. *Colloids and Surfaces a-Physicochemical and Engineering Aspects* **1999**, *153* (1-3), 47-59.
68. Reisch, A.; Klymchenko, A. S., Fluorescent Polymer Nanoparticles Based on Dyes: Seeking Brighter Tools for Bioimaging. *Small* **2016**, *12* (15), 1968-1992.
69. Mora-Huertas, C. E.; Fessi, H.; Elaissari, A., Influence of process and formulation parameters on the formation of submicron particles by solvent displacement and emulsification-diffusion methods Critical comparison. *Advances in Colloid and Interface Science* **2011**, *163* (2), 90-122.
70. Geng, J.; Li, K.; Qin, W.; Ma, L.; Gurzadyan, G. G.; Tang, B. Z.; Liu, B., Eccentric Loading of Fluorogen with Aggregation-Induced Emission in PLGA Matrix Increases Nanoparticle Fluorescence Quantum Yield for Targeted Cellular Imaging. *Small* **2013**, *9* (11), 2012-2019.
71. Kwon, G. S.; Kataoka, K., Block copolymer micelles as long-circulating drug vehicles. *Advanced Drug Delivery Reviews* **2012**, *64*, 237-245.
72. Pegaz, B.; Debeve, E.; Borle, F.; Ballini, J. P.; van den Bergh, H.; Kouakou-Konan, Y. N., Encapsulation of porphyrins and chlorins in biodegradable nanoparticles: The effect of dye lipophilicity on the extravasation and the photothrombic activity. A comparative study. *Journal of Photochemistry and Photobiology B-Biology* **2005**, *80* (1), 19-27.
73. Chen, H. T.; Kim, S. W.; Li, L.; Wang, S. Y.; Park, K.; Cheng, J. X., Release of hydrophobic molecules from polymer micelles into cell membranes revealed by Forster resonance energy transfer imaging. *Proceedings of the National Academy of Sciences of the United States of America* **2008**, *105* (18), 6596-6601.
74. Wagh, A.; Qian, S. Y.; Law, B., Development of Biocompatible Polymeric Nanoparticles for in Vivo NIR and FRET Imaging. *Bioconjugate Chemistry* **2012**, *23* (5), 981-992.
75. Salvati, A.; Aberg, C.; dos Santos, T.; Varela, J.; Pinto, P.; Lynch, I.; Dawson, K. A., Experimental and theoretical comparison of intracellular import of polymeric nanoparticles and small molecules: toward models of uptake kinetics. *Nanomedicine-Nanotechnology Biology and Medicine* **2011**, *7* (6), 818-826.
76. Tenuta, T.; Monopoli, M. P.; Kim, J.; Salvati, A.; Dawson, K. A.; Sandin, P.; Lynch, I., Elution of Labile Fluorescent Dye from Nanoparticles during Biological Use. *Plos One* **2011**, *6* (10), 6.
77. Klymchenko, A. S.; Roger, E.; Anton, N.; Anton, H.; Shulov, I.; Vermot, J.; Mely, Y.; Vandamme, T. F., Highly lipophilic fluorescent dyes in nano-emulsions: towards bright non-leaking nano-droplets. *Rsc Advances* **2012**, *2* (31), 11876-11886.
78. Bastiat, G.; Pritz, C. O.; Roider, C.; Fouchet, F.; Lignieres, E.; Jesacher, A.; Glueckert, R.; Ritsch-Marte, M.; Schrott-Fischer, A.; Saulnier, P.; Benoit, J. P., A new tool to ensure the fluorescent dye labeling stability of nanocarriers: A real challenge for fluorescence imaging. *Journal of Controlled Release* **2013**, *170* (3), 334-342.
79. Simonsson, C.; Bastiat, G.; Pitorre, M.; Klymchenko, A. S.; Bejaud, J.; Mely, Y.; Benoit, J. P., Inter-nanocarrier and nanocarrier-to-cell transfer assays demonstrate the risk of an immediate unloading of dye from labeled lipid nanocapsules. *European Journal of Pharmaceutics and Biopharmaceutics* **2016**, *98*, 47-56.

80. Petersen, S.; Fahr, A.; Bunjes, H., Flow Cytometry as a New Approach To Investigate Drug Transfer between Lipid Particles. *Molecular Pharmaceutics* **2010**, *7* (2), 350-363.
81. Snipstad, S.; Hak, S.; Baghirov, H.; Sulheim, E.; Mørch, Ý.; Llu, S.; von Haartman, E.; Bck, M.; Nilsson, K. P. R.; Klymchenko, A. S.; de Lange Davies, C.; Åslund, A. K. O., Labeling nanoparticles: Dye leakage and altered cellular uptake. *Cytometry Part A* **2016**, n/a-n/a.
82. Sletten, E. M.; Swager, T. M., Fluorofluorophores: Fluorescent Fluorous Chemical Tools Spanning the Visible Spectrum. *Journal of the American Chemical Society* **2014**, *136* (39), 13574-13577.
83. Kilin, V. N.; Anton, H.; Anton, N.; Steed, E.; Vermot, J.; Vandamme, T. E.; Mely, Y.; Klymchenko, A. S., Counterion-enhanced cyanine dye loading into lipid nanodroplets for single-particle tracking in zebrafish. *Biomaterials* **2014**, *35* (18), 4950-4957.
84. Breul, A. M.; Hager, M. D.; Schubert, U. S., Fluorescent monomers as building blocks for dye labeled polymers: synthesis and application in energy conversion, biolabeling and sensors. *Chemical Society Reviews* **2013**, *42* (12), 5366-5407.
85. Sun, G.; Berezin, M. Y.; Fan, J.; Lee, H.; Ma, J.; Zhang, K.; Wooley, K. L.; Achilefu, S., Bright fluorescent nanoparticles for developing potential optical imaging contrast agents. *Nanoscale* **2010**, *2* (4), 548-558.
86. Errede, L. A.; Hanson, S. C., POLYMER SWELLING .15. SWELLING AND DESWELLING STUDIES OF POLYSTYRENE LIQUID-SYSTEMS IN BINARY-SOLUTIONS. *Journal of Applied Polymer Science* **1994**, *54* (5), 619-647.
87. Zhu, H. G.; McShane, M. J., Loading of hydrophobic materials into polymer particles: Implications for fluorescent nanosensors and drug delivery. *Journal of the American Chemical Society* **2005**, *127* (39), 13448-13449.
88. Behnke, T.; Wuerth, C.; Laux, E.-M.; Hoffmann, K.; Resch-Genger, U., Simple strategies towards bright polymer particles via one-step staining procedures. *Dyes and Pigments* **2012**, *94* (2), 247-257.
89. Monguzzi, A.; Frigoli, M.; Larpent, C.; Meinardi, F., Laser dye doped nanoparticles for highly photostable optical nanoamplifiers. *Rsc Advances* **2012**, *2* (31), 11731-11736.
90. Rodriguez, V. B.; Henry, S. M.; Hoffman, A. S.; Stayton, P. S.; Li, X.; Pun, S. H., Encapsulation and stabilization of indocyanine green within poly(styrene-alt-maleic anhydride) block-poly(styrene) micelles for near-infrared imaging. *Journal of Biomedical Optics* **2008**, *13* (1).
91. Martin, V.; Banuelos, J.; Enciso, E.; Lopez Arbeloa, I.; Costela, A.; Garcia-Moreno, I., Photophysical and Lasing Properties of Rhodamine 6G Confined in Polymeric Nanoparticles. *Journal of Physical Chemistry C* **2011**, *115* (10), 3926-3933.
92. Lee, Y.-D.; Lim, C.-K.; Kim, S.; Kwon, I. C.; Kim, J., Squaraine-Doped Functional Nanoprobes: Lipophilically Protected Near-Infrared Fluorescence for Bioimaging. *Advanced Functional Materials* **2010**, *20* (17), 2786-2793.
93. Gazon, C.; Rieger, J.; Charleux, B.; Clavier, G.; Meallet-Renault, R., Ultrabright BODIPY-Tagged Polystyrene Nanoparticles: Study of Concentration Effect on Photophysical Properties. *Journal of Physical Chemistry C* **2014**, *118* (25), 13945-13952.
94. Gazon, C.; Rieger, J.; Meallet-Renault, R.; Charleux, B.; Clavier, G., Ultrabright Fluorescent Polymeric Nanoparticles Made from a New Family of BODIPY Monomers. *Macromolecules* **2013**, *46* (13), 5167-5176.

95. Zhang, X.; Chen, Z.; Wuerthner, F., Morphology control of fluorescent nanoaggregates by co-self-assembly of wedge- and dumbbell-shaped amphiphilic perylene bisimides. *Journal of the American Chemical Society* **2007**, *129* (16), 4886-+.
96. Yang, Z.; Yuan, Y.; Jiang, R.; Fu, N.; Lu, X.; Tian, C.; Hu, W.; Fan, Q.; Huang, W., Homogeneous near-infrared emissive polymeric nanoparticles based on amphiphilic diblock copolymers with perylene diimide and PEG pendants: self-assembly behavior and cellular imaging application. *Polymer Chemistry* **2014**, *5* (4), 1372-1380.
97. Meallet-Renault, R.; Herault, A.; Vachon, J. J.; Pansu, R. B.; Amigoni-Gerbier, S.; Larpent, C., Fluorescent nanoparticles as selective Cu(II) sensors. *Photochemical & Photobiological Sciences* **2006**, *5* (3), 300-310.
98. Wurthner, F., Perylene bisimide dyes as versatile building blocks for functional supramolecular architectures. *Chemical Communications* **2004**, (14), 1564-1579.
99. Colby, K. A.; Burdett, J. J.; Frisbee, R. F.; Zhu, L.; Dillon, R. J.; Bardeen, C. J., Electronic Energy Migration on Different Time Scales: Concentration Dependence of the Time-Resolved Anisotropy and Fluorescence Quenching of Lumogen Red in Poly(methyl methacrylate). *Journal of Physical Chemistry A* **2010**, *114* (10), 3471-3482.
100. Trofymchuk, K.; Reisch, A.; Shulov, I.; Mely, Y.; Klymchenko, A. S., Tuning the color and photostability of perylene diimides inside polymer nanoparticles: towards biodegradable substitutes of quantum dots. *Nanoscale* **2014**, *6* (21), 12934-12942.
101. Zhang, X.; Gohl, D.; Stepanenko, V.; Wurthner, F., Hierarchical Growth of Fluorescent Dye Aggregates in Water by Fusion of Segmented Nanostructures. *Angewandte Chemie-International Edition* **2014**, *53* (5), 1270-1274.
102. Gohl, D.; Zhang, X.; Wurthner, F., Molecular Assemblies of Perylene Bisimide Dyes in Water. *Angewandte Chemie-International Edition* **2012**, *51* (26), 6328-6348.
103. Banal, J. L.; Soleimaninejad, H.; Jradi, F. M.; Liu, M. Y.; White, J. M.; Blakers, A. W.; Cooper, M. W.; Jones, D. J.; Ghiggino, K. P.; Marder, S. R.; Smith, T. A.; Wong, W. W. H., Energy Migration in Organic Solar Concentrators with a Molecularly Insulated Perylene Diimide. *Journal of Physical Chemistry C* **2016**, *120* (24), 12952-12958.
104. Luo, J. D.; Xie, Z. L.; Lam, J. W. Y.; Cheng, L.; Chen, H. Y.; Qiu, C. F.; Kwok, H. S.; Zhan, X. W.; Liu, Y. Q.; Zhu, D. B.; Tang, B. Z., Aggregation-induced emission of 1-methyl-1,2,3,4,5-pentaphenylsilole. *Chemical Communications* **2001**, (18), 1740-1741.
105. Hong, Y.; Lam, J. W. Y.; Tang, B. Z., Aggregation-induced emission. *Chemical Society Reviews* **2011**, *40* (11), 5361-5388.
106. Grabowski, Z. R.; Rotkiewicz, K.; Rettig, W., Structural changes accompanying intramolecular electron transfer: Focus on twisted intramolecular charge-transfer states and structures. *Chemical Reviews* **2003**, *103* (10), 3899-4031.
107. Li, K.; Liu, B., Polymer-encapsulated organic nanoparticles for fluorescence and photoacoustic imaging. *Chemical Society Reviews* **2014**, *43* (18), 6570-6597.
108. Li, K.; Qin, W.; Ding, D.; Tomczak, N.; Geng, J. L.; Liu, R. R.; Liu, J. Z.; Zhang, X. H.; Liu, H. W.; Liu, B.; Tang, B. Z., Photostable fluorescent organic dots with aggregation-induced emission (AIE dots) for noninvasive long-term cell tracing. *Scientific Reports* **2013**, *3*, 10.
109. Krossing, I.; Raabe, I., Noncoordinating anions - Fact or fiction? A survey of likely candidates. *Angewandte Chemie-International Edition* **2004**, *43* (16), 2066-2090.

110. Engesser, T.; Lichtenthaler, M.; Schleep, M.; Krossing, I., Reactive p-block cations stabilized by weakly coordinating anions. *Chemical Society Reviews* **2016**, *45* (4), 789-899.
111. HONEYCHUCK, R.; HERSH, W., COORDINATION OF NONCOORDINATING ANIONS - SYNTHESIS, CHARACTERIZATION, AND X-RAY CRYSTAL-STRUCTURES OF FLUORINE-BRIDGED [SBF<sub>6</sub>]<sup>-</sup>, [BF<sub>4</sub>]<sup>-</sup>, AND [PF<sub>6</sub>]<sup>-</sup> ADDUCTS OF [R<sub>3</sub>P(CO)<sub>3</sub>(NO)W]<sup>+</sup> - AN UNCONVENTIONAL ORDER OF ANION DONOR STRENGTH. *Inorganic Chemistry* **1989**, *28* (14), 2869-2886.
112. Jia, M.; Bandini, M., Counterion Effects in Homogeneous Gold Catalysis. *Acc Catalysis* **2015**, *5* (3), 1638-1652.
113. Geiger, W.; Barriere, F., Organometallic Electrochemistry Based on Electrolytes Containing Weakly-Coordinating Fluoroarylborate Anions. *Accounts of Chemical Research* **2010**, *43* (7), 1030-1039.
114. Aubrey, M.; Long, J., A Dual-Ion Battery Cathode via Oxidative Insertion of Anions in a Metal-Organic Framework. *Journal of the American Chemical Society* **2015**, *137* (42), 13594-13602.
115. Raabe, I.; Wagner, K.; Gutsche, K.; Wang, M.; Gratzel, M.; Santiso-Quinones, G.; Krossing, I., Tetraalkylammonium Salts of Weakly Coordinating Aluminates: Ionic Liquids, Materials for Electrochemical Applications and Useful Compounds for Anion Investigation. *Chemistry-a European Journal* **2009**, *15* (8), 1966-1976.
116. Fischer, S.; Schmidt, J.; Strauch, P.; Thomas, A., An Anionic Microporous Polymer Network Prepared by the Polymerization of Weakly Coordinating Anions. *Angewandte Chemie-International Edition* **2013**, *52* (46), 12174-12178.
117. Bakker, E.; Buhlmann, P.; Pretsch, E., Carrier-based ion-selective electrodes and bulk optodes. 1. General characteristics. *Chemical Reviews* **1997**, *97* (8), 3083-3132.
118. Xie, X.; Gutierrez, A.; Trofimov, V.; Szilagyi, I.; Soldati, T.; Bakker, E., Charged Solvatochromic Dyes as Signal Transducers in pH Independent Fluorescent and Colorimetric Ion Selective Nanosensors. *Analytical Chemistry* **2015**, *87* (19), 9954-9959.
119. Chen, L.; Tan, Y.; Liu, X.; Chen, Y., Counterion induced facile self-doping and tunable interfacial dipoles of small molecular electrolytes for efficient polymer solar cells. *Nano Energy* **2016**, *27*, 492-498.
120. Ma, D.; Zhang, C.; Qiu, Y.; Duan, L., Highly efficient blue-green organic light-emitting diodes achieved by controlling the anionic migration of cationic iridium(III) complexes. *Journal of Materials Chemistry C* **2016**, *4* (24), 5731-5738.
121. TATIKOLOV, A.; SHVEDOVA, L.; DEREVYANKO, N.; ISHCHENKO, A.; KUZMIN, V., THE INFLUENCE OF COUNTERION ON PHOTOCHEMISTRY OF CATIONIC INDOPOLYCARBOCYANINE DYES IN ION-PAIRS. *Chemical Physics Letters* **1992**, *190* (3-4), 291-297.
122. TATIKOLOV, A.; DZHULIBEKOV, K.; SHVEDOVA, L.; KUZMIN, V.; ISHCHENKO, A., INFLUENCE OF INERT COUNTERIONS ON THE PHOTOCHEMISTRY OF SOME CATIONIC POLYMETHINE DYES. *Journal of Physical Chemistry* **1995**, *99* (17), 6525-6529.
123. Ishchenko, A.; Derevyanko, N.; Popov, S.; Slominskii, Y.; Koval, V.; Shapovalov, S.; MchedlovPetrosyan, N., Interaction of chromophores in dissimilar associates of cationic and anionic polymethine dyes in water. *Russian Chemical Bulletin* **1997**, *46* (5), 910-915.
124. Bouit, P.; Aronica, C.; Toupet, L.; Le Guennic, B.; Andraud, C.; Maury, O., Continuous Symmetry Breaking Induced by Ion Pairing Effect in Heptamethine

Cyanine Dyes: Beyond the Cyanine Limit. *Journal of the American Chemical Society* **2010**, *132* (12), 4328-4335.

125. Veron, A. C.; Zhang, H.; Linden, A.; Nuesch, F.; Heier, J.; Hany, R.; Geiger, T., NIR-Absorbing Heptamethine Dyes with Tailor-Made Counterions for Application in Light to Energy Conversion. *Organic Letters* **2014**, *16* (4), 1044-1047.

126. Funabiki, K.; Yagi, K.; Ueta, M.; Nakajima, M.; Horiuchi, M.; Kubota, Y.; Mastui, M., Rational Molecular Design and Synthesis of Highly Thermo- and Photostable Near-Infrared-Absorbing Heptamethine Cyanine Dyes with the Use of Fluorine Atoms. *Chemistry-a European Journal* **2016**, *22* (35), 12282-12285.

127. Ou, Z.; Yao, H.; Kimura, K., Organic nanoparticles of cyanine dye in aqueous solution. *Bulletin of the Chemical Society of Japan* **2007**, *80* (2), 295-302.

128. Funada, T.; Hirose, T.; Tamai, N.; Yao, H., Organic nanoparticles of malachite green with enhanced far-red emission: size-dependence of particle rigidity. *Physical Chemistry Chemical Physics* **2015**, *17* (16), 11006-11013.

129. Yao, H.; Ashiba, K., Highly fluorescent organic nanoparticles of thiacyanine dye: A synergetic effect of intermolecular H-aggregation and restricted intramolecular rotation. *Rsc Advances* **2011**, *1* (5), 834-838.

130. Bwambok, D. K.; El-Zahab, B.; Challa, S. K.; Li, M.; Chandler, L.; Baker, G. A.; Warner, I. M., Near-Infrared Fluorescent NanoGUMBOS for Biomedical Imaging. *ACS Nano* **2009**, *3* (12), 3854-3860.

131. Jordan, A. N.; Das, S.; Siraj, N.; de Rooy, S. L.; Li, M.; El-Zahab, B.; Chandler, L.; Baker, G. A.; Warner, I. M., Anion-controlled morphologies and spectral features of cyanine-based nanoGUMBOS - an improved photosensitizer. *Nanoscale* **2012**, *4* (16), 5031-5038.

132. Magut, P.; Das, S.; Fernand, V.; Losso, J.; McDonough, K.; Naylor, B.; Aggarwal, S.; Warner, I., Tunable Cytotoxicity of Rhodamine 6G via Anion Variations. *Journal of the American Chemical Society* **2013**, *135* (42), 15873-15879.

133. Soulie, M.; Carayon, C.; Saffon, N.; Blanc, S.; Fery-Forgues, S., A comparative study of nine berberine salts in the solid state: optimization of the photoluminescence and self-association properties through the choice of the anion. *Physical Chemistry Chemical Physics* **2016**, *18* (43), 29999-30008.

134. Soulie, M.; Frongia, C.; Lobjois, V.; Fery-Forgues, S., Fluorescent organic ion pairs based on berberine: counter-ion effect on the formation of particles and on the uptake by colon cancer cells. *Rsc Advances* **2015**, *5* (2), 1181-1190.

135. Reisch, A.; Didier, P.; Richert, L.; Oncul, S.; Arntz, Y.; Mely, Y.; Klymchenko, A. S., Collective fluorescence switching of counterion-assembled dyes in polymer nanoparticles. *Nature Communications* **2014**, *5*.

136. Reisch, A.; Runser, A.; Arntz, Y.; Mely, Y.; Klymchenko, A. S., Charge-Controlled Nanoprecipitation as a Modular Approach to Ultrasmall Polymer Nanocarriers: Making Bright and Stable Nanoparticles. *ACS Nano* **2015**, *9* (5), 5104-5116.

137. Shulov, I.; Oncul, S.; Reisch, A.; Arntz, Y.; Collot, M.; Mely, Y.; Klymchenko, A., Fluorinated counterion-enhanced emission of rhodamine aggregates: ultrabright nanoparticles for bioimaging and light-harvesting. *Nanoscale* **2015**, *7* (43), 18198-18210.

## 4. Resume of thesis in English

### Introduction

Fluorescence imaging is a very powerful method in modern biological research, as it is fast, non-invasive and can be used both *in vitro* and *in vivo*. This technique uses different luminescent objects, like organic fluorophores<sup>1</sup>, fluorescent proteins<sup>2</sup> or fluorescent/luminescent nanoparticles<sup>3</sup>. The latter are usually much brighter and significantly bigger than single organic fluorophores, which makes them more attractive, when higher brightness is important and small fluorophore size is not crucial.

Inorganic nanoparticles, like metal clusters, quantum dots, carbon dots or silica nanoparticles are not biodegradable, moreover, some of them are made of toxic elements. An attractive substitution for them might be organic nanoparticles<sup>4</sup>. They can be made of biodegradable polymers, and encapsulation of different fluorophores can give any desired colour of fluorescence, independently on their size (unlike quantum dots or metal clusters). However, one of the major problems of organic dye-loaded fluorescent nanoparticles is aggregation-caused quenching (ACQ) – at high concentrations dyes tend to form non-fluorescent aggregates inside nanoparticles, which strongly decreases their brightness.

A new method of fighting ACQ was recently introduced<sup>5,6</sup>, which consisted of adding bulky counterions to cationic dyes. When encapsulated inside polymer nanoparticles, such ion pairs demonstrate minimal self-quenching, making possible creation of fluorescent organic nanoparticles thousands times brighter than single fluorophores. Moreover, such nanoparticles start behaving like single fluorophores – they switch on and off (blink) upon irradiation, which was unprecedented for nanoparticles encapsulating hundreds of dyes.

**The aim of my PhD** is to develop ultra-bright dye-loaded polymer nanoparticles with tuneable properties, based on the concept of using bulky counterions; to investigate and gain control of counterion-driven self-assembly of cationic dyes inside

polymer nanoparticles; to find new counterions that could prevent self-quenching of dyes inside nanoparticles.

### **Enhancing emission of cyanine dyes**

As the counterion-enhanced emission approach was validated only for rhodamine B derivative, it was important to show that system works for different dyes. We chose five cyanine dyes, emitting from green to near-infrared, and tested their ion pairs with four different counterions (Fig. 1A) in PLGA (poly(lactide-co-glycolide)) nanoparticles at different dye loadings (5, 20 and 50 mM).

It was found that with increasing size and hydrophobicity of the counterion, quantum yields of fluorescent nanoparticles increase independently on the cyanine dye, and the most performant counterion is **F12** (Fig. 1B). Size of the nanoparticles is also affected by counterion nature, in line with previous results: derivatives of tetraphenylborate enable encapsulation of dyes inside nanoparticles without changing their size (40-50 nm). By contrast, chloride/perchlorate counterions give nanoparticles of several hundreds nanometres, that are not colloidally stable. Independently of dye and counterion, quantum yield drops upon increasing dye loading, however in case of bulky **F5** and **F12** counterions this drop is not as dramatic, as in case of chloride/perchlorate. Drop of quantum yield is also observed upon increasing the conjugation length of the cyanine (Fig. 1B) independently on the counterion.

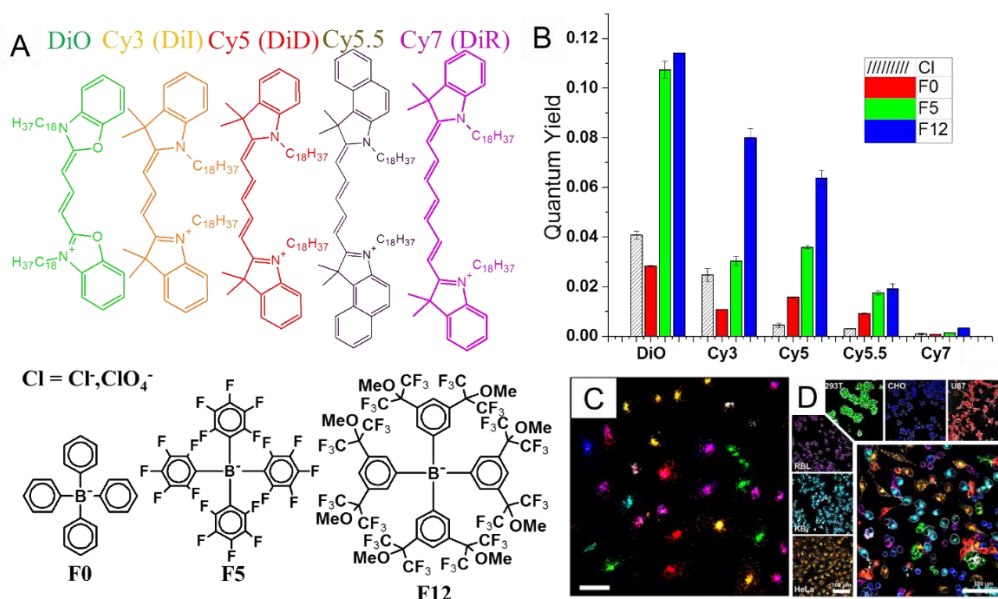


**Figure 1. (A)** Chemical structures of dyes and counterions used in this study. **(B)** Quantum yields of 50 mM-loaded nanoparticles of different dyes with different counterions. **(C)** Confocal image of a mixture of seven cell populations of different colors four days after labelling. **(D)** Confocal image of six cell types (HeLa, KB, 293T, U87, RBL, and CHO) mixed and co-cultured for 24 h. Each cell type was labeled with an RGB color code (orange, cyan, green, red, magenta, and blue, respectively), also shown separately in the smaller images.

Based on the obtained data, we chose **DiO**, **Dil** and **DiD** dyes with **F12** counterion at 20 mM loading to develop a colour coding system for long-term tracking of living cells. By mixing these 3 types of particles in different proportions, it was possible to create up to 13 colour codes (seven are presented in Fig. 1C) for cell labelling. The technique was validated on 6 cell lines (Fig. 1D), that could be distinguished by colour code even after 24 hrs of co-incubation. Developed method was further applied for tracking of tumour cells in a living zebrafish embryo (in collaboration with Jacky GOETZ) and cell tracking in the developing zebrafish embryo (4 or 8-cell stage, in collaboration with Nadine PEYRIÉRAS). Results of the project were published in *Small*.

## **Counterion-enhanced encapsulation and emission of cationic dyes in polymeric nanoparticles: the role of counterion nature.**

To further investigate the influence of a counterion on nanoparticles properties, we designed a project where ten counterions of different size and hydrophobicity (Fig. 2A) were encapsulated with octadecylrhodamine B (**R18**) inside PLGA nanoparticles.

The results have shown that counterions of higher hydrophobicity encapsulate **R18** in nanoparticles much better than their hydrophilic rivals (>98% encapsulation for **R18/F12-TPB** vs ~50% for **R18/CIO<sub>4</sub>**). This higher degree of encapsulation also results in decrease of nanoparticles size from ~300 nm (**R18/CIO<sub>4</sub>**) to ~45 nm (**R18/F12-TPB**), because the adsorption of **R18** at the nanoparticle surface is prevented. Importantly, all studied bulky hydrophobic counterions **B<sub>21</sub>H<sub>18</sub>**, **F5-TPB**, **F6-TPB** and **F12-TPB** (“hydrophobic group”) produced particles with similar high quantum yield (~50%) at 50 mM dye loading. More hydrophilic counterions, like **CIO<sub>4</sub>**, **BF<sub>4</sub>**, **PF<sub>6</sub>** and **B(CN)<sub>4</sub>** (“hydrophilic group”) show lower quantum yields (~7%) at these conditions.

One of the ways to study communication of dyes inside nanoparticles is fluorescence anisotropy measurements – when the dyes have efficient energy transfer, anisotropy decreases comparing to the case without communication. Anisotropy measurements suggest that “hydrophobic group” enables strong interfluorophore communication, while “hydrophilic group” does not. **R18/B(CF<sub>3</sub>)<sub>4</sub>** and **R18/F5-3PB-OH**, despite having higher hydrophobicity and quantum yields than “hydrophilic group”, demonstrate poor dye communication. The results, obtained from anisotropy data, are confirmed during single particle microscopy, showing that all “hydrophobic group” demonstrates on/off switching of the whole particle, whereas **R18/B(CF<sub>3</sub>)<sub>4</sub>** and **R18/F5-3PB-OH** do not (Fig. 2B). As for single particle brightness, 50 mM-loaded **R18/F5-TPB**, for example, are ~44 times brighter than quantum dots QD585 at the same laser wavelength (532 nm) and excitation power (0.08 W/cm<sup>2</sup>).

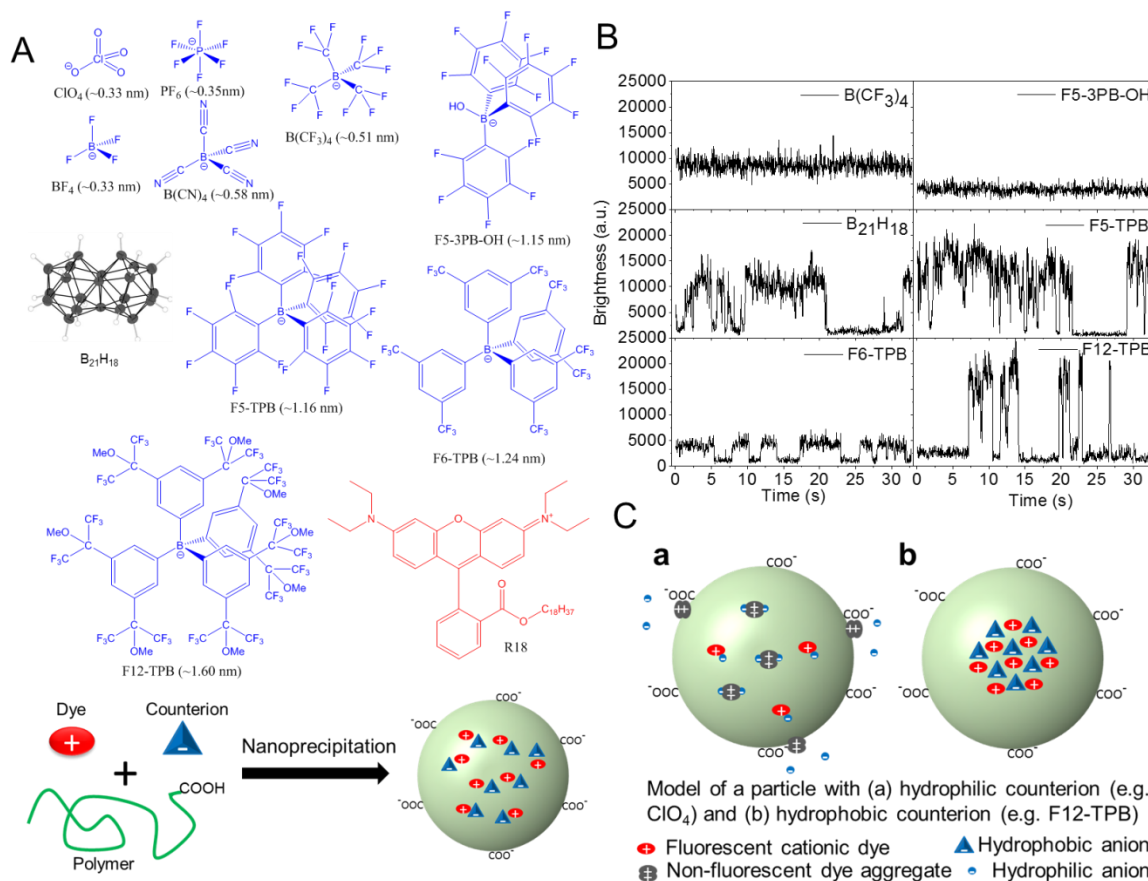


**Figure 2. (A)** Chemical structures of dyes and counterions used in this study, schematic representation of nanoprecipitation process. **(B)** Representative single-particle traces of 50mM NPs loaded with R18 and various counterions recorded under wide-field microscope. Excitation power density at 532 nm was  $0.08 \text{ W cm}^{-2}$ . **(C)** Proposed models of dyes organisation inside PLGA nanoparticles for hydrophilic (a) and hydrophobic (b) counterions.

Cell labelling was performed by incubating KB cells with nanoparticles, diluted in medium, during 3 hours. Afterwards, confocal microscopy reveals that all studied hydrophilic counterions show strong dye leaching inside the cells, whereas hydrophobic counterions prevent effectively this dye leaching.

The obtained results allow us to propose two models of dye organisation inside polymer nanoparticles depending on the counterion type. In the “hydrophilic group” single dyes and non-fluorescent dye aggregates are more or less homogeneously distributed inside polymer nanoparticle, with significant amount of dye being adsorbed on the nanoparticles surface (Fig. 2C(a)). In the case of “hydrophobic group”, dyes are assembled by the counterion inside the hydrophobic core, while polymer forms a shell around it (Fig. 2C(b)). Results of the project will be submitted to *Chemical Science*.

## Aluminium-based fluorinated counterion for enhanced encapsulation and emission of dyes in biodegradable polymer nanoparticles

Despite high performance of fluorinated derivatives of tetraphenylborates in *counterion-enhanced encapsulation and emission* approach, it is of high interest to substitute them with other counterions, which are simpler in synthesis, cheaper and more bio- and eco-friendly. However, they also must have sufficiently high hydrophobicity and large size to ensure efficient encapsulation of dyes inside nanoparticles and prevent ACQ.

One of the promising candidates is tetrakis[perfluoro-*tert*-butoxy]aluminate (noted **F9-AI**) (Fig. 3A), which is highly hydrophobic and has similar size with **F5-TPB**. It was synthesized in one step according to a known protocol<sup>7</sup> from inexpensive lithium aluminium hydride and perfluorinated *tert*-butanol. After comparison of nanoparticles, loaded with **R18/F9-AI**, with the ones, loaded with **R18/F5-TPB**, it is found that they have similar size (Fig. 3B), quantum yields (Fig. 3C), absorption and fluorescence bands, fluorescence anisotropy (Fig. 3D), single particle brightness and they both blink under laser illumination. The only significant difference was observed in encapsulation efficiency of the two ion pairs inside nanoparticles - ~96% for **R18/F9-AI** versus ~92% for **R18/F5-TPB**. This difference becomes important during cell labelling: even at 50 mM loading, particles, loaded with **R18/F9-AI**, demonstrate no dye leaching inside the cells (Fig. 3F), while their **R18/F5-TPB** rivals do show some leaching (Fig. 3E).

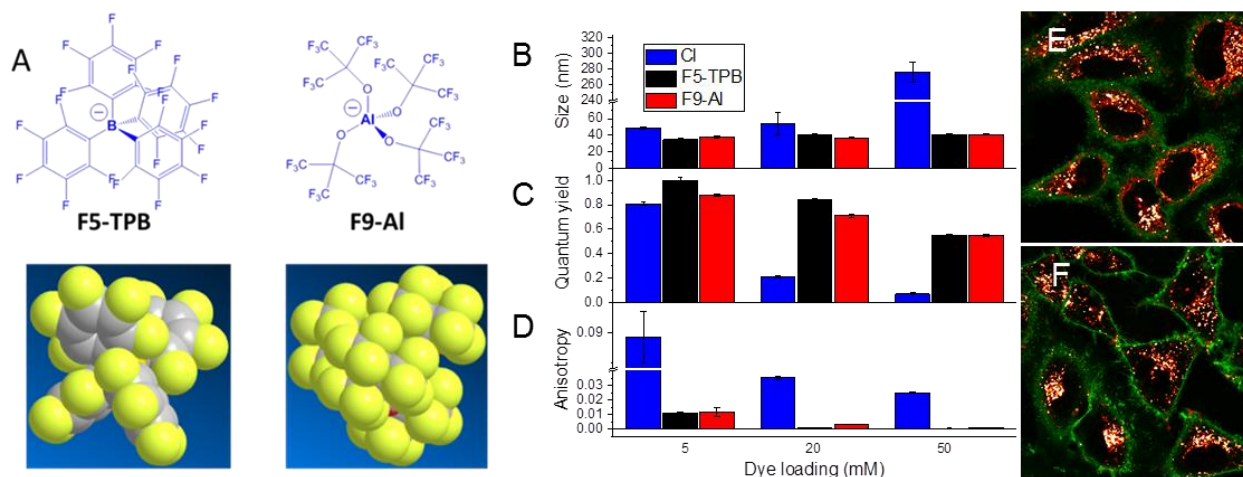


**Figure 3.** (A) Chemical structures and molecular models of counterions used in this study to encapsulate R18 inside polymer nanoparticles. (B) Hydrodynamic diameter of NPs. (C) Quantum yield of NPs. (D) Anisotropy of NPs. (E,F) Confocal images of HeLa cells, incubated with R18/F5-TPB, and R18/F9-AI loaded nanoparticles, respectively. Dye loading was 50 mM.

Taking into account all the aforementioned, we can conclude that *counterion-enhanced encapsulation and emission* approach is not limited only to derivatives of fluorinated tetraphenylborate, but can be extended to other types of anions that can even exceed them in properties. Results of the project were published in *Materials Chemistry Frontiers*.

### **Bulky hydrophobic barbiturates for enhanced encapsulation and emission of cationic dyes inside polymer nanoparticles**

Finally, after it was proven that the scope of counterions for *counterion-enhanced emission approach* is not limited only to fluorinated tetraphenylborates, the next challenge was to find an easily customisable organic scaffold for creating finely tuneable counterions. C-Acylated barbiturates were considered good candidates, as they have several sites for modification, which allows making them enough bulky and hydrophobic, and attaching groups for covalent conjugation. Moreover, negative charge of such barbiturate would be delocalised over multiple electron-withdrawing groups of the barbituric core.

Therefore, a series of barbiturates was synthesized (Fig. 4A) and an attempt was made to form ion pairs of the corresponding barbiturates with R18 dye. From the first set of tested barbiturates (compounds **1**, **2** and **BarC6**) only **BarC6** could form stable ion pairs with **R18**, most likely due to additional electron-withdrawing effect of pentafluorophenyl ring. Quantum yields tests have shown, that **BarC6** can decrease ACQ of **R18** inside PLGA nanoparticles (Fig. 4B), but less efficiently than **F5-TPB** or **F9-AI**. Probable reason of such underperformance could be insufficient bulk of **BarC6**. Therefore, much bulkier barbituric derivative, **BarPh2**, was synthesized (Fig. 4A), its ion pair with **R18** was successfully formed, and the quantum yield of 50 mM-loaded PLGA NPs has reached ~52% (Fig. 4B).

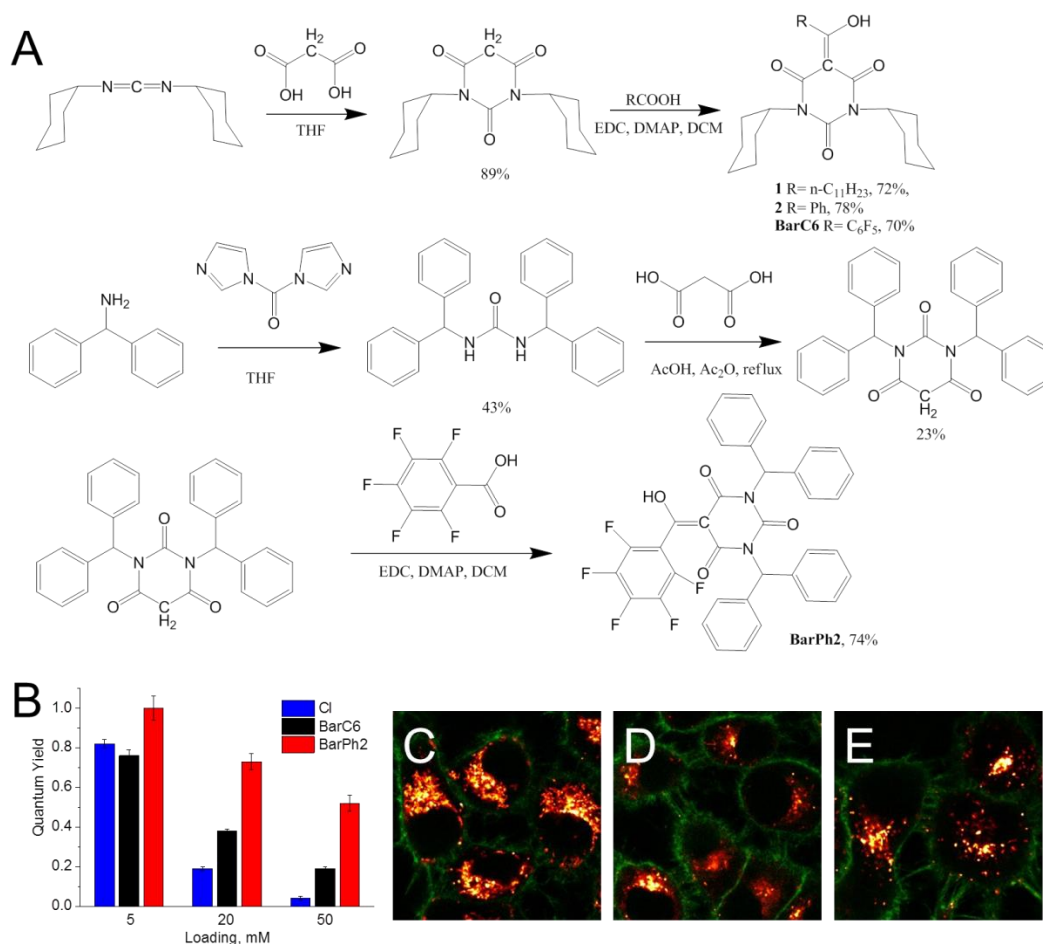


**Figure 4. (A)** Scheme of synthesis of the target barbiturates. **(B)** Quantum yield of NPs. **(C,D,E)** Confocal images of HeLa cells, incubated with **R18/F5-TPB**, **R18/ BarC6** and **R18/BarPh2** loaded nanoparticles, respectively. Dye loading was 50 mM.

Moreover, **R18/BarPh2** NPs blink under laser illumination and even outperform **R18/F5-TPB** and **R18/BarC6** NPs in cell labelling. Indeed, **R18/BarPh2** NPs show no dye leaching in the cells (Fig. 4E), being localised in endosomes and appearing as bright dots, whereas **R18/F5-TPB** and **R18/BarC6** (Fig. 4C and 4D, respectively) demonstrate some dye leakage and mitochondria staining.

The obtained results show that creating tailor-made counterions based on barbiturate scaffold can not only substitute fluorinated tetraphenylborates in *counterion-enhanced emission* approach, but also opens path for endless variations of customisable counterions. The manuscript is under preparation.

## Conclusions

Summing up more than 3 years of research, several key points about *counterion-enhanced emission* approach should be highlighted:

1. Hydrophobic cationic dyes of different colours are eligible for the approach, however quantum yield is strongly dependent on the dye (the smaller conjugation – the better) and the counterion (the larger – the better).

2. Counterion size and hydrophobicity strongly affect self-assembly during nanoprecipitation, therefore only the most hydrophobic ones form a dye-counterion cores inside nanoparticles, inducing high cooperativity of dyes, while large size of the counterion is essential to prevent ACQ.

3. The approach is not limited only to fluorinated tetraphenylborates, as they can be successfully substituted by fluorinated alkoxyaluminates or derivatives of barbituric acid. The latter are especially interesting, as they have several sites for modifications and covalent conjugation to dyes, polymers, etc.

## References

1. Lavis, L.D. and R.T. Raines, *Bright Ideas for Chemical Biology*. ACS Chemical Biology, 2008. **3**(3): p. 142-155.
2. Chudakov, D.M., et al., *Fluorescent Proteins and Their Applications in Imaging Living Cells and Tissues*. Physiological Reviews, 2010. **90**(3): p. 1103-1163.

3. Burns, A., et al., *Core/Shell Fluorescent Silica Nanoparticles for Chemical Sensing: Towards Single-Particle Laboratories*. *Small*, 2006. **2**(6): p. 723-726.
4. Reisch, A. and A.S. Klymchenko, *Fluorescent Polymer Nanoparticles Based on Dyes: Seeking Brighter Tools for Bioimaging*. *Small*, 2016. **12**(15): p. 1968-1992.
5. Reisch, A., et al., *Collective fluorescence switching of counterion-assembled dyes in polymer nanoparticles*. *Nature Communications*, 2014. **5**, 4089.
6. Reisch, A., et al., *Charge-Controlled Nanoprecipitation as a Modular Approach to Ultrasmall Polymer Nanocarriers: Making Bright and Stable Nanoparticles*. *ACS Nano* 2015, 9, (5), 5104-5116.
7. Crossing, I. *Chemistry - a European Journal* 2009, 15, **8**, 1966-1976.

## 5. Résumé de these en Français

### Introduction

L'imagerie de fluorescence est une méthode très efficace à l'heure actuelle pour la recherche en biologie, étant rapide, non invasive et pouvant être utilisée à la fois *in vitro* et *in vivo*. Cette technique utilise différents objets luminescents, comme les fluorophores organiques<sup>1</sup>, les protéines fluorescentes<sup>2</sup> ou les nanoparticules fluorescentes/luminescentes<sup>3</sup>. Ces dernières sont généralement beaucoup plus brillantes et significativement de plus grande taille que les simples fluorophores organiques, ce qui les rend plus intéressantes quand une luminosité plus élevée s'avère importante et qu'une petite taille du fluorophore n'est pas cruciale.

Les nanoparticules inorganiques, comme les *clusters* métalliques, les *quantum dots*, les *carbon dots* ou les nanoparticules de silice ne sont pas biodégradables, de plus certains d'entre eux comportent des éléments toxiques. Une solution de substitution attrayante pourrait être les nanoparticules organiques<sup>4</sup>. Celles-ci peuvent être constituées de polymères biodégradables et l'encapsulation de différents fluorophores peut leur procurer toute couleur de fluorescence souhaitée, indépendamment de leur taille (contrairement aux *quantum dots* et *clusters* métalliques). Cependant, l'un des problèmes majeurs de ces nanoparticules chargées de colorants fluorescents est l'inhibition de fluorescence causée par l'agrégation (ICA) - à des concentrations élevées, les colorants tendent à former des agrégats non fluorescents à l'intérieur des nanoparticules, ce qui diminue fortement leur luminosité.

Une nouvelle méthode pour empêcher l'ICA a été récemment introduite<sup>5,6</sup>, consistant à ajouter des contre-ions à fort encombrement stérique aux colorants cationiques. Encapsulées à l'intérieur de nanoparticules de polymère, de telles paires d'ions présentent une auto-inhibition minimale, rendant possible la création de nanoparticules organiques fluorescentes mille fois plus brillantes que les fluorophores uniques. En outre, ces nanoparticules commencent à se comporter comme de simples fluorophores : elles s'allument et s'éteignent (clignotent) lors de l'irradiation, ce qui n'était jamais le cas pour les nanoparticules encapsulant des centaines de colorants.

**L'objectif de ma thèse** est de développer des nanoparticules de polymère chargées en colorants, ultra-lumineuses, dont les propriétés puissent être modulées en se basant sur l' utilisation des contre-ions volumineux; d'étudier et de contrôler l'auto-assemblage des colorants cationiques par les contre-ions à l'intérieur de ces nanoparticules; de trouver de nouveaux contre-ions pouvant empêcher l'auto-inhibition des colorants à l'intérieur des nanoparticules.

### **Amélioration de l'émission de colorants cyanines**

Comme l'approche de l'émission stimulée *via* le contre-ion n'a été validée que pour les dérivés de la rhodamine B, il était important de montrer que le système fonctionne pour différents autres colorants. Nous avons choisi cinq colorants cyanine, émettant du vert à l'infrarouge proche et avons testé leurs paires d'ions avec quatre contre-ions différents (Fig. 1A) dans des nanoparticules de PLGA [poly (lactide-co-glycolide)] à différentes charges de colorant (5, 20 et 50 mM).

Nous avons montré qu'en augmentant la taille et l'hydrophobicité du contre-ion, les rendements quantiques des nanoparticules fluorescentes augmentent de façon indépendamment du colorant cyanine et que **F12** s'avère le contre-ion le plus performant (Fig. 1B). La taille des nanoparticules est également affectée par la nature du contre-ion, en accord avec les résultats précédents. Ainsi les dérivés du tétraphénylborate permettent l'encapsulation des colorants à l'intérieur des nanoparticules sans changer leur taille (40-50 nm), alors que les contre-ions chlorure/perchlorate donnent des nanoparticules de plusieurs centaines de nanomètres, non colloïdalement stables. Indépendamment du colorant et du contre-ion, le rendement quantique chute lors de l'augmentation de charge du colorant, mais pour des contre-ions volumineux (**F5** et **F12**), cette baisse n'est pas aussi dramatique, ainsi dans le cas chlorure/perchlorate. On observe également une chute du rendement quantique en augmentant la longueur de conjugaison de la cyanine (Fig.1B) indépendamment du contre-ion.

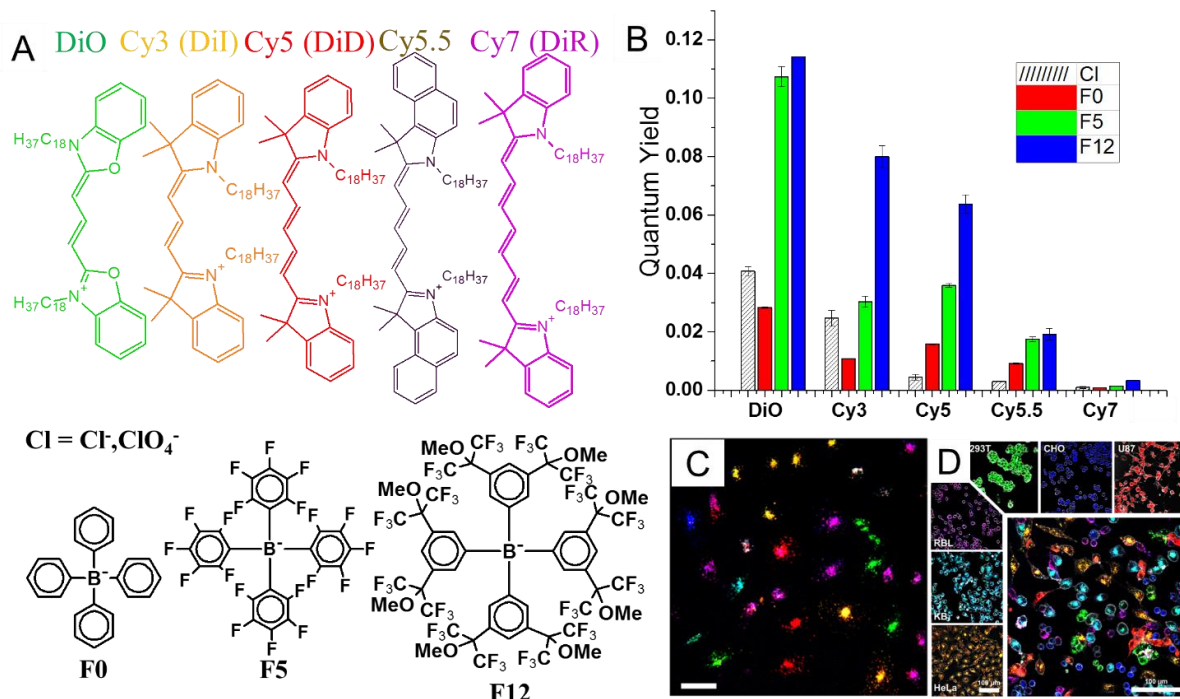


**Figure 1. (A) :** Structures chimiques des colorants et des contre-ions utilisés dans cette étude. **(B) :** Rendements quantiques des nanoparticules chargées à 50 mM par différents colorants avec différents contre-ions. **(C) :** Image confocale d'un mélange de sept populations de cellules de différentes couleurs, quatre jours après le marquage. **(D) :** Image confocale de six types cellulaires (HeLa, KB, 293T, U87, RBL, et CHO) mélangés et co-cultivées pendant 24 h. Chaque type de cellule a été étiqueté avec un code de couleur RVB (orange, cyan, vert, rouge, magenta et bleu, respectivement), également montré séparément dans les plus petites images.

Sur la base des résultats obtenus, nous avons choisi les colorants **DiO**, **DiI** et **DiD** avec le contre-ion **F12**, chargés à 20 mM, pour développer un système de codage couleur pour la traçabilité à long terme des cellules vivantes. En mélangeant ces trois types de particules dans des proportions différentes, il a été possible de créer jusqu'à 13 codes couleur (sept sont présentés sur la Fig. 1C) pour l'étiquetage des cellules. La technique a été validée sur 6 lignées cellulaires (Fig. 1D), qui ont pu être distinguées par code couleur même après 24 h de co-incubation. La méthode ainsi développée a été appliquée pour la traçabilité des cellules tumorales dans l'embryon de poisson zèbre vivant (en collaboration avec Jacky GOETZ) et celle des cellules dans l'embryon de poisson-zèbre en développement (stade à 4 ou 8 cellules, en collaboration avec Nadine PEYRIÉRAS). Les résultats du projet ont été publiés à *Small*.

## Encapsulation et émission de colorants cationiques améliorée par contre-ion dans des nanoparticules polymériques: le rôle de la nature de contre-ion.

Pour étudier plus avant l'influence d'un contre-ion sur les propriétés des nanoparticules, nous avons conçu un projet où dix contre-ions de différentes tailles et hydrophobicité (Fig. 2A) ont été encapsulés avec de l'octadecylrhodamine B (**R18**) à l'intérieur de nanoparticules de PLGA.

Les résultats ont montré que les contre-ions de plus grande hydrophobicité permettent d'encapsuler **R18** dans des nanoparticules beaucoup mieux que leurs rivaux hydrophiles (>98% d'encapsulation pour **R18/F12-TPB** vs ~50% pour **R18/CIO<sub>4</sub>**). Ce degré élevé d'encapsulation se traduit également par une diminution de la taille des nanoparticules de ~300 nm (**R18/CIO<sub>4</sub>**) jusqu'à ~45 nm (**R18/F12-TPB**), car l'adsorption de **R18** à la surface des nanoparticules est empêchée. Il est important de noter que tous les contre-ions hydrophobes étudiés, à fort encombrement stérique, **B<sub>21</sub>H<sub>18</sub>**, **F5-TPB**, **F6-TPB** et **F12-TPB** ("groupe hydrophobe") produisent des particules avec un rendement quantique identique élevé (~50%) pour une charge de colorant de 50 mM. Les contre-ions plus hydrophiles, comme **CIO<sub>4</sub>**, **BF<sub>4</sub>**, **PF<sub>6</sub>** et **B(CN)<sub>4</sub>** ("groupe hydrophile") montrent des rendements quantiques inférieurs (~7%) pour les mêmes conditions.

L'une des façons d'étudier la communication des colorants à l'intérieur des nanoparticules est de mesurer leur anisotropie de fluorescence - lorsque les colorants présentent un transfert d'énergie efficace, l'anisotropie diminue en comparant au cas sans communication. Les mesures d'anisotropie suggèrent que le "groupe hydrophobe" permet une communication interfluorophore forte, alors que le "groupe hydrophile" ne le permet pas. **R18/B(CF<sub>3</sub>)<sub>4</sub>** et **R18/F5-3PB-OH**, en dépit de leurs hydrophobie et rendement quantique supérieurs au "groupe hydrophile", démontrent une communication limitée des colorants. Les résultats obtenus à partir de données d'anisotropie sont confirmés par la microscopie à particule unique, montrant que tout "groupe hydrophobe" déclenche la commutation *on/off* de toute la particule, alors que ce n'est pas le cas de **R18/B(CF<sub>3</sub>)<sub>4</sub>** et **R18/F5-3PB-OH** (Fig. 2B). S'agissant de la luminosité de la particule, par exemple **R18 / F5-TPB** chargés à 50 mM, elles sont ~

44 fois plus brillantes que les *quantum dots* QD585 à longueur d'onde laser (532 nm) et puissance d'excitation (0,08 W/cm<sup>2</sup>) identiques.

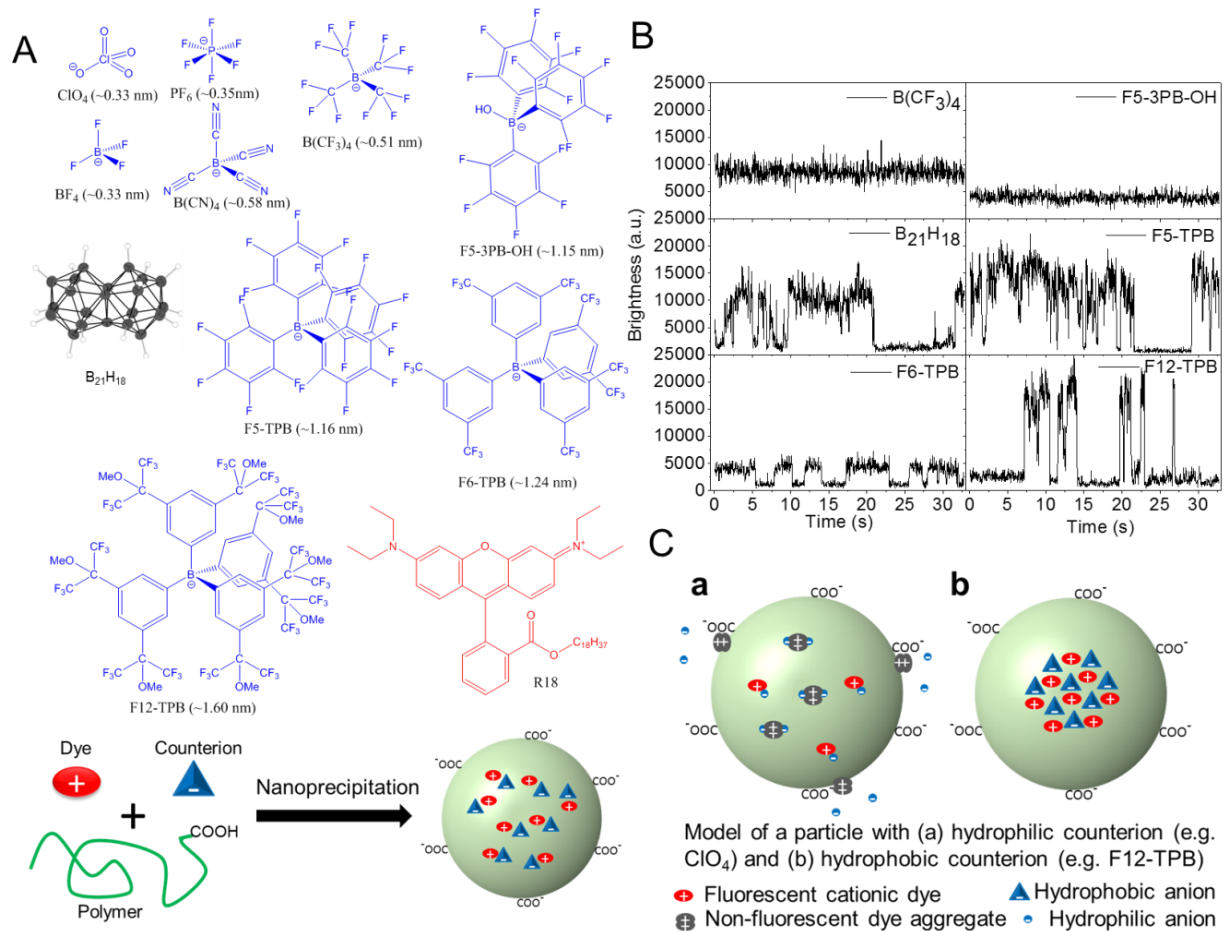


**Figure 2. (A) :** Structures chimiques des colorants et des contre-ions utilisés dans cette étude, avec représentation schématique du processus de nanoprecipitation. **(B) :** Tracés représentatifs de particules uniques pour des NPs chargés à 50 mM de R18 et différents contre-ions, enregistrés sous microscope à champ large. Puissance d'excitation à 532 nm : 0.08 W/cm<sup>2</sup>. **(C) :** Modèles proposés pour l'organisation des colorants à l'intérieur de nanoparticules de PLGA pour des contre-ions hydrophiles (a) et hydrophobes (b).

L'étiquetage cellulaire a été réalisé en incubant des cellules KB avec des nanoparticules, diluées dans du milieu, pendant 3 heures. Ensuite, la microscopie confocale révèle que tous les contre-ions hydrophiles étudiés présentent une fuite importante des colorants de l'intérieur des cellules, alors que les contre-ions hydrophobes empêchent efficacement cette fuite de colorants.

Les résultats obtenus nous permettent de proposer deux modèles d'organisation des colorants à l'intérieur des nanoparticules de polymères en fonction du type de contre-ion. Dans le "groupe hydrophile", les molécules de colorants et les agrégats de colorants non fluorescents sont répartis de façon plus ou moins homogène à l'intérieur de ces nanoparticules, une quantité importante de colorant étant adsorbée sur la surface des nanoparticules (figure 2C (a)). Dans le cas du "groupe hydrophobe", les colorants sont assemblés par le contre-ion à l'intérieur du coeur hydrophobe, tandis que le polymère forme une coquille autour de celui-ci (figure 2C (b)). Les résultats de l'étude seront soumis à *Chemical Science*.

### **Contre-ion fluoré à base d'aluminium pour une encapsulation et une émission améliorée de colorants dans des nanoparticules de polymères biodégradables**

Malgré la haute efficacité des dérivés fluorés de tétraphénylborate dans une approche de *l'encapsulation et de l'émission améliorées par contre-ion*, il est d'un grand intérêt de les remplacer par d'autres contre-ions, présentant une synthèse plus simple, moins chère et davantage bio- et eco-compatibles. Cependant, ils doivent également présenter une forte hydrophobicité et une taille suffisamment grande permettant une encapsulation efficace des colorants à l'intérieur des nanoparticules et empêchant l'ICA.

L'un des candidats prometteur est le tétrakis[perfluoro-*tert*-butoxy]aluminate (noté **F9-AI**) (Fig. 3A), qui est très hydrophobe, avec une taille similaire à **F5-TPB**. Il a été synthétisé en une seule étape selon un protocole connu<sup>7</sup>, à partir d'hydrure de lithium et d'aluminium peu coûteux et de *tert*-butanol perfluoré. Après comparaison des nanoparticules chargées avec **R18/F9-AI** avec celles chargés avec **R18/F5-TPB**, l'on constate qu'elles présentent des tailles (Fig. 3B), des rendements quantiques (Fig. 3C), une absorption, une fluorescence, une anisotropie de fluorescence (Fig. 3D) et une brillance en particule unique similaires, et que les deux types clignotent sous illumination laser. La seule différence significative a été observée dans le rendement d'encapsulation des deux paires d'ions à l'intérieur des nanoparticules : ~96% pour **R18/F9-AI** vs ~92% pour **R18/F5-TPB**. Cette différence

devient importante au cours du marquage cellulaire: même chargées à 50 mM, les particules contenant **R18/F9-AI** ne montrent aucune perte en colorant à l'intérieur des cellules (Fig. 3F), alors que celles contenant **R18/F5-TPB** montrent une fuite en colorant (Fig. 3E).

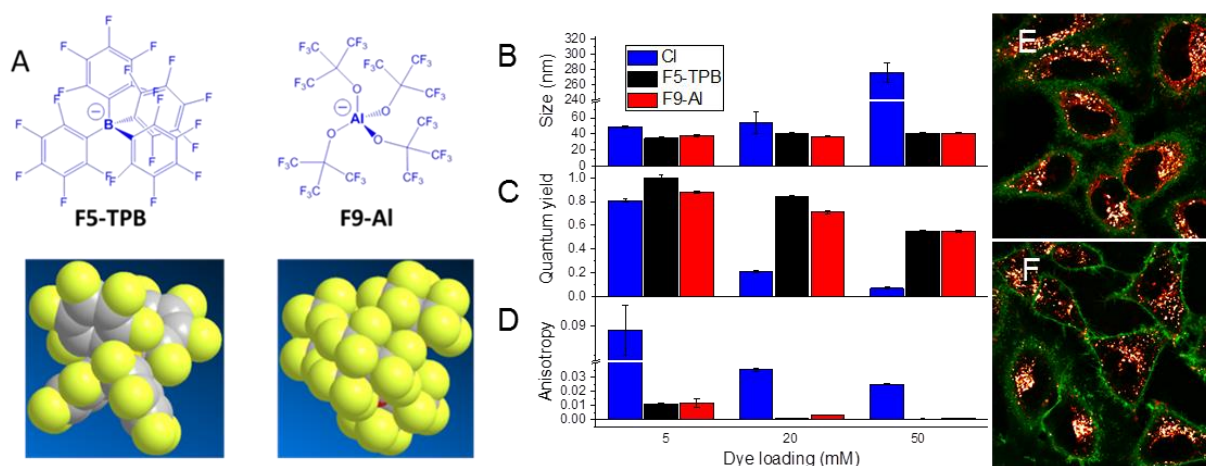


**Figure 3.** (A) : Structures chimiques et modèles moléculaires des contre-ions utilisés dans cette étude pour encapsuler R18 à l'intérieur des nanoparticules de polymère. (B) : Diamètre hydrodynamique des NPs. (C) : Rendement quantique des NPs. (D) : Anisotropie de fluorescence des NPs. (E, F) : Images confocales de cellules HeLa, incubées avec des nanoparticules chargées respectivement avec 50 nm de **R18/F5-TPB** et **R18/F9-AI**.

En tenant compte de tout ce qui précède, nous pouvons conclure que l'approche de l'encapsulation et de l'émission améliorées par contre-ion ne se limite pas seulement aux dérivés fluorés de tétraphénylborate, mais peut être étendue à d'autres types d'anions qui peuvent se révéler à même d'améliorer leurs propriétés. Les résultats de l'étude ont été publiés à *Materials Chemistry Frontiers*.

## Des barbiturates hydrophobes volumineux pour une encapsulation et une émission améliorée de colorants cationiques à l'intérieur de nanoparticules de polymère

Enfin, après avoir prouvé que la gamme de contre-ions dans l'approche de *l'encapsulation et de l'émission améliorées par contre-ion* ne se limite pas seulement aux tetraphenylborates fluorés, le prochain défi fût de trouver une matrice organique facilement modulable dans le but de créer des contre-ions adaptés. Les barbituriques C-acylés ont été considérés comme de bons candidats, car ils possèdent plusieurs sites de modification, ce qui permet de les rendre suffisamment volumineux et hydrophobes, et de leur fixer des groupements en vue d'une conjugaison covalente. En outre, la charge négative de ces barbituriques serait délocalisée sur les multiples groupes électro-attracteurs de leur noyau.

Par conséquent, une série de dérivés de barbituriques a été synthétisée (Fig. 4A) et une tentative a été faite pour former des paires d'ions de ces dérivés avec le colorant R18. A partir de la première série de dérivés de barbituriques testés (composés **1**, **2** et **BarC6**), seul **BarC6** a pu former des paires d'ions stables avec **R18**, très probablement en raison de l'effet électro-attracteur supplémentaire du cycle pentafluorophényle. Les mesures de rendement quantique ont montré que **BarC6** peut diminuer l'ICA de **R18** à l'intérieur des nanoparticules de PLGA (Fig. 4B), mais moins efficacement que **F5-TPB** ou **F9-AI**. La raison probable de cette sous-performance pourrait être la taille insuffisante de **BarC6**. Par conséquent, un dérivé barbiturique beaucoup plus volumineux, **BarPh2**, a été synthétisé (Fig. 4A) ; la paire d'ions avec **R18** s'est alors formée avec succès et le rendement quantique des NPs de PLGA chargées à 50 mM a atteint ~ 52% (Fig. 4B).

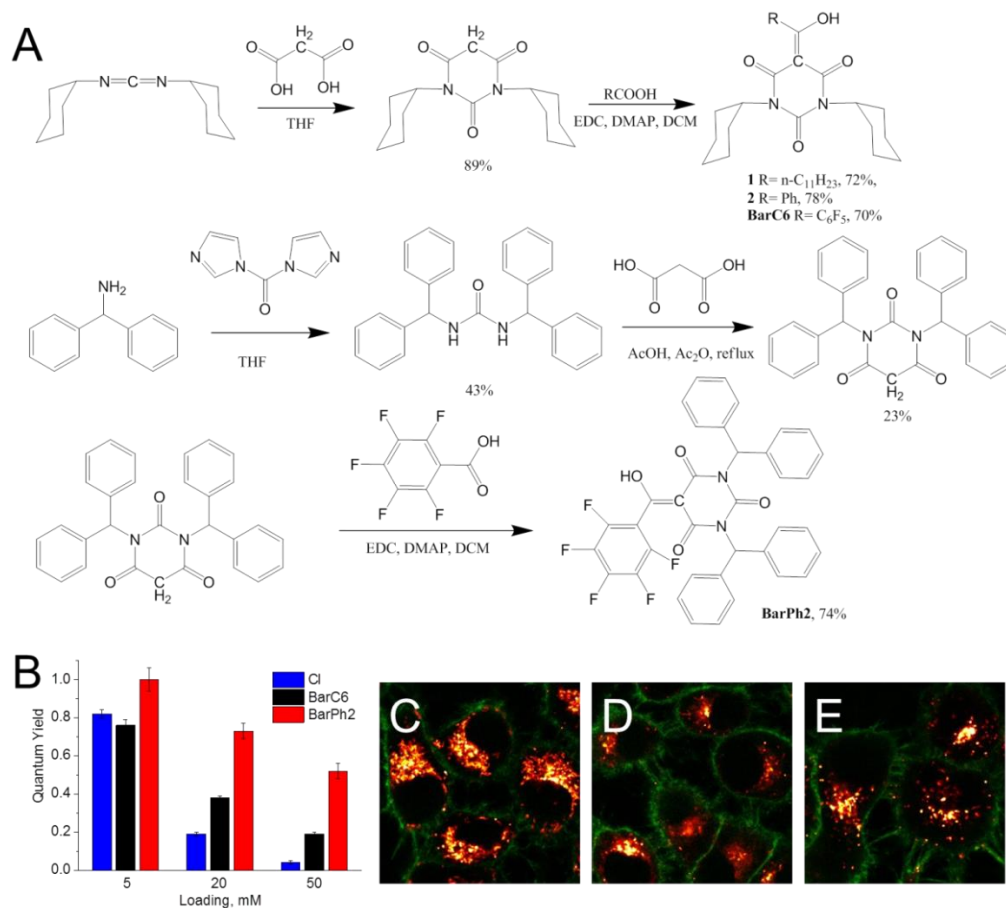


**Figure 4. (A) :** Schéma de synthèse des barbituriques cibles. **(B) :** Rendements quantiques des NPs. **(C, D, E) :** Images confocale de cellules HeLa incubées avec des NPs chargées respectivement en **R18 / F5-TPB**, **R18 / R18 BarC6** et **BarPh2**, à 50 mM de charge.

En outre, les NPs de **R18/BarPh2** clignotent sous illumination laser et même surpassent en efficacité les NPs **R18/F5-TPB** et **R18/BarC6** pour le marquage cellulaire. En effet, les NPs **R18/BarPh2** ne montrent aucune fuite de colorant dans les cellules (Fig. 4E), étant localisées dans les endosomes et apparaissant comme des points lumineux, tandis que les NPs **R18/F5-TPB** et **R18/BarC6** (respectivement Fig.4C et 4D) montrent une certaine fuite des colorants et une coloration des mitochondries.

Les résultats obtenus montrent que les contre-ions conçus à partir d'une matrice de barbituriques peuvent non seulement remplacer les tétraphénylborates fluorés dans l'approche de *l'encapsulation et de l'émission améliorées par contre-ion*, mais ouvre également la voie à une variation quasi-infinies de contre-ions dédiés. Un manuscrit est en préparation.

## Conclusions

Pour résumer plus de 3 années de recherche, plusieurs points clés concernant l'approche *de l'encapsulation et de l'émission améliorées par contre-ion* doivent être mis en exergue:

1. Les colorants cationiques hydrophobes de différentes couleurs sont éligibles à cette approche, cependant leur rendement quantique est fortement dépendant du colorant (la conjugaison plus petite étant la meilleure) et du contre-ion (la plus grande taille étant la meilleure).

2. La taille et l'hydrophobicité du contre-ion affectent fortement l'auto-assemblage pendant la nanoprécipitation, donc seuls les plus hydrophobes forment des coeurs de colorant/contre-ion à l'intérieur des nanoparticules, induisant une forte coopérativité des colorants, la grande taille du contre-ion étant tant qu'à elle essentielle pour prévenir l'ICA.

3. L'approche ne se limite pas aux tétraphénylborates fluorés, car ils peuvent être substitués avec succès par des alkoxy-aluminates fluorés ou des dérivés de l'acide barbiturique. Ces derniers sont particulièrement intéressants, car ils possèdent plusieurs sites pour des modifications et une conjugaison covalente à des colorants, des polymères, etc.

## Références

1. Lavis, L.D. and R.T. Raines, *Bright Ideas for Chemical Biology*. ACS Chemical Biology, 2008. **3**(3): p. 142-155.
2. Chudakov, D.M., et al., *Fluorescent Proteins and Their Applications in Imaging Living Cells and Tissues*. Physiological Reviews, 2010. **90**(3): p. 1103-1163.
3. Burns, A., et al., *Core/Shell Fluorescent Silica Nanoparticles for Chemical Sensing: Towards Single-Particle Laboratories*. Small, 2006. **2**(6): p. 723-726.
4. Reisch, A. and A.S. Klymchenko, *Fluorescent Polymer Nanoparticles Based on Dyes: Seeking Brighter Tools for Bioimaging*. Small, 2016. **12**(15): p. 1968-1992.
5. Reisch, A., et al., *Collective fluorescence switching of counterion-assembled dyes in polymer nanoparticles*. Nature Communications, 2014. **5**, 4089.

6. Reisch, A., et al., *Charge-Controlled Nanoprecipitation as a Modular Approach to Ultrasmall Polymer Nanocarriers: Making Bright and Stable Nanoparticles*. ACS Nano 2015, 9, (5), 5104-5116.
7. Krossing, I. *Chemistry - a European Journal* 2009, 15, **8**, 1966-1976.

## List of publications

1. Bohdan Andreiuk, Andreas Reisch, Marion Lindecker, Gautier Follain, Nadine Peyri ras, Jacky G. Goetz, Andrey S. Klymchenko, Fluorescent Polymer Nanoparticles for Cell Barcoding in Vitro and in Vivo, accepted to *Small*.
2. Bohdan Andreiuk, Andreas Reisch, Vasyl G. Pivovarenko, Andrey S. Klymchenko, Aluminium-based fluorinated counterion for enhanced encapsulation and emission of dyes in biodegradable polymer nanoparticles, under revision in *Materials Chemistry Frontiers* (minor revision).
3. Bohdan Andreiuk, Andreas Reisch, Andrey S. Klymchenko, Counterion-enhanced encapsulation and emission of cationic dyes in polymeric nanoparticles: the role of counterion nature (manuscript in preparation)
4. Bohdan Andreiuk, Andreas Reisch, Andrey S. Klymchenko, Barbiturate-based counterions for enhancing encapsulation and emission in cationic dye-loaded fluorescent nanoparticles (manuscript in preparation).
5. Redouane Bouchaala, Luc Mercier, Bohdan Andreiuk, Yves M ly, Thierry Vandamme, Nicolas Anton, Jacky G. Goetz, Andrey S. Klymchenko, Integrity of lipid nanocarriers in bloodstream and tumor quantified by near-infrared ratiometric FRET imaging in living mice, *Journal of Controlled Release*, **2016**, 236, 57-67.
6. Seong-Ho Kong, Nazim Haouchine, Renato Soares, Andrey Klymchenko, Bohdan Andreiuk, Bruno Marques, Galyna Shabat, Thierry Piechaud, Michele Diana, St phane Cotin, Jacques Marescaux, Robust augmented reality registration method for localization of solid organs' tumors using CT-derived virtual biomechanical model and fluorescent fiducials, *Surgical Endoscopy*, **2016**, DOI 10.1007/s00464-016-5297-8.
7. Dunja Sobot, Simona Mura, Semen O. Yesylevskyy, Laura Dalbin, Fanny Cayre, Guillaume Bort, Julie Mouglin, Didier Desma le, Sinda Lepetre-Mouelhi, Gr gory Pieters, Bohdan Andreiuk, Andrey S. Klymchenko, Jean-Louis Paul, Christophe Ramseyer & Patrick Couvreur, Conjugation of squalene to gemcitabine as unique approach exploiting endogenous lipoproteins for drug delivery, *Nature Communications*, **2017**, 15678 DOI: 10.1038/ncomms15678.

8. Fanny Cayre, Simona Mura, Bohdan Andreiuk, Dunja Sobot, Sandrine Gouazou, Didier Desmaele, Andrey S. Klymchenko and Patrick Couvreur, In Vivo FRET Imaging to Predict the Risk Associated with Hepatic Accumulation of Squalene-Based Prodrug Nanoparticles, submitted to *Advanced Healthcare Materials*.
9. Oleksandra Bugera, Bohdan Andreiuk, Andrey Klymchenko, Yves Mely, Vasyl G. Pivovarenko, Strong Electrofluorochromic Red Edge Effect of Adenosine 5'-Triphosphate Anion on the Fluorescence of New Cationic and Zwitterionic Flavonols in Aqueous Buffer (manuscript in preparation).

## List of presentations

1. Bohdan Andreiuk, Mayeul Collot, Andreas Reisch, Yves Mely, Vasyl Pivovarenko, Andrey Klymchenko, Novel ultra-bright fluorescent nanoparticles based on cationic BODIPY molecules, *Journée Campus Illkirch (Illkirch, France)*, **2015** (poster presentation).
2. Bohdan Andreiuk, Andreas Reisch, Yves Mely, Andrey S. Klymchenko, Efficient encapsulation of cyanine dyes with minimized self-quenching: bright fluorescent polymer nanoparticles, *14th conference on methods and applications in fluorescence (Wurzburg, Germany)*, **2015** (poster presentation).
3. Bohdan Andreiuk, Andreas Reisch, Yves Mely, Andrey S. Klymchenko, Efficient encapsulation of cyanine dyes with minimized self-quenching: bright fluorescent polymer nanoparticles, *Journée Campus Illkirch (Illkirch, France)*, **2016** (poster presentation).
4. Bohdan Andreiuk, Andreas Reisch and Andrey S. Klymchenko, Enhancing encapsulation and emission of cationic dyes inside biodegradable nanoparticles using hydrophobic counterions, *BioNanoMed (Krems, Austria)*, **2017** (poster presentation).
5. Bohdan Andreiuk, Andreas Reisch, Marion Lindecker, Gautier Follain, Nadine Peyri ras, Jacky G. Goetz, Andrey S. Klymchenko, Counterion-enhanced encapsulation and emission of cationic dyes inside nanoparticles for multicolour long-term tracking of living cells, *Journ e Campus Illkirch (Illkirch, France)*, **2017** (oral presentation).
6. Bohdan Andreiuk, Andreas Reisch, Marion Lindecker and Andrey S. Klymchenko, Counterion-enhanced emission approach to develop ultrabright cyanine-loaded fluorescent polymer nanoparticles for cell barcoding, *28th International Conference on Photochemistry (Strasbourg, France)*, **2017** (poster presentation).

**Self-assembly of ionic fluorescent dyes  
inside polymer nanoparticles:  
engineering bright fluorescence and  
switching****Résumé**

L'encapsulation dans des nanomatériaux de polymères de colorants ioniques à l'aide de contre-ions hydrophobes volumineux apparaît être une méthode très efficace pour générer des nanoparticules (NPs) fluorescentes ultra-brillantes pour la bioimagerie. Nous avons d'abord étendu cette approche par contre-ions aux colorants cyanine opérant dans la gamme du bleu au proche infra-rouge. A partir de NPs chargés en cyanines, une méthode de code-barre multicolore pour le traçage cellulaire à long terme a été développé. Ensuite, le rôle des contre-ions hydrophobes volumineux dans l'auto-assemblage des colorants cationiques à l'intérieur des NPs de polymères a été étudié en testant une large collection d'anions. Nous avons montré qu'une forte hydrophobicité du contre-ion augmente l'encapsulation du colorant, régule son *clustering* et empêche l'agrégation de nanoparticules, alors qu'une grande taille empêche l'auto-inhibition de fluorescence. Enfin, nous avons introduit les contre-ions à base d'aluminates et de barbiturates, qui sur-performent les tétraphénylborates fluorés. Ce travail procure une base solide au concept d'émission et d'encapsulation augmentées par contre-ions pour la préparation de NPs chargés en colorants fluorescents.

Mots clefs : Nanoparticules polymériques fluorescentes, encapsulation de colorants, inhibition de fluorescence par agrégation, émission augmentée par contre-ions.

**Résumé en anglais**

Encapsulation of ionic dyes with help of bulky hydrophobic counterions into polymer nanomaterials emerged as powerful method for generating ultrabright fluorescent nanoparticles (NPs) for bioimaging. Here, this counterion-based approach is extended to cyanine dyes, operating from blue to near-infrared range. Based on cyanine-loaded NPs, a multicolour cell barcoding method for long-term cell tracking is developed. Second, the role of bulky hydrophobic counterion in self-assembly of cationic dyes inside polymeric NPs is studied by testing a large library of anions. We show that high hydrophobicity of a counterion enhances dye encapsulation, prevents particle aggregation and tunes dye clustering, while large size prevents dyes from self-quenching. Third, counterions based on aluminates and barbiturates are shown to outperform fluorinated tetraphenylborates. This work provides a solid basis for counterion-enhanced encapsulation and emission concept in preparation of dye-loaded fluorescent NPs.

Keywords: fluorescent polymer nanoparticles, dye encapsulation, aggregation-caused fluorescence quenching, counterion-enhanced emission.